Differentiation and Magmatism on the HED Parent Body

Helen Olivia Ashcroft

Thesis submitted to the University of Oxford
for the degree of Doctor of Philosophy
in
Experimental Petrology

Department of Earth Sciences
and St Anne's College,
University of Oxford

Trinity 2016

Supervised by Professor Bernard Wood

Declaration

The contents of this thesis are all my own work, except where otherwise stated. The views and opinions expressed herein are mine and not necessarily those of any other person or body unless so attributed.

Citation: Helen Olivia Ashcroft (2016), Differentiation and Magmatism on the HED Parent Body, D.Phil. Thesis, University of Oxford, Department of Earth Sciences, Oxford, UK.

Keywords: Experimental Petrology

This thesis has been typeset using LaTeX 2$_\varepsilon$ and references were compiled using BibTeX. Many of the figures and calculations were produced using Wolfram Mathematica, *Wolfram Research* (2012).

Printed in the United Kingdom.

ABSTRACT

The Howardite-Eucrite-Diogenite (HED) meteorites are a suite of basalts, cumulates and breccias which originate from one differentiated parent body, and are linked to the asteroid Vesta. The HEDs are petrologically diverse with a range of major, minor and trace element compositions. Early crystallisation ages are recorded and so the HEDs provide us with a unique snapshot into the early solar system. The aim of this thesis is to investigate the petrogenesis of the eucrites and diogenites by addressing two questions. What is the Bulk Silicate Vesta (BSV) composition? What differentiation and magmatic processes have occurred? Putative BSV compositions were derived from the geochemistry of the meteorites and geophysical observations of Vesta. Series of one-atmosphere experiments and thermodynamic models investigated the BSV phase relations. Olivine crystallised at ∼1625 ^{o}C, followed by orthopyroxene at ∼1350 ^{o}C and feldspar at ∼1125 ^{o}C. Low-Ca pyroxene-melt partition coefficients for the minor and trace elements were measured. The compatibility of the REEs and HFSEs in low-Ca pyroxene increased by a factor of three, as temperature decreased from 1300-1125 ^{o}C and calcium content increased from $Wo_{0.5}$-Wo_{8}. These partition coefficients were combined with the observed phase relations to perform geochemical trace element calculations of differentiation and magmatic processes. My results suggest that BSV had an Mg#(100*(Mg/(Mg+Fe^{2+})) between 75-80, >43 wt. % SiO_2, 2.5× CI refractory lithophile elements, 0.5 wt. % MnO and 0.75 wt. % Cr_2O_3. A three stage model for Vesta's evolution is suggested. Firstly, extensive if not global partial melting of BSV. Then, equilibrium crystallisation of the mantle and fractional crystallisation of mantle-derived melts produced diogenitic cumulates and eucrite liquids, accounting for the range in major and trace element abundances. The re-equilibration of trapped melt in cumulates is also thought to have occurred. Finally, crustal anatexis produced the range in trace element fractionations seen.

EXTENDED ABSTRACT

The Howardite-Eucrite-Diogenite (HED) meteorites are the most abundant group of achondrites and are a suite of basalts, cumulates and breccias which originate from one differentiated parent body. The HED meteorites are unique as we can link them to their parent body, the asteroid 4 Vesta. The DAWN mission visited Vesta for one year in 2011-2012, producing a detailed map of the surface composition, and geophysical observations. This allows the HEDs to be placed into a geological context and make Vesta one of four planetary bodies that we can sample directly, the others being the Earth, Moon and Mars. The HEDs record early crystallisation ages and give us insight into the early solar system conditions and planet-forming processes. The HEDs are petrologically diverse with a range of major, minor and trace element compositions. The eucrites are basalts and gabbro cumulates, and the diogenites are cumulates spanning the sequence of dunites, harzburgites, orthopyroxenites and norites. The range in trace element compositions varies by $\sim$4 orders of magnitude, and a decoupling is seen between the major and trace element compositions. Although the eucrites and diogenites originate from one parent body, the exact genetic link between the petrologic types is unknown and debated.

The aim of this thesis is to investigate the petrogenesis of the eucrites and diogenites by addressing two key questions. Firstly, what is the Bulk Silicate Vesta (BSV) composition? Secondly, what differentiation and magmatic processes have occurred to produce the eucrites and diogenites? A multidisciplinary approach was taken to answer these questions combining laboratory experiments, thermodynamic and geochemical models.

Chapter 2 combines geochemical measurements of the meteorites with geophysical observations of Vesta to derive potential Bulk Silicate Vesta (BSV) compositions. One-atmosphere experiments were performed on these BSV compositions and their

derived melts to investigate partial melting and fractional crystallisation processes. The phase relations of these BSV compositions were observed with olivine crystallising first at ∼1625 ^{o}C, followed by orthopyroxene at ∼1350 ^{o}C and feldspar at ∼1125 ^{o}C. The results of these experiments suggested that a multistage model was required to produce eucrite liquids and diogenite cumulates. Firstly extensive, if not global, melting of Vesta occurred, likely forming a magma ocean. During the cooling of the planetesimal, equilibrium crystallisation of the magma ocean occurred until the crystal fraction was so high (between 55-70 %) that convection could not continue. The residual melt (30-45 % partial melt of Vesta) was extruded to the surface where it fractionally crystallised diogenite cumulates resulting in a residual eucritic melt, below temperatures of 1250 ^{o}C. The experiments were also used to test the applicability of the alphaMELTS thermodynamic software to the HED system. AlphaMELTS predicts the mineralogy and composition well, although it overestimates the pyroxene liquidus temperature by upto ∼70 ^{o}C and does not deal well with the minor elements. AlphaMELTS was then used to refine the major element Bulk Silicate Vesta composition to an Mg#(100*(Mg/(Mg+Fe^{2+})) between 75 and 80 and $>$ 43 wt. % SiO_2, with other elements in chondritic proportions.

In order to perform geochemical calculations for the minor and trace elements, appropriate mineral-melt partition coefficients have to be selected. Trace element partitioning behaviour varies with temperature, pressure, composition and oxygen fugacity. Calcium content and temperature have been observed to affect the partitioning behaviour of trace elements into pyroxene, although there is not a comprehensive, quantitative understanding. As low-Ca pyroxene is the most abundant mineral across the eucrites and diogenites, it will have the largest influence on the trace element budget during diogenite and eucrite formation. Therefore, in Chapter 3 mineral-melt partition coefficients were calculated from the experiments reported in Chapter 2, in addition to a further series of experiments where larger crystals were grown and a wider range

of trace elements were observed. The partitioning of 3^+ and 4^+ ions into pyroxene's M1 site and 2^+ and 3^+ ions into the M2 site were considered. Low-Ca pyroxene-melt partition coefficients for the minor and trace elements were measured. The compatibility of the Rare Earth Elements (REEs) and High Field Strength Elements (HFSEs) in low-Ca pyroxene increased by a factor of three, as temperature decreased from 1300-1125 ^{o}C and pyroxene Ca content increased from $Wo_{0.5}$ to Wo_8. For example for the 3^+ ions substituting into the M2 site, the D_o increased from 0.1 to 0.35. An increase in Al_2O_3 content was also observed to increase the compatibility of the REEs and HFSE elements. The lattice strain model was fit to the data of each experiment and lattice strain parameters were calculated. These parameters allowed the partitioning behaviour of each isovalent series to be compared within this suite of experiments, in addition to literature studies of partitioning in other planetary basalt suites. Lattice strain parameters were calculated using the predictive models of *Sun and Liang* (2013) and compared with the experimental results. The predictive models have much larger uncertainties than the experimental data and significantly underestimate the D_o of the HFSEs. The models are not sensitive enough to ascertain the change in partition coefficients over the HED range.

Chapter 4 combines the partition coefficients measured in Chapter 3 with the thermodynamic models of Chapter 2 in geochemical calculations to investigate possible differentiation and magmatic models of Vesta for the minor and trace elements. In the models for Cr_2O_3, an additional Cr-spinel phase was included in addition to the other main mantle minerals of olivine, orthopyroxene, clinopyroxene and feldspar. Firstly, the petrogenetic model suggested in Chapter 2 was tested, for partial melting followed by fractional crystallisation. The differentiation model predicts that the Dy/Yb ratio will decrease in the first 10 % partial melting of Vesta before remaining constant at a value of 1 for the liquids and 0.6 for the cumulates as the abundance of trace elements increases. Fractional crystallisation does not increase or decrease the Dy/Yb value,

however the trace element abundance increases as crystallisation progresses. Measured Dy/Yb ratios in the cumulates can be as low as 0.01 and also there are cumulates which contain higher than predicted Dy/Yb ratios for a given abundance. Therefore further processes are required. Re-equilibration of trapped melt in cumulates and subsequent crystallisation was considered, and this process was found to increase the trace element abundances and fractionations, accounting for the more enriched and less fractionated meteorites. Crustal anatexis, causing partial melting of eucrites and diogenites, can produce cumulates which have lower Dy/Yb ratios and trace element abundances. Both batch and fractional melting may occur within cumulates, and this re-melting mechanism can account for the granulite eucrites in addition to the most depleted and highly fractionated diogenites. The partial melts produced are more enriched in trace elements and, if mixed with average eucrite melts, can produce the Stannern group eucrites.

Although not required to explain the trace element variations, further magmatic processes may have occurred including crustal assimilation and magma chamber recharge. Accessory phases are also thought to contribute to the trace element signatures, but these have not been evaluated in this study.

These models were also used to refine the trace and minor element composition of Bulk Silicate Vesta as containing 2.5×CI refractory lithophile elements (the incompatible REEs, HFSEs and TiO_2), 0.5 wt. % MnO and 0.75 wt. % Cr_2O_3.

Therefore the work in this thesis has refined the major, minor and trace element composition of the Bulk Silicate Vesta. A three stage model of interior evolution is suggested of differentiation, crystallisation and crustal re-melting.

ACKNOWLEDGEMENTS

Firstly I would like thank my supervisor Professor Bernard Wood. Your lectures in thermodynamics and geochemistry inspired me to study the planets through experimental petrology. I'm honoured you gave me the opportunity to work in your lab during my undergraduate degree, and even more so that you helped me develop the project into a PhD (and get funding). Thank you for your patience, training, insight and discussions throughout the PhD. I will always be in awe of your knowledge and inherent understanding of thermodynamics and chemistry.

I would also like to thank all of the Experimental Petrology group for their support, encouragement and friendship. It's been a challenging and fun four years, and I've learnt so much from all of you (some of it even about science). Particularly Andrew Matzen, for patiently training me in the lab, letting me help take apart the furnaces, and the discussions regarding my project and data evaluation. I would like to thank Kate Kiseeva for her continual support, discussions and guidance throughout the project, and Jon Wade for some insightful discussions about my thesis topic and direction, and training in the laboratory.

I would like to thank everyone who assisted and trained me in geochemical analysis. Thanks go to Norman Charnley for his patience and guidance with the carbon coater and the old SEM, Jon Wade with the new SEM, Vicky Smith, Ashley Norris and Kate Kiseeva with the EPMA, and Ashley Norris and Duane Smythe with the LA-ICP-MS.

I particularly want to thank my fellow PhD student William Nash, for the moral and academic support, especially during some of the long days doing experiments and getting analysis. I am very grateful to Mel Murphy for her encouragement with my professional development and guidance with scientific writing and presentations, and David Pyle and Don Porcelli as my college advisors for the useful discussions.

I would like to acknowledge the STFC council for funding my project and the

Meteoritical Society, Department of Earth Sciences and St Anne's college for providing additional funding to attend conferences. I would like to thank all of those people who I have met and had discussions with at conferences, particularly at UKPF and LPSC. I would particularly like to thank Duck Mittlefehldt, Jean-Alix Barrat and Richard Greenwood for their insightful discussions about the HED meteorites. I would also like to acknowledge and thank my examiners Hilary Downes and Don Fraser for their interesting and critical discussion of my work during my viva.

I am very grateful for the valuable discussions with my fellow PhD students about my project and the write up; particularly Brendan Dyck, Nikita Kaushal, Mike Stock, Tim Middleton, James Moore. Laura Ludtke, Tash Ryan, Alex Lewis - thanks for coercing me into attending the college wine tastings and joining St Anne's MCR committee. I would like to thank Delphine Vaneecke for the reminder that there is a life outside of academia, and encouraging me to be more sociable (and go to the gym).

I'd also like to thank my fellow geologists from my undergraduate days who are doing PhDs, particularly Emma Liu, for going through this process together despite our reunions being few and far between, and coinciding with conferences or weddings.

Choristers of Hertford College: thanks for introducing me to wide range of music and my husband. The years of parlour games, lawn games, fireworks, gowns, tours, dinners and singing of Mozart's Requiem around the piano into the small hours will never be forgotten.

Thanks to my parents for 26 years of love, support and encouragement, not just with the thesis but for everything. Last, and definitely not least, my husband Andrew Furniss. I wouldn't be where I am today without you.

DEFINITIONS

General

- CAI - Calcium Aluminium Inclusion. CAI's are the oldest material in our solar system, and used as the age for the start of our solar system.
- CI chondrite - A group of Carbonaceous (C) chondrites named after the type locality Ivuna (I). They are traditionally seen as some of the most primitive meteorites, which have the strongest similarity to the composition of the solar nebula. Due to this reason they are commonly used for comparison with other planetary samples.
- BSV - Bulk Silicate Vesta
- HED - Howardite Eucrite Diogenite
- IW - Iron-Wustite oxygen buffer.
- $\Delta^{17}O = \delta^{17}O$ - 0.52 $\delta^{18}O$. This equation relates the abundances of the isotopes ^{17}O and ^{18}O to each other.

Minerals and Composition

- Mg# = $100 \times \left(\frac{Mg}{Mg+Fe^{2+}}\right)$
- An - Anorthite. Calcium end-member of feldspar. $CaAl_2Si_2O_8$
- Wo - Wollastonite. Calcium end-member of pyroxene. $CaSiO_3$
- En - Enstatite. Calcium end-member of pyroxene. $MgSiO_3$
- Fs - Ferrosilite. Calcium end-member of pyroxene. $FeSiO_3$
- Fo - Forsterite. Magnesium end-member of olivine. Mg_2SiO_4

- Fa - Fayalite. Iron end-member of olivine. Fe_2SiO_4

Geochemical Elements

- HFSE - High Field Strength Elements
- HSE - Highly Siderophile Elements
- REE - Rare Earth Elements
- HREE - Heavy Rare Earth Element
- MREE - Middle Rare Earth Element
- LREE - Light Rare Earth Element
- KREEP - An evolved geochemical component observed in lunar rocks, containing high quantities of potassium, REEs and phosphorus.

Analytical techniques

- 1 atm - 1 atmosphere pressure.
- BSE - Back Scattered Electron image
- SEM - Scanning Electron Microscope
- EPMA - Electron Probe MicroAnalyser
- LA-ICP-MS - Laser Ablation Inductively Coupled Plasma Mass Spectrometry

Contents

List of Figures

List of Tables

Chapter 1

Introduction

The objectives of this chapter are to review what is known about the howardite-eucrite-diogenite (HED) meteorites and their geological setting, the asteroid Vesta, with a particular emphasis of what we have learnt from the recent DAWN mission. The formation and differentiation of Vesta will be discussed, including its evolution and possible petrogenetic models to produce the geochemistry of the HED meteorites. Then the gaps in the current knowledge will be identified, the thesis objectives defined and an overview of each subsequent chapter.

1.1 HED Meteorites

The HED group of meteorites are the most common group of differentiated or achondrite meteorites, accounting for around 5 % of all meteorite falls and 1332 kg of material in total (`http://www.nasa.gov`). The eucrite meteorites are basalts and cumulate rocks, and the diogenites are cumulates ranging from dunitic to norite in composition (*Mittlefehldt*, 2015), and together they represent the crustal rocks of a small differentiated body. Often these samples have undergone alteration and brecciation. Surface breccias containing a mixture of eucrite and diogenite lithologies, both greater than 10 %, are classified as howardites; and can also contain exogenic material including chondritic material (*Zolensky et al.*, 1996). Evidence for both impact and thermal

metamorphism can be found in the meteorites. HED meteorites have been recovered globally as both finds and falls. Eucrites are the dominant subtype found, for example 35 out of the 62 witnessed falls are eucritic, 11 are diogenitic and 16 are howardites (`http://www.mindat.org`). Likewise, out of the 275 HED meteorites recovered from the Antarctic, 149 are eucrites, 17 are diogenites and 29 are howardites (*McSween et al.*, 2013a). The HED meteorites are volatile-depleted, compared to Earth, and the occurrence of small amounts of Fe metal and sulphide (FeS) suggest that they formed on a reduced planetesimal, whilst the mineralogy suggests a low pressure body. In addition to the co-occurrence of eucrites and diogenites in howardites, the other link which suggests that the HED meteorites originate from the same parent are the homogeneous oxygen isotope signatures. The range of plagioclase and olivine compositions are shown in Figure 1.1 and pyroxene compositions in Figure 1.2; both figures are taken from *Mittlefehldt* (2015). The fractionation of REE elements (demonstrated by the Dy/Yb ratio) for the subgroups of the HED meteorites are plotted against the abundance of REE elements (Yb) and bulk Mg# in Figure 1.3 to demonstrate the range in trace element abundances and fractionation.

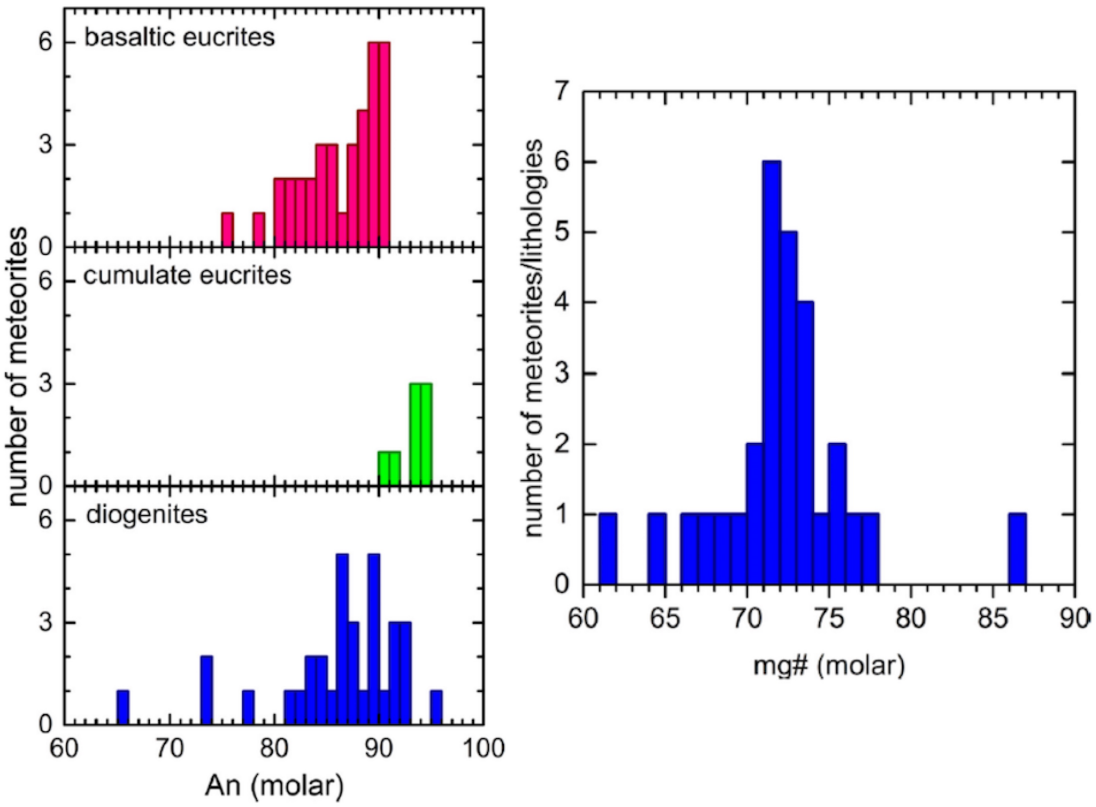

Figure 1.1: On the left histograms of HED plagioclase compositions are shown (molar An) (Figure 8 from *Mittlefehldt* (2015)) and on the right a histogram of the diogenitic olivine Mg#s. (Figure 6 from *Mittlefehldt* (2015))

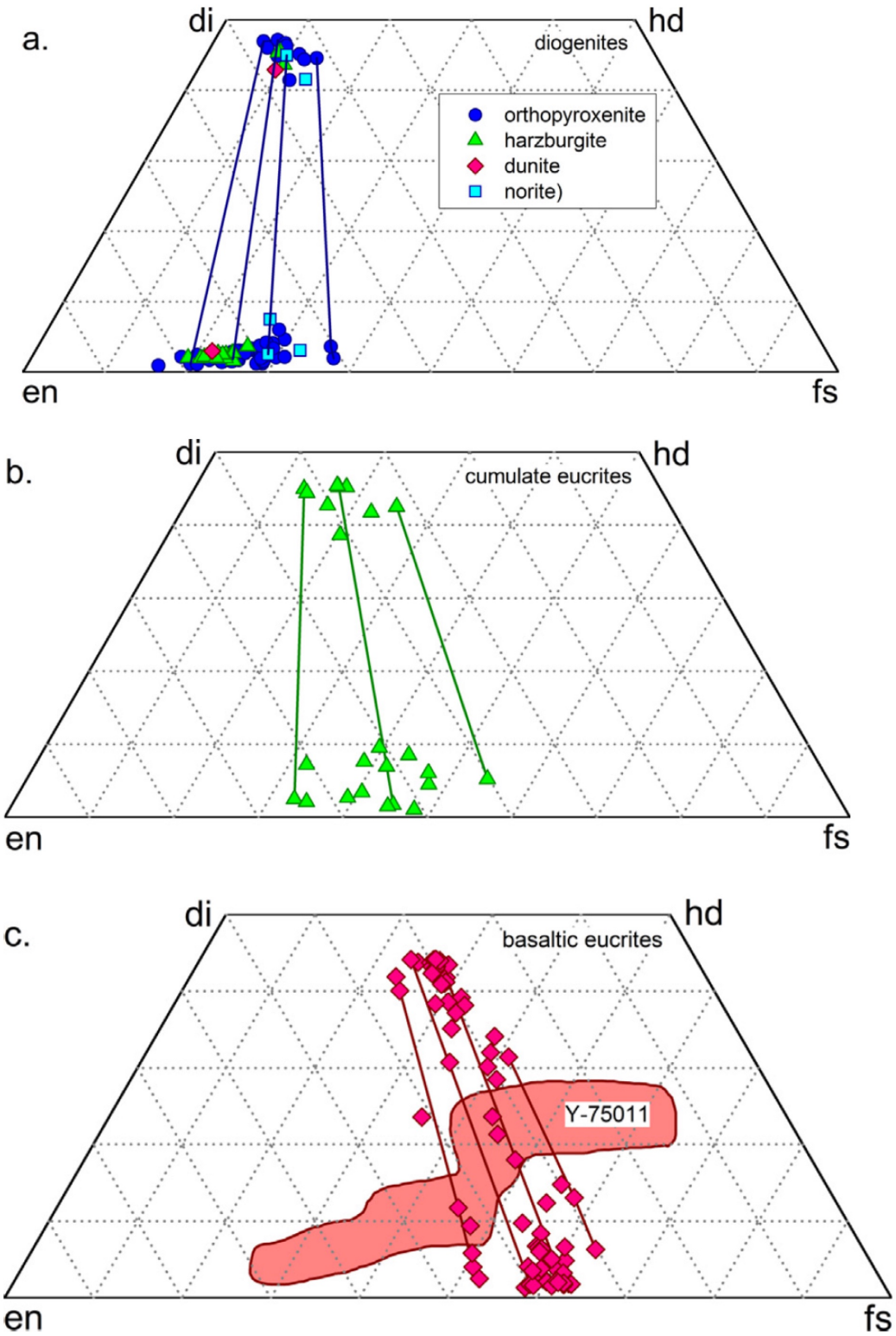

Figure 1.2: HED pyroxenes plotted in the pyroxene quadrilateral. Di = Diopside, hd = hedenbergite, en = enstatite, fs = ferrosilite. Range of Pyroxene compositions in a) diogenites, b) cumulate eucrites and c) basaltic units. Tie lines between low-Ca and high-Ca pyroxenes link together host pyroxene and exsolved pyroxene lamellae in individual meteorite compositions. The Y-75011 area denotes the composition of primary pyroxenes seen in unmetamorphosed basaltic clasts. Tie lines between points denote coexisting low-Ca pyroxene hosts and high-Ca pyroxene exsolutions. (Taken from Figure 3 in *Mittlefehldt* (2015)).

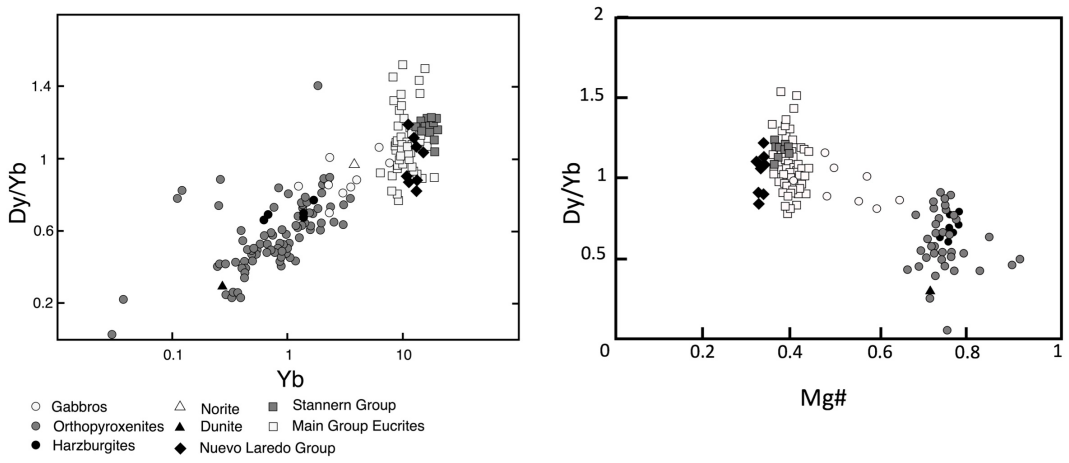

Figure 1.3: On the left the Dy/Yb vs Yb abundance in the diogenites and eucrites and on the right the Dy/Yb ratio vs bulk Mg# for eucrites and diogenites are plotted. The Yb and Dy/Yb terms are normalised to CI chondrite (CI values taken from *McDonough and Sun* (1995)). Meteorite data taken from *Mittlefehldt* (2015).

Oxygen isotopes were first used to classify chondrite and achondrite meteorites by *Clayton et al.* (1976) who noted that different meteorite groups exhibit differences in oxygen isotope signatures, which are also different from those of the Earth. Three isotope plots demonstrate mass dependent and independent fractions seen in the terrestrial and extraterrestrial rock record (*Greenwood et al.* (2015), Figure 1.4). The samples from any particular body (e.g. Earth, Mars, Vesta) plot as separate, straight lines. The offset between the lines on Figure 1.4 demonstrate the mass independent offset in Δ^{17}O of each parent body compared to the terrestrial line. This offset is thought to be due to heterogeneity in oxygen isotope distribution across the early solar system. Mass dependent fractionation causes changes in δ^{18}O by processes such as crystallisation and so samples from each parent body define fractionation lines, e.g. Terrestrial Fractionation Line (TFL) and the Eucrite Parent Body (EPB).

The eucrites and diogenites show a constant average value of Δ^{17}O = -0.239 $\pm$ 0.007 ‰(*Greenwood et al.*, 2005) consistent with their origin from a homogenised source on

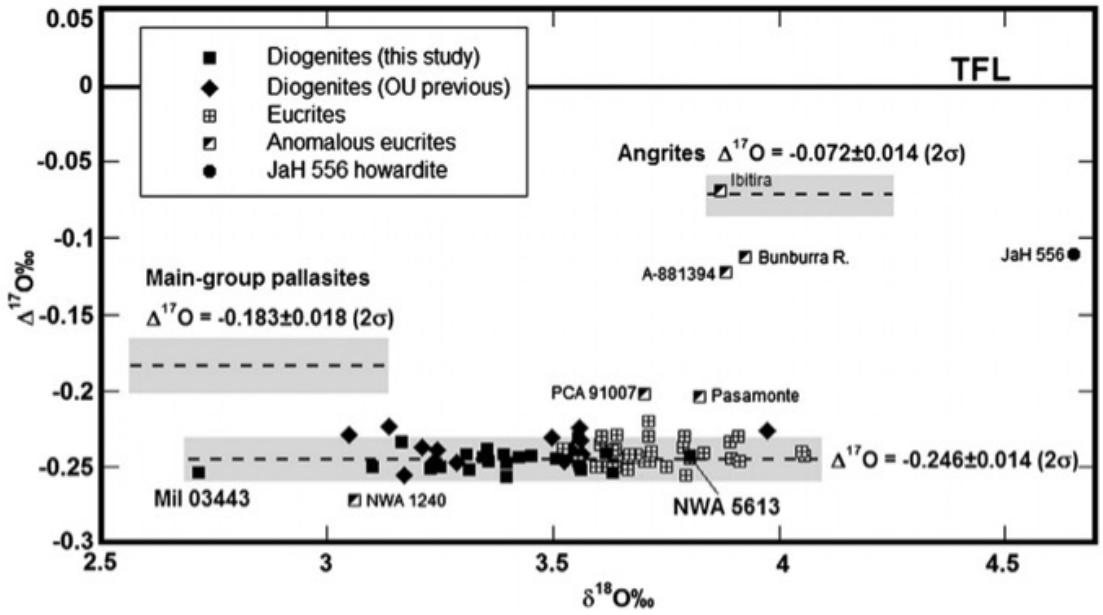

Figure 1.4: Oxygen Isotopes in the HED Meteorites. Δ^{17}O represents the mass independent isotope fractionation, and δ^{18}O represents the mass dependent fractionation. Taken from *Greenwood et al.* (2014). The HED meteorites clearly plot out their own fractionation line.

one parent body. Diogenites have very slightly lower Δ^{17}O values than eucrites, shown by the further measurements by *Greenwood et al.* (2014) where Δ^{17}O: -0.246 $\pm$ 0.014 ‰. Diogenites also show generally lower δ^{18}O values than eucrites, with a much larger range of $\sim$ 2.7-4 ‰compared to the eucrites' values of between 3.5-4 ‰.

1.1.1 Eucrites

Basaltic eucrites

The basaltic eucrites are a texturally diverse group of fine- to medium- grained rocks of basaltic composition which generally exhibit ophitic or subophitic, and more rarely, vitrophyric textures. The mineralogy of these rocks is predominantly Ca-rich plagioclase and pigeonite in relative modal proportions of 40:60 with minor olivine, spinel, quartz and phosphates. The basaltic eucrites are subdivided into groups based on their major and trace element concentrations- the Main group, Nuevo Laredo group, and the Stannern group. The Main group eucrites exhibit wide variations in Mg# (35-42)

but limited variation in incompatible elements, whereas the Stannern group eucrites demonstrate significant incompatible element variation but limited Mg# variation (Yamaguchi et al. 2009). Brecciated eucrites are classified as monomict if their clasts are compositionally coherent (one type of eucrite) or polymict if more than one type of eucrite clast is seen. The average compositions of the primary igneous mineralogy of the non-cumulate eucrites (Main group) are An_{81-93} and $Wo4_{11\pm6}En_{36\pm4}Fs_{54\pm6}$, Two subgroups of eucrites can be defined: the Stannern and Nuevo Laredo groups. The Stannern group eucrites have higher Ti and incompatible trace element abundances compared with the majority of non-cumulate eucrites but with similar major element composition. The Nuevo Laredo group are more evolved (bulk Mg# = 33, *Mittlefehldt* 2015) in terms of their major element compositions, and some are more enriched in trace elements than the Main group eucrites. Backscattered Electron (BSE) images of two non-cumulate eucrites Bereba (Main group) and Stannern (Stannern group) are shown in Figure 1.5, displaying a variety of crystal textures and extent of brecciation. *Barrat et al.* (2007) suggested that the Stannern and Nuevo Laredo groups could represent anatectic melts produced by the partial melting of eucritic crust, and *Yamaguchi et al.* (2009) suggested that the group of thermally metamorphosed 'granulite' eucrites could represent the depleted restite. In terms of the Rare Earth Elements (REE), the main group eucrites show flat REE patterns (Dy/Yb values close to 1 in Figure 1.3) and with around 10 times enrichment compared with CI chondrites. The granulite eucrites have relatively flat REE patterns with 3-10×CI enrichment and also a slight enrichment in Eu. The Stannern group eucrites are slightly more enriched compared to CI chondrites than the main group eucrites and show a slight depletion in Eu. Representative HED REE patterns for the eucrites and diogenites can be seen in Appendix F.

Cumulate Eucrites

The cumulate eucrites are medium-coarse grained, equigranular gabbroic rocks with average plagioclase and pyroxene compositions of An_{91-95} and $Wo_{7\pm2}En_{49\pm6}Fs_{44\pm6}$. The

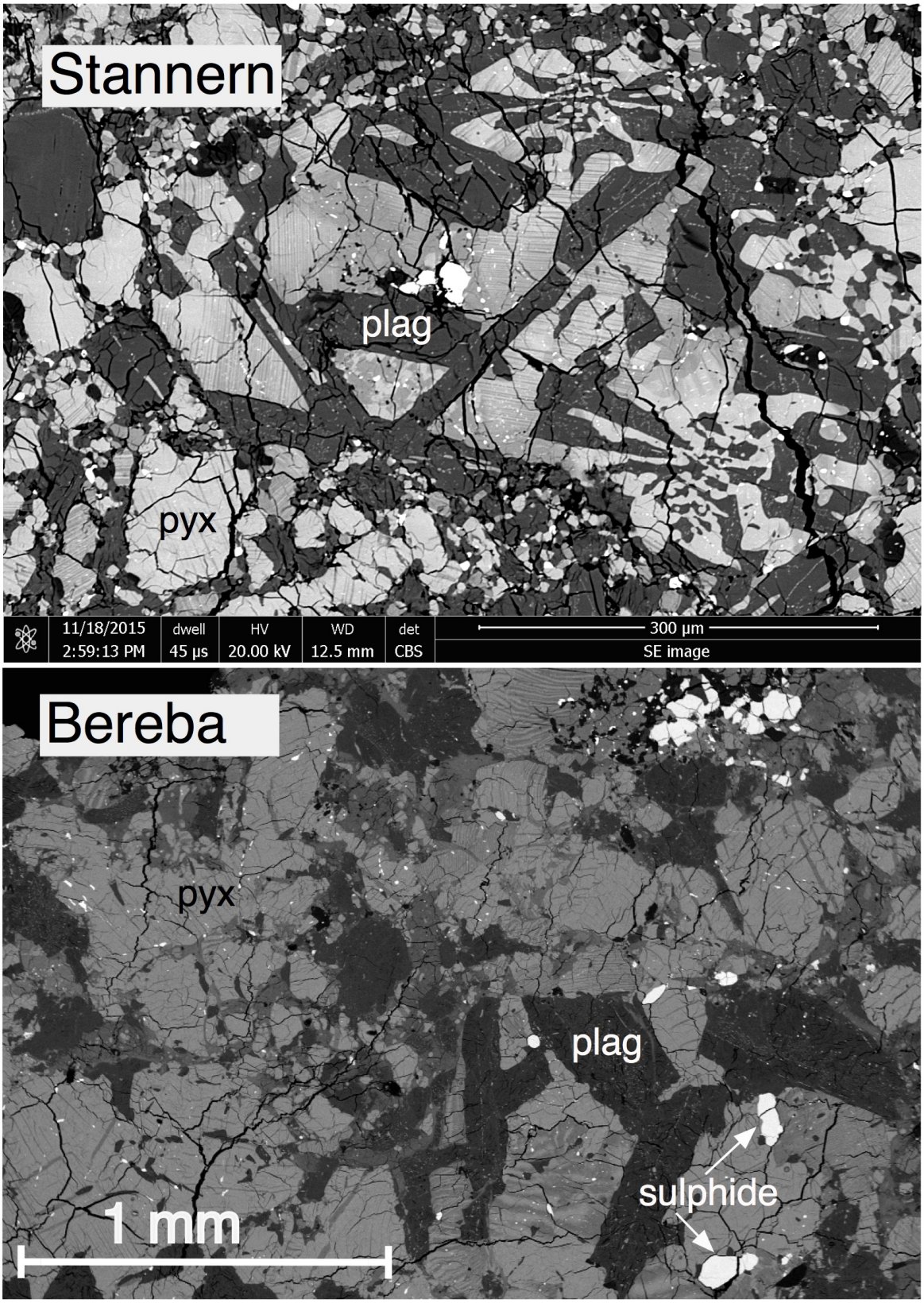

Figure 1.5: A BSE image of two eucrites, Bereba and Stannern taken on the FEI Quanta FEG 650 SEM, Department of Earth Sciences, University of Oxford. Pyroxene, plagioclase and sulphide phases have been labelled. Features of interest include impact melting, exsolution lamellae of augite in some pyroxene crystals and some crystal zoning.

cumulate eucrites have relatively flat REE patterns with 0.1-10 times CI abundances. The cumulate eucrites show trace element signatures similar to the basaltic eucrites.

1.1.2 Diogenites

The diogenites are coarse-grained orthopyroxene-rich cumulates which can be classified as dunite, harzburgite, orthopyroxenite or norite depending on their modal mineralogy of orthopyroxene, olivine and plagioclase (*Beck and McSween* (2010), *Beck et al.* (2012), *Beck et al.* (2013)). Low-Ca pyroxene is the predominant mineral in the diogenite group with a relatively small range in major element compositions $Wo_{2\pm1}En_{72\pm2}Fs_{24\pm1}$, and can also contain olivine (Mg# = 70-75) and plagioclase (An_{80-92}). Compared with the relatively narrow range in major element compositions, the diogenites show a much larger range in minor and trace element abundances. Al and Cr contents vary by a factor of five, Ti by a factor of 17 (*Mittlefehldt*, 2015). The diogenites have much lower REE abundances than eucrites, showing a range of abundances spanning four orders of magnitude from 0.001 to 1×CI enrichment. Some diogenites show fractionated REE patterns (characterised by low Dy/Yb ratios seen in Figure 1.3), with more depleted LREE than HREE, and some show slight depletions relative to the general trend in Eu. This Eu depletion indicates a minor amount of plagioclase crystallisation from their parent melt, and also the reducing conditions under which they formed. The incompatible and minor elements are independent of the major element composition of the pyroxene but correlate with each other (*Fowler et al.*, 1994, 1995; *Shearer et al.*, 2010). The diogenites either occur as intact cumulate samples, or breccias containing compositionally distinct clasts. A BSE image of two diogenites: Johnstown and Shalka are shown in Figure 1.6.

1.1.3 Howardites

The Howardites are polymict impact breccias which contain fragments of diogenites, eucrites and other petrogenetically distinct material including CM, CI and CR Chondrite material (*Zolensky et al.*, 1996). The howarditic layer is the regolith which makes

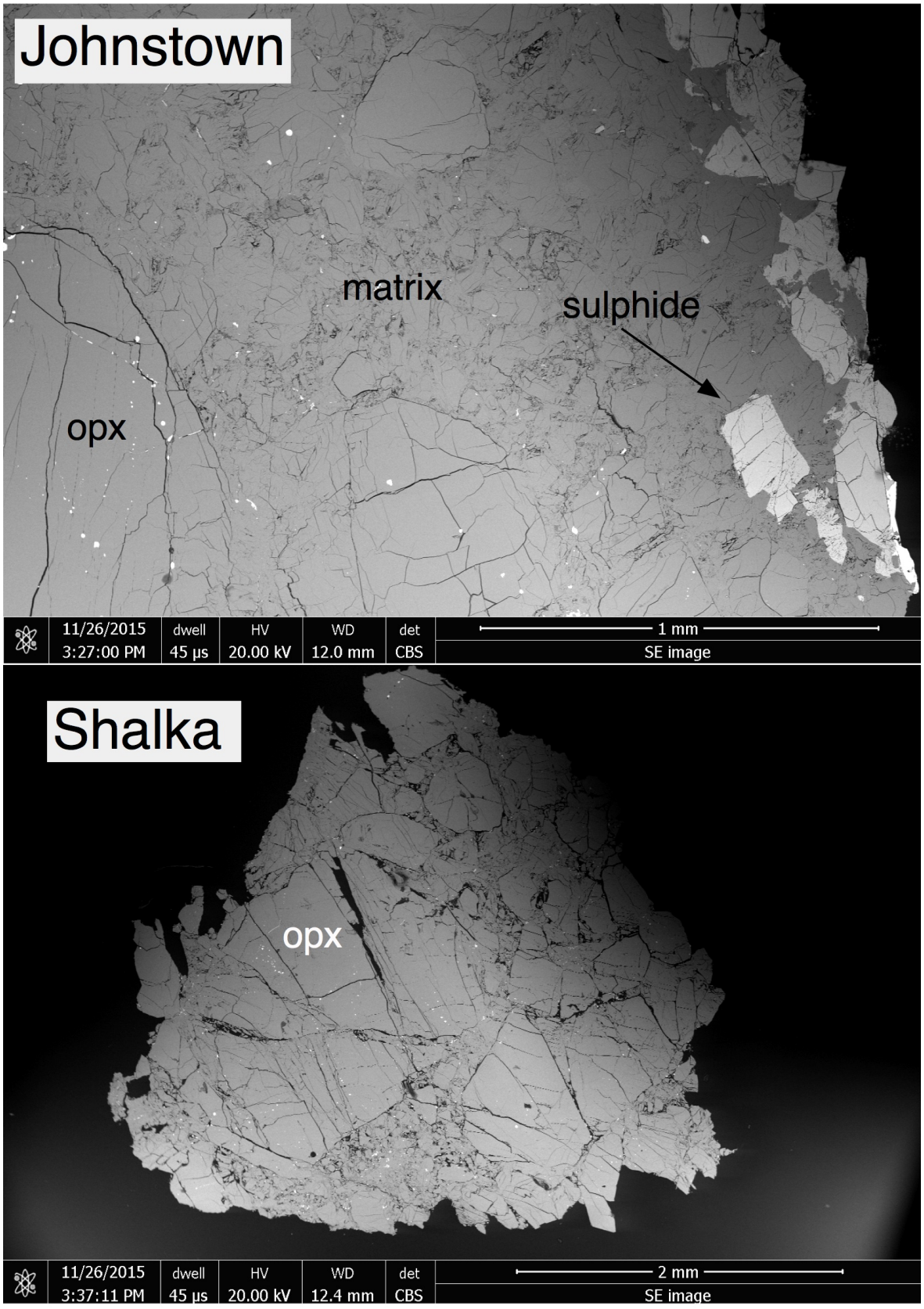

Figure 1.6: A BSE image of two diogenites, Johnstown and Shalka taken on the FEI Quanta FEG 650 SEM, Department of Earth Sciences, University of Oxford of the Johnstown and Shalka diogenites. Pyroxene, plagioclase and sulphide phases have been labelled.

up the top 1-2 km of Vesta's surface (as seen by DAWN (*Jaumann et al.*, 2012)) . Although howardites predominantly contain eucrite and diogenite material, some unusual clasts of plagioclase, ferroan olivine and silica are found which are believed to originate from a source which is more evolved than the eucrite source (*Barrat et al.*, 2012) and are interpreted texturally as debris from dykes or lava flows. This more evolved material does not resemble the mesostasis areas within eucrites and may either represent material not yet seen on Vesta or be unrepresentative eucrite material. These clasts suggest that KREEP-like lithologies may occur on Vesta and could be formed by the extensive crystallisation of a eucrite composition, i.e. they may represent a more evolved sample of the partial melts of eucrites which are described by *Yamaguchi et al.* (2009). The howardites can be lithologically complex, but generally show a 2:1 abundance of eucrite to diogenite material. Some particularly Mg-rich olivine and and orthopyroxene clasts and minerals have been identified in the howardites, which may represent mantle minerals (*Lunning et al.*, 2015). BSE images of two howardites: Camel Donga and Kapoeta are shown in Figure 1.7.

1.1.4 Alteration and Metamorphism

Many of the HED meteorites exhibit post-crystallisation alteration and metamorphism, with some samples providing evidence for thermal metamorphism with peak temperatures up to 1100 ^{o}C. This metamorphism overprints any primary pyroxene zoning and partial melting up to granulite facies has been observed. The extent of thermal metamorphism has been studied in detail, with *Takeda and Graham* (1991) splitting the eucrite meteorites into seven groups of increasing metamorphism. The eucrites are assigned a relevant group depending on the chemical zoning and exsolution which is seen in the pyroxene crystals. Most eucrites show some evidence of secondary reheating events with average temperatures of 700-1000 ^{o}C (*Takeda and Graham*, 1991) . *Yamaguchi et al.* (1996) proposed an emplacement mechanism for eucrite lavas that were erupted then rapidly buried by subsequent lava eruptions, which provided enough heat for metamorphism to occur. Recrystallisation within eucrite samples can also

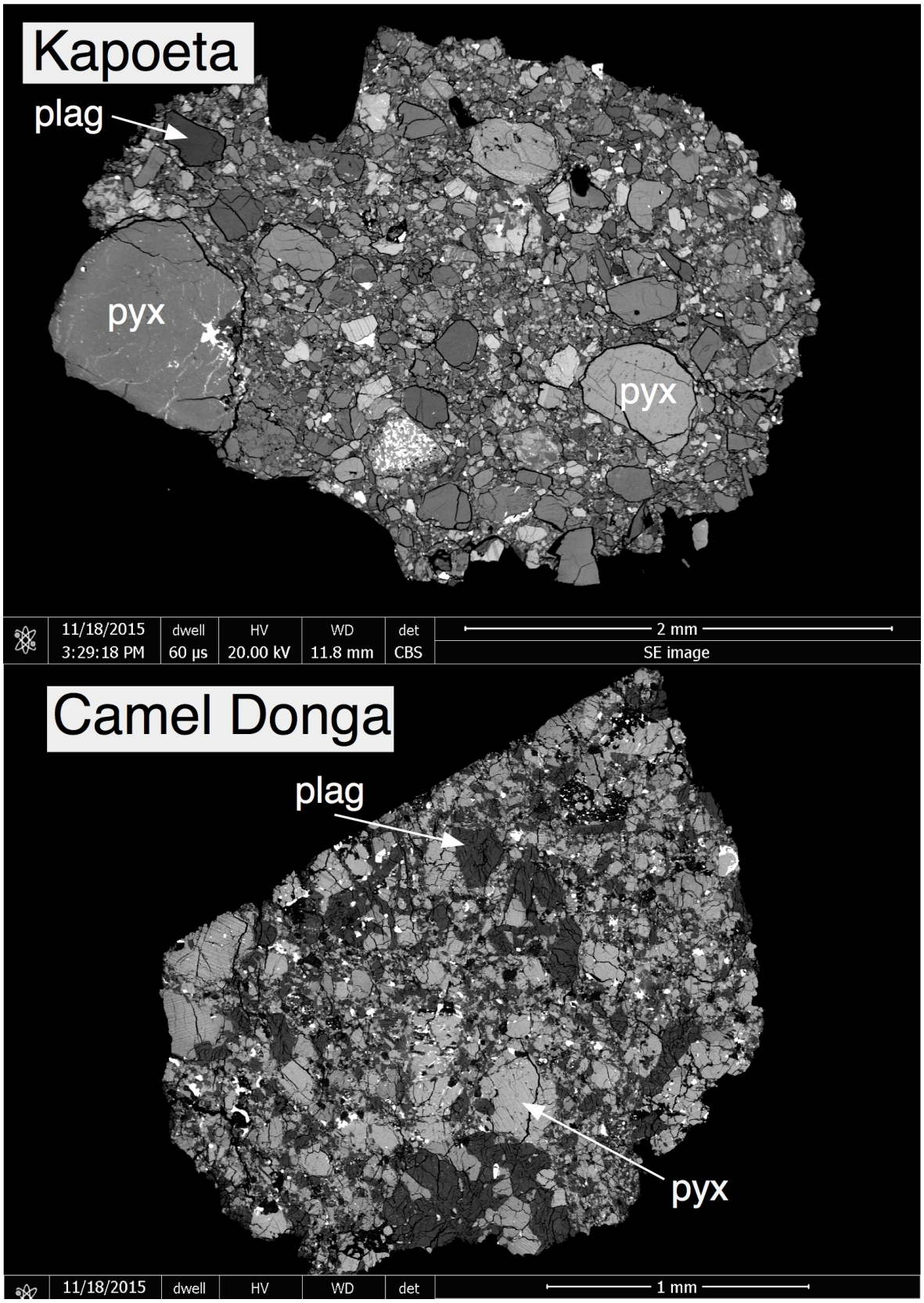

Figure 1.7: A BSE image of two howardites Kapoeta and Camel Donga, taken on the FEI Quanta FEG 650 SEM, Department of Earth Sciences, University of Oxford of the Kapoeta and Camel Donga howardites. Pyroxene and plagioclase crystals have been labelled.

occur through impact melting. *Warren and Kallemeyn* (2001) observed that the less metamorphosed (type 1-4) eucrites (Stannern trend) are more enriched in incompatible elements compared with the more metamorphosed (type 5-7) eucrites (Main Group). *Yamaguchi et al.* (2009) dispute this and suggest a two phase thermal history for Vesta with a long-term heating of eucrites to temperatures of 800-1000 ^{o}C due to the burial of material by subsequent eruptions, with shorter term potentially more localised heating events due to emplacement of new eucrite magmas or impact melting (1100 ^{o}C) which caused brief partial melting events of the granulite facies eucrites. Evidence for long-term moderate heating comes from pyroxene exsolution lamellae which require slow cooling rates to form, and the evidence for shorter higher temperature events is derived from laths of tridymite, which would invert to quartz over a long time period, and so the preservation suggests a short event.

1.2 Vesta

1.2.1 Physical Properties

Vesta was first discovered in 1807 by Heinrich Olbers and is the second largest asteroid by mass, and third largest by volume in our solar system. Vesta lies in the inner asteroid belt at an average distance of 2.35 AU from the sun. Vesta's shape is most accurately described as an oblate spheroid with major semi-axes of 286.3, 278.6 and 223.2 km (*Russell et al.*, 2012). Vesta is unique in that it has been identified as the only large remaining differentiated asteroid with a basaltic surface. Vesta is considered an asteroid rather than a dwarf planet as its non-spherical shape suggests that hydrostatic equilibrium has not been reached, although finite element modelling of Vesta by *Fu and Elkins-Tanton* (2014) suggests that Vesta may have been able to reach near hydrostatic equilibrium in the first 20 Ma after solar system formation. After this Vesta would have been too cold to relax viscously, which is why hydrostatic equilibrium was not reached after the Venenia and Rheasilvia impact basin formation.

1.2.2 Spectral Properties

Asteroids are classified from Earth-based telescope observations of their spectral reflectance at different electromagnetic wavelengths, and the most recent taxonomy can be found in *DeMeo et al.* (2009). These spectra are a function of particle size, mineral structure and composition. Laboratory-based measurements of meteorite groups can also be performed on physical samples, and (*McCord et al.*, 1970) observed that the InfraRed (IR) spectra of the HED meteorites matched the IR spectra of the asteroid Vesta. This is one of the few matches between meteorite groups and asteroids which have been made to date, and was the first link between any meteorite groups and a potential parent body. The Vestan IR spectra are dominated by the mineral pyroxene which has absorptions at 0.9 microns and around 2 microns (*McCord et al.*, 1970; *Adams*, 1974) which are attributed to the distribution of cations, particularly Fe^{2+} iron in the M1 and M2 sites of the pyroxene mineral. The other common basaltic minerals olivine and plagioclase do not have such a strong influence on the spectra. Although other basaltic meteorites exhibit similar spectra, the absorption bands are specific to the composition of the mineralogy. Thus the spectra for Vesta and the HEDs are characteristic for this parent body.

Based on IR spectra of Vesta, *Gaffey* (1997) presented a geological map for Vesta detailing the compositional heterogeneity across the surface. *Gaffey* (1997) identified a diogenite-rich region in the southern hemisphere, and some potential eucritic or olivine regions around the equator, but with the majority of the surface comprising a spectral mixture of eucrite and diogenite material.

Spectroscopic observations of more than half a million km to 100s km sized planetary bodies in the asteroid belt have been made. The asteroids can be classified into different taxonomic groups based on this composition. The asteroid Vesta lends its name to the V-type of asteroids, which comprise ~ 6 % of the asteroid belt (*DeMeo et al.*, 2009). Vesta is the only large (100s km) sized asteroid which shows a basaltic surface, and is therefore unique. However 20 asteroids < 10 km in size have been classified as V-type, and are called the 'Vestoids'. These were identified by *Binzel and Xu*

(1993), and six match diogenite compositions, and 14 eucrites. *Burbine et al.* (2001) performed a more detailed study of the spectra of HED meteorites and comparison with the Vesta and Vestoid compositions (shown in Figure 1.8). The range in spectral signatures observed can be attributed to variations in mineralogy and composition between samples, and also the size of particles which can alter the intensity of the spectra (*Burbine et al.*, 2001). The Vestoids are interpreted to be blocks of Vesta that have been excavated from the surface of the asteroid. The Vestoids are thought to to be the source of the HED meteorites which are delivered to Earth, due to their location in the asteroid belt in one of the planetary gaps where orbital resonances promote the dynamical movement of material through the solar system (*Burbine et al.*, 2001).

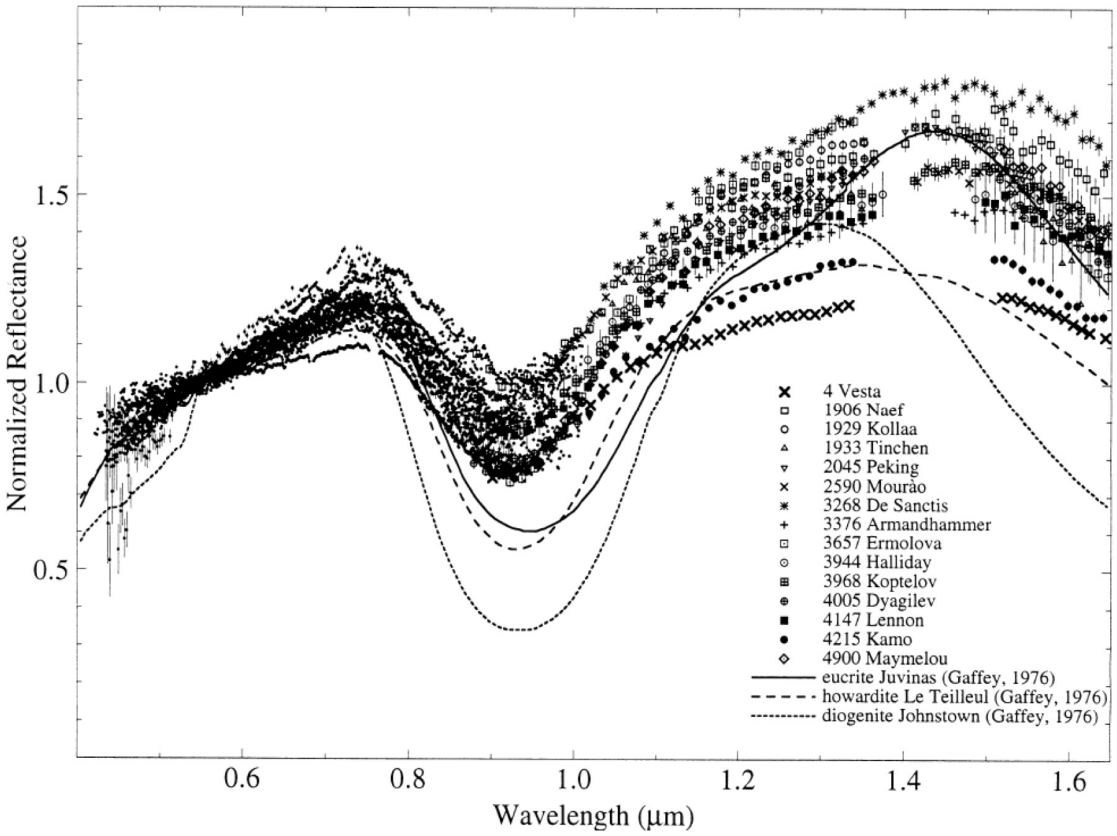

Figure 1.8: IR surface spectra of Vesta (x), the Vestoids (other symbols) and laboratory based IR measurements of representative eucrite, howardite and diogenite meteorites. All show the characteristic absorption at 0.92 microns. Taken from *Burbine et al.* (2001).

The Hubble Space Telescope images were used to estimate Vesta's size and shape

as an ellipsoid of 280 x 272 x 227 km, with a mean density of Vesta being 3.8±0.6 gcm^{-3}. This density is higher than that measured for the HEDs, suggesting that Vesta contains a metal core in addition to its basaltic crust (*Thomas et al.*, 1997). A large 20-30 km deep, 460 km wide impact crater across the south pole of Vesta was also identified.

1.2.3 DAWN at Vesta

The main objectives of the NASA DAWN mission were to map Vesta's topography, surface composition and geophysical properties, and the payload on the space craft included a Framing Camera (FC), Visible and Infrared Spectrometer (VIR) and a Gamma Ray and Neutron Detector (GRaND) in addition to radio tracking of the spacecraft. Measurements were taken in three orbits: Survey, Low Altitude Mapping Orbit (LAMO) and High Altitude Mapping Orbit (HAMO) at 2700, 684 and 210 km above Vesta's surface respectively.

The Framing Camera took stereo images of the asteroid's topography in addition to spectra recording global colour variations in the High Altitude Mapping Orbit. The Framing Camera operates in the visible to near-IR spectral range and the absorption spectra between 0.4 and 1 microns can be used to determine pyroxene composition and assess the degree of space weathering (*Buratti et al.*, 2013). The spectral resolution of the Framing camera was 60 m/pixel in the HAMO, and 16 m/pixel at LAMO, and mapped the surface topography and composition in detail. The impact crater at the south pole was identified as being two superimposed craters, the younger one named Rheasilvia (500 km wide) and the older Venenia Crater (400 km wide) which were dated using crater density as having the relatively 'young' solar system ages of 1 Ga and 2 Ga (*Schenk et al.*, 2012). The 1 Ga age of the Rheasilvia Impact is consistent with the suggested ages for the Vestoids, dependent on dynamical and modelled ages (*Marchi et al.*, 2012; *Nesvorny et al.*, 2008; *Marzari et al.*, 1996), and so the HED meteorites which fall to Earth are believed to originate from the Vestoids, and all samples are part of the Southern Hemisphere crust. Figure 1.9 shows a mosaic picture of Vesta, taken

by the DAWN mission.

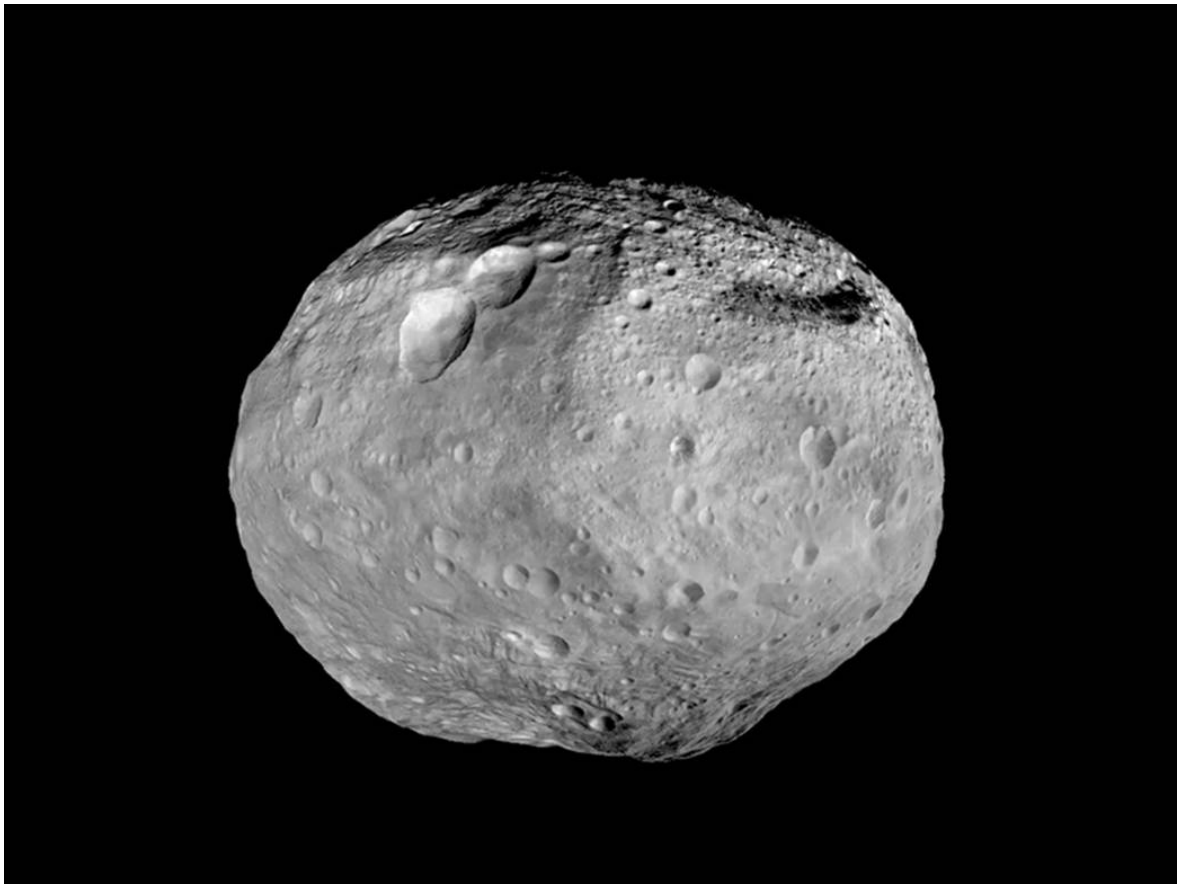

Figure 1.9: A mosaic picture of Vesta made up of Framing Camera images taken on DAWN's approach to Vesta. Scale as mentioned in the text. Image Credit: NASA/JPL-Caltech/UCAL/MPS/DLR/IDA

These high-resolution FC spectra allowed for a more detailed comparison of Vesta's surface with Vestoids, HED meteorites, and other asteroids observed in Near Earth Orbits (identified by *Hicks et al.* (2014)). *Buratti et al.* (2013) concluded that the Vestoids and diogenite meteorites were spectrally similar, and are a closer match to the spectra of the Rheasilvia basin than to Vesta as a whole. There is not a large spectral difference between the Rheasilvia and bulk Vesta spectra, however, suggesting that the Rheasilvia impact sampled a relatively well-mixed area of crust.

DAWN's high resolution Visible and Infrared Spectrometer (VIR) imaged 65 % of the Vestan surface between 700 to 70 m/pixel, depending on which orbit the spacecraft occupied. *De Sanctis et al.* (2012) used the 700 m/pixel data taken in the survey orbit

and identified vertical and horizontal compositional variations on the 100s of metre to 20 km scale, interpreting different spectral signatures to represent different mineralogies. Compositional variation at this scale suggests a complex geological history and that Vesta differentiated before impact bombardment. *Ammannito et al.* (2013) consider the lithological map produced from this VIR data, and conclude that the majority of Vesta's surface is howarditic or basaltic eucrite in composition. Diogenite-rich areas were also identified for example in the base of the Rheasilvia crater, and *Ammannito et al.* (2013) identified small olivine-rich areas.

The Rheasiliva crater is believed to sample up to 45 km depth in the Vestan crust, and so the mineralogy of the interior was studied at 200 m/pixel resolution using VIR and also GRaND measurements (*McSween et al.*, 2013b), in order to search for evidence of olivine. Eucritic material was observed to overlie diogenitic material in the crater, however, there was no evidence for olivine, which has implications for the internal structure and mineralogy of Vesta (*McSween et al.*, 2013b).

The third instrument investigating compositional differences across the Vestan surface is the GRaND which measures some of the elemental composition of the surface, particularly the Fe/O and Fe/Si ratios (*Prettyman et al.*, 2012). Areas that were rich in hydrogen were identified on the asteroid's surface, and attributed to volatile addition by chondritic impactors, in agreement with the CM, CR and CI material found within howardites (*Zolensky et al.*, 1996).

The combined VIR, FC and GRaND surface and composition data were combined to produce a global geological map of Vesta (*Yingst et al.*, 2014; *Williams et al.*, 2014). (Figure 1.10), complete with a chronostratigraphic column. Using asteroid-dating techniques, four main time epochs have been assigned tentatively as: pre-Venenian >2.1 Ba, Venenian (2.1-1 Ba), Rheasilivian (1-0.3 Ba) and Marcian (<0.3 Ba), all are named after significant impacts which created major surface changes during Vesta's history.

1.2.4 Interior Structure

Thomas et al. (1997) estimated Vesta's shape as a triaxial ellipsoid from the Hubble

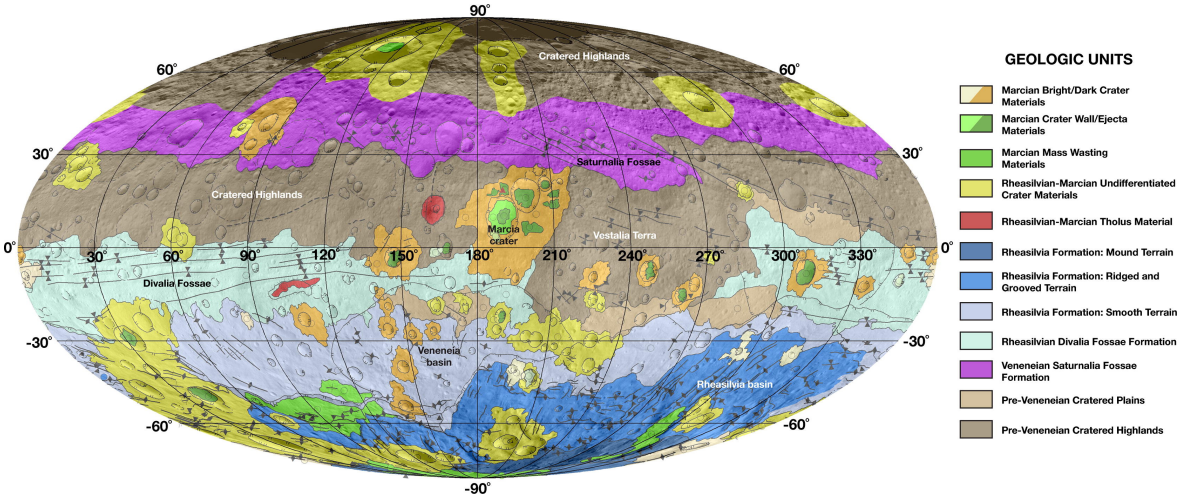

Figure 1.10: Geological Map of Vesta's surface with stratigraphic column taken from *Williams et al.* (2014). The beige units (cratered plains) around the North Hemisphere and equator are Pre-Venenian, the magenta unit is Venenian age, the blue units around the Southern Pole are Rheasilvian in age, and the red, yellow, green and orange units are the youngest and Marcian in age. For discussion of the ages of the units, see text.

Space Telescope images, and the Framing Camera onboard the DAWN mission mapped 80 % of Vesta's surface to a resolution of 260 m/pixel from a 2700 km altitude (*Jaumann et al.*, 2012). This accurate shape model allows the volume of Vesta to be calculated more accurately as 74.970 x 10^6 km^3 (*Russell et al.*, 2012).

The other main physical property of Vesta to be refined by DAWN was the mass of Vesta, which had previously been calculated as 2.6 $\pm$ 0.3$\times$ 10^{20} kg (*Konopliv et al.*, 2011) by the perturbations of Mars and other asteroids by Vesta. This estimate was refined to 2.59076 $\pm$ 0.00001$\times$ 10^{20} kg (*Russell et al.*, 2012) from measurements of radiometric tracking of the DAWN spacecraft around Vesta. DAWN measured the gravity field around Vesta up to degree 20 (*Konopliv et al.*, 2014). Combining the new estimates for shape and mass led to a new estimate of the bulk density of Vesta as 3456 kgm^{-3} (*Russell et al.*, 2012).

Spherical harmonics are used to describe the shape of a planet or asteroid, and the strength of its gravitational field. The equation for gravitational field is:

$$U(r,\phi,\lambda) = \frac{GM}{r} + \frac{GM}{r}\sum_{n=2}^{\infty}\left(\frac{R_o}{r}\right)^n \sum_{m=0}^{n}(C_{nm}cos(m\lambda)+S_{nm}sin(m\lambda))P_{nm}sin(\phi) \quad (1.1)$$

taken from *Konopliv et al.* (2014), originally derived in *Kaula* (1966). This equation can be used to predict the gravity field at any point on the surface of Vesta. U is the gravitational potential, GM is the gravitational constant multiplied by the mass of the planet, m is the order, n is the degree, C_{nm} and S_{nm} are the normalized spherical harmonic coefficients. R_o is the reference radius of the gravity model (for Vesta is 265 km (*Konopliv et al.*, 2014)), λ is the longitude, and ϕ is the latitude. The zonal coefficients are given by: J_n=-C_{n0}.

J_2 (degree 2, order 0) is the spherical harmonic coefficient that describes the gravitational flattening of a planet around its equator (orthogonal to its rotation axis), and is linked to the shape and interior density structure of a planet. For Vesta J_2 = 0.03178, suggesting that there is mass concentrated in the centre of the planet as a homogeneous density would predict a J_2 of 0.0350 (*Russell et al.*, 2012).

Ermakov et al. (2014) combine the shape, gravity and rotation rate to assess Vesta's proximity to hydrostatic equilibrium and find that early on in Vesta's history both the core and outer shape of Vesta were likely to have reached close to hydrostatic equilibrium. However, later impacts like Rheasiliva and Venenenia may have altered the global shape, and the asteroid may not have viscously relaxed afterwards.

Russell et al. (2012) consider Vesta as a two-layer asteroid, with a metal core and a silicate mantle portion. Assuming a core density between 7100 and 7800 kgm^{-3} (iron meteorite densities) and silicate density from the HED meteorites, a two layer mass balance model is used to reproduce J_2, and suggest an 18 % core mass and radius between 107-113 km. Porosity and sulphur content are not incorporated in this model. *Ermakov et al.* (2014) refine this model by considering Vesta as a three layer (crust-mantle-core) body and use the shape model of *Jaumann et al.* (2012) and the gravity model determined by *Konopliv et al.* (2014)), along with the geochemical information provided by the HED meteorites. A set of unique solutions are produced with core sizes which vary between 110-138 km, and density between 6000-8000 kgm^{-3}, depending on the sulphur content.

Another measure of interior density is the polar moment of inertia, and *Rambaux*

(2013) used the measured gravity coefficients to calculate this value for Vesta to be in the range 0.38-0.42, depending on the estimated core size and density, This is also lower than the predicted value for Vesta's shape and implies that there is a central mass concentration.

1.3 Formation and Evolution

There are three main stages in the formation of any planet: accretion, differentiation and evolution.

1.3.1 Accretion

A good summary of the physical and dynamic accretion processes can be found in *Righter and O'Brien* (2011). Collisions between dust and gas particles in the proto-planetary disk initiated the accretion process producing progressively larger planetary bodies, from pebbles through to planetesimals (Vesta) and eventually planets (Earth). Ages of these formation stages are inferred from isotope analysis from meteorites and planetary samples. Evidence for the existence of short-lived radiogenic nuclides ^{26}Al, ^{60}Fe and ^{53}Mn have been found in the HED meteorites (*Srinivasan et al.*, 1999; *Schiller et al.*, 2011; *Shukolyukov and Lugmair*, 1993; *Lugmair and Shukolyukov*, 1998) suggesting that Vesta formed within the first 4-6 Ma after solar system formation.

1.3.2 Differentiation

Our knowledge of the planetary differentiation processes comes from the geochemistry of the meteorites, in addition to thermochemical and numerical modelling.

Geochemistry

Long-lived radiogenic isotope systems can give us information on core formation and crustal formation. The hafnium-tungsten Hf-W system suggests that core formation occurred on the HED body within 1 Ma of planetesimal formation, and that there

are three clusters of ages for basaltic volcanism at 4 Ma, 11 Ma and 22 Ma (*Touboul et al.*, 2015). These ages for basaltic magmatism could also represent times of thermal metamorphism, e.g. during the burial of the crust by subsequent lava flows. The cumulate eucrites have Hf-W ages of 38± 21 Ma after CAI formation (*Touboul et al.*, 2015), suggesting that crystallisation took longer, or that cumulate formation occurred over a longer timescale. Hf-W measurements of zircons provided ages of eucrite crystallisation $<$ 7 Ma after metal-silicate differentiation (Srinivason et al. 2007). The samarium-neodymium system has also been measured, both ^{146}Sm-^{142}Nd and ^{147}Sm-^{143}Nd, producing an absolute formation age of the eucrites at 4547 Ma which is in agreement with the Hf-W system (*Boyet et al.*, 2010). *Bouvier et al.* (2015) consider the ^{147}Sm-^{143}Nd and ^{176}Lu-^{176}Hf systematics of some basaltic and cumulate eucrites, and find evidence for some of cumulate formation occurring 40 Ma after the basalts.

Thermal Evolution

Studies of the thermal evolution of the interior of a planetesimal model the extent of melting which may occur in a planet, in addition to the timescales involved.

Evidence for differentiation processes across the solar system can be seen on the terrestrial planets and from the range of meteorite and asteroid compositions. The variety in meteorite compositions suggests that the extent of differentiation which an asteroid experienced varied from complete (e.g. the iron meteorites, the HEDs, the planet Earth) to undifferentiated (e.g. some chondrites). More recently, evidence for a diverse range of partial melting scenarios within asteroids has been identified. The asteroid Lutetia is observed to have a chondritic surface but the average density is higher than chondritic values and more similar to that of Vesta, suggesting that there is a metal core (*Weiss et al.*, 2012). Further evidence for bodies with chondritic surfaces and metal cores (i.e. partially differentiated) comes from remanent magnetism recorded in some chondrite meteorites (*Weiss et al.*, 2012). This finding is significant as it suggests that chondritic crusts can be retained on a partially melted asteroid.

The extent of differentiation which can occur on a planetesimal is a function of the

amount of initial heat the body had. The heat source for early planetesimal formation is ^{26}Al and ^{60}Fe, with half-lives of 0.72 Ma and 2.4 Ma respectively (*Norris et al.*, 1983; *Rugel et al.*, 2009). ^{26}Al was present in a higher abundance than ^{60}Fe in the early solar system, and was the predominant source of heat prior to 2 Ma after solar system formation. Both the amount of these isotopes in a body and the time of formation (i.e. how much of the short-lived radionuclide was available to provide heat), in addition to the planetesimal size affect the extent of differentiation in a planetesimal.

The partial or complete melting of an asteroid or planetesimal can result in a magma ocean, i.e. where >10 % melt is present, and crystals are suspended in this melt (*Elkins-Tanton*, 2012). The crystallisation of this magma ocean can occur either through fractional crystallisation or batch crystallisation, but for small planetesimals like Vesta, where the gravity is not very large, crystal settling (fractional crystallisation) is less likely as turbulent flow and the low gravity regime hinder crystal settling.

Numerical simulations of the thermal evolution of Vesta were first performed by *Ghosh and McSween* (1998) who simulated Vesta's thermal history using the ^{26}Al concentration as a starting point and suggested that interior heat on Vesta could be sustained for 100 Ma after solar system formation, if Vesta formed before 3 Ma after CAI formation. This model does not account for the partitioning of ^{26}Al into the silicate melt during melt formation and migration to the surface or the cooling due to convection during the magma ocean stage. *Gupta and Sahijpal* (2010) used ^{26}Al and ^{60}Fe as the source of heat during conductive planetesimal heating and differentiation and investigated the plausibility of both the partial melting and magma ocean models. Their results suggest that Vesta had to accrete in the initial 2 Ma after CAI formation to produce a magma ocean, and in order to produce the eucrites and diogenites, the primitive insulating crust would have to be removed via impact processing, to account for the early crystallisation ages of the eucrites and diogenites.

In accordance with the theory that a more exotic range of asteroidal interior structures may exist (including 'onion shell' bodies with undifferentiated crusts and 'hidden' partial melts (*Weiss et al.*, 2012)), recent work has explored the option that Vesta may

have only differentiated partially. *Wilson and Keil* (2012) reviewed volcanic processes on differentiated asteroids and suggested that on large asteroids such as Vesta, the removal of silicate melt from partial melt zones would have been very efficient, due to the development of veins and dykes, which would restrict the size of melt pockets which could form. *Formisano et al.* (2013) investigated the first 5 Ma of Vesta's thermal history using a 1D heat conduction model and suggested that Vesta would have to form earlier than 0.8 Ma after CAIs in order to differentiate fully, but could still melt significantly (50-100 %) if formation occurred before 1.4 Ma.

The first stage in any magma ocean model is the onset of metal/metal-sulphide melting. The Fe,Ni-FeS eutectic is 950 ^{o}C, and so a metal melt forms, and percolates into the centre of the planetesimal due to its negative buoyancy (*Scheinberg et al.*, 2015). The silicate melt will start to form around 1100-1150 ^{o}C. Asteroids and planetesimals are small bodies, which cooled quickly in the early solar system ($<$ 10s of millions of years) due to their small surface area to volume ratio, and these magma ponds or oceans crystallise.

^{26}Al is lithophilic and therefore is concentrated in the silicate melt phase which forms; if this melt moves towards the surface of the asteroid then subsequent heating may be hindered. ^{60}Fe on the other hand, could be incorporated into the core. The bulk S composition of the planetesimal that is forming will determine the gap between core formation and silicate melt formation. If the planetesimal contains a high proportion of sulphur then the liquid is close to the Fe-Ni-S eutectic, meaning that the metal phase will be completely molten prior to silicate melting. However, if the amount of sulphur is low the liquidus temperature will be $\sim$1350 -1400 ^{o}C and so metal and silicate melting will occur concurrently (*Kiefer and Mittlefehldt*, 2014). The flow mechanisms of the metal melt will differ due to differences in density and viscosity. The composition and size of the planetesimal will also affect the evolution of the silicate portion of the asteroid, and for the low pressures in Vesta suggest that olivine, orthopyroxene, clinopyroxene and feldspar will be the predominant phases to form. Porosity of a planetesimal affects the melt connectivity and flow within partially molten asteroids

and volatile content will affect the silicate melt buoyancy and behaviour, particularly eruptive style (*Wilson and Keil*, 2012). If the silicate melts that form are not positively buoyant, then they may remain underneath an undifferentiated or chondritic lid that may trap heat inside the planetesimal (*Fu and Elkins-Tanton*, 2014). This chondritic lid may be broken up/destroyed either through basaltic volcanism reaching the surface or through impacts (*Weiss et al.*, 2012; *Fu and Elkins-Tanton*, 2014). Generally volatiles will produce more explosive volcanism and will be lost early in planetesimal evolution (*Fu and Elkins-Tanton*, 2014; *Weiss et al.*, 2012; *Elkins-Tanton*, 2012). An initial water content of 0.6 wt % and potentially some Cl has been inferred for Vesta from the study of apatite crystals in basaltic and cumulate eucrites (e.g. *Sarafian et al.* (2014) and references therein).

Neumann et al. (2014) expanded on the previous studies in order to refine the time scales of differentiation in addition to the process. *Neumann et al.* (2014) used the physical data from the DAWN mission and considered the differentiation of Vesta through a multitude of different processes including melting, porous flow, advective heat transport, convective heat transport and cooling. *Neumann et al.* (2014)'s results suggest that only a partial magma ocean was capable of forming on the asteroid Vesta, due to ^{26}Al partitioning into the silicate melt which formed and migrated to the surface, restricting the asteroid from further melting. Their suggested magma ocean was between 1 km and 10 km thick and cooled rapidly within 10^4-10^6 years. Usually magma ocean crystallisation is thought to occur from the inside out (*Scheinberg et al.*, 2015), however if a ^{26}Al-rich layer was transported to the surface, particularly through an efficient and extensive dyke and vein system (*Wilson and Keil*, 2012), then the differentiation process may start to occur from the outside inwards.

1.3.3 Evolution

Vesta formed and at least partially melted early in solar system history, however its accretion was prematurely terminated by the formation of the gas giant Jupiter, and because of the asteroid's large surface area to volume ratio, the planetesimal cooled

completely. The main source of information about the planetesimal's cooling comes from the HED meteorites, whose geochemistry provides details of their formation and sources. In addition to chemical measurements, thermodynamic and chemical models can also be used to investigate the interior evolution of Vesta.

Petrogenetic models of the HEDs

Petrogenetic models for the origin of eucrites and diogenites initially invoked conventional principles of equilibrium partial melting and fractional crystallisation. *Stolper* (1977), for example, suggested that a eucrite source region composed of olivine ($\sim Fo_{65}$), pyroxene ($\sim Wo_5En_{65}$), plagioclase ($\sim An_{94}$), Cr-rich spinel and metal underwent various degrees of partial melting to produce liquids approximated by Stannern and Sioux County eucrites. Other eucritic compositions could then, he argued, be generated by low-pressure fractionation of liquids similar in composition to Sioux County. In this model, the magnesian pyroxenes and olivines of diogenites crystallised from melt produced after plagioclase was exhausted from the eucrite source regions. The alternative hypothesis (*Ikeda and Takeda*, 1985) invoked global melting of the HED parent body followed by crystal accumulation in the magma ocean to generate diogenites, with non-cumulate eucrites being formed by subsequent crystallisation of the residual melts (*Ruzicka et al.*, 1997; *Takeda*, 1997). This magma ocean model was extended by *Righter and Drake* (1997) who proposed that large-scale melting of the HED parent body was accompanied by metallic core segregation and silicate crystallisation in two stages. The first stage involved ∼80 % of equilibrium crystallisation. The remaining 20 % melt segregated when the fraction of crystals became too high for the magma ocean to convect efficiently. The segregated melt then underwent fractional crystallisation to produce differentiated eucrites as the melts and crystalline diogenites as the fractionating crystals. More recently, *Mandler and Elkins-Tanton* (2013) used the MELTS software (*Ghiorso and Sack*, 1995) to upgrade this model and argued for a lesser extent of equilibrium crystallisation of the magma ocean (60-70 %) before melt segregation.

Although useful starting points, neither the partial melting nor the magma ocean

model accounts for the entire range of lithologies and compositions found in the meteorite record. The partial melting or serial magmatism hypothesis can account for the large variations in major and trace element abundances seen in eucrites and diogenites given more than one source composition and multiple melting events (e.g. *Barrat et al.* 2000). The residual liquids after diogenite crystallisation are not, however, represented by meteorites (*Mittlefehldt et al.*, 2012). The magma ocean model can crystallise general eucrite and diogenite compositions from one source composition but cannot account for the observed ranges in trace element abundances particularly in the diogenites (*Beck and McSween*, 2010). Furthermore, thermochemical modelling of asteroidal melting (*Wilson and Keil*, 2012; *Neumann et al.*, 2014) suggests that Vesta may not have been able to sustain a global magma ocean. In contrast, either the magma ocean or partial melting model could be consistent with W- and Mg-isotopic observations indicating that diogenites crystallised before eucrites (*Schiller et al.*, 2011).

Although the thermal and magmatic histories of Vesta are uncertain, there is widespread evidence for the thermal metamorphism of the eucrites (*Yamaguchi et al.*, 1996). Crustal anatexis produced partial melts which were incorporated into erupting eucrite magmas, a process whose trace element signature is seen in the Stannern trend eucrites (*Barrat et al.*, 2007) and which left behind depleted granulitic eucrites (*Yamaguchi et al.*, 2009). Similar partial melting of early ultramafic cumulates may also have generated diogenites (*Barrat and Yamaguchi*, 2014).

1.4 Bulk Composition

Any petrogenetic model of Vesta hinges, naturally, on its bulk composition and on the composition of its silicate envelope. Bulk silicate Vesta appears to be like Earth, Mars and the Moon in that the refractory lithophile elements are in approximately chondritic proportions (Morgan et al. 1978). For this reason, chondrite-like compositions are often used as putative starting bulk compositions for the HED parent body, and *Righter and Drake* (1997) and *Toplis et al.* (2013) have both explored the crystallisation paths of

a wide range of different chondritic starting compositions using the MELTS program (*Ghiorso and Sack*, 1995).

Righter and Drake (1997) derived a range of starting compositions by using the abundances of moderately siderophile elements to model core formation and estimate a mantle composition. A 30:70 mixture of CV and L type chondrites was selected as an optimal composition for their equilibrium and fractional crystallisation models; this satisfies the Fe/Mn ratios seen in HED meteorites and their oxygen isotopes. The molar Mg# (=100*(Mg/(Mg+Fe^{2+})), atomic) of this starting composition was 74 and equilibrium and fractional crystallisation simulations were performed over the 1530-1150 ^{o}C temperature range.

Ruzicka et al. (1997) suggested that the siderophile element depletions in HED meteorites are consistent with the presence of a metal core and used mass balance calculations of the Vestan interior to predict a size of between 0-25 % of the mass of Vesta, with the higher values accounting for possible porosity of the rocks. *Ruzicka et al.* (1997)'s modelling of the differentiation of Vesta is similar to that of *Dreibus and Wanke* (1980). *Ruzicka et al.* (1997) combine the observed geochemistry of the meteorites with Stokes' equations of crystal settling to suggest that Vesta contained a magma ocean. *Ruzicka et al.* (1997) also suggest that bulk Vesta has chondritic Al/Sc and Mg/Si ratios, and that the refactory lithophile elements are enriched by a factor of 2.5-3.5 compared to the CI chondrites. *Ruzicka et al.* (1997) suggested that Vesta's upper crust was eucritic, and the lower crust diogenitic with an underlying olivine-rich mantle, with the diogenites and eucrites crystallising as a continuous sequence.

1.5 Summary and Research Objectives

The recent DAWN mission has allowed the HED meteorites to be placed in a geological context. The results from DAWN suggest that the eucrites and diogenites are representative of the surface of Vesta, and there are no other major lithologies which need to be accounted for in petrogenetic models. The DAWN results also report that eucritic

lithologies overlie diogenitic, both of which are overlain with < 2km of howardite regolith. However, the lateral extent of different lithologies and the relationship between them, particularly sub-surface is unknown, and the stratigraphic occurrence of eucrites and diogenites is not definitively known. Currently, the two main unknowns regarding Vesta are its bulk composition, and the exact petrogenetic processes which have produced the eucrites and diogenites. The new information from DAWN confirms that Vesta is the source of the HED meteorites, and is more akin to the terrestrial planets than other asteroids. Vesta is a 'baby planet' in terms of its near hydrostatic equilibrium, metal core and extensively differentiated interior (*Russell et al.*, 2012). Therefore, Vesta can be included in discussions of comparative planetology alongside Mercury, Earth, Mars and the Moon. In a similar manner to the other terrestrial planets, Vesta's differentiation and evolution can be investigated using experimental and igneous petrology. Experimental petrology can simulate the processes and conditions of planetary formation. The detailed study of chemical behaviour in this Fe-rich reduced, volatile-poor system will allow the geochemical signatures observed in the eucrites and diogenites to be unraveled.

The aims of this thesis are to explore the differentiation of Vesta and the magmatic processes which could produce the eucrites and diogenites. This can be split into two main questions:

- What is the bulk composition of Vesta?
- What igneous processes can produce the range in major and trace element geochemistry of the eucrites and diogenites?

Throughout this thesis I will endeavour to answer these questions using a combination of experiments, thermodynamic and geochemical modelling. I will compare my results at all stages against the natural samples and observations of the parent body.

Chapter 2 derives two potential major element compositions for the Bulk Silicate Vesta (BSV) based on the olivine compositions and refractory lithophile abundances observed in the HED meteorites. To ensure that these compositions are plausible

compared with the physical observations of Vesta, the BSV compositions are used to calculate interior density structures from the moment of inertia and mass of Vesta. A three layer model of Vesta is assumed with a metal Fe-Ni core, a silicate mantle, and a silicate crust comprising eucritic and diogenitic material. The BSV compositions are then used as the starting point for a series of one atmosphere experiments. Equilibrium and fractional crystallisation were simulated and liquid lines of descent were derived for Vesta. These experiments will test the current petrogenetic models. In addition these experiments will be compared with the thermodynamic models to test the applicability of the alphaMELTS software to model Fe-rich volatile-poor basaltic compositions at low pressure and reducing conditions. AlphaMELTS will then be used to refine the range of major element bulk compositions that Vesta may have which could produce eucrites and diogenites.

Chapter 3 investigates the partitioning behaviour of incompatible trace elements between low-Ca pyroxene and anhydrous Fe-rich basaltic melts over the range of compositions and compositions under which eucrites and diogenites form under. The purpose of this is so that appropriate partition coefficients can be selected for geochemical modelling. In addition to the experiments reported in Chapter 2, further experiments were performed in order to measure D values across a range of temperatures and compositions with varying Al_2O_3 and CaO compositions. The lattice strain model was fit to the results of each experiment and lattice strain parameters were calculated. These parameters allow the partitioning behaviour of different isovalent series of ions to be interpreted and compared. Low-Ca pyroxene was selected as it is the most predominant mineral in the HEDs, and as its partitioning behaviour is currently the least well understood. A comparison with other planetary basalts will be made, in addition to testing published predictive models.

Chapter 4 combines the results and methods of Chapters 2 and 3 in order to test the possible differentiation and magmatic models of Vesta for the minor and incompatible trace elements. Firstly, geochemical calculations of the partial melting of Vesta, fractional crystallisation of partial melts, assimilation and fractional crystallisation of

partial melts, the partial batch and fractional melting of basalts and cumulates and the magma chamber process of recharge, eruption, assimilation and fractional crystallisation are performed in MATLAB for the incompatible trace elements. The liquid line of descent and modal mineral proportions from the alphaMELTS calculations are used within this model, and the partition coefficients are calculated from the data and observations in Chapter 3. The minor elements are then considered, and further assumptions need to be made for Cr due to the presence of spinel. The minor element bulk composition of Vesta can be refined.

Chapter 5 is a summary and discussion of the findings, and contains future directions.

Chapter 2

An experimental study of partial melting and fractional crystallisation on the HED parent body

The objectives of this chapter are to derive putative Bulk Silicate Vesta (BSV) compositions. These BSV compositions will then be investigated experimentally to see whether eucritic liquids and eucrite and diogenite cumulates can be produced, either through the postulated partial melting and magma ocean models. The results from these experiments have been used to test the ability of different thermodynamic models (Petrolog and MELTS) to model the HED system in terms of composition and conditions. Some of the results of this Chapter have been published in Meteoritics and Planetary Science in the paper: 'An experimental study of partial melting and fractional crystallisation on the HED parent body' *Ashcroft and Wood* (2015). I performed all of the experiments, analysis and modelling in this paper.

2.1 Introduction

2.1.1 Previous experimental work

Although the study of the HED meteorites has been active for the past 40 years, not a lot of experimental work has been performed. Previous studies have focused on melting basaltic eucrite compositions, or crystallising different mixtures of chondrite groups. The first experimental study of the HEDs was by *Stolper* (1975) who performed a series of one atmosphere melting experiments on the Juvinas eucrite composition at the Iron Wustite (IW) buffer. *Stolper* (1975) showed that under reducing conditions and temperature ranges of 1160-1200 ^{o}C Juvinas is multiply saturated with olivine, pigeonite, plagioclase, and spinel at the liquidus. This suggests that the eucrites are compositionally representative of their source melt composition. During crystallisation of the eucrites, a small amount of olivine crystallises but is subsequently reabsorbed during pyroxene crystallisation. This demonstrates the peritectic nature of the olivine-pyroxene boundary and explains both the observation of olivine saturation in the melt and the absence of olivine in eucrites. *Stolper* (1977) expanded on the work to compositions of another basaltic eucrite, Sioux County, and suggested that the diogenites and cumulate eucrites crystallised from higher degree partial melts of the parent body, and that the variety in eucrite compositions was due to fractional crystallisation.

Bartels and Grove (1991) performed a series of partial melting experiments on two magnesium-rich eucrite clasts; Kapoeta and Yamato 7308 (to approximate eucrite source composition): at 1 atm and 1 kilobar, with oxygen fugacities between IW and IQF. Their results agree with *Stolper* (1977)'s in that they suggest heterogeneous partial melting of a planetesimal and that the basaltic and cumulate eucrites fractionally crystallised from a Mg-rich partial melt between 1 kbar to 1 atm. In addition, the olivine-pyroxene boundary is a reaction boundary at 1 atm but at 1 kbar is cotectic and olivine can co-crystallise with pyroxene. *Grove and Bartels* (1992) used their data to model the formation of diogenites, postulating that diogenites may form at 500 bar in the mid-crust, although their pigeonite Ca content is higher than that of

observed meteorite orthopyroxenes (Wo_7 compared to Wo_2). *Jurewicz et al.* (1993) experimentally melted two different chondrites: Allende (CV) and Murchison (CM) across a range of oxygen fugacities and found that, under reducing compositions and appropriate temperatures, a melt of broadly eucrite composition could form.

Boesenberg and Delaney (1997) proposed that the bulk composition of the HED parent body may be a combination of different chondrite types/compositions in order to match the oxygen isotope signatures. They hypothesised a bulk Vesta which was a 70:30 mixture of H chondrite and CM chondrite composition based on the oxygen isotopes and Fe-Mn-Mg composition of the HEDs. They suggested that the residual melt composition after the formation of a metal/metal-sulphide core and significant olivine crystallisation would be eucritic. *Boesenberg and Delaney* (1997) suggested a less evolved melt composition would be responsible for the diogenites, which would form at a higher pressure. In order to test these theories *Boesenberg and Delaney* (1997) performed one-atm experiments 0.5 to 1.5 log units below the IW buffer on synthetic and natural samples, however their glass compositions did not match the observed Fe/Mn and Mg#s in natural eucrites.

Holzheid and Palme (2007) investigated the metal-silicate partitioning behaviour of Fe, Ni, Co, Mo and W into eucritic liquids under a range of oxygen fugacities and temperatures to investigate core formation processes on Vesta. Their results suggest that, to match the siderophile element abundances seen in eucrites, complete melting with core formation and fractional crystallisation of olivine and orthopyroxene must have occurred, rather than a one stage model of partial planetary melting.

As can be seen, previous experimental work has focused on eucrite production, and so I decided to investigate both eucrite and diogenite formation. The objectives of my experimental campaign are to produce both eucrites and diogenites experimentally, and test the different petrogenetic models directly. In addition different thermodynamic software will be tested for its suitability for modelling the HED compositions and conditions.

	Mg#70 (PM1)	Mg#80 (PM2)	0.30CV-0.70L	0.75H-0.25CM
MgO	29.67	32.77	29.31	27.92
Al_2O_3	3.01	3.33	3.12	2.70
SiO_2	42.3	46.6	46.1	42.59
CaO	2.40	2.65	2.49	2.20
FeO	22.6	14.6	18.21	24.42

Table 2.1: Major element compositions for two putative mantle compositions. The 0.30CV-0.70L chondrite mixture is the preferred composition of *Righter and Drake* (1997) and the 0.75H-0.25CM chondrite mixture is the preferred composition of *Toplis et al.* (2013). These two compositions are shown for comparison and are discussed in more detail in the text. Oxides are presented in wt. %

2.1.2 Estimates of HED parent body mantle composition

The first step in this investigation was to derive a bulk composition for the silicate portion of Vesta (BSV). I derived two mantle compositions based on the geophysics of Vesta and the geochemistry of the HEDs.

Applying the geophysical constraints together with the assumption of chondritic refractory element ratios provides the starting point for my model of Vesta. An additional constraint I applied was that the mantle should be able to generate both eucrite and diogenite lithologies. Given this, Mg# numbers of 70 and 80 were selected as end-member starting points for the putative mantle composition, from the average range of olivine compositions sampled in diogenites (e.g. *Sack et al.*, 1991; *Beck et al.*, 2012). The abundances of the other major element components in silicate Vesta were subsequently calculated from chondritic element ratios. These starting compositions are shown in Table 2.1 and are referred to as PM1 and PM2 from here onwards.

An interior model of the HED parent body was calculated in order to check the plausibility of the putative mantle composition. Vesta can be modelled as a triaxial ellipsoid with three interior layers (crust, mantle, core). Equations for the bulk density (ρ_{bulk}) and polar moment of inertia (I_{zz}) are then derived as follows:

$$I_{zz} = \frac{8\pi}{15}\left[\left(\rho_{crust}{a_1}^4 c_1\right) + \left(\left(\left(\rho_{mantle} - \rho_{crust}\right){a_2}^4 c_2\right) + \left(\left(\rho_{core} - \rho_{mantle}\right){a_3}^4 c_3\right)\right] \quad (2.1)$$

$$\rho_{bulk} = \rho_{crust} {a_1}^2 c_1 + (\rho_{mantle} - \rho_{crust})\, {a_2}^2 c_2 + (\rho_{core} - \rho_{mantle})\, {a_3}^2 c_3 \qquad (2.2)$$

where a_1 and c_1 are the major and minor axes of the body, a_2 and c_2 are the mantle radii, a_3 and c_3 the core radii, and the ρ denotes the density of each layer. This approach is an augmentation of the approach that *Zuber et al.* (2011) undertook, when considering Vesta as a two layer tri-axial ellipsoid.

Firstly the mantle density is calculated using Equation 2.2. I assumed that the core is made of FeNi metal with a density between 7100 and 7800 kgm^{-3}, an assumption supported by the depletions of siderophile elements in the HED meteorites (*Righter and Drake*, 1997), and used the bulk density of the Vesta calculated by DAWN: 3456 kgm^{-3} (*Russell et al.*, 2012). An average density of eucrites and diogenites taken from *Britt et al.* (2010) was used to estimate a crustal density of 2900 kgm^{-3}, while I_{zz} was calculated for a range of crustal thicknesses (20-50 km) and core densities (7000-8000 kgm^{-3}). The size of the core was calculated using the Fe/Mg ratio to calculate the depletion of the mantle Fe/Mg ratio compared to bulk chondrite, assuming that all of the depletion was due to core formation. I obtained polar moments of inertia between 0.4 and 0.42 (comparable with the 0.38-0.42 of the two layer model calculated by *Rambaux* (2013)). A range of core sizes and masses are calculated as: 15-20 % by mass of Vesta, with mean core radii (assuming a spherical core) of ∼110-120 km depending on the core density used. The associated mantle densities are predicted to be 2900-3500 kgm^{-3}.

Figures 2.1 and 2.2 show the results of my calculated mantle densities vs. calculated polar moment of inertia (not corrected for porosity), and the variation in start composition and crustal thickness. From Figure 2.1 it can be seen that PM1 produces higher mantle densities than PM2 for a given crustal thickness, and a higher moment of inertia (i.e. there is less mass concentrated in the centre of the asteroid). The more dense Vesta's core is, the lower the moment of inertia and corresponding mantle density. Increasing crustal thickness increases the required mantle density. Figure 2.2 shows that PM1 predicts denser, smaller radii cores than PM2 for any crustal thickness. Denser

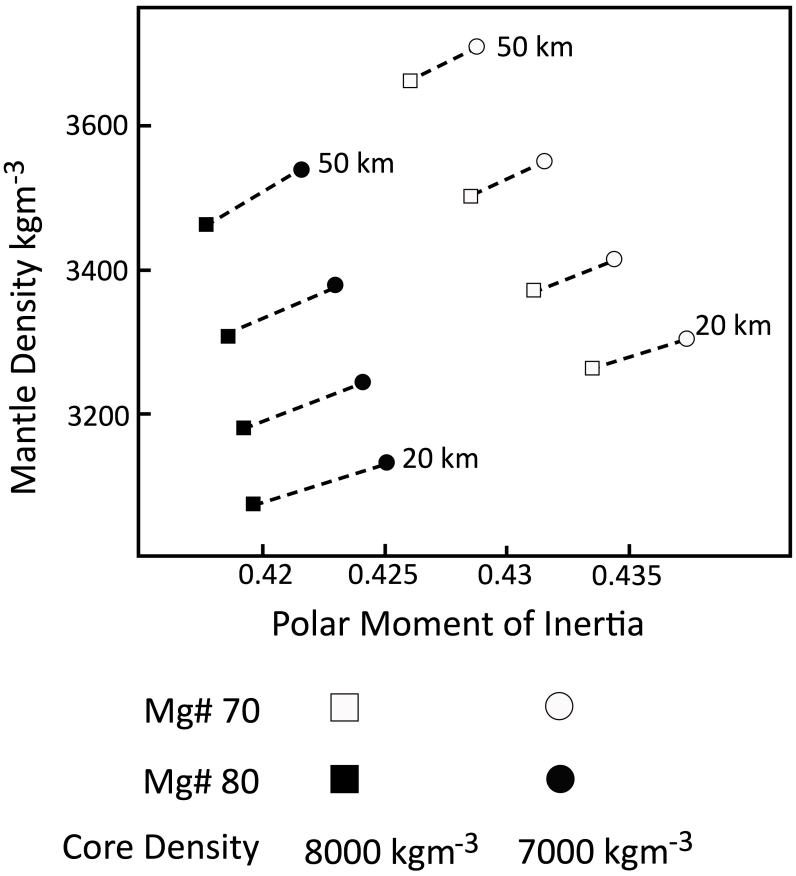

Figure 2.1: Calculated mantle density vs. calculated polar moment of inertia for start Bulk Silicate Vesta (BSV) compositions with Mg# 70 (PM1) and Mg# 80 (PM2), and ranges in core density between 7000-8000 kgm^{-3}. The results BSV with 20, 30, 40 and 50 km crustal thickness are shown with the 20 and 50 km results labelled.

cores correlate with smaller core radii, and smaller cores exist with smaller crusts. It can be seen that the interior structure of Vesta is a non-unique system dependent on many variables (core and crust density and size), and bulk starting composition.

In order to refine these models further, an independent estimate of the mantle density can be made from the presumed mineralogy (olivine and low-Ca pyroxene), and the density of a mantle comprising 60 % olivine and 40 % pyroxene is around 3200 kgm^{-3}. Crustal thicknesses can be estimated from this value as 10-20 km thick with a mantle Mg# = 70 and 30 - 40 km thick if the mantle Mg# = 80. This estimate is comparable to that of *Russell et al.* (2012), who estimate a core that is 18 % by

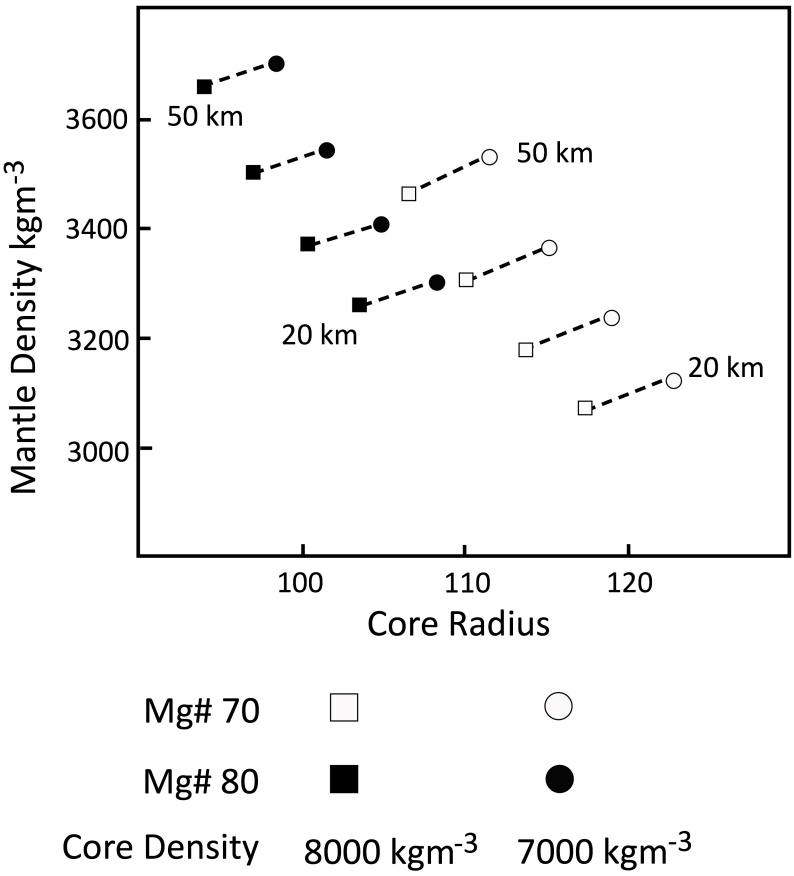

Figure 2.2: Calculated mantle density vs. calculated core radius for start Bulk Silicate Vesta (BSV) compositions with Mg#70 (PM1) and Mg# 80 (PM2), and ranges in core density between 7000-8000 kgm^{-3}. The results BSV with 20, 30, 40 and 50 km crustal thickness are shown with the 20 and 50 km results labelled.

mass of Vesta with a radius of 107-113 km and *Park et al.* (2014)'s fit to Vesta's gravity model, which produced a spheroidal core (117 x 105 km) which is 17 % by mass of Vesta. In addition our result is comparable to the results of the geochemical modelling of core-mantle partitioning of the moderately siderophile elements by *Righter and Drake* (1997) which indicate a core of 15-25 % of Vesta's mass. Although these solutions are not unique, and the calculations are simplified and do not account for the possible porosities of different layers, these comparisons indicate that my putative mantle composition is a reasonable starting composition.

2.2 Experimental Methods

2.2.1 Sample Preparation

Starting compositions were prepared from mixtures of analytical grade oxide and carbonate powders. The oxides were fired overnight at 1100 ^{o}C to remove CO_2 and H_2O. I ground the mixtures under ethanol in an agate mortar and partially decarbonated by heating from 500 to 900 ^{o}C over several hours. Next I reground, pelletised and reduced the pellets overnight at 900 ^{o}C in a vertical gas-mixing furnace at an oxygen fugacity (fO_2) just above the IW buffer. After reduction, the pellets were reground under ethanol, before being pressed into pellets of around 500 mg, from which 50 -100 mg chips were broken off and used in the experiments.

2.2.2 One-Atmosphere Experiments

All of the experiments performed for this thesis were done in a GERO HTRH/HTRV one-atmosphere gas mixing vertical furnace (named 'Eric') in the Experimental Petrology Laboratory in the Department of Earth Sciences, University of Oxford. Figure 2.3 includes a photographic and a schematic diagram of the experimental equipment. The heating element is made of the electrically conductive $MoSi_2$, which is resistant to oxidation up to temperatures of 1800 ^{o}C, and the insulation material is fabricated from ceramic fibre insulation. The sample assembly was custom designed for the furnace to ensure that the sample was held in the hot spot of the furnace. This distance was measured by determining the thermal gradient through the furnace using a Pt-Rh thermocouple. The temperature measured where the sample sits is 3 ^{o}C lower than measured at the furnace control thermocouple, but this was deemed a minor offset.

In these series of experiments the solid samples (around 50-100 mg) were mounted onto a 0.25 mm metal wire, occasionally with a small dab of PVA glue to hold the material in place. This loop was attached to a small ceramic disk that was suspended from two thick platinum wires using a 0.1 mm diameter platinum wire. To perform an experiment the sample assembly was lowered carefully into the furnace and sealed

using a steel lid. Two types of temperature profiles were used for experiments: one where the sample was taken to the temperature of choice (at 500 ^{o}C/hour) and left to equilibrate and crystallise, and one where the sample was taken above the temperature of choice at 500 ^{o}C/hour and slowly crystallised down to temperature at a rate of ∼0.5-50 ^{o}C/hour to the required temperature. The latter profile could be repeated, cycling the temperature, which can promote crystal growth. To terminate an experiment a high electrical current was passed through the sample assembly, melting the 0.1 mm platinum wire and causing the ceramic disk to fall into a beaker of cold de-ionised water, thus quenching the sample and preserving the high temperature assemblage.

The oxygen fugacity of the furnace chamber was controlled by fixing the relative flows of carbon dioxide and carbon monoxide gas through the furnace. The exchange reaction for CO-CO_2 is:

$$CO + \frac{1}{2}O_2 = CO_2 \tag{2.3}$$

The equilibrium constant for this reaction is:

$$K = \frac{PCO_2}{PCO \times PO_2^{\frac{1}{2}}} = \left[\frac{XCO}{XCO_2}\right] \times \left(\frac{1}{PO_2^{\frac{1}{2}}}\right) \tag{2.4}$$

where the partial pressure of oxygen is the same as the oxygen fugacity when the activity = 1, and so the oxygen fugacity is linked to the mixture of carbon dioxide and carbon monoxide gas through the equation:

$$fO_2 = \left[\frac{XCO}{XCO_2}\right]^2 \times \left(\frac{1}{K}\right)^2 \tag{2.5}$$

K is temperature dependent and values can be found in tables of thermodynamic properties (*Deines et al.*, 1974). The fO_2 inside the furnace is checked by using an yttria-doped zirconia sensor that measures the electromotive force (emf) through the furnace between two platinum wire electrodes. The emf is related to the oxygen fugacity

using the Nernst equation:

$$emf(volts) = \frac{-RT}{zF} lnfO_2 \tag{2.6}$$

where z is the ionic valence, which for oxygen gas is 4 and F is the Faraday constant. The fO_2 within the furnace is stable, and the fO_2 sensor is precise. The offset between the measured and calculated fO_2 is usually within 0.1 log units, and the minor uncertainty is due to the Mass Flow Controllers. The experiments performed in this thesis were run at oxygen fugacities between IW -2 to IW +2, temperatures between 1100-1650 ^{o}C and on timescales of hours to weeks.

2.2.3 Piston Cylinder

In addition to the one atmosphere experiments, some preliminary experiments were run using an end-loaded Boyd-England Piston Cylinder apparatus. Samples were run in graphite capsules in a calcium fluoride (CaF_2) sleeve. Experiments were performed between 1200-1400 ^{o}C and at 10 kbar. The temperature was controlled using a $W_{95}Re_5$-$W_{74}Re_{26}$ thermocouple and experiments were run on timescales of hours to days. Experiments were quenched by cutting the power to the system while maintaining run pressure. The experiments I performed were at the lower end of the piston cylinder's pressure capabilities and the thermocouple oxidised easily causing experimental failure due to a power surge, as the thermocouple lost its ability to measure the temperature.

The maximum pressure at the centre of Vesta can be estimated as $\sim$ 2 kbar using the equation P= ρgz, where z is the depth, g is gravity and ρ is the bulk density of Vesta. As the interior of Vesta is at such a low pressure I am justified in using one atmosphere experiments in order to explore the petrogenetic relationships in the silicate portion of Vesta, rather than using the piston cylinder. This approach also enables direct oxygen fugacity control under strictly anhydrous conditions. Samples were suspended on a loop of 0.25 mm diameter Re wire in a flowing CO-CO_2 gas mixture to control the oxygen fugacity. At the end of the experiment the sample was

drop-quenched into water.

2.2.4 Scanning Electron Microscope (SEM) and Electron Microprobe (EPMA)

After experiments were terminated, samples were set in KEMET Acrylic Resin in 25 mm circular mounts, which were then carbon coated. Samples were observed either using the recently retired Jeol JSM-840A SEM, Department of Earth Sciences, University of Oxford or the new FEI Quanta FEG 650, Department of Earth Sciences, University of Oxford, to get a Backscattered Electron (BSE) image. The abundance, size and distribution of crystals and melt could be determined and a basic composition for the minerals and glass present in each experimental charge was gained using the Energy Dispersive Spectrometer (EDS) with the 'old' SEM. This work was done as preparation before a more in-depth analysis was performed using the JEOL-8600 Microprobe in the Research Laboratory for Archaeology and the History of Art, University of Oxford.

Both the Scanning Electron Microscope (SEM) and the Electron Probe Microanalyser (EPMA) use an electron gun (a tungsten filament which is electrically heated) to produce a source of electrons, which are then focused by lenses into a beam which is accelerated towards the sample. Next the electron beam interacts with the sample producing secondary electrons from the sample (inelastic scattering) or the backscattered electrons (elastic scattering). In BSE images chemical elements with a greater atomic number reflect more electrons than lighter chemical elements, and so mineral phases that are enriched in heavier elements appear brighter in the images. Backscattered electrons can be used to detect different phases by contrast differences. EDS was used to establish an approximation of the chemical composition of different phases. EDS measures the energy of X-rays which are emitted when electrons move from higher to lower energy shells when the electron beam ejects electrons from surface atoms. The energy of the X-ray is characteristic of each atom and energy shell. When the electron beam interacts with the sample the atoms become excited, and electrons are ejected causing other electrons to move from higher energy shells to lower energy shells to fill

this gap, simultaneously emitting an X-ray which is characteristic for each atom, and each shell. The EDS detector measures the intensity of X-rays produced over a wide range of energies. Different minerals produce different characteristic spectra allowing each phase to be identified.

EPMA analysis uses Wavelength Dispersive Spectrometry (WDS) which has a higher resolution than EDS. WDS measures the intensity of X-rays diffracted at different wavelengths by different crystals in the spectrometers, one wavelength at a time. The wavelength of the X-ray and the crystal's lattice spacings are related by Bragg's law and so the crystal used is varied depending on which element is being measured. For a quantitative analysis, the X-ray line intensities are measured and the elemental concentrations are calculated from the ratios of these intensities to those from standard samples with known concentrations. These analyses are then corrected for atomic number, absorption and fluorescence differences between a sample and the standard using the PAP correction (*Pouchou and Pichoir*, 1991). All phases were analysed using a 15 kV accelerating voltage, with a 10 nA beam current and a focused beam. The detection limits are around 0.03 wt % for most of the major elements. Counting times were typically 30-50 s on peak and 15-25 s on backgrounds. Natural and synthetic standards were used for calibration and during analytical sessions an almandine crystal was analysed together with the experimental charges to check calibration and ensure internal consistency. Crystal Analyses were accepted if their totals were between 98-101 wt. % and glass analyses with totals over 97 wt. % were accepted generally because the glasses typically contain up to 1 wt. % trace elements.

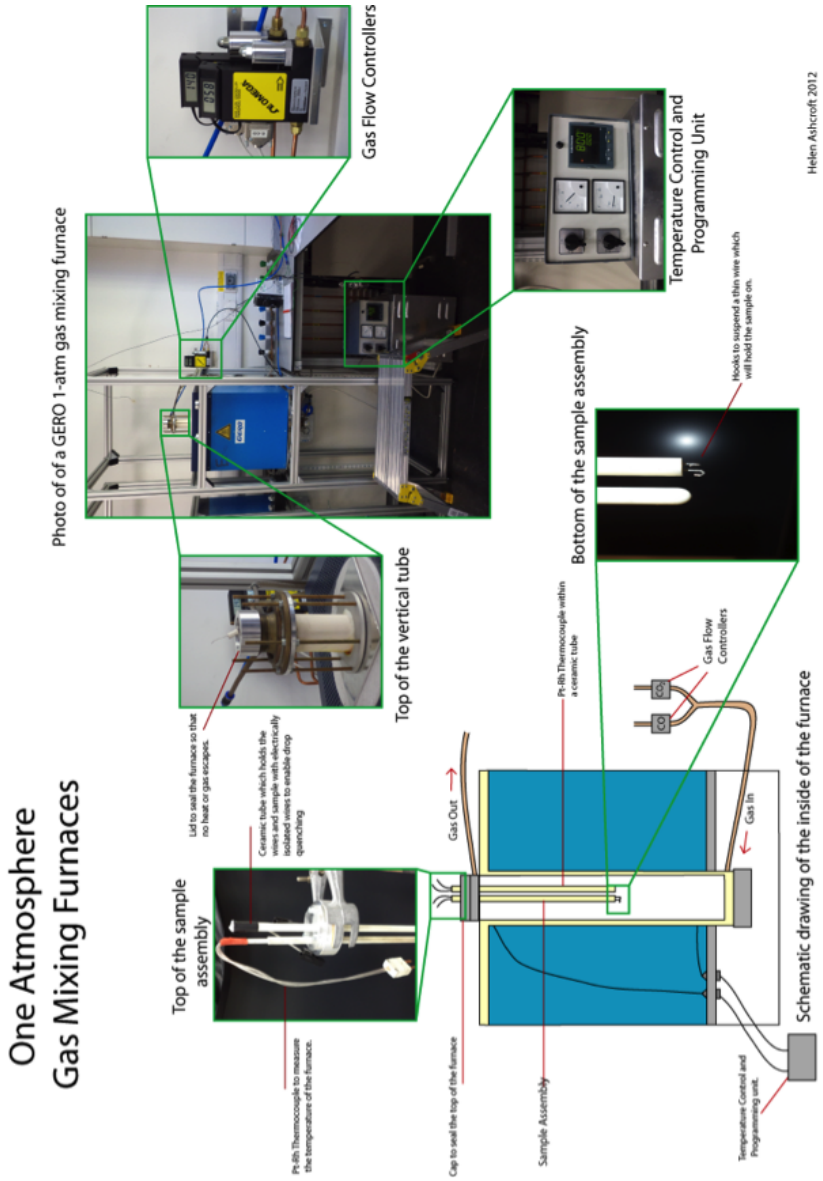

Figure 2.3: The One Atmosphere Experimental Assembly. The top right shows a photograph of the furnace, the Mass Flow Controllers, which control the volume of CO and CO_2 gas passing through the furnace and the Temperature control unit. The Schematic Diagram (Bottom left) shows the interior of the furnace, including the chamber and sample assembly in situ with close up photographs of the sample assembly.

2.3 Preliminary Investigations

2.3.1 Wire Selection

The 'container problem' is the nemesis of many experimental petrologists (outlined in the *Basaltic Volcanism Study Project*, 1981) and often refers to the loss of Fe from experiments under reducing conditions (e.g. Fe was observed to be lost from the experiments of *Stolper* (1977)). The reaction of iron with the wire material occurs progressively over time and can alter the bulk composition of the system, affecting the mineralogy and the equilibrium. Fe has a strong affinity for reacting with the noble metals like Pt, which otherwise have the optimal properties for an experimental container: high melting temperature, the appropriate physical properties to support the sample (not too brittle), stability at high temperature over the experimental conditions and timescales. Therefore I performed a preliminary series of experiments to assess Pt, Fe, Mo, Re and Ni as suitable wires for experiments on HED compositions and conditions. In all of the wires studied, Fe or Fe-Ni metal blobs were observed in experiments below the IW oxygen fugacity buffer. If Pt, Ni or Fe was used then the wire was noted to react with the sample, and in experiments with the Mo and Re wire, Fe-Ni metal blobs formed in the experiments.

Above the IW buffer Mo wire reacted with the sample forming significant Mo silicates (as the Mo-MoO_2 buffer is close to the IW buffer), and Fe is known to have an affinity for Pt, Ni and Fe wire. Also in Fe wire experiments, the high iron content makes it difficult to buffer the fO_2. At 1-2 units above the IW buffer, Re wire was not noted to react significantly with the sample over several day time scales. This is in keeping with the study of *Borisov and Jones* (1999) who explored the use of Re wire instead of Pt in one-atmosphere experiments over a range of timescales, temperatures and reducing conditions. Their experimental campaign investigated the stability of Re loops at 1400 ^{o}C over a range of fO_2 conditions, and found that Fe loss was negligible. Additionally *Borisov and Jones* (1999) found that Re stability increases with decreasing fO_2, and that at 1400 ^{o}C, an experiment performed around the IW buffer will be

stable on the order of weeks. Our own observations from experiments performed to investigate a problem in the furnace, suggest that at higher temperatures of 1500 ^{o}C and the same fO_2 the stability time is less than 24 hours, and increasing the oxygen fugacity by 0.5 log units at a temperature 1400 ^{o}C, also decreases the stability to the order of a few days. Therefore Re was decided on as a suitable experimental wire, and mass balance and equilibrium checks on experimental compositions (detailed below) to determine no material was lost or gained from the system confirmed my choice.

2.3.2 Early Experimental Series

The wire investigation series, and the piston cylinder experiments I performed, investigated the phase relations of the Juvinas and Sioux County compositions over a range of temperatures 1100-1300 ^{o}C, and the effects of adding in olivine, orthopyroxene or one of the two putative mantle compositions. This addition of more mafic minerals thought to have crystallised from the source region is a common technique in experimental petrology, particularly with olivine (*Basaltic Volcanism Study Project*, 1981). This experimental path was selected, as the multiple saturation of eucrite liquids suggests eucrites are in equilibrium with their source composition. However, although this technique can elucidate whether the system is likely to be in equilibrium with the phase which is being added, it does not help to calculate the nature of the reactions during crystallisation (e.g. is it cotectic or peritectic?) and cannot be used to predict the mineral proportions (and therefore the source composition). In addition, the eucrites and diogenites are not thought to have crystallised necessarily from the same source composition. Therefore the bulk of the experiments performed in this thesis were investigations into whether the eucrites and diogenites could be produced directly from the putative mantle compositions, particularly focusing on the more Mg-rich starting composition PM2.

2.4 Major element test of the Magma Ocean and the Partial Melting Models

In order to determine the liquid line of descent and the compositions of mantle partial melts, crystallisation experiments were performed on PM2 at 50 ^{o}C temperature intervals between 1300 and 1650 ^{o}C and an fO_2 1.8 log units above the IW buffer. This fO_2 was selected to ensure a very high Fe^{2+}/Fe^{3+} ratio in the melt, no metallic Fe precipitation and no significant iron loss to the Re wire. The 50 ^{o}C intervals between experimental temperatures were selected in order to monitor the evolution of the liquid composition at a resolvable temperature interval, with the expectation that no major phases would be missed in the crystallisation sequence. Several experiments were also run on the PM1 composition, at 1450 ^{o}C (HAPM1_01) and 1400 ^{o}C (HAPM1_02), and a 90:10 mixture of the olivine and melt composition observed in the HAPM1_02 experiment at 1400 ^{o}C (HAPM1_04).

In order to simulate fractional crystallisation, or the second stage of possible magma ocean evolution, the glass compositions observed at 1300 ^{o}C and 1350 ^{o}C (after 55 % and 63 % equilibrium crystallisation respectively, and corresponding to 45 % and 37 % partial melting) were synthesised (HA4 and HA6). A sequence of crystallisation experiments was performed on the 55 % melt composition (HA4) from 1350 ^{o}C to 1250 ^{o}C. The glass composition in the 1250 ^{o}C experiment was then synthesised (HA5) and crystallisation experiments were performed between 1250 and 1150 ^{o}C. The melt produced at 1150 ^{o}C (HA7) was then separated, synthesised and crystallised down to 1125 ^{o}C. Experiments on the HA6 composition were performed from 1300-1150 ^{o}C. All of the starting compositions are presented in Table A.1. The run conditions of the experimental series are shown in Table A.2 and the major element compositions of the experimental phases are shown in Table A.3.

2.4.1 Attainment of Equilibrium

Several approaches were taken in order to determine whether equilibrium was reached and whether Fe was being lost to the Re loop. Firstly the phase compositions from experiment HAPM2_05 were synthesised separately and mechanically mixed together in a 70:15:15 ratio of melt:pyroxene:olivine to form the HA3 composition. These proportions were chosen in order to grow fewer and larger crystals for better analysis. A time series of experiments was performed using this composition for 24 (HA3_01) and 48 (HA3_03) hours, and two experiments were run on the same Re loop (HA3_01 and HA3_02). Experiments where the charge was heated up to the run temperature from 800 ^{o}C (e.g. Experiment HA3_01), as well as an experiment where the charge was heated from 800 to 1400 ^{o}C before being cooled to 1350 ^{o}C (HA3_06) were performed. From Table A.3 it can be seen that the phase proportions and Mg# of each experimental charge are all within uncertainty of each other, indicating that equilibrium was approached. Although no detectable Fe was lost from the charges, Ni was lost.

2.4.2 Phase Proportion Calculations

The calculation of modal proportions in each experiment from mass balance employed the non-linear least squares approach of *Albarede and Provost* (1977). This method involves calculating a bulk composition from the individual phase compositions iteratively by varying the modal proportions of the phases, until the differences between the measured and calculated compositions have been minimised. The results are shown in Table A.2. These calculations are sensitive to minor changes in phase composition, which accounts for the minor differences between the calculated modal proportions for HAPM2_05 (45% melt and 55 % olivine) and HAPM2_09 (48 % melt and 52% olivine). The minor differences in phase composition are due to the higher concentrations of trace elements in HAPM2_09.

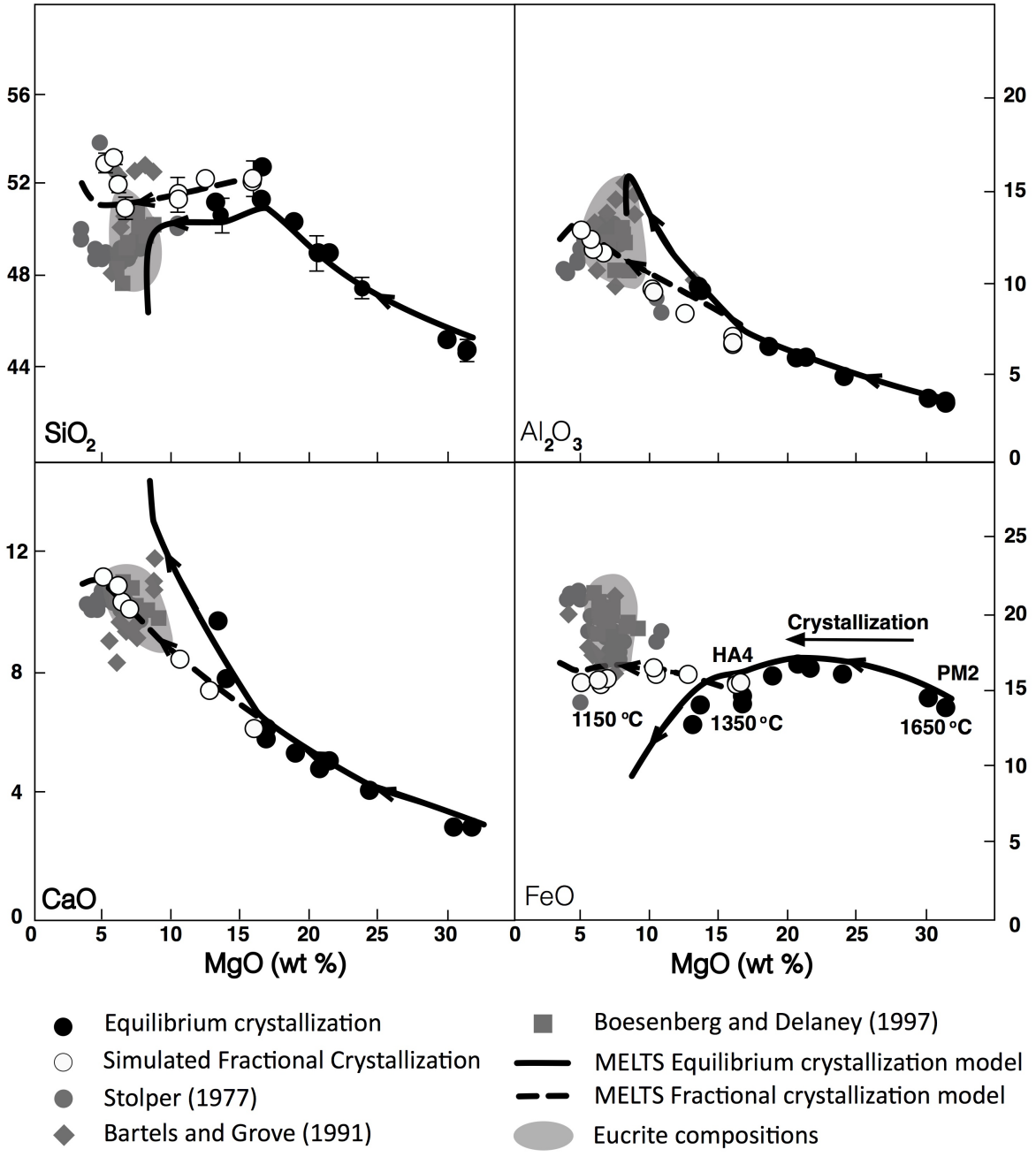

Figure 2.4: Compositions of glasses from equilibrium crystallisation (filled circles) and fractional crystallisation (open circles) series of experiments: PM2, HA4, HA5, HA7, together with the corresponding MELTS models (lines). All results in weight %. The eucrite field covers the majority of non-cumulate monomict eucrite compositions taken from *Warren et al.* (2009) and *Barrat et al.* (2000).The experimental data of *Stolper* (1977), *Bartels and Grove* (1991), and the experimental data where no significant iron loss occurred of *Boesenberg and Delaney* (1997) have been plotted for comparison (filled grey symbols). The arrows on the continuous lines denote the evolution of the crystallising melt; where error bars are absent, they are smaller than the symbols. This is Figure 1 in *Ashcroft and Wood* (2015).

2.4.3 Results - Partial Melting of the BSV

Crystallisation Sequence

Olivine is the liquidus phase in our putative mantle composition and was first observed at 1600 ^{o}C. Orthopyroxene is the next phase to crystallise, first observed at 1350 ^{o}C. Spinel is present in experiments containing Cr_2O_3 from 1350 ^{o}C down-temperature. Only one accurate EPMA analysis of this phase was possible, however (in experiment HAPM2_15) due to its small size and low abundance. In the PM1 series of experiments olivine was present at both 1450 ^{o}C and 1400 ^{o}C. Melt compositions have been plotted on major element oxide diagrams in Figures 2.4 and 2.5 and have also been projected into the Fo-An-Qz ternary in Figure 2.6. Figures 2.4 and 2.6 a) are the figures published in *Ashcroft and Wood* (2015), comparing the PM2 data, the fractional crystallisation data of the 45 % partial melt (1350 ^{o}C), concurrent alphaMELTS models, published meteorite data and the data from previous experimental campaigns (*Boesenberg and Delaney*, 1997; *Stolper*, 1977; *Bartels and Grove*, 1991). Figures 2.4 and 2.6 show the experimental data of PM2, HA4, HA5, HA6, HA7, and the corresponding MELTS models compared with the literature meteorite data, in order to compare the evolution of the 45 % partial melt, and the 38 % partial melt.

Melt Compositions

The experimental glass compositions for PM2 are shown in Figure 2.4 plotted as wt. % SiO_2, Al_2O_3, CaO and FeO as a function of MgO wt. %. As the primitive mantle crystallises olivine and the temperature declines from 1600 to 1300 ^{o}C, the melt becomes richer in SiO_2 (44.68-50.63 wt. %), Al_2O_3 (3.59-9.55 wt. %) and CaO (3.06-7.87 wt. %) and poorer in MgO (31.02-13.34 wt. %). There is also a slight increase in TiO_2 over this temperature interval and FeO and Cr_2O_3, increase slightly as olivine crystallises but then decrease as pyroxene and spinel join the crystalline assemblage. The Mg# of the melt decreases from 80 to 63. The melt compositions have also been projected into the Fo-An-Qz ternary in Figure. 2.6, with the MELTS models, and appropriate

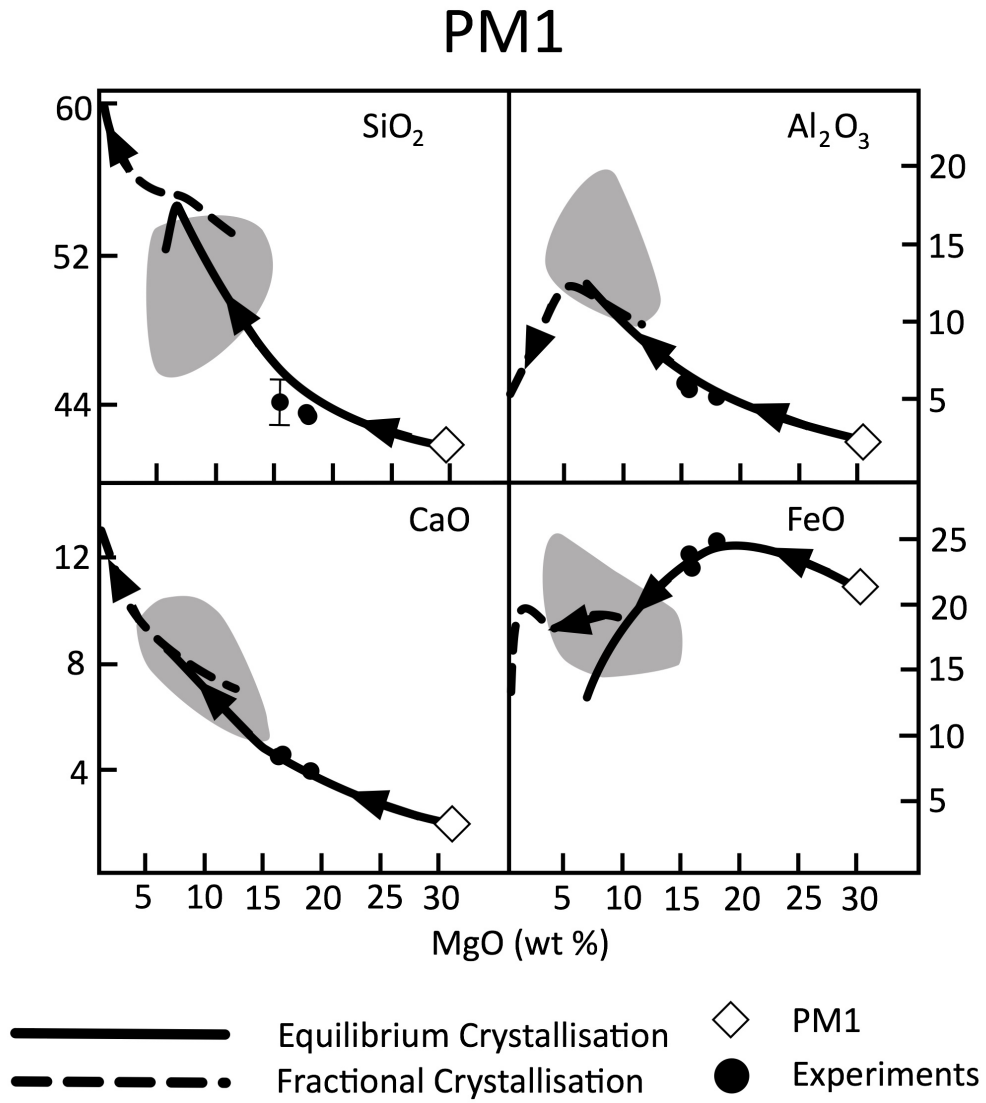

Figure 2.5: Compositions of glasses from the equilibrium crystallisation (black circles) series of experiments on PM1 together with the corresponding MELTS models (lines). All results in wt. %. The eucrite field covers same range as Figure 2.4. The bulk PM1 composition is shown by the diamond.

experimental melts from *Stolper* (1977), *Bartels and Grove* (1991) and *Boesenberg and Delaney* (1997) plotted for comparison. PM1 melts are more iron-rich than PM2 and show similar trends with Al_2O_3 and CaO increases as temperature decreased from 1450-1400 ^oC from 5.6 to 6.3 wt. %, and 4.8 to 5.6 wt. % respectively, a slight increase in SiO_2 from 43.7 to 44.2 wt. % and a slight decrease in FeO and MgO from 26.2 to

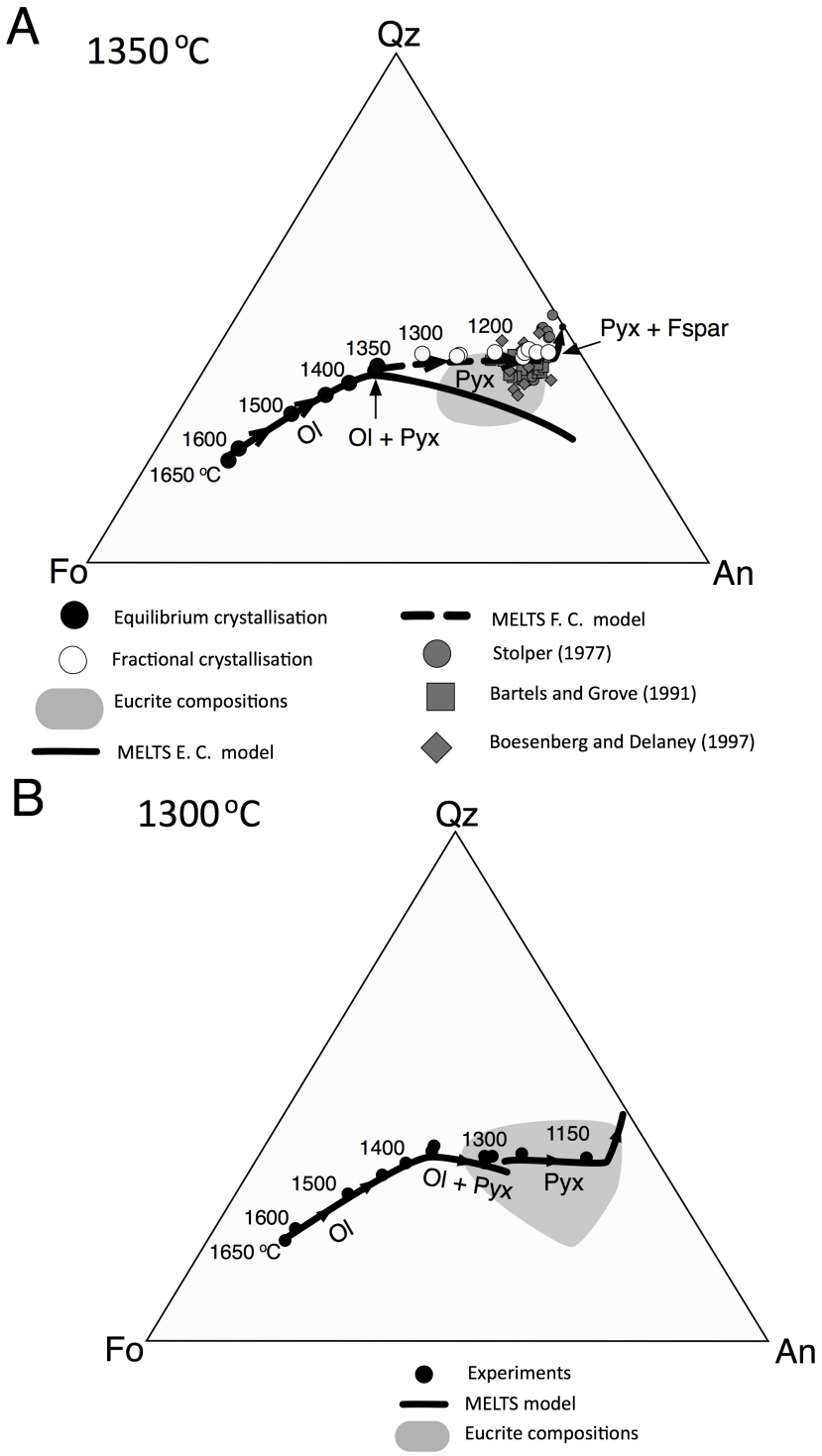

Figure 2.6: Experimental melt compositions projected into the Fo-An-Qz pseudo-ternary diagram from Diopside. A (top) is the ternary diagram of PM2 crystallisation where the melt is extracted and fractionated after 55 % olivine and pyroxene crystallisation, and is figure 2 in *Ashcroft and Wood* (2015). B is the ternary diagram of PM2 crystallisation where melt is extracted and fractionally crystallised after 63 % olivine and pyroxene crystallisation. A contains the experimental data of the PM2, HA4, HA5 and HA7 series, and B shows the PM2 and HA6 series. The MELTS models and eucrite compositions have been plotted, and in addition the previous experimental work has been included in A.

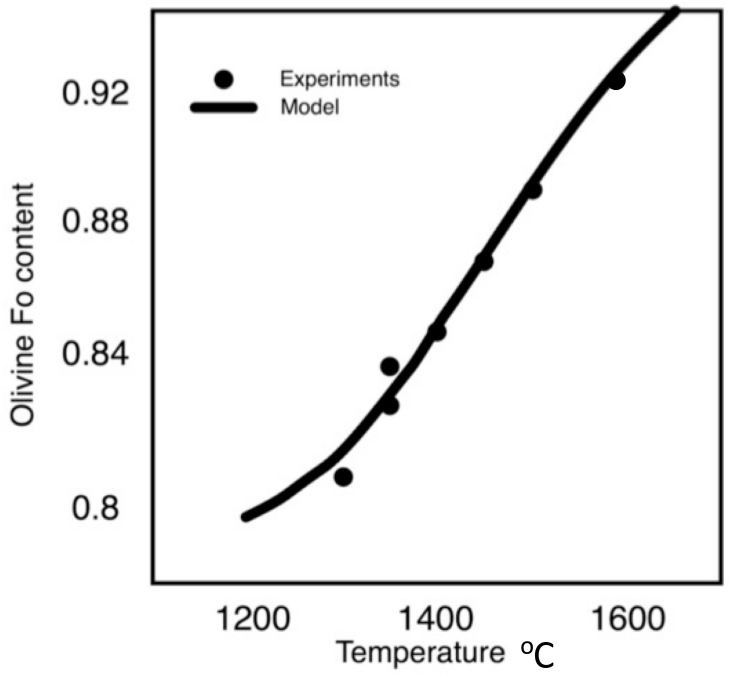

Figure 2.7: Olivine composition vs. temperature in the PM2 series of experiments and MELTS models.

24.8 and 17.7 to 15.5 wt. %.

Crystal Compositions

The Fo content (100*(Mg/(Mg+Fe^{2+})) of olivine in the PM2 series of experiments decreases with decreasing temperature from 92 at 1600 ^{o}C to 83 at 1300 ^{o}C, shown in Figure 2.7. This range corresponds well to the range of olivine clasts observed in the GRO 95 Howardite paired group (*Lunning et al.*, 2015), implying that melting and crystallisation of Vesta left a heterogeneous residuum. The experimental pyroxene compositions are plotted in Figure. 2.8. Orthopyroxene was first observed as a few very small crystals at 1350 ^{o}C. It has the composition $Wo_{1.18}En_{84.39}Fs_{14.43}$ at 1300 ^{o}C. The olivine Fo content in the PM1 series decreases from 80 at 1450 ^{o}C to 78 at 1400 ^{o}C.

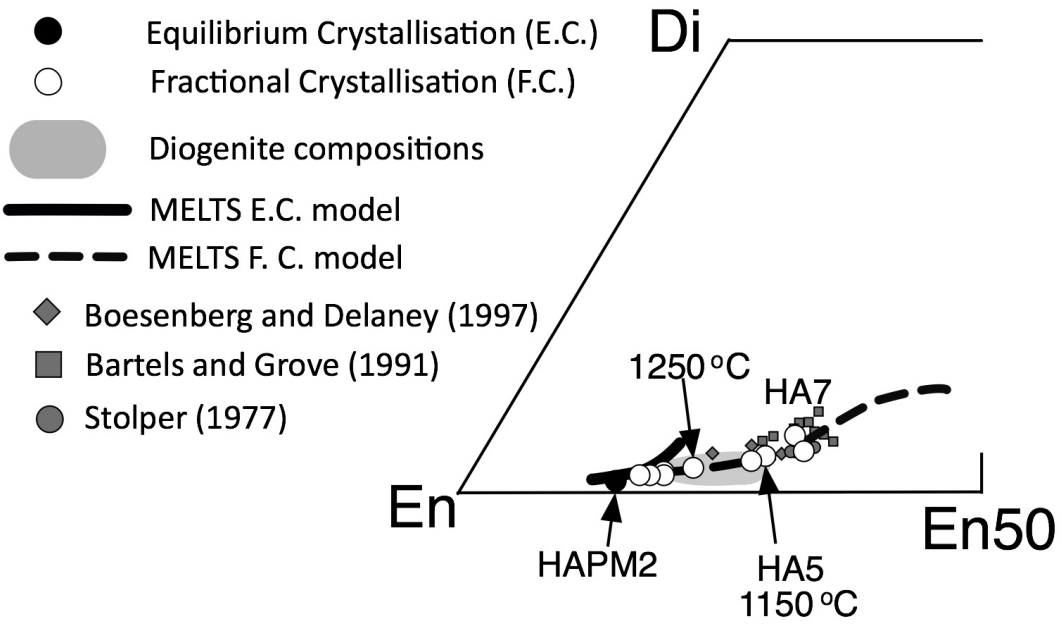

Figure 2.8a: Compositions of the experimental pyroxenes (filled and open circles) and the calculated compositions (lines) projected into the Wo-En-Fs ternary. The grey field corresponds to diogenite compositions taken from *Fowler et al.* (1995), *Barrat et al.* (2000), *Warren et al.* (2009), *Mittlefehldt et al.* (2012), *Beck et al.* (2013). The experimental pyroxenes of *Stolper* (1977), *Bartels and Grove* (1991) and *Boesenberg and Delaney* (1997) have been plotted for comparison. This figure shows the evolutionary path where melt is extract after 55% olivine and pyroxene crystallisation, and is figure 3 in *Ashcroft and Wood* (2015)

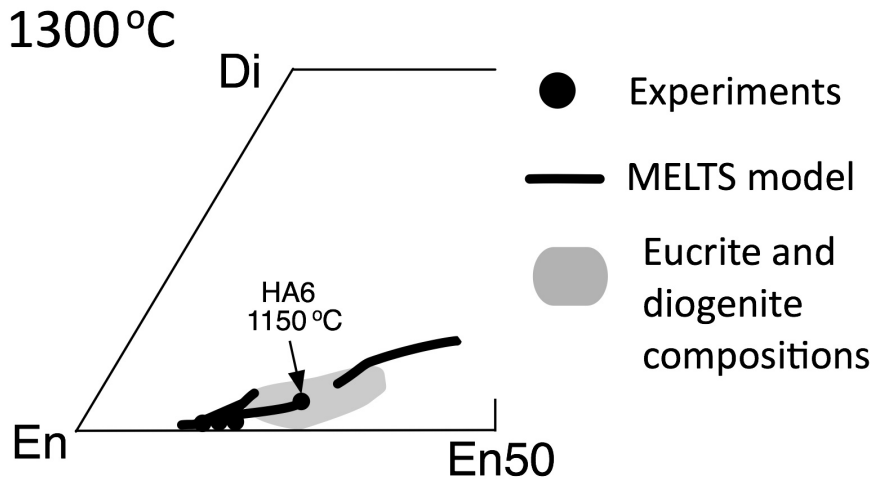

Figure 2.8b: This figure shows the evolutionary path of silicate Vesta where the melt is extracted after 63% olivine and pyroxene crystallisation.

K_d checks for equilibrium

Roeder and Emslie (1970) demonstrated that the olivine-liquid exchange partition coefficient $K_{d_{Fe^{2+}-Mg}} = (FeO/MgO)_{Ol}/(FeO/MgO)_{liq}$ in terrestrial basalts is constant at

a value of 0.30±0.03. Later work showed, however, that $K_{d_{Fe^{2+}-Mg}}$ depends to some extent on liquid composition (*Sack et al.*, 1980), and that different $K_{d_{Fe^{2+}-Mg}}$ values need, therefore to be used for different petrogenetic environments. In order to calculate $K_{d_{Fe^{2+}-Mg}}$ I made a small correction for the Fe^{3+} content using equation 12 from (*Jayasuriya et al.*, 2004). I calculated the amount of ferric iron in the liquids generated from PM2 at an oxygen fugacity of IW+ 1.8. After subtracting Fe^{3+}, a mean value of $K_{d_{Fe^{2+}-Mg}}$ of 0.34±0.01 was obtained for our experiments, shown in Figure 2.9. This is comparable with the values of 0.345±0.009 for high-MgO Hawaiian picrites (*Matzen et al.*, 2011) and 0.35±0.01 for the high-FeO, low-Al_2O_3 Martian basalts (*Filiberto and Dasgupta*, 2011). The attainment of a constant $Kd_{Fe^{2+}-Mg}$ over the composition and temperature range studied provides further evidence for attainment of equilibrium.

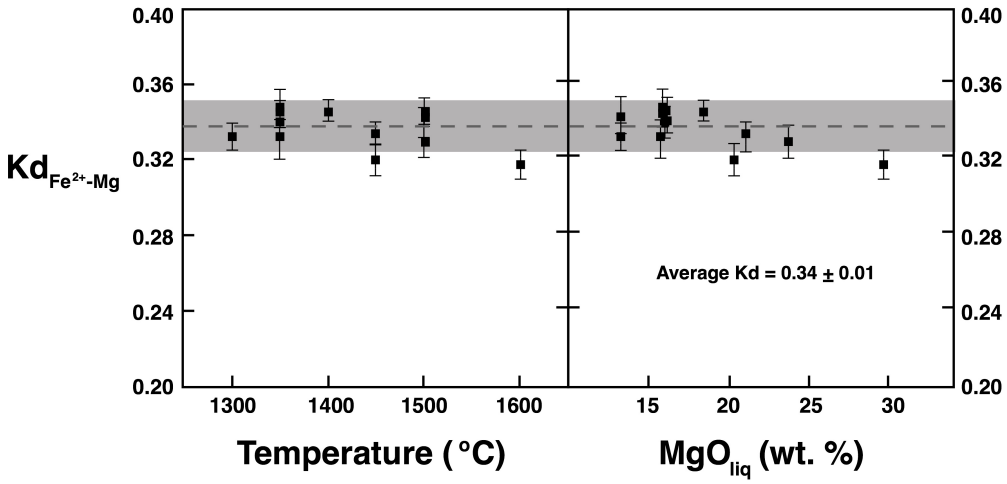

Figure 2.9: $K_{d_{Fe^{2+}-Mg}}$ vs Temperature and MgO_{liq} for olivines in the PM2 and HA3 series of experiments.

2.4.4 Results - Fractional Crystallisation of melts extracted from the mantle at 1300 ^{o}C and 1350 ^{o}C

The partial melt produced from the primitive mantle composition at 1350 ^{o}C was analysed, synthesised and then crystallised in a stepwise fashion down to 1125 ^{o}C in order to simulate fractional crystallisation. The partial melt produced from the primitive mantle composition at 1300 ^{o}C was crystallised in an equilibrium manner from 1300 down to 1150 ^{o}C. This will not directly compare with the fractional crystallisation path of the 1350 ^{o}C, but provides a basic comparison between melt evolution from different fractions.

Crystallisation Sequence

Orthopyroxene, which appeared between 1350 and 1300 ^{o}C, was the first crystalline phase observed in the fractional crystallisation sequence of liquid separated from the primitive mantle at 1350 ^{o}C. Feldspar then crystallised between 1150 and 1125 ^{o}C. Small spinel crystals were present at all temperatures in experiments with bulk compositions containing small amounts of Cr_2O_3. In the HA6 series, low-Ca pyroxene crystallised between 1300-1250 ^{o}C with 10 % pyroxene seen at 1250 ^{o}C increasing to 32 % at 1150 ^{o}C.

Melt Compositions

As fractional crystallisation proceeds through the temperature interval from 1350 ^{o}C to 1125 ^{o}C, the liquid composition increases in SiO_2 (from 51 to 53 wt. %), CaO (from 8 to 11 wt. %) and Al_2O_3 (from 9 to 13 wt. %). It also decreases in MgO (from 10 to 5 wt. %). The Mg# of the melt decreases from 53 at 1350 ^{o}C, to 36 at 1125 ^{o}C. The melt compositions become eucritic below 1300 ^{o}C. In the HA6 series as temperature decreases from 1300 to 1150 ^{o}C, the MgO content of the melt decreases, and the CaO and Al_2O_3 content increases, with other elements remaining roughly the same. The melt compositions become eucritic at 1200 ^{o}C. The melts produced by 45

% batch partial melting of our primitive mantle composition followed by fractional crystallisation of the 1350 ^{o}C melt are compositionally similar to those generated in the earlier studies. They tend, however, to be slightly richer in SiO_2 and poorer in FeO.

Crystalline phase compositions

In the fractional crystallisation sequence of the melt segregated from the mantle at 1350 ^{o}C, pyroxene becomes richer in CaO, FeO, Al_2O_3, and Cr_2O_3 and poorer in MgO as temperature decreases, with orthopyroxene of composition $Wo_{1.31}En_{81.25}Fs_{17.44}$ at 1300 ^{o}C giving way to pigeonite below 1200 ^{o}C and the latter approaching $Wo_{6.42}En_{63.34}Fs_{30.24}$ at 1125 ^{o}C. The experimentally produced pyroxenes first become diogenitic in composition around 1250 ^{o}C. The pyroxene compositions become more Ca-rich from $Wo_{1.95}En_{80}Fs_{17.85}$ to $Wo_{4.50}En_{71.48}Fs_{24.02}$in the HA6 series. However, the most evolved pyroxene compositions I produced match the low-Ca pyroxene compositions found in eucrites and in the *Stolper* (1977), *Bartels and Grove* (1991) and *Boesenberg and Delaney* (1997) experiments.

2.5 Thermodynamic Models

2.5.1 AlphaMelts vs. Petrolog

Two software packages were used to investigate crystallisation paths of a Vestan mantle and the melts it produces: MELTS (*Ghiorso and Sack*, 1995) and Petrolog3 (*Danyushevsky and Plechov*, 2011). Both models are well calibrated for terrestrial basaltic (and to an extent mantle) compositions at low pressures and temperatures. With both programs the input is the starting composition, temperature, pressure and melt oxidation states and either equilibrium or fractional crystallisation can be specified.

Petrolog

Petrolog3 (*Danyushevsky and Plechov*, 2011) is software designed to model fractional and equilibrium crystallisation at varying temperature, pressure and melt oxidation state. To use Petrolog I defined the start melting composition, pressure and oxidation state. In addition I selected the minerals required to crystallise from the melt: olivine, pyroxene and selected an appropriate mineral-melt model. Within the software there is a choice of mineral-melt models: 16 olivine models, 16 pyroxene and nine feldspar models. For a mineral-melt model to be incorporated into this program, the temperature at which a mineral appears on the liquidus of a melt and its composition must be able to be calculated for a melt composition at a given pressure and oxidation state. Either pure equilibrium or fractional crystallisation can be selected (or some mixture of the two) and the increments for the calculation can be set, and I chose temperature intervals of 1 ^{o}C until complete crystallisation had occurred. Petrolog3 then considers the melt composition at each temperature step, calculating the liquidus temperature for each selected mineral that would be in equilibrium with the melt, and if that temperature is lower or equal to the actual temperature, that mineral is crystallised. The amount of crystallisation is determined by using mass-balance equations to subtract the composition of the minerals formed, and by the size of the calculation step. Then, if equilibrium crystallisation is being modelled the calculations are repeated for the original bulk composition at the next model step. If fractional crystallisation is being modelled the remaining melt composition after mineral crystallisation is used as the new 'bulk' composition. The algorithm for calculating fractional and equilibrium crystallisation is model-independent, however the selection of each mineral-melt equilibria model is key for correctly modelling the processes.

AlphaMELTS

MELTS computes the equilibrium phase relations in igneous systems in a series of temperature and pressure steps by minimising the Gibbs Free Energy. The mineral phase models are built up from thermodynamic data that are independent from the low-

pressure experimental phase equilibria used for the liquid phase models. The MELTS algorithm (*Ghiorso and Sack*, 1995) is a regular solution thermodynamic model that uses Gibbs Free Energy minimisation to predict the phase assemblage and compositions of phases present at a given temperature, pressure and oxidation state. The regular solution model describes the melt composition in the system: SiO_2-TiO_2-Al_2O_3-Fe_2O_3-Cr_2O_3–FeO-MnO-MgO-NiO-CoO-CaO-Na_2O-K_2O-P_2O_5-H_2O. The MELTS thermodynamic model is derived from the internally consistent models for solid solutions of the most common igneous rock-forming minerals: olivines, pyroxenes, feldspars, spinels and oxides. MELTS calculates the interaction parameters from the solid-liquid equilibria data. MELTS uses the least squares fit to calculate the interaction parameters with the minimum Gibbs Free Energy for a range of phases, their compositions and liquid in equilibrium with the melts. MELTS is calibrated against measured thermodynamical data from experiments and natural samples. There are several options for using the MELTS software: one is using a Graphical User Interface available online, or the other is using the alphaMELTS software (*Smith and Asimow*, 2005). AlphaMELTS is a text-menu driver for MELTS, pMELTS and pHMELTS allowing users to switch between calibrations and also incorporate trace element calculations. The MELTS algorithm is well calibrated for pressures lower than 3 GPa in a wide range of terrestrial basaltic compositions. AlphaMELTS was used and to run a MELTS calculation the starting bulk composition, temperature, pressure and oxidation state were entered and then equilibrium or fractional crystallisation was selected.

In both the Petrolog3 and MELTS models PM1 and PM2 were used as starting points and equilibrium and fractional crystallisation models were run, for both one stage and two stage (magma ocean) models. Factors that were varied include the oxygen fugacity, pressure, volatile content and Petrolog3 calculations were performed using different mineral melt models.

There are advantages and disadvantages to each software program. In Petrolog the most appropriate mineral-melt equilibria model can be selected. However, when none of the mineral-melt models are particularly relevant for the system under scrutiny, this

can lead to some confusion in which is the most appropriate model to use. Although the calibration database for the MELTS software includes studies of HED compositions (*Stolper*, 1977; *Longhi and Pan*, 1988; *Bartels and Grove*, 1991; *Grove and Bartels*, 1992) and of other relevant chondritic compositions (*Jurewicz et al.*, 1991, 1993), modelling of partial melting and crystallisation of the HED parent body requires extrapolation outside of the compositionally calibrated range. The issue with this is that the accuracy or amount of error cannot be estimated and a recent study by *Balta and McSween* (2013) highlighted several issues with the applicability of MELTS to similar Martian compositions. In addition the MELTS algorithm is known to overestimate liquidus temperatures of pyroxene by up to ~ 50 ^{o}C and the treatment of spinel is not fully accurate. Similarly I found that Petrolog calculations break down when all of the minor elements (MnO, Cr_2O_3 and TiO_2) are considered. Presumably this is due to the fact that the mineral-melt models do not fully incorporate these elements. In general varying the oxygen fugacity by several log units, or by varying the pressure by a couple of hundred bars does not seriously affect the outcome of the models in either software. More important are the compositional input and the mineral-melt models selected in Petrolog3.

Figure 2.10 shows the results of the AlphaMELTS and Petrolog3 thermodynamic models compared with the experiments, and literature data of eucrite compositions and previous experimental studies. It can be seen that the alphaMELTS models are able to predict the evolution of the melt composition better that Petrolog3, as the melt evolves to a lower MgO content, and particularly in the fractional crystallisation path. Due to the more accurate fit to the observed experimental data, the MELTS software was selected for modelling.

2.5.2 AlphaMelts Models

An equilibrium crystallisation model was run on the primitive mantle composition from 1700 ^{o}C down temperature at 1 ^{o}C temperature decrements and fractional crystallisation models were run on the HA4 composition below 1350 ^{o}C. All models were run

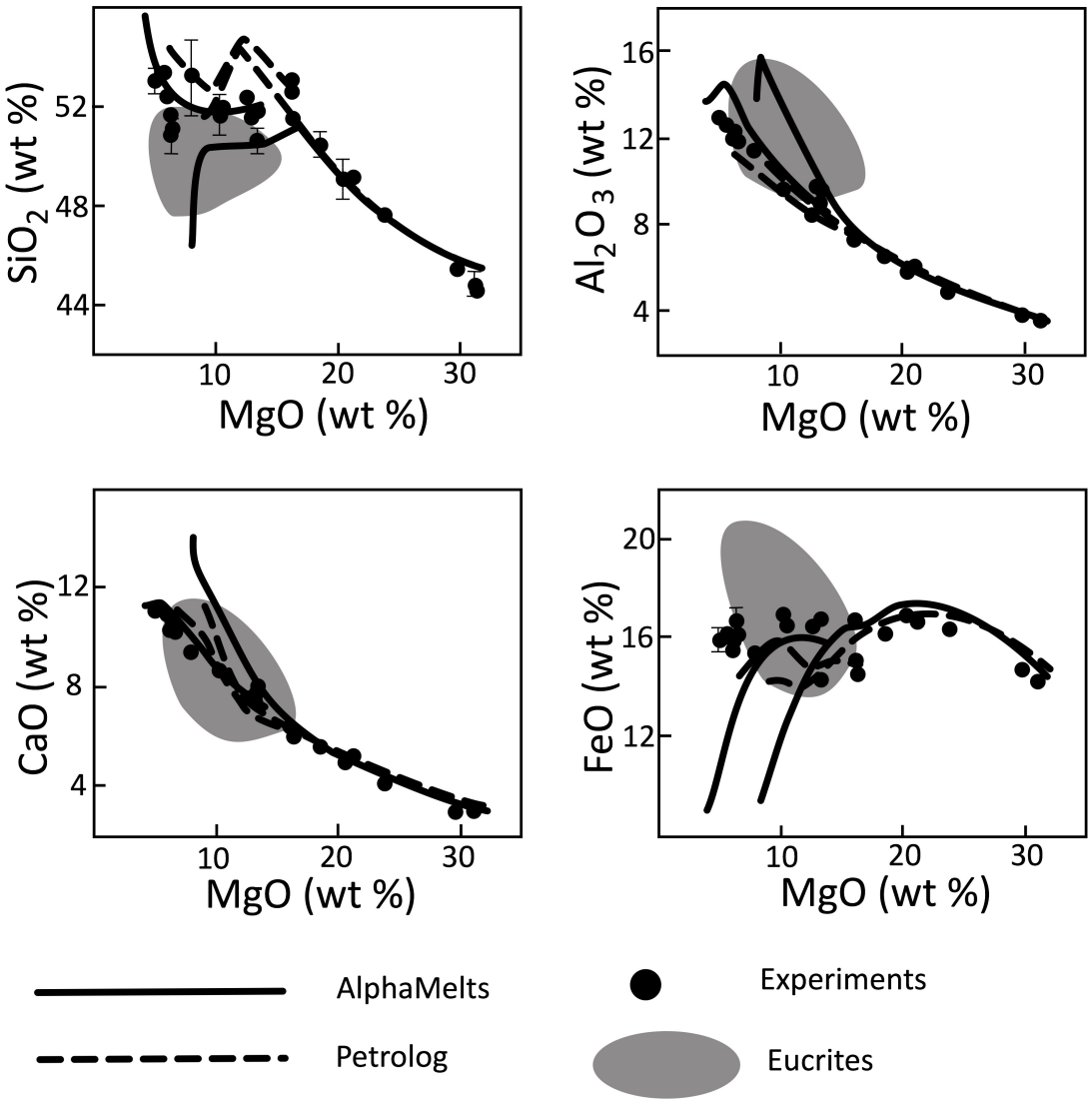

Figure 2.10: Petrolog (dashed lines) and AlphaMelts models (continuous lines) of the two stage model of crystallisation for PM2, with experiments (black filled circles) and eucrite compositions (plotted from the same source as figure 2.4 and shown by the grey region).

at atmospheric pressure and the oxygen fugacity was fixed at IW +1.8. The MELTS model results are plotted on Figures 2.4, 2.6-2.8a, 2.10, 2.11, for comparison with the observed experimental compositions of PM2 and 2.5 shows the comparison of the experimental and modelled melts for PM1.

2.5.3 Comparison of thermodynamic models and experimental data

Modal proportions of different phases for the complete crystallisation paths (equilibrium and fractional) are plotted against temperature in Figure 2.11 for PM2 when the melt is extracted after 55 % and 63 % crystallisation, along with the corresponding MELTS models. From Figures 2.4-2.8a, 2.10 and 2.11 it can be seen that MELTS correctly predicts the observed crystallisation sequence for the PM2 composition with olivine crystallising first at 1634 ^{o}C, and orthopyroxene at 1417 ^{o}C. However, although the predicted olivine crystallisation temperature is in good agreement with my results, the temperature of orthopyroxene appearance from MELTS is overestimated by more than 50 ^{o}C. Other known issues with the MELTS software are the way it deals with minor components of the crystalline phases, and the lack of calibration between the IW buffer. Cr_2O_3 is a significant element during mantle evolution due to the formation of spinel, however alphaMELTS does not incorporate Cr_2O_3 into any other crystalline phase. This may have some effect on the predicted liquidus of orthopyroxene because this phase generally contains some Cr_2O_3. It should be noted, however, that although the orthopyroxene model in MELTS is oversimplified, the lack of consideration of a Cr-bearing component is unlikely to be responsible for the significant error in its calculated liquidus temperature. This is because addition of Cr- or Fe^{3+}- bearing components increases the entropy of the phase and hence tend to increase rather than decrease its stability.

Figures 2.4−2.8a, 2.10 and 2.11 show that MELTS predicts the correct trend for the liquid line of descent and melt evolution. The calculated melt compositions become increasingly offset from the observed compositions. This is due to the overestimation of orthopyroxene crystallisation temperature, which causes the MELTS program to overestimate the modal proportion of orthopyroxene and underestimate the proportion of melt at any given temperature.

Despite the discrepancy noted above, the MELTS model reproduces the melt and

olivine major element compositions within 1 wt.% of the measured experimental compositions in the olivine phase field. Furthermore, MELTS reproduces the crystalline phase compositions at any given melt MgO content very well (on the order of 1 wt. %), as illustrated in Figure. 2.7 and 2.8a.

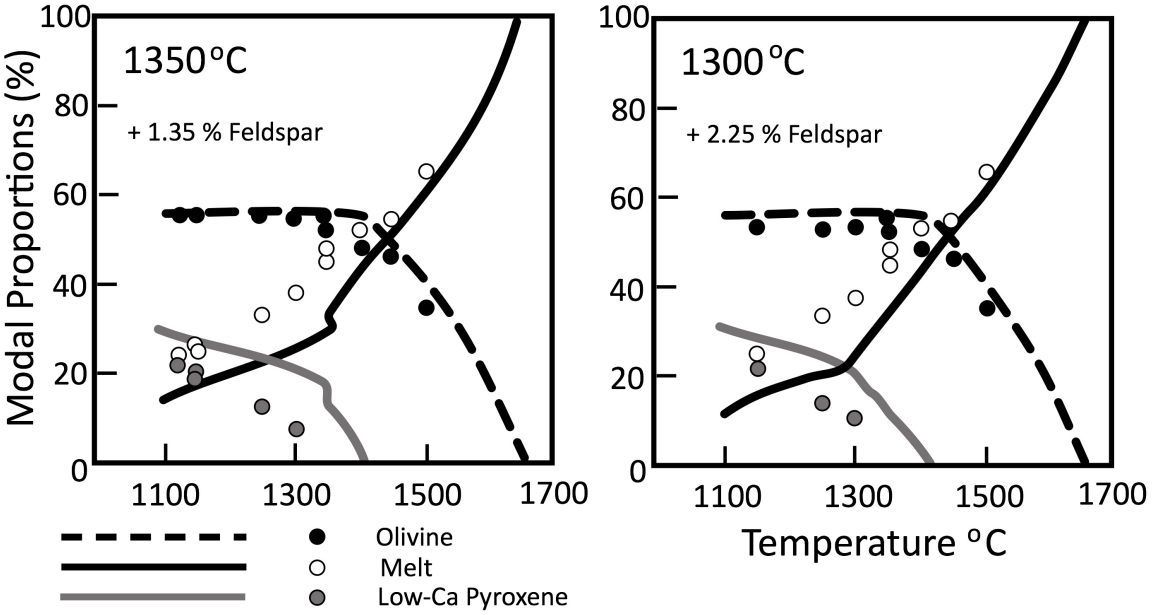

Figure 2.11: Modal proportions of different phases are plotted against temperature. In the left figure, the experimental data of PM2, HA4, HA5 and HA7 have been plotted, and on the right; PM2 and HA6. The proportion of feldspar crystallised are also labelled on each graph.

Likewise with the fractional crystallisation model, the temperature that MELTS predicts orthopyroxene crystallisation is overestimated in the simulated fractional crystallisation paths, but the temperature at which feldspar crystallises is correct. In the latter case MELTS predicts the correct sequence of crystallisation, and reproduces the crystalline phase compositions. For example, in the HA4 experiments MELTS predicts that there should already be 14 % orthopyroxene at 1350 ^{o}C, and for the HA6 composition at 1300 ^{o}C there should already be 16 % pyroxene. The errors in MELTS' predicted orthopyroxene liquidus temperature (50-100 ^{o}C) has been noted in other studies of martian and terrestrial compositions (discussed in more detail by *Balta and McSween* (2013)). The final experimentally-determined phase proportions from the

two stage crystallisation path of PM2 with melt extracted at 1350 ^{o}C and fractionally crystallised to 1125 ^{o}C are 24.2 % melt, 52 % olivine, 23.5 % pyroxene and 0.3 % feldspar. MELTS predicts similar proportions of 18.8 % melt, 48.9 % olivine, 32.1 % pyroxene and 0.15 % feldspar. The phase proportions for the two stage crystallisation path of the PM2 composition when melt is extracted at 1300 ^{o}C is 25.2 % melt, 52.0 % olivine, 21.8 % pyroxene and MELTS predicts 19.3 % melt, 48.0 % olivine, and 29.5 % pyroxene.

To investigate how the extent of partial melting prior to melt extraction affects the liquid-solid relationships, the fractional crystallisation path of partial melt of our Mg# 80 primitive mantle determined experimentally at 1300 ^{o}C (after 37 % partial melting) can be compared with the fractional crystallisation path of the 1350 ^{o}C melt (after 45 % partial melting). The extracted melt and its crystallisation path generates liquids higher in SiO_2, CaO and Al_2O_3 with lower FeO contents than the partial melt at 1350 ^{o}C (after 45 % melting). The liquid line of descent is not significantly different, however, and eucritic liquids and diogenitic pyroxenes are both produced. I am aware that the error in the orthopyroxene liquidus calculated by MELTS may lead to a slight overestimate of the degree of partial melting required to generate eucrites from any given mantle composition. However, the general agreement between my experimentally produced melt compositions and those calculated by MELTS means that the effects of changing bulk composition given by MELTS should be reasonably accurate. An alphaMELTS model of the fractional crystallisation of the predicted melt produced at 1250 ^{o}C (25 % partial melt) can also be calculated and is compared with the 1300 ^{o}C and 1350 ^{o}C melts in Figure 2.12. It can be seen that as the temperature that melt is extracted increases (and amount of partial melt that increases), the partial melt is less evolved/more primitive in composition and able to crystallise more pyroxene than plagioclase. In fact if a $\sim$50 % partial melt of Vesta were fractionally crystallised, olivine would be on the liquidus and a small amount could crystallise ($<$5 %).

To compare the models directly with the HED meteorites, minor amounts of Na_2O (0.11 wt. %) and K_2O (0.01 wt. %) were added to the primitive mantle composition,

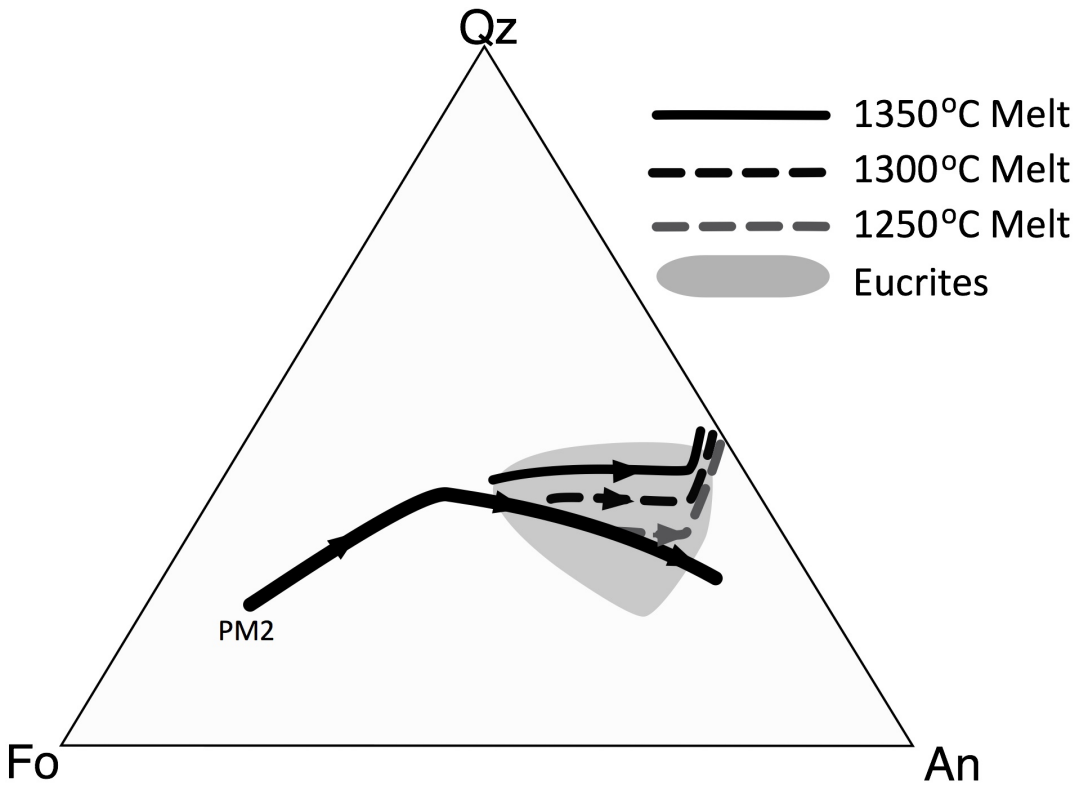

Figure 2.12: Predicted Melt Evolution of PM2 and its extracted melts at 1250 (grey dashed line), 1300 (black dashed line) and 1350 ^{o}C (black line) projected into the Fo-An-Qz ternary. Eucrite compositions are shown for comparison and are taken from the references outlined in Figure 2.4

and MELTS calculations were repeated at IW - 1 (following *Mandler and Elkins-Tanton* (2013)). The calculated crystallisation sequence at IW - 1 is virtually identical to that calculated at IW + 1.8 which indicates that these experiments performed at IW + 1.8 are appropriate representations of eucrite crystallisation. MELTS calculations at slightly elevated pressures of 500 bars were also performed on the alkali-bearing primitive mantle composition. In this case a few % olivine crystallises before orthopyroxene in the fractional crystallisation part of the model, but apart from this, the crystallisation sequence and phase compositions are essentially the same. In terms of phase proportions, the MELTS algorithm predicts that 55 % equilibrium crystallisation (45

% partial melting) and subsequent fractional crystallisation of our primitive mantle composition would yield a mantle which is 85 % olivine, 15 % orthopyroxene, and a crust which is contains equal amounts of eucrite and diogenite material. This is consistent with the relative proportions of eucritic to diogenitic meteorite material. The phase proportions do not alter much if the melt is extracted after 63 % crystallisation, and the mantle would contain 75 % olivine, 25 % orthopyroxene, and a crust which is $\sim$ 3:2 eucrite to diogenite. The PM2 composition which has chondritic ratios of refractory lithophile elements is too olivine-rich and has too high an Mg# to generate eucritic liquids and diogenitic pyroxenes directly through equilibrium crystallisation (E.g. Figure 2.4). However, if a 45 % equilibrium partial melt of such a mantle were extracted, then fractional crystallisation of the melt would generate eucritic melts and diogenitic pyroxenes at temperatures of 1250 ^{o}C and below (Figures 2.4, 2.7 and 2.8a). The primitive mantle composition derived here is compositionally similar to the 0.3 CV-0.7 L mixture of CV and L type chondrites that *Righter and Drake* (1997) favour, but has a higher Mg# of 80 compared to their value of 74. In the latter case optimal eucrite and diogenite compositions should be generated after about 60-70 % equilibrium crystallisation of the magma ocean (*Mandler and Elkins-Tanton*, 2013). As both compositions can produce eucrites and diogenites, there is obviously a range of acceptable mantle compositions. Therefore I selected my PM2 estimate of Vesta's mantle as a starting point for further investigation of the possible range of mantle compositions and crystallisation sequences.

2.6 Discussion of Primitive Mantle Composition

The Mg# of the starting mantle and the extent of equilibrium crystallisation prior to melt extraction were varied systematically between 65 and 85, and 50 % to 90 % respectively, in a series of MELTS calculations in order to determine the range of mantle compositions capable of producing eucrites and diogenites. The relative proportions of the other major elements were kept chondritic. The calculation was

considered successful if, during the fractional crystallisation path, the melt evolved into the eucrite composition field and orthopyroxenes of diogenite composition could crystallise independently of other solid phases.

As the Mg# increases from 65 to 85, the olivine liquidus temperature increases from 1617 to 1661 ^{o}C. Orthopyroxene is the second phase to crystallise in mantle compositions with Mg# $\geq$ 70 with the liquidus increasing from 1319 ^{o}C to 1460 ^{o}C. For comparison with the experimental work here, melts extracted at 1350 ^{o}C can be compared. The extent of crystallisation varies from 55 to 71 % as Mg# increases from 65 to 85, and the Mg# of the extracted melt increases from 44 to 72. This affects the subsequent mineralogy of the Vestan crust, with the proportion of pyroxene to olivine crystallised from the extracted melt increasing with starting mantle Mg#. The starting mantle composition with a Mg# of 85 does not crystallise olivine in addition to pyroxene, and the extracted melt from the mantle composition with Mg# 65 does not crystallise pyroxene in addition to olivine. An essential requirement for the formation of the diogenites through a two-stage model is that the extracted partial melts crystallise dominantly pyroxene and have a high pyroxene:olivine ratio during fractional crystallisation. The extracted melt from the Mg# 70 mantle crystallises equal proportions of olivine and pyroxene so a lower limit of Mg# $\sim$ 75 can be placed on the starting mantle compositions. Assuming that the proportions of refractory elements, excluding Fe, in the mantle are chondritic, then melts in the range of eucrite compositions are produced from starting compositions with Mg# of 75-80 through the magma ocean model. If the Mg# is higher, the melts are more SiO_2-rich and FeO-poor than the eucrite field, and if the starting Mg# is lower the melts are lower in SiO_2, CaO, and Al_2O_3 and more FeO-rich than the eucrite composition field. Therefore, assuming development of an early magma ocean, the plausible range of Mg# for the starting Vestan mantle is $\sim$75-80.

The alternative partial melting model can yield eucritic melts by 20 % partial melting of a mantle of Mg# $\sim$ 70. In such cases, however, the residuum would be olivine-rich and the accumulating pyroxene too low in Mg# to represent the most

magnesian diogenites. More magnesian orthopyroxenes of Mg# 80 could be produced by crystallisation from melts extracted after 30-50 % partial melting but the fractionating melts do not become eucritic, and there is no appropriate lithology in the meteorite record. The only plausible way, therefore, in which both eucrites and diogenites could be produced from Mg# 70 mantle is if this source region were heterogeneous or if it underwent successive melting and crystallisation events. Such explanations would be in accord with the observed wide range of trace element abundances including the Ni and Co contents of Mg-rich clasts *Lunning et al.* (2015) and Dy/Yb ratios of diogenites (*Barrat and Yamaguchi*, 2014).

For starting mantle compositions with Mg# of ∼80, melt extraction after 35-45 % partial melting is required to generate eucritic liquids. The partial melts produced are in the eucrite field, and continue to evolve as the MgO content decreases and crystallisation proceeds. For lower degrees of partial melting the melt is not in the eucrite field and is too poor in FeO and rich in SiO_2 to be able to generate eucrites. For starting mantle compositions with Mg# of 75, a slightly lower degree of partial melting (30-40 %) produces a partial melt which is eucritic in composition and can continue to evolve in the eucrite field. If melt is extracted at a higher temperature/degree of partial melting, the melt composition is not within the eucrite field and is too FeO-rich, CaO-and Al_2O_3-poor to become eucritic while low degrees of partial melting (<30 %) leads to melts which are too poor in MgO and FeO to produce eucrites.

Finally, a more general investigation into the primitive mantle composition was performed using a Monte-Carlo approach. Starting compositions were generated by randomly selecting the concentrations of each major element (MgO, FeO, CaO, Al_2O_3, SiO_2) within a ± 10 % relative window about the primitive mantle composition. These values were then normalised to 100 % to produce a new bulk mantle composition. These ± 10 % variations in MgO, FeO, CaO and Al_2O_3 do not significantly affect the crystallisation sequence and phase proportions, however, I found that that a starting mantle with >43 wt% SiO_2 is required to generate orthopyroxene during fractional crystallisation.

The results from the experimental and modelling work performed here indicate that the different petrogenetic models require different bulk silicate Vesta compositions, given the underlying assumption that CaO, MgO, Al_2O_3 and SiO_2 are in chondritic proportions to one another. A range of HED mantle compositions between our PM2 (Table 2.1) with Mg# 80, and the 0.3 CV-0.7 L composition of *Righter and Drake* (1997) with Mg# 75 can produce the major element compositions of both eucrites and diogenites through the two-stage model of partial melting, melt extraction and fractional crystallisation. Eucritic crustal compositions (but not the full range of diogenite cumulates) can also be produced by partial melting of a HED mantle composition with a slightly lower Mg# of 70. The latter is similar in composition to the mixture of H and CM chondrites favoured by *Boesenberg and Delaney* (1997) and *Toplis et al.* (2013).

2.7 Conclusions

A HED parent body with refractory elements (including Mg and Si) in chondritic proportions results in a model consistent with the density and moment of inertia of Vesta if the mantle has an Mg# of about 80. In this case the core would be 15-20 % of the mass of Vesta and the mantle would contain olivine of approximately the same Mg# as the most Mg-rich diogenites. The liquidus temperature of the mantle is ∼1625 ^{o}C with olivine being the sole precipitating phase in the interval 1625-1350 ^{o}C. Separation of the mantle melt at 1350 ^{o}C, the point at which orthopyroxene appears, simulates equilibrium partial melting of the mantle and ensures that the liquid line of descent is dominated by pyroxene fractionation. Under these conditions, 45 % equilibrium partial melting of the mantle leads to a melt which, during fractional crystallisation, produces eucritic liquids and diogenitic solid assemblages at temperatures below ∼1300 ^{o}C. My mantle composition appears to be in the acceptable range for the generation of the HED meteorites by equilibrium partial melting followed by fractional crystallisation of the segregated melt as suggested by *Righter and Drake* (1997).

I found that the MELTS program performs well at predicting the olivine liquidus

temperature, overestimates the orthopyroxene liquidus by $\sim$ 70 ^{o}C and predicts melt compositions in good agreement with those observed at any given MgO content. Given its utility, I used the MELTS program to investigate the range of mantle compositions which can lead to eucritic melt compositions and which precipitate pyroxenes of diogenitic composition. I found that, given the assumption of chondritic ratios of refractory lithophile elements, the range of mantle Mg#s which generate eucrites and diogenites by the 2-stage process is 75-80. In particular, a lower limit of Mg# 75 can be placed on the starting composition for the mantle in order to crystallise plausible proportions of olivine and pyroxene. A Monte Carlo approach suggests that small variations ($\pm$ 10 % relative to their major element abundance) in CaO, MgO and Al_2O_3 content of the HED parent body mantle remain consistent with generation of eucrites (liquids) and diogenites but that the SiO_2 content of the mantle must be greater than 43 wt. % in order to generate orthopyroxene during fractional crystallisation of the segregated partial melts.

Chapter 3

An Experimental study of REE and HFSE partitioning between low-Ca pyroxene and anhydrous Fe-rich silicate melt at 1 atm

3.1 Introduction

Having refined the compositional range of Vesta and the processes which are capable of producing the mineralogy and major element compositions seen in the HEDs, the next step is to investigate the minor and trace elements. As discussed in Chapter 1, the eucrites and diogenites display a diverse range of trace element abundances and signatures. Trace elements are a good indicator of different igneous processes and so unraveling their signatures is key to our understanding of Vesta. Trace elements are fractionated during Vesta's igneous evolution between the crystallising minerals and melt. The main minerals which are present in the interior of a small planetary body like Vesta are olivine, pyroxene (ortho-, pigeonite and clino-) and feldspar. Low-Ca pyroxene (orthopyroxene and pigeonite) is the most ubiquitous mineral observed in the HED lithologies and so understanding how it fractionates trace elements is paramount

to understanding the interior evolution of Vesta and other protoplanetary bodies. In terms of planetary mantle minerals, the extent to which low-Ca pyroxene fractionates trace elements is the least understood (compared to clinopyroxene or garnet).

Temperature, melt and crystal composition have been noted to affect the trace element coefficients (e.g. *Weill and McKay* 1975), however the interplay between the factors is complex. The partition coefficients for trace elements into low-Ca pyroxene vary over four orders of magnitude (shown in *van Kan Parker et al.* 2011) across a range of igneous systems. Even within one experimental study of mineral-melt partitioning in lunar compositions, *Weill and McKay* (1975) noted an increase in the partition coefficients of REE elements of up to a factor of three as temperature decreased from 1340 to 1200 ^{o}C and the melt composition evolved.

Although several studies have performed geochemical calculations to model the magmatic evolution of Vesta's interior (e.g. *Mittlefehldt* 1994; *Fowler et al.* 1995, 1994; *Shearer et al.* 1997; *Barrat et al.* 2008), partition coefficients specific to the HEDs have not been measured directly. Partition coefficients have been selected or predicted from a number of sources. *Mittlefehldt* (1994) used the model of *Colson et al.* (1988) to calculate partition coefficients, which predicted a 3-fold increase in REE partitioning over the temperature interval over which the diogenites are thought to crystallise. The simple thermodynamic model derived by *Colson et al.* (1988) calculated partition coefficients based on melt composition and temperature and was calibrated from a series of orthopyroxene-melt partitioning data from a range of terrestrial compositions. *Mittlefehldt* (1994) and *Shearer et al.* (1997) use the REE orthopyroxene-melt partition coefficients measured by *McKay et al.* (1991) on lunar compositions, also assuming a factor of three increase based on *Mittlefehldt* (1994) and *Colson et al.* (1988). This increase in compatibility significantly affects the distribution of trace elements between the cumulates and melt during magmatic evolution (*Mittlefehldt*, 1994; *Fowler et al.*, 1994). *Barrat et al.* (2008) use constant opx-melt coefficients measured by *Schwandt and McKay* (1998) for enstatite-basaltic achondrite melt compositions.

Recently the investigation of trace element fractionation by orthopyroxene has re-

gained popularity to try and gain a quantitative understanding of partitioning, particularly to investigate lunar magma ocean processes. In order to build predictive models which can account for changes in conditions and composition, the database of experimental data needed to be expanded. Experimental studies on lunar compositions at a range of pressure of temperatures have been performed (*van Kan Parker et al.*, 2011; *Sun and Liang*, 2013) and predictive models have been developed (*Yao et al.*, 2012; *Sun and Liang*, 2013). However, direct measurements of trace element partitioning for HED compositions and conditions have not been made.

The objective of this chapter is to extend the current database of trace element partition coefficients to reducing conditions at 1 atmosphere and high temperature between low-Ca pyroxene (orthopyroxene and pigeonite) and anhydrous, Fe-rich basaltic melt. This will then enable a more thorough and detailed investigation into the differentiation and magmatic processes capable of producing the trace element variations in eucrites and diogenites. The results will also have implications for protoplanet and early terrestrial planetary formation.

3.1.1 Theory behind Trace Element Partitioning

Trace elements are chemical elements which occur in very low abundances (parts per billion to parts per million) in a system and which do not form major components of the crystal or liquid phases present. Trace element ions can replace major element ions in crystal lattices. The variations in trace elements across a suite of rocks can vary over several orders of magnitude, and different igneous processes affect the trace element budget in different ways. Therefore trace elements are a useful tracer of igneous processes. The distribution of a trace element between two phases is:

$$D_i^{\alpha-\beta} = \frac{C_i^{\alpha}}{C_i^{\beta}} \tag{3.1}$$

Equation 3.1 is known as the Nernst partition coefficient, and is the ratio of the concentration of element i between the two phases (α and β). Trace elements often pref-

erentially favour one phase over another depending on their geochemical behaviour. *Goldschmidt* (1937) classified the trace elements into groups depending on their geochemical behaviour, e.g. lithophile elements that have an affinity for silicate phases, siderophile elements that have an affinity for metallic liquids (planetary cores). *Goldschmidt* (1937) also formulated some rules for partitioning: e.g. an ion of one element can replace an ion of another in a phase if they are similar in size and charge. *Ringwood* (1955) built on Goldschmidt's rules to account for differences in electronegativities and bonding character of the two ions. The thermodynamics (e.g. *Wood and Fraser* 1976) of trace element partitioning can be considered in order to gain a quantitative understanding.

The substitution of trace elements into minerals can be considered as trace components entering mineral phases as solid solutions. Due to differences in size and charge between the major ion and its substituting trace ion, the mixing between major and trace components should be non-ideal. However, the low abundance of trace components and equal distribution of trace components across a crystal lattice mean that their behaviour can be described by Henry's Law for ideal solutions. This is because the trace components are so diluted, that even doubling their concentration will not affect their average chemical environment. Therefore their activity coefficient remains constant. Henry's Law can be expressed as:

$$a_i^j = k_i^j X_i^j \tag{3.2}$$

where a_i^j is the activity of element i in phase j, k is the proportionality constant and X_i^j is the concentration of element i in phase j.

This simple activity-composition relationship can be used to describe the trace element distribution between two different phases, for example the component XYZ_2O_6 between pyroxene and melt. At equilibrium the chemical potential of component XYZ_2O_6 in the melt will be equal to the chemical potential of XYZ_2O_6 in the py-

roxene and so:

$$\mu^{melt}_{XYZ_2O_6} = \mu^{pyroxene}_{XYZ_2O_6} \tag{3.3}$$

which can be rewritten as:

$$\mu^{melt,o}_{XYZ_2O_6} + RTlna^{melt}_{XYZ_2O_6} = \mu^{pyroxene,o}_{XYZ_2O_6} + RTlna^{pyroxene}_{XYZ_2O_6} \tag{3.4}$$

where the μ^o terms are the chemical potentials at standard state and R is the gas constant (8.314 J/molK).

Applying Henry's Law this equation becomes:

$$-\Delta G^o = RTln\frac{k^{pyroxene}_{XYZ_2O_6}X^{pyroxene}_{XYZ_2O_6}}{k^{melt}_{XYZ_2O_6}X^{melt}_{XYZ_2O_6}} = RTlnK \tag{3.5}$$

Where $-\Delta G^o$ is the free energy of exchanging component XYZ_2O_6 between the mineral and melt phases at standard state, and K is the equilibrium constant for the crystal melt reaction. From 3.5 we can see that:

$$K = \frac{k^{pyroxene}_{XYZ_2O_6}X^{pyroxene}_{XYZ_2O_6}}{k^{melt}_{XYZ_2O_6}X^{melt}_{XYZ_2O_6}} \tag{3.6}$$

$$K\frac{k^{melt}_{XYZ_2O_6}}{k^{pyroxene}_{XYZ_2O_6}} = \frac{X^{pyroxene}_{XYZ_2O_6}}{X^{ol}_{XYZ_2O_6}} = D \tag{3.7}$$

and

$$D_i^{pyroxene-melt} = exp(\frac{-\Delta G^o}{RT}) \tag{3.8}$$

and so for ideal solutions $D_i^{pyroxene-melt}$ is dependent on temperature in the same way the equilibrium constant is. $D_i^{pyroxene-melt}$ is also dependent on pressure in a similar manner. The activity coefficient k is dependent on crystal composition and so $D_i^{pyroxene-melt}$ is dependent on pressure, temperature and crystal composition. Therefore, in many igneous processes, the $D_i^{pyroxene-melt}$ cannot be assumed to be constant. It is not always possible to determine partition coefficients directly from natural samples (or their speculated source compositions), and so quantitative and predictive models

have been developed.

I will now outline some of the key advances in the development of predictive models, particularly focused on the variation of partition coefficient with ionic radii. *Nagasawa* (1966) used the theory of lattice defects in ionic crystals to consider trace element partitioning quantitatively. *Nagasawa* (1966) calculated theoretical partition coefficients, via the free energy change associated with substituting a major ion with a trace ion that has a larger ionic radius into the lattice. This free energy change is the strain energy of a lattice to accommodate the larger ion.

Onuma et al. (1968) continued this work by measuring the distribution of trace elements with different charges (1^+, 2^+, 3^+, 4^+) between augite (clinopyroxene)-melt and bronzite (orthopyroxene)-melt. *Onuma et al.* (1968) plotted the partition coefficients vs. ionic radii and observed that the partition coefficients for series of isovalent ions fit parallel parabolic curves. The ionic radii at the maxima of these parabola coincided with the ionic radii of the major element ions in the mineral: Mg^{2+} and Ca^{2+} for augite and Mg^{2+} for bronzite. This supports the theory that trace elements were substituting into lattice sites. *Onuma et al.* (1968) interpreted the parallel nature of the parabolae to mean that the free energy change required to balance the difference in radius between the host ion and substituting ion is constant for each isovalent series. Also, that the charge effect is independent of, and less significant than, the effect of ionic radii on partitioning.

Brice (1975) considered the crystal lattice as an elastic continuum with the lattice sites as spherical shells and derived an equation for the lattice strain energy:

$$\Delta G_{strain} = 4\pi E N_A [\frac{r_o}{2}(r_i - r_o)^2 + \frac{1}{3}(r_i - r_o)^3] \tag{3.9}$$

E is the Young's Modulus (a measure of the elasticity/stiffness) of the lattice site, N_A is Avogadro's Constant, r_o is the ideal radii of an ion in the site and r_i is the radii of a trace ion substituting into the site. ΔG_{strain} is the work done (or energy expended) as the lattice expands the distance (r_i-r_o) to accommodate the larger ion.

Blundy and Wood (1994) built on this work and developed a predictive model to calculate partition coefficients using the elasticity and size of lattice sites.

The free energy change of substituting a trace ion into a lattice (Equation 3.5) can be divided into two components:

$$-\Delta G^{o} = \Delta G^{mineral}_{fusion} - \Delta G^{y-i}_{exchange} \tag{3.10}$$

$\Delta G^{mineral}_{fusion}$ is the standard state free energy of mineral formation which has the major cation y. $\Delta G^{y-i}_{exchange}$ is the free energy associated with removing element i from the melt and substituting it for major ion y in the crystal and simultaneously removing y from the crystal and adding it to the melt. $\Delta G^{y-i}_{exchange}$ is a function of the ΔG_{strain} of the crystal and melt, however in this case is assumed to be $\sim \Delta G^{crystal}_{strain}$ (which can be described by Equation 3.9), as the strain energy in the melt phase is assumed to be negligble.

Blundy and Wood (1994) combine equations 3.9 and 3.10 to derive the equation:

$$D_i^{crystal-melt}(P,T,X) = D_o^{crystal-melt}(P,T,X) exp\left[\frac{-4\pi E N_A[\frac{r_o}{2}(r_i - r_o)^2 + \frac{1}{3}(r_i - r_o)^3]}{RT}\right] \tag{3.11}$$

$D_o^{crystal-melt}$(P,T,X) is the strain-compensated partition coefficient, which describes the strain free substitution of a cation with r_i=r_o, and this term incorporates the $\Delta G^{mineral}_{fusion}$. The theoretical dependence of D_i on r_o is plotted in Figure 3.1a. It can be seen that D_i is almost symmetrical about the r_o of the site, where D_i is at a maximum. The Young's modulus (E) dictates how 'tight' the parabola is and is dependent on pressure and temperature, and r_o is mainly dependent on crystal composition.

The partitioning of any element i into a lattice site can be predicted as long as the r_o, E and D_o (maximum D) are known for the site and charge of interest. These values can be calculated by fitting equation 3.10 to experimentally measured data.

Electrostatic work is expended when the trace element ions have different charges compared with the site into which they are being substituted, and often coupled substitutions occur to compensate for the charge difference. For example, Al can replace

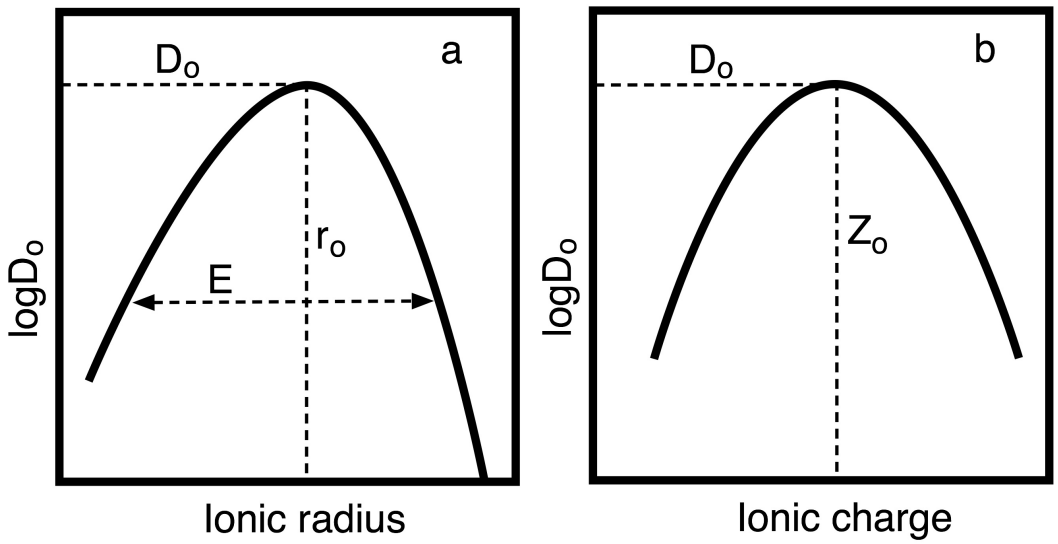

Figure 3.1: Redrawn from *Blundy and Wood* (2003) a) shows the dependence of D_o on the ionic radius. The maximum of the parabola represents the scenario where an ion of the same size as the lattice site is substituting for the major ion, and so no elastic strain energy is expended. b) shows the dependence of D_o on ionic charge. The maxima of the parabola coincides with the scenario that an ion with the same ionic charge is substituting into the lattice and so no electrostatic energy is expended.

Si in the tetrahedral site of pyroxene which means that more M2 sites in pyroxene will have a local 3^+ charge and so, in the case of Al-rich compositions, the partition coefficients for the 3^+ ions in the M2 site should be higher. Common coupled substitutions into pyroxene (taken from *Fowler et al.* 1994) include:

1. $^{VI}Cr^{3+}$-$^{IV}Al^{3+} \rightleftharpoons {}^{VI}M^{2+}$-$^{IV}Si^{4+}$
2. $^{VI}Ti^{4+}$-$2^{IV}Al^{3+} \rightleftharpoons {}^{VI}M^{2+}$-$2^{IV}Si^{4+}$
3. $^{VI}Al^{3+}$-$^{IV}Al^{3+} \rightleftharpoons {}^{VI}M^{2+}$-$^{IV}Si^{4+}$
4. $^{VI}REE^{3+}$-$^{IV}Al^{3+} \rightleftharpoons {}^{VI}M^{2+}$-$^{IV}Si^{4+}$

Sites also have ideal charges and Figure 3.1b shows that ionic charge can be considered in a similar way to ionic radii, with partition coefficients decreasing when the ionic charge is significantly higher or lower than the ion for which is being substituted.

We can see that the D value for any element entering any mineral is specific to the particular igneous situation, and so when investigating geochemical models appropriate partition coefficients have to be selected.

3.1.2 Objectives

The objectives of this chapter are to measure appropriate partition coefficients for the HED system, for use in trace element models. Due to its importance in the crystallisation sequence of the diogenites and eucrites, low-Ca pyroxene has been selected as the main mineral to study. Measurements were made on some of the experimental charges reported in Chapter 2, in addition to further experimental series detailed below. The calculated partition coefficients are then evaluated using the lattice strain model (*Blundy and Wood*, 1994). A comparison will be made with literature studies on similar suites of rocks (e.g. lunar). The recently published predictive model for low-Ca pyroxene partitioning (*Sun and Liang*, 2013) will then be tested.

Two groups of elements were selected for close study: the lanthanide group + Yttrium, commonly known as the Rare Earth Elements (REEs), and the High Field Strength Elements (HFSE). The REEs are transition metals and behave in the same way geochemically. The REEs are incompatible in most rock-forming minerals, due to their large size and high (3^+) charge. The incompatibility of the REEs decreases across the group as atomic mass increases and ionic radii decreases for the minerals of interest in this system. Systematic differences in partitioning behaviour due to this radii difference mean that the REEs are very sensitive to the crystallisation of different minerals. The HFSE elements are also usually incompatible in rock-forming phases as although they are similar in size to the main cations (Mg^{2+}, Fe^{2+}) they have a higher ionic charge (e.g. Hf^{4+}). Both groups are useful tracers of igneous processes.

The pyroxene group of minerals are inosilicates (chain silicates) with the general formula XYZ_2O_6, where X is the M2 site, Y is the M1 site and Z is the tetrahedral site, which usually contains Si with minor Al. Generally the M2 site is filled with Mg, Fe, Ca or Na and is slightly larger ($\sim$0.2 $\mathring{A}$) than the M1 site which contains Mg or Fe.

The cations in the M1 site are octahedrally coordinated to oxygen atoms, whereas the cations in the larger M2 site are coordinated to either 6 or 8 oxygens depending on the size of the ion. The cations that can reside in each site are shown in Figure 3.2 taken from *Papike et al.* (2005). Pyroxene compositions can be described in terms of the Mg, Fe and Ca end-members: Enstatite (En), Ferrosilite (Fs) and Wollastonite (Wo) and plotted into the pyroxene tetrahedron (shown in Figure 3.3). In Figure 3.3 the boundaries of different pyroxene subgroups are shown, derived on their Wo (calcium) contents. Orthopyroxene has $>$ Wo_5, pigeonite has Wo_5-Wo_{15}, subcalcic augite has Wo_{15-25}, augite has Wo_{25}-Wo_{45} and pure diopside hedenbergite has $>$ Wo_{45}. The Ca content of pyroxene affects the crystallographic structure as the ionic radii of Ca is larger than Mg and Fe. Pyroxene is ubiquitous across the solar system, and as the major and trace element composition reflects the source composition and formation conditions, a lot of information can be recorded. Comparisons between the pyroxenes formed on different planetary bodies can be made, increasing our understanding of partitioning and magmatic processes.

Orthopyroxene has two octahedral sites a large VI-fold M2 site, and the smaller VI- fold M1 site, similar to the clinopyroxene M1 site (*Wood and Blundy*, 2003). The trivalent REEs, Y and divalent Mn are assumed to partition preferentially into the larger M2 site, whereas the tetravalent high field strength elements Ti, Hf, Zr and trivalent transition metals Cr, Sc and Al should partition into the smaller M1 site in place of Mg and Fe. Partitioning into both of the sites can be described by the lattice strain model (*Blundy and Wood*, 1994), and is the focus of this chapter.

Previous studies have determined partitioning of a range of elements, including the REEs and HFSEs, between low-Ca pyroxene and basaltic melt on a range of terrestrial, martian, lunar, chondritic and simplified synthetic compositions (e.g. *Weill and McKay* 1975; *Colson et al.* 1988; *McKay et al.* 1991; *Schwandt and McKay* 1998; *Frei et al.* 2009; *van Kan Parker et al.* 2010, 2011; *Sun and Liang* 2013; *Blinova and Herd* 2009; *Cartier et al.* 2014). These pyroxene compositions have been compared with the experimental ones in Figure 3.4, and the partition coefficients compared with the

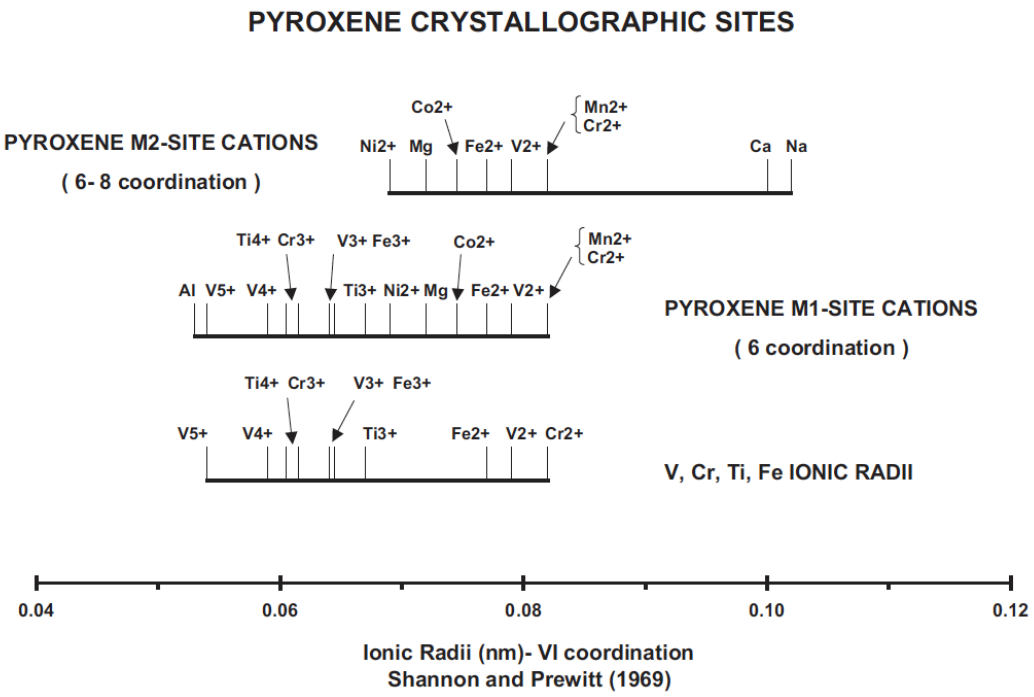

Figure 3.2: Taken from *Papike et al.* (2005). The VI coordination ionic radii of different cations able to enter pyroxene, and the crystallographic sites in which they can enter.

experimental data in Figure 3.5. It can be seen that the partition coefficients vary by an order of magnitude and this range reflects the expected variations in sample composition and experimental conditions of oxygen fugacity pressure and temperature (*Blundy and Wood*, 1994; *Wood and Blundy*, 2003).

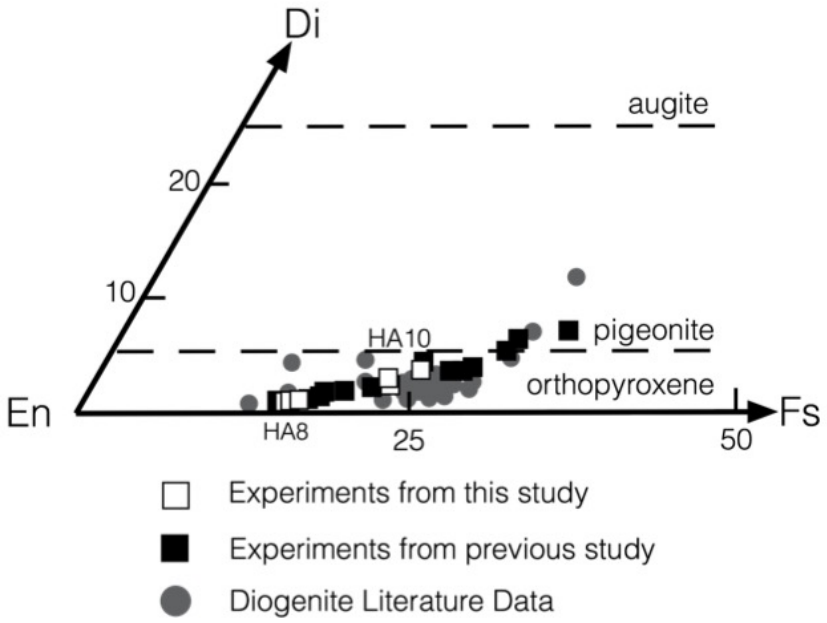

Figure 3.3: Experimental Pyroxene compositions, plotted in the pyroxene quadrilateral, along with diogenite data (taken from *Mittlefehldt* 2015). The black squares are the compositions of experiments presented in Chapter 2 and published in *Ashcroft and Wood* (2015)) and the white squares are the compositions of the experiments performed in this chapter.

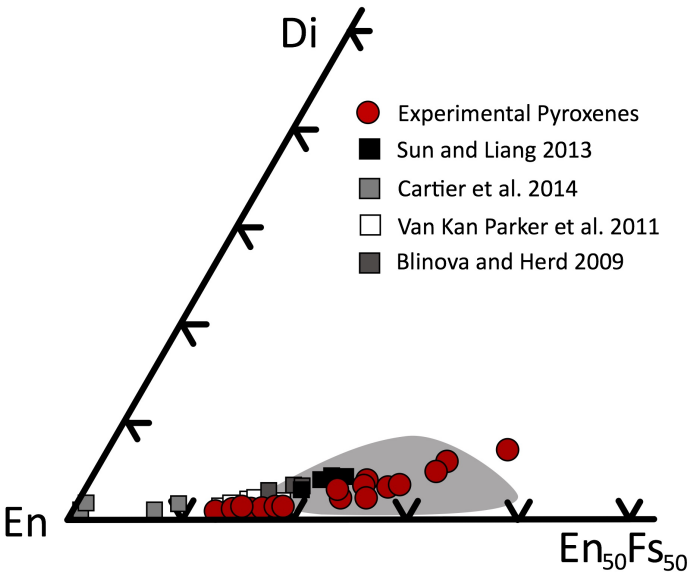

Figure 3.4: Experimental Pyroxene compositions (red circles), plotted in the pyroxene quadrilateral, along with diogenite data (from *Mittlefehldt* 2015) and the literature values of lunar studies (*Sun and Liang*, 2013; *van Kan Parker et al.*, 2011), martian (*Blinova and Herd*, 2009) and enstatite chondites (*Cartier et al.*, 2014).

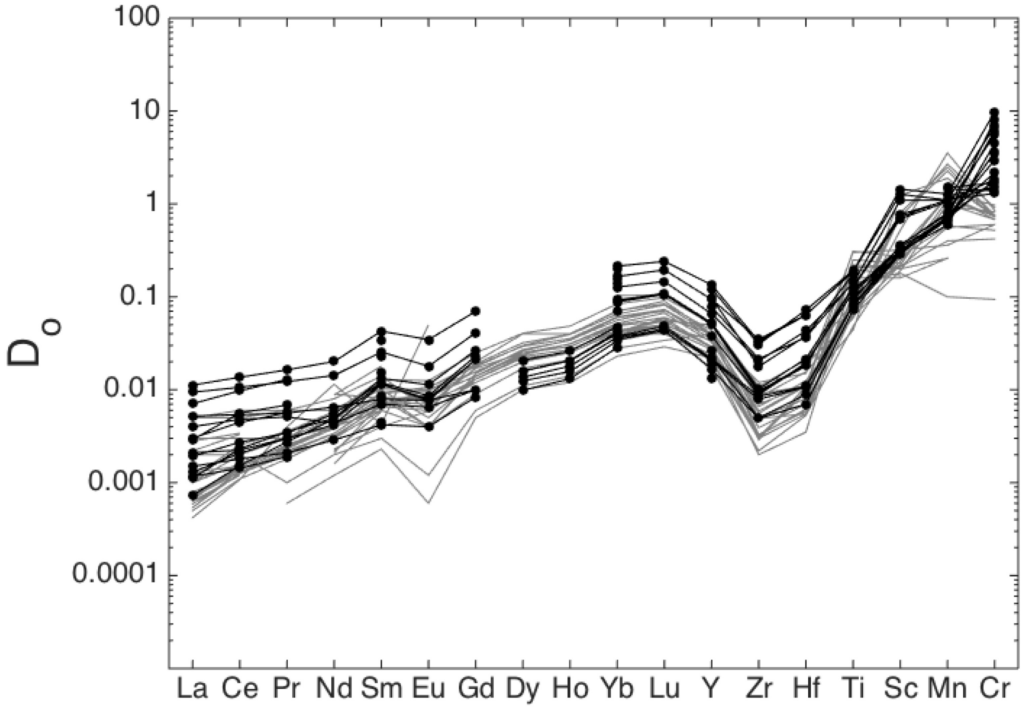

Figure 3.5: Measured low-Ca pyroxene- melt partition coefficients for a range of trace elements of the experiments (black lines and dots), and the literature studies of *Sun and Liang* (2013), *van Kan Parker et al.* (2011), *Frei et al.* (2009) and *Cartier et al.* (2014), shown by the grey lines.

3.2 Experiments

3.2.1 Experimental and Analytical Methods

Some of the experimental charges in Chapter 2 (and published in *Ashcroft and Wood* 2015) were doped with trace elements and so mineral-melt partitioning could be measured directly. However the small crystal size (e.g. in HA2_05) provided analytical challenges for the LA-ICP-MS method. Therefore new starting compositions were made and additional series of experiments were performed. All of the starting compositions can be found in Table A.1. The HA8 composition has the same major element composition of HA4, which is an estimated 45 % partial melt of silicate Vesta, but with trace elements added. Experiments were performed on this composition in the temperature range 1450-1115 ^{o}C to investigate partitioning into liquidus pyroxene. At temperatures below 1300 ^{o}C, however, crystals were too small for LA-ICP-MS analysis. Therefore, the pyroxene and melt compositions of HA8_06 (1200^{o}C) experiment were synthesised separately and mixed together in a 5:95 pyroxene:melt ratio, to make the HA10 mixture. This mixture of a small fraction of crystals to a large fraction of melt promotes the nucleation of a few crystals and combined with slow cooling rates in the experiment, allows these crystals to grow to a large size, particularly when cooled from just above the liquidus to just below. Another starting composition (HA11) was made which is the HA10 composition with an additional 5 wt % Al_2O_3 added, in order to investigate the affect of Al content on opx-melt partitioning. Experiments on this composition were performed at 1200, 1170 and 1140 ^{o}C. Starting materials were synthesised in a similar manner described in Chapter 2. The samples were also doped with trace elements between 50 and 1000 ppm depending on the sample composition and trace element from oxide solutions which were usually in the concentration of 1000 mg/l apart from U and Th which were at 10 000 mg/l. The amount of each trace element in any sample was selected so that there was enough to be detected but that the total amount of trace elements never exceeded 1 wt %, in an attempt to ensure that Henry's Law was obeyed. The pellets were reground under ethanol after reduction, and repelletised

into $\sim$ 500 mg disks, from which 50-100 mg chips were cut off and used in experiments. The experimental run conditions, including full compositional details of the start compositions and experimental products are described in Table A.2. Experiments were performed in a one atmosphere vertical gas-mixing furnace across the 1150-1650 ^{o}C temperature range in the Experimental Petrology Laboratory, Department of Earth Sciences, Oxford. Samples were mounted on a 0.25 mm Re wire loop, and experiments were performed at constant fO_2 of 1.8 log units above the IW buffer using a flowing CO-CO_2 gas mixture. These conditions are identical to the ones in Chapter 2, and are justified for the study of HEDs due to the small size of Vesta, and therefore low interior pressures. An fO_2 just above the IW buffer was chosen to satisfy the requirements of having a high Fe^{2+}/Fe^{3+} ratio in the melt, no Fe metal precipitation and insignificant Fe loss from the sample to the Re wire. The experiments were run in a GERO one-atmosphere gas mixing furnace, in the Experimental Petrology Laboratory, Department of Earth Sciences, University of Oxford on timescales of hours to days. The major element compositions of the experimental phases were determined using the JEOL JXA-8600 Electron Microprobe in the Research Laboratory for Archeology and the History of Art (RLAHA) in the Department of Archeology, University of Oxford. WDS analyses were performed using a 15 kV accelerating voltage, and either a 10 or 20 nA beam current, with a defocused beam. Counting times were 30-50s on the peak, and 15-25 seconds background for the major and minor elements, Si, Al, Fe, Ca, Mg, Mn, Ti, Cr. Na was also determined. A range of natural and synthetic samples were used as standards for calibration. Natural wollastonite was used for Ca and Si. Other standards were synthetic periclase (Mg), rutile (Ti), natural albite (Na, Al) and hematite (Fe). Natural almandine was used as a secondary silicate standard. The data were reduced using the PAP procedure of (*Pouchou and Pichoir*, 1991). Crystal analyses were accepted if their totals were between 98-101 wt %. Glass analyses were often slightly lower than this, particularly in the experiments with up to 1 wt % heavy trace elements (e.g. REEs).These elements are not measured on the microprobe, and so are not corrected for in the data reduction. Therefore totals above 96.5 wt % were

accepted for the glass phases, with the exception of experiment HA8_03 where the average glass composition total was 95.00 wt %. The composition of the selected glasses of HA8_03 are comparable to the isothermal HA8_01 and HA8_04 experiments. Time series experiments were performed to monitor the approach to major and trace element equilibrium. The HA8 series of experiments comprised three experiments on the same starting composition where the material was taken up to 1350 ^{o}C, cooled at a rate of 5 ^{o}C an hour and left at 1300 ^{o}C for 21 hours (HA8_04), 48 hours (HA8_01) and 89 hours (HA8_03). From the major element analyses it can be seen that the mineral and glass compositions and phase proportions within each charge are within uncertainty of each other and imply that equilibrium was approached. No trends with time are observed in their measured trace element abundances and indicating equilibrium is achieved. No zoning or heterogeneity was observed within the crystals or melt within each sample demonstrated by the small standard errors seen in the major and trace element analyses. SEM images of samples HA8_03 and HA10_03 are shown in Figures 3.6a and 3.6b. No significant iron loss was recorded from the experiments, and modal proportions were calculated from the non-linear least squares approach of *Albarede and Provost* (1977). Bulk compositions are calculated iteratively from the individual phase compositions, varying the modal proportions of the phases until the difference between the measured and calculated compositions is minimised. Major element compositions of each phase are recorded in Table A.3, with the calculated modal proportions in Table A.2.

Trace element analyses were determined using Laser Ablation Inductively Coupled Mass Spectrometry (LA-ICP-MS). The concentrations of a range of trace elements in the crystal and glass phases were measured by a Perkin Elmer Nexion quadrupole mass spectrometer, coupled with a New Wave Research UP213 Nd:YAG laser in the Department of Earth Sciences, University of Oxford. Spot sizes of 20, 40 or 50 μm were used depending on crystal size. The following masses were counted when appropriate for the sample: ^{24}Mg, ^{29}Si, ^{44}Ca, ^{53}Cr, ^{55}Mn, ^{45}Sc, ^{47}Ti, ^{60}Ni, ^{89}Y, ^{90}Zr, ^{93}Nb, ^{141}Pr, ^{152}Sm, ^{174}Yb, ^{181}Ta, ^{232}Th, ^{177}Hf, ^{187}Re, ^{140}Ce, ^{139}La, ^{88}Sr, ^{142}Nd, ^{143}Nd, ^{153}Eu, ^{155}Gd,

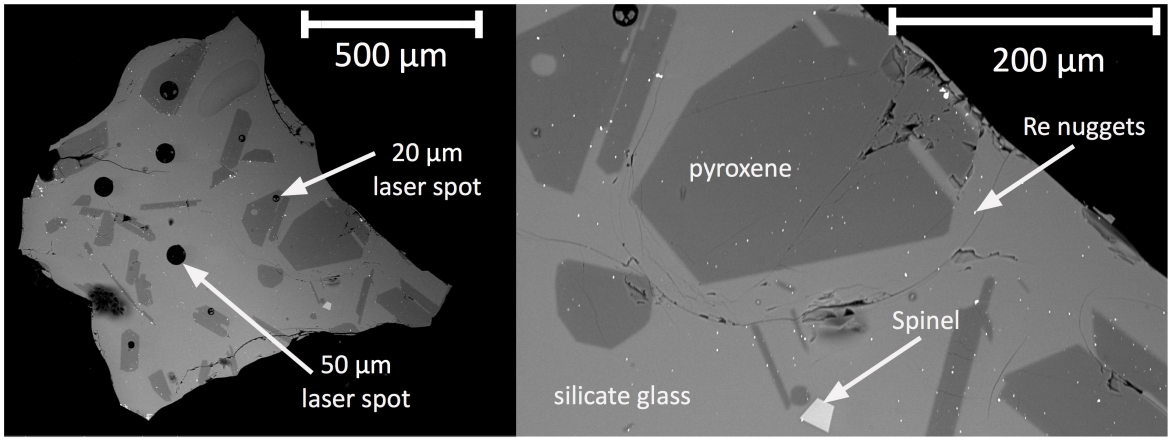

Figure 3.6a: Backscattered Electron image (BSE) of sample HA8_03, taken on the SEM. Representative pyroxene, glass and spinel phases have been labelled, along with pits from Laser Ablation Analysis

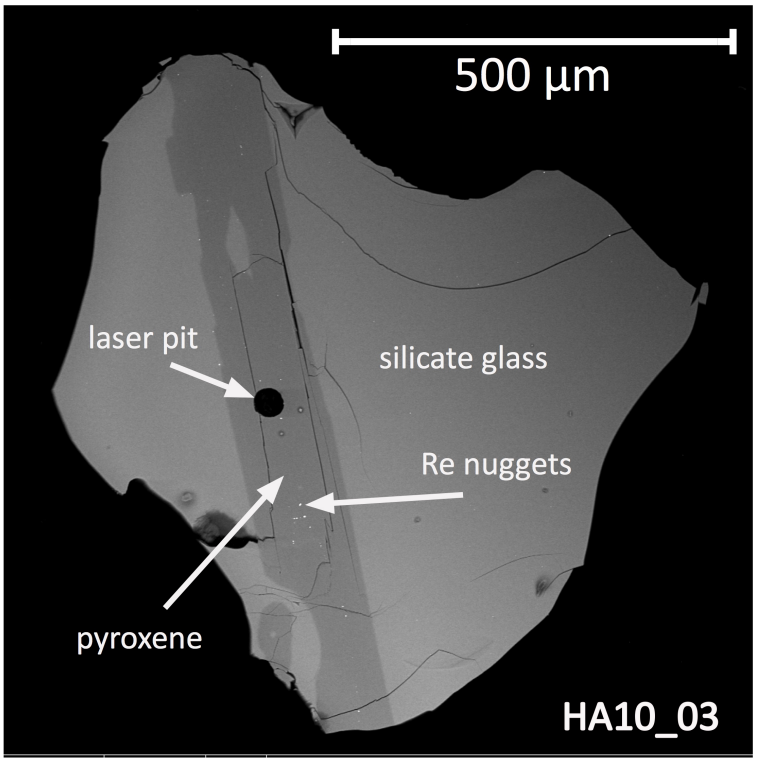

Figure 3.6b: Backscattered Electron image (BSE) of sample HA10_03. Representative pyroxene and glass phases have been labelled, along with pits from Laser Ablation Analysis.

^{156}Gd, ^{158}Gd, ^{175}Lu, ^{238}U, ^{163}Dy, ^{165}Ho, ^{182}W. Yields were calibrated on the NIST 610 standard as the primary standard with USGS glass BCR-2G used as a secondary standard to check the accuracy of the calibration. The standards were measured after every 10-20 analyses and the results corrected for calibrated drift. Ca was used as the internal standard for both the silicate melts and crystal phases. The LA-ICP-MS

analyses involved 20 seconds of a background count, followed by 40 seconds of ablation, with background being minimised by including a 60 second washout between each data collection. The Glitter (`www.es.mq.edu.au/gemoc/glitter`) software package was used for data reduction and allowed each ablation to be viewed separately, and screened for heterogeneities including small Re nuggets or compositional variations with depth through the sample, for example melt inclusions or thin crystals.

3.2.2 Results

Major Elements

The two main phases present across the range of experiments are low-Ca pyroxene and melt. Spinel is a minor phase in some experiments, but is too small to find and analyse with the Electron Microprobe. The orthopyroxenes are generally euhedral, and vary in size between 5 μm—1 mm. The pyroxenes appear homogeneous in composition and the trace element compositions are not observed to vary from core to rim along any dimension of the crystals. The major element compositions and uncertainties are shown in Table A.3, and the experimental pyroxene compositions are plotted on the pyroxene quadrilateral in Figures 3.3 and 3.4. The measured trace element abundances for the experiments performed here and in Chapter 2 are recorded in Table A.4. Glass totals are generally lower than pyroxene totals due to the presence of up to 1 wt. % trace elements. As temperature increases from 1150 to 1450 ^{o}C, the melt compositions generally increase in MgO content, while decreasing in Al_2O_3 and CaO content in keeping with crystallisation. The pyroxene compositions produced are all orthopyroxene or pigeonite and their Wo contents increased from 1.10 to 4.50 as temperature decreased from 1300-1150 ^{o}C . A $Kd_{Fe^{2+}-Mg}$ was calculated for these experiments and an average value of 0.281 $\pm$ 0.018 was calculated, which is slightly higher than the generally accepted value of 0.27 (*Stolper*, 1979; *Bartels and Grove*, 1991), shown in Figure 3.7. The addition of Al_2O_3 to HA10 to produce the HA11 composition lowers the liquidus temperature by $\sim$ 30 ^{o}C, and produces more Al-rich melts and crystals in the HA11

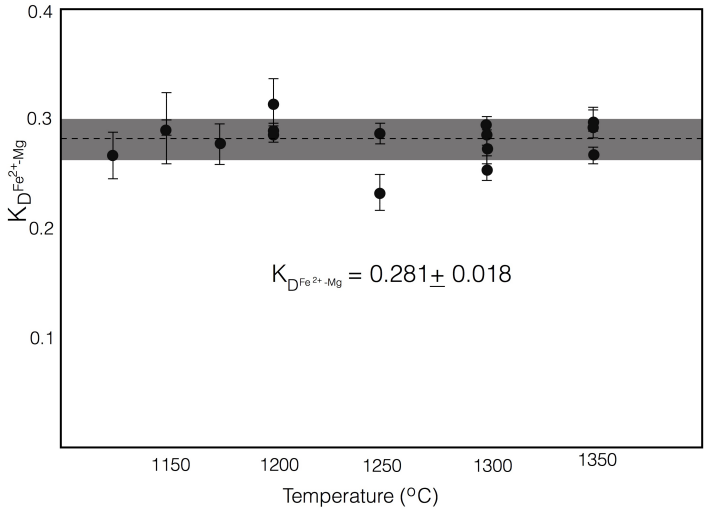

Figure 3.7: $Kd_{Fe^{2+}-Mg}$ for the experimental pyroxenes vs. temperature, along with their mean value, and plotted standard error.

series compared to the HA10 series, but with a similar Wo content.

Trace Elements

The concentration of trace elements in the melt phase is dependent on the starting abundance, amount of crystallisation and compatibility of each element. For example in experiment HA10_02 where there was approximately 93 % melt and 7 % orthopyroxene, the trace element abundances of REEs in the melt were $\sim$ 100-400 ppm, close to their start doping concentration, whereas in experiment HA10_03, where 12 % pyroxene coexisted with 88 % melt, the REEs are enriched in the melt by 10 % for the Heavy Rare Earth Elements (HREEs) and 7 % for the more compatible Light Rare Earth Elements (LREEs). The D_{REE} and D_{HFSE} values are higher for the HA11 series of experiments than for the HA10 series, for example and average $D_{La} = 0.0053$ compared with 0.0013, $D_{Yb} = 0.1463$ compared with 0.0907, and D_{Hf} of 0.0535 compared with 0.0195. The D_{Mn} and D_{Fe} are similar, however D_{Cr} is higher, at 8.88 compared with 3.88.

3.2.3 Calculation of Partition Coefficients

Low-Ca pyroxene

Mineral-melt partition coefficients (D) were calculated for each element (i) using Equation 3.1. The pyroxene-melt partition coefficients for all of the measured trace elements and their standard errors are shown in Table A.5. The D values for our set of experimental data vary on the order of one magnitude for all of the elements studied, with incompatible elements generally increasing in compatibility as temperature decreases, and Wo content of the pyroxene increases (Figures 3.5 and 3.8). Figure 3.5 shows a comparison to other measured literature values, and 3.8 shows the experimental data alone complete with errors for each data point. It should be noted that the partition coefficients of Ti, Sc, Mn and Cr differ to the other studies slightly, likely due to the effect of spinel crystallising. The oxygen fugacity in this study is 2 log units higher than the other studies, and the spinel which forms has a different composition, hence the difference in D values for these elements.

The REE partition coefficients increase gradually with decreasing ionic radius with the average D_{La} being 0.0032 compared to an average D_{Lu} of 0.1002 and D_{Yb} of 0.0796. There is a small dip in the compatibility of D_{Eu}, reflecting that Eu^{2+} is present under reducing oxygen fugacity conditions as opposed to Eu^{3+}. The D_{La} increases from 0.004 at 1300 ^{o}C to 0.0071 at 1125 ^{o}C, and the D_{Yb} increases from 0.0286 at 1350 ^{o}C to 0.2008 at 1125 ^{o}C. The fractionation between HREE and LREE can be calculated, and at 1125 ^{o}C the D_{La}/D_{Yb} is 0.0352 increasing to 0.1114 at 1300 ^{o}C. This means that there is more fractionation between the HREE and LREE at lower temperatures, in keeping with previous studies (*Frei et al.*, 2009).

The HFSE partition coefficients increase with decreasing temperature and increasing Wo content of the pyroxene with D_{Ti} increasing from 0.1205 to 0.1928, D_{Hf} from 0.0107 to 0.0720 and D_{Zr} from 0.0079 to 0.0310.

The trivalent and divalent transition metals also show increasing compatibility with decreasing temperature and increasing Wo content of the pyroxenes with D_{Al} increasing

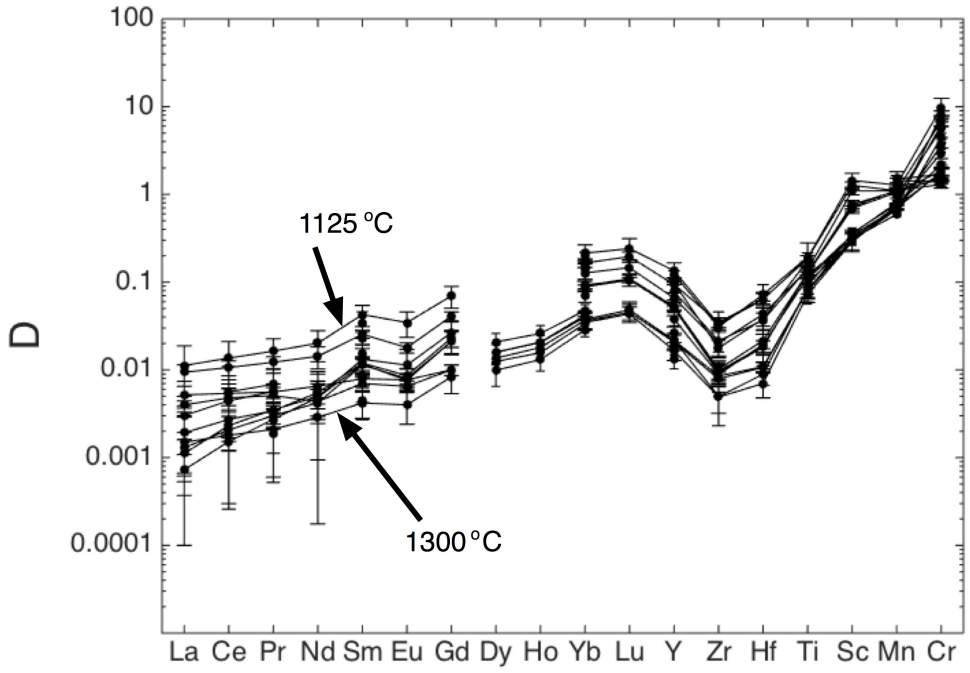

Figure 3.8: Measured low-Ca pyroxene-melt partition coefficients for the experiments. The analytical errors are plotted, and are larger for the less compatible elements, due to the abundances in the pyroxene crystals being close to the detection limits ∼few ppm level or below). Two lines have been labelled with the T of the experiment to demonstrate the increase in D with decreasing T.

from 0.0515 to 0.151, D_{Cr} from 1.30 to 8.06, D_{Sc} from 0.3127 to 1.09, D_{Mn} from 0.5920 to 1.50, and D_{Fe} from 0.5552 to 1.16. U and Th partition coefficients were also calculated and decrease with decreasing temperature and increasing Wo content, with D_U decreasing from 0.0020 to 0.0005 and D_{Th} decreasing from 0.0032 to 0.0005 from 1300 ^{o}C down to 1175 ^{o}C.

3.3 Lattice Strain Model

D_o, r_o and E values can be derived for individual experiments by fitting model curves to the experimental data. Firstly the experimental D values and their errors were plotted vs. the ionic radii (taken from *Shannon* 1976). The curve fitting function of

the Kaleidagraph software (`http://www.synergy.com/wordpress_650164087/`) was then used to produce a best fit parabola to the partition coefficients for each individual experiment, and iteratively calculated D_o, r_o and E values whilst minimising errors. The analytical errors associated with the data points were used to weight the routines. For the experiments in this study the lattice strain model can be fitted for the M1 site for 4^+ and 3^+ ions, and for 2^+ and 3^+ ions in the M2 site. When fitting the lattice strain model for D^{3+}_{M2} ions, the $r^{3+}_{o(M2)}$ was calculated using the equation:

$$r^{3+}_{o(M2)} = 0.753 + 0.118Al^T + 0.114Ca^{M2} \tag{3.12}$$

Taken from *Wood and Blundy* (2003), where Al^T and Ca^{M2} denote the amount of atoms per 6-oxygen formula unit for orthopyroxene, and D_o and E were fitted. For the M2 2^+, M1 3^+ and M1 4^+ ions, D_o, r_o and E were all fitted using the routine, except for the M1 4^+ ions of the HA8 series where an r_o of 0.65 (from *van Kan Parker et al.* 2010) was selected, as the fitting routine otherwise failed to converge on a result (it is harder to fit curves to 3 data points, compared with 7 or 8). The D_o, r_o and Young's Modulus (E) data for each valence of cations in each crystallographic site were fitted using a nonlinear least squares routine, and weighted according to the standard deviation of the partition coefficient. E, D_o and r_o for the REE and HFSE elements are plotted in Figure 3.9 and the D_o for each isovalent series are plotted against temperature in Figure 3.10. The experimental results, reported in Table A.7, are shown on Onuma diagrams in Appendix C along with the calculated D values from the experiments (shown in Table A.5). Although U and Th were measured in some of the experiments, it was not possible to calculate a best fit D_o, r_o, and E due to the extremely incompatible nature of U and Th, resulting in low abundances in the crystals at the level of analytical detection.

In order to calculate the Al^T and Ca^{M2} and Mg^{M2} (used in equations below) the mineral formula for each pyroxene crystal was calculated from the major element composition. Firstly the molar proportions of oxygen and each cation were calculated,

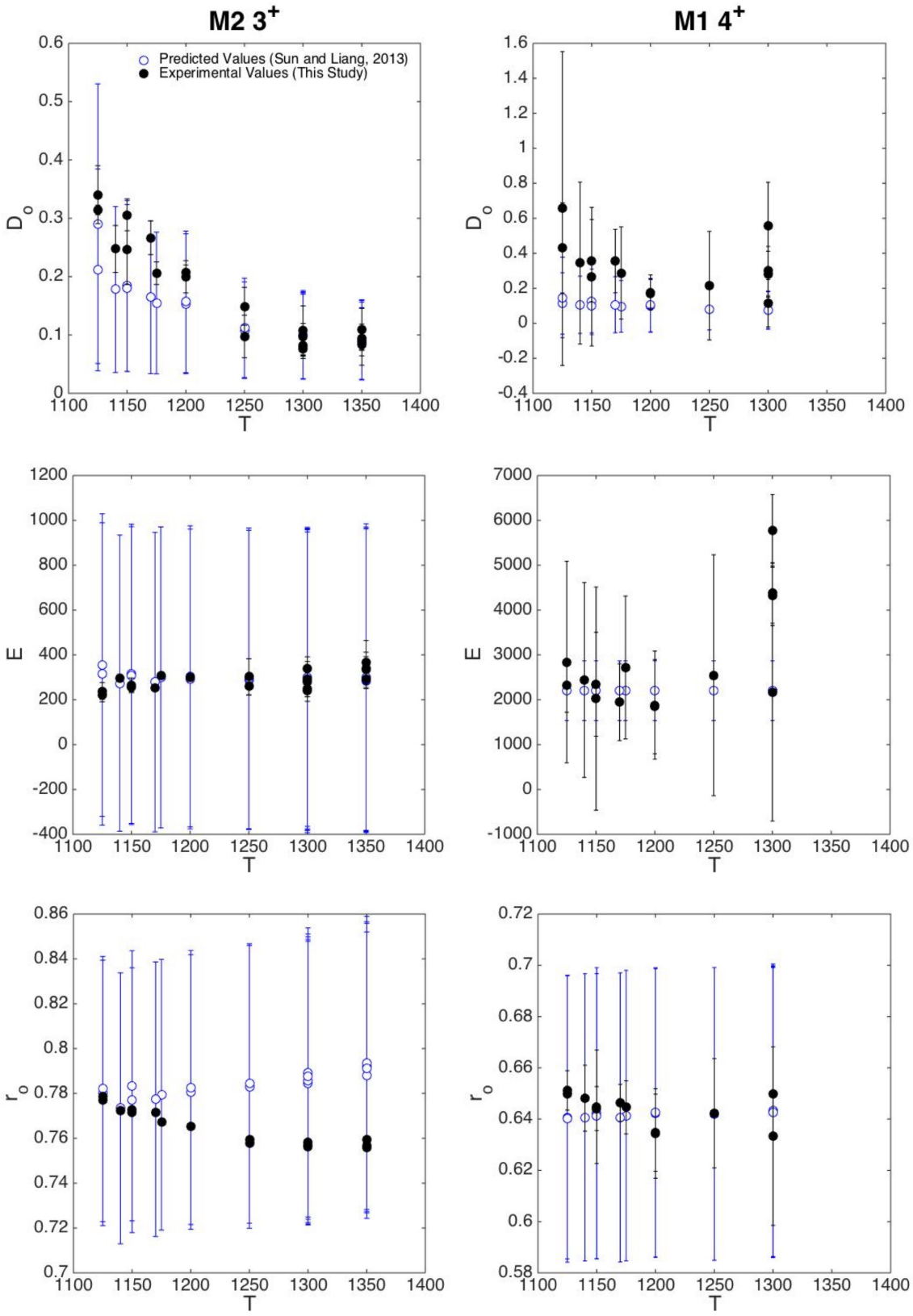

Figure 3.9: r_o, D_o and E vs. temperature for the experimental data (black circles) and compared with the calculated values from *Sun and Liang* (2013)'s predictive model (white circles).

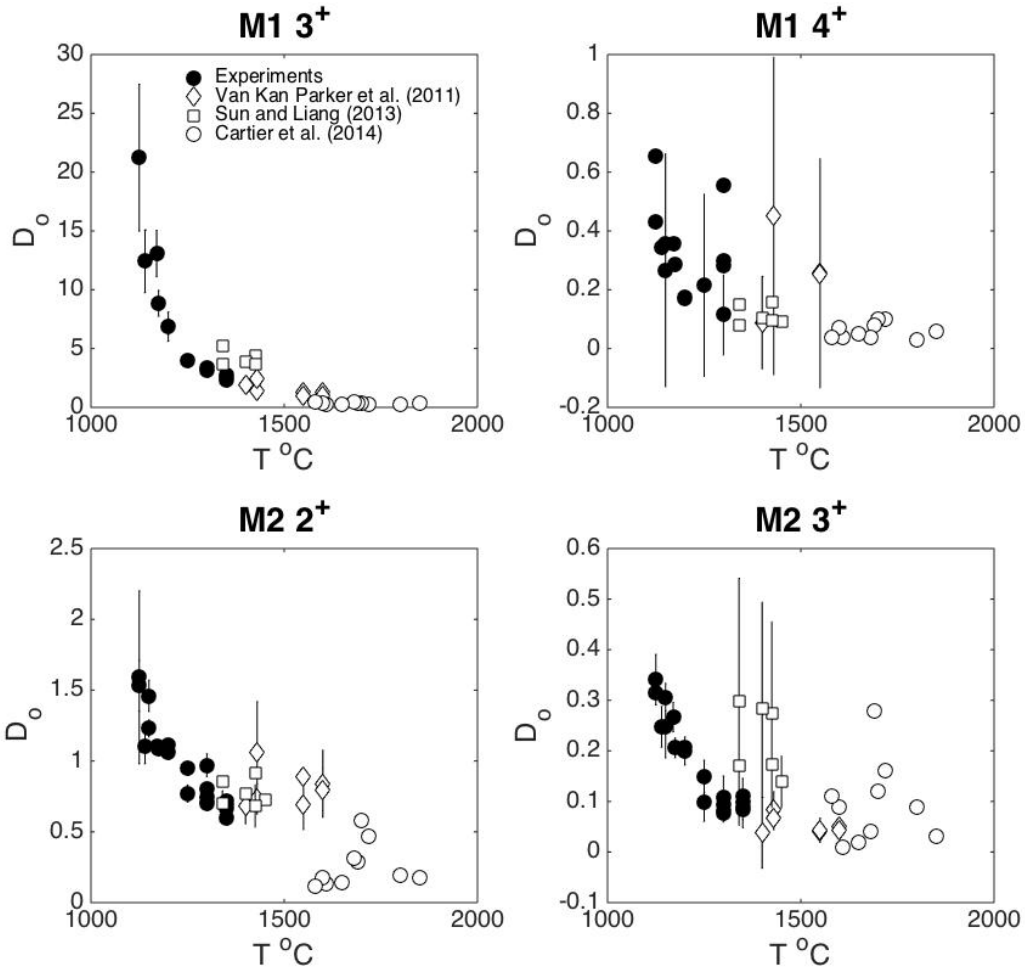

Figure 3.10: D_o plotted vs temperature for each isovalent series studied for the experimental data (black circles), and literature data of lunar studies (white diamonds and white squares) and enstatite chondrites (white circles). D_o can be seen to increase with decreasing temperature for each series.

followed by atoms per 6-oxygen formula units. Then the cations were assigned to the X, Y and Z sites of pyroxene starting with the smallest cations and smallest sites. Si is assigned to the Z site, followed by Al if there is any remaining space. The M1 Y site is then filled with the remaining Al, Ti and Fe^{3+}. Fe^{2+} and Mg are assigned to both the Y and M2 X site, and the larger Ca, Na and Mn ions are also assigned to the octahedral M2 site.

3.3.1 Fit to Experimental Data

In order of increasing compatibility into orthopyroxene are the trivalent REEs, the tetravalent HFSE (Ti, Hf and Zr) elements, the 2^+ ions (Fe, Mn, Ca) and the smaller trivalent Cr, Al and Sc. The best fit ionic radii for each set of elements increase from the HFSE elements, the small trivalent ions, the REEs and Y to the 2^+ ions and suggest that the HFSE elements and small trivalent ions partition into the M1 site and the REEs, Y and the 2^+ ions partition into the larger M2 site. The calculated E values, suggest that the M1 site is more rigid than the M2 site as expected (e.g. *Blundy and Wood* 2003).

M1

It can be seen that the 4^+ ions have a higher Young's Modulus than 3^+ ions, by a factor of *ca.* 2 of ∼3000 GPa compared to 1500 GPa, the 3^+ ions are generally more compatible with a D_o of up to two orders of magnitude higher, with an average of 4.15 compared to 0.301 for the 4^+ ions. The 3^+ ions also have a higher average r_o by 0.02 $\mathring{A}$ of 0.66 $\mathring{A}$ compared to 0.64 $\mathring{A}$. For the 3^+ ions, the D_o increases with increasing Wo content of the pyroxene, and decreasing temperature from 2.2985 at $Wo_{0.44}$ at 1350 ^{o}C to 21.226 at $Wo_{7.69}$ at 1125 ^{o}C. There are no obvious trends in E or r_o with temperature or pyroxene composition which have average values of 1533 (±54) GPa and 0.6613 (±0.0009) $\mathring{A}$. For the 4^+ ions, there is a slight trend of increasing D_o with increasing Wo content from 0.11 at $Wo_{1.18}$ to 0.656 at $Wo_{6.42}$. E is constant over the temperature and composition interval with a value of 2300 (± 380) GPa, for all samples except the HA8 series, which have a higher E value of 4318-5766 GPa. The r_o is fairly constant at 0.6412 (±0.0064) $\mathring{A}$ for all of the samples, except HA8 where r_o was fixed at 0.65 $\mathring{A}$.

The 3^+ and 4^+ ions are more compatible in the more Al-rich HA11 series than HA10, with a D_o of 12.75 and 0.350 for the 3^+ and 4^+ ions respectively, but with similar r_o and E values.

M2

The 2^+ cations are more compatible than the 3^+ ions by nearly an order of magnitude with an average D_o of 0.9301 compared to 0.1511. For both valences the Young's Modulus falls within a similar range of 200-400 GPa. The 2^+ ions have a slightly higher average r_o of 0.8306 $\AA$ compared to 0.7617 $\AA$ for the 3^+ ions. For the 2^+ ions on the M2 site, the D_o increases with increasing Wo content and decreasing temperature from 0.6021 at $Wo_{1.52}$ and 1350 ^{o}C to 1.52 at $Wo_{7.69}$ and 1125 ^{o}C. The E value increases slightly with temperature, and decrease in Wo content from an average of 220 GPa at 1125 ^{o}C and $Wo_{5.45}$ to 287 GPa at 1350 ^{o}C and $Wo_{0.758}$.

For the 3^+ ions (REE elements), r_o increases with increasing Wo content and decreasing temperature from $\sim$ 0.78 $\AA$ at 1125 ^{o}C and $Wo_{6.50}$ to 0.75 $\AA$ at 1350 ^{o}C at $Wo_{0.44}$. There is a decrease in E as the pyroxene becomes more Ca-rich, and temperature decreases from around the predicted 360 GPa (*Wood and Blundy*, 2003) to $\sim$ 250 GPa at 1125 ^{o}C, and higher Wo content. The D_o increases with increasing Wo content and decreasing temperature from 0.0835 at 1350 ^{o}C and $Wo_{0.44}$ to 0.3406 at 1125 ^{o}C and $Wo_{7.69}$. The increase in D_o with decreasing temperature and increasing Wo content is not linear, and beneath 1250 ^{o}C when the Wo content of the orthopyroxene becomes more than 1 % the increase in partition coefficients is greater. There is not enough information here to assess the individual contributions of composition and temperature to this dependence.

The partitioning of the 2^+ ions into the M2 site does not change small with increases of Al to the system (HA11 series), and the r_o and E values are also similar for the 3^+ ions, but the D_o is marginally higher at 0.257 compared to 0.204 for the HA10 series.

3.4 Comparison with Literature studies

Despite differences in the pressure, temperature and fO_2 conditions and compositions for each planetary body, the similarities in mineralogy and fO_2 composition allow for some direct comparison. The measured fO_2 for planetary bodies in our solar system is

plotted vs. planetary size in Figure 3.11 and it can be seen that the HED meteorites record reducing conditions (IW -1), as do lunar basalts, and depleted shergottites, and some chondrites.

Although previous studies of trace element partitioning have not been performed directly for HED compositions, studies of lunar, martian and chondrite lithologies will provide some comparison. Trace element partition coefficients for shergottite compositions were measured by *Blinova and Herd* (2009), enstatite chondrites from *Cartier et al.* (2014), and lunar samples from *van Kan Parker et al.* (2011), and *Sun and Liang* (2013) shown in Figure 3.5. The calculated lattice strain parameters for these experiments can also be compared with low-Ca pyroxene data from the studies of iron-free systems (*Frei et al.*, 2009), lunar studies (*van Kan Parker et al.*, 2010, 2011; *Sun and Liang*, 2013), and a study on enstatite chondrites (*Cartier et al.*, 2014). These literature lattice strain parameters are summarised in Table A.8.

Blinova and Herd (2009) investigated REE partitioning in shergottite compositions, at 1.2-1.6 GPa, 1400 -1600 ^{o}C at an oxygen fugacity (fO_2) of IW +1. The two lunar studies considered here are those of *van Kan Parker et al.* (2011), who consider lunar picrites at 1.1-3.2 GPa and 1300-1600 ^{o}C, and *Sun and Liang* (2013), who considered slightly more evolved lunar compositions with varying TiO_2 content at 2 GPa and 1340-1450 ^{o}C, at fO_2 conditions just under the IW buffer. *Cartier et al.* (2014) considered enstatite chondrite compositions at 5 GPa and 1580-1850 ^{o}C, and a range of fO_2 conditions from 0.8 to 8.2 log units below the IW buffer. The major element compositions of both the low-Ca pyroxene and melts produced in the lunar studies of *van Kan Parker et al.* (2011) *Sun and Liang* (2013), and the depleted shergottite composition of *Blinova and Herd* (2009) and this thesis are very similar. The *Sun and Liang* (2013) experiments are more Ca- and Al- rich than the *van Kan Parker et al.* (2011) experiments, and are similar to the compositions seen in the more evolved, lower temperature experiment of this study (e.g. HA7, HA10, HA11) whereas the orthopyroxenes produced by *van Kan Parker et al.* (2011) are more similar to the higher temperature experiments of this thesis (e.g. HA3, HA4, HA8). Both are slightly enriched in TiO_2

compared with the HED compositions. The pyroxene compositions from this study, *Sun and Liang* (2013), *van Kan Parker et al.* (2011), *Cartier et al.* (2014) and *Blinova and Herd* (2009) have been plotted in Figure 3.3. At oxygen fugacities below IW -1, metal formation removed Fe and Ni from the silicate portion of the experiments of *Cartier et al.* (2014), resulting in effectively iron-free melt and pyroxene phases.

In general the lattice strain parameters, and hence the partition coefficients, measured here for the HED suite of basalts are in agreement with the work of other studies, lunar and martian studies. There are small variations, discussed in more detail below, which can be attributed to variations in experimental pyroxene and melt composition, temperature, pressure and oxygen fugacity conditions. My experiments on the HED compositions are at a lower pressure and temperatures than the other studies. Here I compare the lattice strain parameters with temperature and Wo content of the low-Ca pyroxene in order to determine temperature and compositional dependence. The calculated D_o for each site and cation valence are shown in Figure 3.10, and it can be seen that the partitioning of the incompatible elements increases as temperature decreases.

M1

For the 3^+ ions D_o increases with decreasing temperature and increasing Wo content from ∼1-9. R_o does not seem to vary with temperature and Wo content, at just with an average r_o = 0.661 (± 0.001) $\AA$. The Young's Modulus E is fairly constant over temperature and Wo content with a general range of 1000-2000 GPa for the 3^+ ions, except for the study by Cartier which is lower with E < 500 GPa. For the 4^+ ions the E values range between ±1000-6000 GPa with the majority lying between 2000-3000 GPa, and r_o is fairly constant between 0.635-0.655 $\AA$ with no trends with temperature or pyroxene Wo content. The strain free partition coefficient does not vary with Wo content, with most values falling between 0.15-0.4 D_o is fairly constant with temperature.

M2

For the M2 site the D_o of 2^+ is reasonably constant at high temperatures and low Wo content of pyroxene with an average value of 0.8 from around 1600-1250 ^{o}C, but then increases with decreasing temperature and increasing Wo content to about 1.5 at 1175 ^{o}C. R_o is constant with an average value of 0.82 $\mathring{A}$, and the E varies between 100-500, with a slight increase with decreasing Wo content. The parameters calculated by *Frei et al.* (2009) for their iron-free experiments have a lower D_o values between 0.002-0.015 and a much lower E of 50 GPa.

For the 3^+ ions r_o is again constant at *ca.* 0.78 $\mathring{A}$ and E ranges between 100-700 GPa with most values between 150-350 GPa and no obvious temperature or Wo content trend. D_o generally increases with increasing Wo content and decreasing temperature.

These observations are of the data set as a whole, and generally the trends in lattice strain parameters are more defined within individual suites of data (e.g. the HED compositions, or the lunar compositions) than the general trends across all data sets, suggesting that other parameters (e.g. other compositional factors, or pressure) apart from temperature and Ca content of the pyroxene may be influencing the partitioning behaviour. This observation reinforces the importance of measuring the trace element partitioning for different igneous suites as the partitioning behaviour of different chemical elements is complex and influenced by many factors, and that calculating the low-Ca pyroxene-melt partition coefficients for the HEDs over their crystallisation interval was a useful and necessary task.

3.5 Test of predictive models for REE and HFSE partitioning

In addition to comparing against other measured experimental data, I have assessed the current predictive models for their applicability to the HED suite.

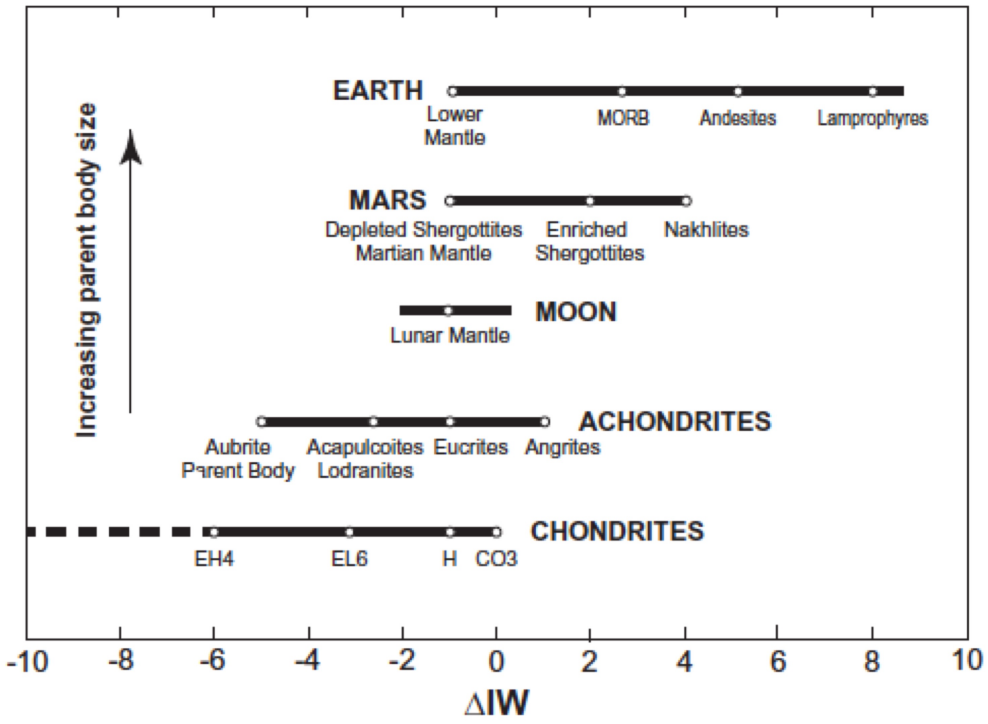

Figure 3.11: Oxygen fugacity (fO_2) and planetary body size for the Earth, Mars, Moon, achondrites and chondrites. Taken from *Cartier et al.* (2014)

Yao et al. (2012) developed a predictive model for the REEs into the M2 orthopyroxene site using 344 data points from 38 experiments investigating partitioning between low-Ca pyroxene and melt, spanning a range of compositions (Pyx Mg#=70-100, Melt Mg# = 40-100, SiO_2 = 39.0-60.6 wt. % in melt, and a range of Ca content (up to Wo ∼20)), temperatures (1080-1660 ^oC) and pressure (1 atm to 3.4 GPa).

This model was developed by conducting multivariable nonlinear least squares analysis to identify the key parameters that affect the lattice strain parameters: D_o, r_o and E and inversion of the experimental data using the identified parameters. *Yao et al.* (2012) found that r_o is a function of Ca^{M2} and Mg^{M2}, which are the cation numbers (per 6 oxygen) of Ca and Mg in the M2 site in pyroxene, E is a function of the r_o and the Ca^{M2} and the logarithm of the D_o is a function of temperature, Ca^{M2} and the Al^T which is the cation number of Al in the tetrahedral site in orthopyroxene. *Sun and Liang* (2013) updated this model to incorporate a term for the melt TiO_2 after further

experiments on lunar compositions (making the range of experimental melt TiO_2 in the experiments vary between 0-16.6 wt.%) and the updated model for partitioning between low-Ca pyroxene and basaltic melts is:

$$ln(D_o) = -5.37(\pm 0.49) + \frac{3.87(\pm 0.74) \times 10^4}{RT} + 3.54(\pm 0.61)Al^T + 3.56(\pm 1.02)Ca^{M2} - 0.84(\pm 0.22)X_{Ti}^{melt} \quad (3.13)$$

$$r_o = 0.693(\pm 0.055) + 0.432(\pm 0.147)Ca^{M2} + 0.228(\pm 0.056)Mg^{M2} \quad (3.14)$$

$$E = [1.85(\pm 0.52) - 1.37(\pm 0.47)r_o - 0.53(\pm 0.11)Ca^{M2}] \times 10^3 \quad (3.15)$$

The model suggests that the partition coefficients of the REE and Y are strongly dependent on temperature, and the Ca and Al content of low-Ca pyroxene, and the amount of Ti in the melt. The ideal radii of the lattice site increases with increasing Ca and Mg content, and the stiffness of the site decreases as the ionic radii and calcium content of pyroxene increase.

Due to the high abundance of TiO_2 in lunar melts, *Sun and Liang* (2013) also developed a model for the partitioning of the HFSE elements Ti, Zr and Hf between low-Ca pyroxene and basaltic melts. They established a predictive model in a similar manner to their REE model, using experimental data for a range of compositions (Mg#=48-100 for melt, TiO_2 = 0-16.6 wt %, and low-Ca pyroxene compositions with Mg# = 73-100, and CaO between 1.35-10.81 wt %).

The models for the lattice strain parameter for the HFSE elements are:

$$ln(D_o) = -4.825(\pm 0.999) + \frac{3.178(\pm 1.348) \times 10^4}{RT} + 4.172(\pm 1.152)Al^T + 8.551(\pm 1.63)Ca^{M2} \times Mg^{M2} - 2.616(\pm 0.856)Fe^{M1} \quad (3.16)$$

$$r_o = 0.618(\pm 0.018) + 0.032(\pm 0.017)Ca^{M2} + 0.03(\pm 0.017)Mg^{M2} \quad (3.17)$$

$$E = 2203(\pm 665) \tag{3.18}$$

Equations 3.13-3.18 were used to calculate the lattice strain parameters for my experimental data. The bootstrap method (N=10,000) was used to propagate the errors in each equation with the assumption that the error on each term was normally distributed. The calculated predicted values are compared with the measured experimental values in Figure 3.9 and the mean values and standard deviations are reported in Table A.7. In order to see if the mean and standard deviation are suitable descriptors of the calculated values, the kurtosis (k) and skew(s) were calculated, with k = 3±0.15 and s = 0±0.1. Kurtosis is a measure of how peaked a distribution is and skew is a measure of symmetry of a distribution of values. These measured k and s values suggest that the calculated values are normally distributed (k = 3, s = 0) and a one sample Kolmogorov-Smirnov test agreed with this at a 95 % significance level. The mean and standard deviations are therefore deemed appropriate descriptors of the calculated values.

Within the series of experiments performed here, Wo content of the pyroxene increases as temperature decreases in keeping with the crystallisation sequence and so I will just discuss the variation of lattice strain parameters with temperature below. The modelled D_o, r_o and E and their associated standard deviation are plotted agains the calculated D_o, r_o and E for the experiments in Figure 3.9. It can be seen that generally the errors on the values predicted are larger than those measured directly from the experimental data. Including the standard deviation errors on the predicted models, the predicted values are in moderate agreement with the experimental data. There are however differences in trends, and outliers, which I will now discuss.

Equation 3.13 successfully predicts the experimental $D_o^{M2,3^+}$ in orthopyroxene, but underestimates the $D_o^{M2,3^+}$ for the experimental pigeonites by up to a factor of two ($\sim$ 0.2 compared with $\sim$ 0.4 at 1125 ^{o}C). Equation 3.16 consistently underestimates the $D_o^{M1,4^+}$ by up to a factor of 4, with $D_o < 0.1$ compared with the 0.3 - 0.7 range observed.

Equation 3.14 predicts an increase in $r_o^{M2,3+}$ with temperature increase with 0.775 at 1125 ^{o}C to 0.79 at 1350 ^{o}C, whereas equation 3.12 (of *Wood and Blundy* (2003)) suggests that $r_o^{M2,3+}$ increases as temperature decreases from 0.775 $\mathring{A}$ at 1125 ^{o}C to 0.755 $\mathring{A}$ at 1350 ^{o}C. *Wood and Blundy* (2003)'s suggestion that $r_o^{M2,3+}$ is dependent on Al content seems more likely, as increases in Al may increase the amount of coupled substitutions). In order to try and resolve which of these calculations may be more accurate, I recalculated the best-fit parameters leaving $r_o^{M2,3+}$ unconstrained. The calculated $r_o^{M2,3+}$ values range between 0.765-0.785 $\mathring{A}$ and do not appear to show a trend with temperature. The $D_o^{M2,3+}$ and $E^{M2,3+}$ did not vary significantly, and so the best fit parameters calculated when $r_o^{M2,3+}$ was calculated using equation 3.14 were used in subsequent models. For the 4^+ ions substituting into the M1 site, Equation 3.17 predicts that $r_o^{M1,4+}$ should decrease from 0.644 $\mathring{A}$ at 1300 ^{o}C to 0.640 $\mathring{A}$ at 1125 ^{o}C, whereas the experimental values predict an increase from 0.633 $\mathring{A}$ at 1300 ^{o}C to 0.651 $\mathring{A}$ at 1125 ^{o}C.

Equation 3.15 predicts the $E^{M2,3+}$ in orthopyroxene well, but overestimates the $E^{M2,3+}$ for pigeonite by around 50 GPa. The measured $E^{M1,4+}$ at 1300 ^{o}C are much higher than equation 3.18 predicts ($\sim$ 4000 compared with 2203).

The parabola predicted by the *Sun and Liang* (2013) model are also plotted on the Onuma diagrams (Appendix C), alongside the best-fit models of experiments. The M2 3^+ parabola are all slightly offset from the calculated parabola from the experiments with regards to the ideal ionic radii, and so do not pass through the measured experimental data points. However, the E and D_o are a good estimate. In contrast the M1 4^+ parabola are in the right region of r, but as D_o has been underestimated, the parabola do not pass through the experimental data points, especially the Ti value suggesting that the predictive model needs to be extended to a wider data set of compositional, temperature and pressure space.

3.6 Conclusions

As ionic radii decrease, the compatibility of the REE elements into the M2 site in low-Ca pyroxene increases, e.g. average D_{La} is 0.0032 compared to D_{Lu} of 0.1002 for these experiments. As temperature decreases, and calcium content of the pyroxene (and bulk system) increases, the compatibility of the REEs, HFSEs, the trivalent and divalent transition metals increases. For example D_{La} increases from 0.004 to 0.0071 and D_{Ti} increases from 0.1205 to 0.1928 as temperature decreases from 1300 ^{o}C to 1125 ^{o}C.

Lattice strain models were fitted to each experiment, weighted by the errors for each element, for the trivalent and divalent cations in the M1 site, and the trivalent and tetravalent cations in the M2 site. The results of these models are:

- In the M1 site the larger trivalent cations are more compatible than the tetravalent ions, with a more elastic lattice site. Although the compatibility increases with decreasing temperature and evolving melt composition (increasing Ca content) the r_o and E remain constant over this suite of experiments.

- In the M2 site the 2^+ cations are more compatible than the 3+ ions by an order of magnitude. The Young's Modulus for the M2 2^+ and 3^+ ions decreases with temperature decrease and melt evolution from 290 to 230 GPa, and 360 to 250 GPa respectively. The *Wood and Blundy* (2003) calculation of r_o for the 3^+ ions predicts an increase in the site radius from 0.75 to 0.78 $\mathring{A}$.

- The experimental results of this study for the orthopyroxenes forming at temperatures $> 1250\ ^oC$, the partitioning of incompatible elements into low-Ca pyroxene is comparable to lunar systems and the depleted shergottites, which are similar compositionally albeit higher pressure systems. Therefore the D values are not greatly affected by small changes in pressure, oxygen fugacity conditions (-1<IW<+2), and the differences at higher temperatures are driven by minor variations in composition.

- The Wo content of the pyroxene (which is correlated with temperature) appears

to have the largest effect on partition coefficients, particularly for trivalent ions into the M2 site, and D_o increases with Wo content. Over the crystallisation sequence of the HED pyroxenes, as the Wo content increases from $Wo_{0.44}$ to $Wo_{7.69}$ the D_o value increases from 0.0835 to 0.3406.

- In addition to fitting the lattice strain model to the measured experimental data values for E, D_o and r_o were also calculated using the predictive models of *Sun and Liang* (2013) for HFSE and REE partitioning.

- *Sun and Liang* (2013)'s predictive model can describe the $r_o^{M1,4^+}$ and $r_o^{M2,3^+}$ ions moderately well. However the predicted trend of r_o with temperature is opposite to that observed experimentally.

- The predictive models are generally in agreement with the experiments for the $E^{M2,3^+}$ of orthopyroxene, however slightly overestimate the $E^{M2,3^+}$ for pigeonite. The predictive models generally underestimate the $E^{M1,4^+}$ particularly at the higher end of the temperature range.

- *Sun and Liang* (2013)'s model generally underestimates the $D_o^{M2,3^+}$ by up to a factor of two, and up to a factor of four for $D_o^{M1,4^+}$. The predicted $D_o^{M2,3^+}$ for orthopyroxene is in agreement with the experiments.

We can see that even across the temperature and composition range over which the HED meteorites formed over, the partition coefficients are not constant, and can vary upto a factor of four. Although the predictive models can provide a reasonable estimate of the lattice parameters, the nuances of the variation with crystal composition and temperature are missed. In order to investigate the trace element abundances and fractionations thoroughly for the HEDs, it was imperative to measure trace element partition coefficients for the system. Underestimating the partition coefficients even by a factor of two will significantly alter the trace element budget. As systematic changes in partitioning with temperature and pyroxene composition have been measured, these details can be incorporated into models.

Chapter 4

Differentiation and magmatic models of Vesta: trace and minor element constraints

4.1 Introduction

Now that appropriate partition coefficients have been measured for the conditions and compositions under which the eucrites and diogenites crystallised under (Chapter 3), geochemical calculations investigating the trace element signatures seen in the HEDs can be performed. First of all the differentiation model suggested in Chapter 2 will be tested, followed by additional magmatic processes which may have occurred on Vesta. In addition to evaluating different petrogenetic models, this chapter will aim to refine the trace and minor composition of the Bulk Silicate Vesta.

The following processes will be considered to investigate the magma ocean and serial magmatism models of differentiation, and secondary igneous processes:

1. Partial melting;
2. Fractional crystallisation;
3. Trapping of intercumulate melt;

4. Re-melting of basalts and cumulates;

5. Assimilation and fractional crystallisation (AFC);

6. Recharge, eruption and AFC.

The incompatible Rare Earth Elements (REE) and High Field Strength Elements (HFSEs) will be considered first, followed by the minor elements, Mn, Ti, and Cr.

4.2 Trace elements

4.2.1 Trace elements in the eucrites and diogenites

The non-cumulate eucrites are subdivided into groups based on their minor and trace element compositions: the Main group (average) eucrites; the Stannern Group eucrites which have higher Ti and incompatible trace element abundances compared to the majority of non-cumulate eucrites but have a similar major element composition, and the Nuevo Laredo group which are more evolved (pyx Mg# = 33, *Mittlefehldt* 2015) in terms of major elements and some are more trace element-enriched than the Main group eucrites. In terms of the REEs the Main group eucrites show flat patterns with a 10×CI abundance enrichment. The cumulate eucrites and granulite eucrites both have relatively flat REE patterns with the cumulates showing 0.1-10×CI abundances. The granulite eucrites show 3-10×CI enrichment. Some granulite eucrites show less depletion in Eu compared to the other REEs, potentially due to the presence of feldspar (*Yamaguchi et al.*, 2009). The Stannern group eucrites are slightly more enriched in REEs than Main group eucrites and show a slight depletion in Eu, suggesting that the melt from which they had formed had already crystallised some feldspar. The cumulate eucrites show trace element signatures similar to the basaltic eucrites.

The diogenites show a much larger range in minor and trace element abundances compared to their relatively narrow range in major element compositions. Al and Cr contents vary by a factor of five and Ti by a factor of 17 (*Mittlefehldt*, 2015). The

diogenites have much lower REE contents, showing a range of abundances spanning four orders of magnitude from 0.001 to 1×CI enrichment. Some diogenites show fractionated REE patterns, with more depleted LREE than HREE, and some show slight depletions relative to the general trend in Eu. This Eu depletion indicates a minor amount of plagioclase crystallisation from their parent melt, and also the reducing conditions under which they form (as Eu is present as Eu^{2+} in addition to Eu^{3+}). The incompatible and minor elements are independent of the major element composition of the pyroxene but correlate with each other (*Mittlefehldt*, 1994; *Fowler et al.*, 1994, 1995; *Shearer et al.*, 2010). The HFSE elements show similar magnitudes of enrichments to the REE elements in the eucrites and diogenites, however in the eucrites Ti is often more depleted than Hf and Zr, whereas the diogenites show a mirrored pattern of a slight enrichment of Ti compared to Hf and Zr.

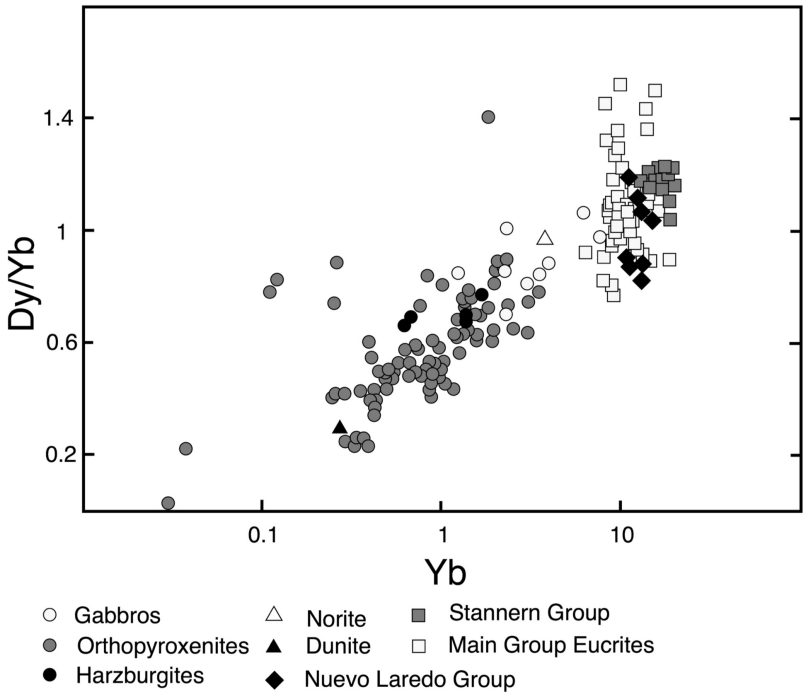

Figure 4.1a: Dy/Yb vs Yb abundance in the diogenites and eucrites. The Yb and Dy/Yb terms are normalised to CI chondrite (taken from *McDonough and Sun* 1995). Different meteorite groups are denoted by different symbols. Data taken from *Mittlefehldt* (2015).

In addition to considering the range of trace element abundances, the fractionation across the REE group can also be considered, as different igneous processes have dif-

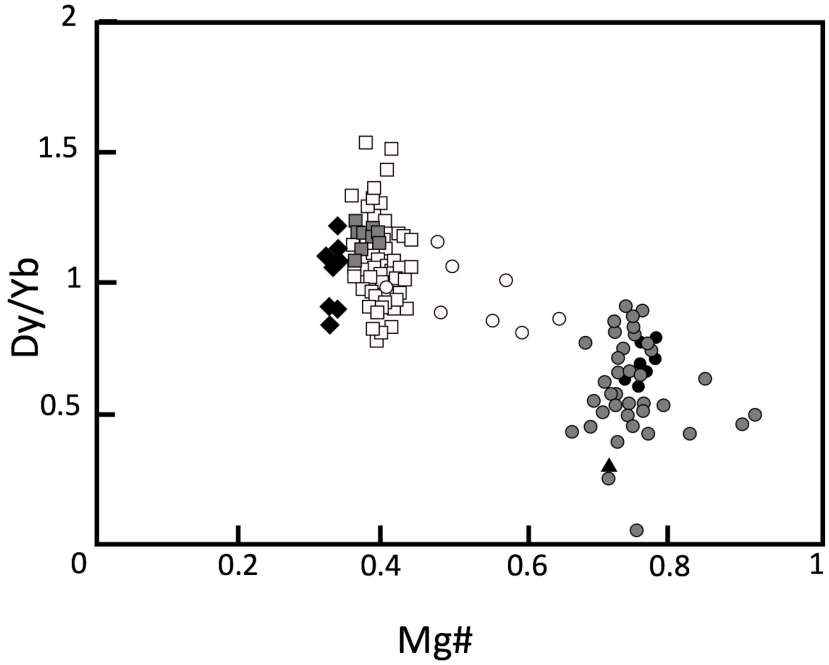

Figure 4.1b: Dy/Yb ratio vs bulk Mg# in the diogenites and eucrites. Symbols are the same as 4.1a. Data taken from *Mittlefehldt* (2015).

ferent effects on the abundance and fractionation. Two elements commonly selected to investigate fractionation across the REE group are the middle REE (MREE) Dy and the heavy REE (HREE) Yb, for example *Barrat and Yamaguchi* (2014). Figures 4.1a and 4.1b shows the Dy/Yb ratio plotted against Yb abundance and Mg#. Non-cumulate eucrites define a narrow range in Dy/Yb vs. Yb, (0.7-1.6, 7-13), and the Stannern Group and Nuevo Laredo Group, show less fractionation (Dy/Yb>1). There is no correlation between the Dy/Yb ratio and Mg# number within the non-cumulate eucrites.

The cumulate lithologies define a trend in Dy/Yb with Mg# and Yb abundance, from low trace element abundance and low Dy/Yb values (high fractionation) to higher Dy/Yb values at higher values ranging between (0.01-10×CI abundance and a Dy/Yb ratio between 0.01-1.4. From Figure 4.1b it can be seen that there is a general increase in incompatible element enrichment and decrease in Mg# reflecting chemical evolution during crystallisation. There is an overlap however, in the cumulate lithologies (gabbro,

norite, orthopyroxenite, harzburgite, dunite). Generally more ultramafic cumulates (e.g. dunite, harzburgites) are more depleted in trace elements with lower Dy/Yb values than more magmatically evolved cumulates (gabbros, norites), but there are overlaps between groups: some orthopyroxenites are more depleted than harzburgites. The cumulates also span a wide range of Mg# (0.4-0.9).

The majority of eucrites exhibit relatively flat chondrite-normalised REE patterns with a small range in Dy/Yb, which are interpreted as formation through fractional crystallisation of partial melts of Vesta (e.g. *Consolmagno and Drake* (1977)). The range in diogenite trace element abundances and fractionations and decoupling from the major element composition suggest a more complex magmatic history. The correlation between the REEs, Ti and Al suggests that the diogenites formed sequentially through fractional crystallisation. However, extensive amounts (up to 90 % *Fowler et al.* 1995) of fractionation of one melt would be required to produce the range in trace element composition and this is unlikely due to the small range in major element variations seen in diogenites. The production of eucrites from this same melt is also unlikely and so multiple melt sources for the diogenites are suggested, different from that of the eucrites (*Mittlefehldt*, 1994; *Fowler et al.*, 1994, 1995; *Shearer et al.*, 2010; *Barrat et al.*, 2008; *Barrat and Yamaguchi*, 2014). Typical crystallisation processes in igneous systems produce increases in incompatible trace element abundances in the residual melt phase as crystallisation progresses. The incompatibility of trace elements in both olivine and orthopyroxene means that the REEs are not normally fractionated with respect to each other. *Barrat and Yamaguchi* (2014) modelled the ratio of Dy/Yb during magma ocean crystallisation of olivine and orthopyroxene and suggested that the cumulates produced would have a constant Dy/Yb ratio of 0.5. The range in chondrite-normalised Dy/Yb in diogenites is ∼0.01-1, however, requiring further explanation.

Suggestions for the variations in Dy/Yb ratios in the cumulate lithologies are multiple source magmas which have different inventories of the REEs (*Mittlefehldt*, 1994; *Shearer et al.*, 2010; *Barrat et al.*, 2008; *Barrat and Yamaguchi*, 2014) or secondary mechanisms which may alter the Dy/Yb ratio. In order to investigate possible pro-

cesses which could produce diogenites, the relationships between orthopyroxenite and harzburgite lithologies have been investigated. *Shearer et al.* (2010) suggest that the diogenites and olivine diogenites formed as layered intrusions into the Vestan crust rather than in a magma ocean, and that some of the range in trace element signatures could be attributed to post-crystallisation metamorphism and subsolidus re-equilibration, masking the original magmatic signatures. This view gained more support from the detailed observations of the trace element compositions of orthopyroxene and harzburgite clasts in dimict diogenite breccias by *Beck et al.* (2013), which suggest that harzburgites and orthopyroxenites can be directly linked by fractional crystallisation of multiple mafic sources.

Suggested secondary processes capable of altering the trace element signatures of the cumulates include magma chamber processes (*Mandler and Elkins-Tanton*, 2013) and partial melting of early formed cumulates, possibly combined with assimilation or crustal melting (e.g. *Barrat and Yamaguchi* 2014). More than one mechanism may be capable of producing pyroxene-rich cumulates. For example, Mg-rich olivine and orthopyroxene crystals with low incompatible elements could represent upper mantle/lower crustal lithologies or more extensive partial melts of the HED parent body (*Tkalcec and Brenker*, 2015; *Lunning et al.*, 2015). More evolved cumulates (orthopyroxenites, norites and gabbros) however could occur as shallow crustal intrusions, of which there has been some evidence from DAWN (*De Sanctis et al.*, 2014).

4.2.2 Methods

In order to investigate different petrogenetic models, thermodynamic models and chemical models were combined. Thermodynamic calculations were performed using the alphaMELTS (*Ghiorso and Sack*, 1995; *Smith and Asimow*, 2005) algorithm and the geochemical calculations were performed using the MATLAB (MATLAB R2015b, The MathWorks Inc., Natick, MA, 2000) software. The alphaMELTS models calculated the mineralogy and major element compositions of crystallising phases, temperature, and modal proportions of phases. MATLAB was used to consider the mass balance

and distribution of trace elements between the crystallising phases and the melt. The four predominant silicate phases seen in the HED meteorites: olivine, orthopyroxene, clinopyroxene and feldspar were considered in these calculations. Appendix D contains details of the MATLAB scripts I wrote to calculate the trace element behaviour during different igneous processes.

The results from the experimental work detailed in Chapters 2 and 3 show that measured pyroxene-melt partition coefficients for the REE elements and Y vary by a factor of >4 over the temperature and composition interval over which the silicate portion of Vesta is likely to have crystallised. This increase occurs exactly when the pyroxenes become diogenitic and over the key temperature interval relevant for Vesta's crustal crystallisation. In order to investigate petrogenetic models thoroughly, this change in partitioning needs to be accounted for in the trace element models.

Selection of partition coefficients

For orthopyroxene the individual D_{REE} and D_{HFSE} partition coefficients were calculated at each stage in the calculations using Equation 3.11, derived by *Blundy and Wood* (1994). For the D_{REE} values, above >1300 ^{o}C, a fixed D_o value of 0.1 was selected, as this is the observed average from the experimental data (Figure 4.2). Between 1300-1125 ^{o}C, a line of best fit (see Figure 4.2) was drawn on the D vs T graph, from the value of ∼0.1 at 1300 ^{o}C to 0.35 at 1125 ^{o}C yielding the equation:

$$D_o = (-0.0013 \times T) + 1.7747 \tag{4.1}$$

For the HFSE elements a fixed D_o value of 0.5 was selected. The D_{REE} and D_{HFSE} were calculated at each temperature step. For clinopyroxene constant D_{HFSE} values were selected with D_{Ti}=0.13, D_{Zr}=0.01 and D_{Hf}=0.02, from the average of the most Ca-rich experiments in this study (which are similar in composition to the eucrite pyroxenes); the D_{REE} were calculated at every temperature step, but with a fixed D_o of 0.4, as observed in the experiments. Constant $D_i^{olivine-melt}$ and $D_i^{plagioclase-melt}$

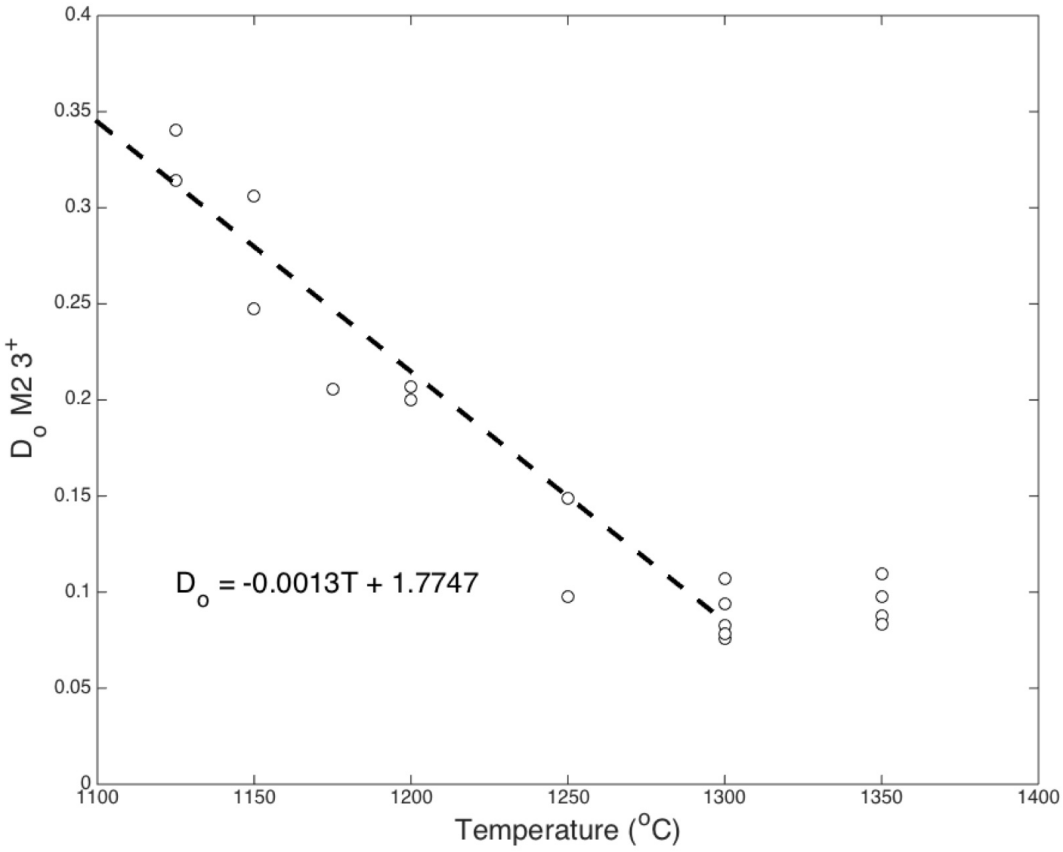

Figure 4.2: D_o (Strain-free partition coefficient for an ion with the ideal r for the lattice site) for the M2 3^+ ions vs temperature. Results taken from Chapter 3. A line of best fit has been taken through the data points, so that the D_o variation with T below 1300 ^{o}C can be accounted for in trace element models.

coefficients were used throughout the calculations and were taken from the experimental measurements of runs HA3_06 and HA7_02 respectively, with the $D_{Hf}^{olivine-melt}$ and $D_{Zr}^{olivine-melt}$ taken from *Fonseca et al.* (2014).

4.2.3 Initial global or partial melting of Vesta

Starting Bulk Silicate Vesta (BSV) compositions with Mg# = 70, 75 and 80 with CaO, Al_2O_3 and SiO_2 in chondritic proportions and minor amounts of Cr_2O_3, TiO_2, MnO and NiO were selected to investigate the potential range of compositions suggested by *Ashcroft and Wood* (2015). The trace element abundances were taken as being in

CI chondrite proportions, but enriched by a factor of 2.5, in agreement with observations from the meteorites (*Morgan et al.*, 1978). Although the trace element models were run on all three starting compositions, and their produced melts, it is those of the BSV with Mg# ∼75 which are discussed in the most detail below. Equilibrium partial melting of each BSV composition was modelled. Equations for modal batch melting/equilibrium crystallisation can be derived from a simple mass balance. Modal batch melting assumes that the melt and solid remain in equilibrium during melting, and that the proportion of minerals undergoing melting is the same proportion as the source. The bulk concentration of an element i of the igneous system can be defined as C_i^o, and so if a small amount of crystallisation occurs then the concentration in the liquid and solid will be related to the bulk composition by:

$$C_i^o = FC_i^{Liquid} + C_i^{Solid}(1 - F) \tag{4.2}$$

where F is the melt fraction. As C_i^{Solid}=$D_i C_i^{Liquid}$ then the evolving trace element abundances in the melt and residual cumulates can be described by the following equations:

$$C_i^{Liquid} = \frac{C_i^o}{F + D_i(1 - F)} \tag{4.3}$$

$$C_i^{Solid} = \frac{D_i C_i^o}{F + D_i(1 - F)} \tag{4.4}$$

C_i^o of element i in the source for the REEs is taken to be that of bulk Vesta or 2.5×CI composition and D_i is the bulk solid-melt partition coefficient for each element i. The bulk partition coefficient for each element is calculated as follows:

$$D_i = X^{opx} \times D_i^{opx-melt} + X^{ol} \times D_i^{ol-melt} + X^{cpx} \times D_i^{cpx-melt} + X^{plag} \times D_i^{plag-melt} \tag{4.5}$$

Where X^{opx}, X^{ol}, X^{cpx}, X^{plag} are the modal proportions by mass of each phase and $D_i^{opx-melt}$, $D_i^{ol-melt}$, $D_i^{cpx-melt}$, $D_i^{plag-melt}$ are the partition coefficients for each element

i for each phase. The melt fraction F, the modal proportions X, and the T used in calculations of $D_i^{mineral-melt}$ were taken from the thermodynamic calculations performed in alphaMELTS reported in Chapter 2. Intervals of 0.01 were selected for F between 0 to 1. The Dy/Yb vs. Yb for the results of partially melting a Bulk Silicate Vesta with mantle Mg# = 75 is shown in Figure 4.3 with comparison to the different eucrite and diogenite trends. Chondrite-normalised REE diagrams for partial melting for Bulk Silicate Vesta compositions with Mg# 70, 75 and 80 are shown in Figure E.1 in Appendix E. Figure E.2 shows that the trends of the partial melting and fractional crystallisation paths do not vary much between different starting models in terms of the Dy/Yb ratios, and also demonstrates the difference in composition of the 10 and 50 % partial melt in each scenario, showing the range of Dy/Yb ratios that are likely to be produced by the partial melting of Vesta.

Progressive melting of each BSV produces melts which decrease in incompatible trace element abundance, for example a 20 % partial melt of the Mg# = 75 bulk composition has 16×CI abundances of trace elements, decreasing to 8×CI abundance at 40 % partial melting, whilst retaining a relatively flat REE pattern (Figure E.1). Trace element abundances similar to those of the eucrites are produced after around 30 % partial melting of the starting BSV. The solid residue after partial melting is depleted in REEs compared to chondrites, with the abundance of incompatible elements also decreasing as melting progresses. As melting progresses there is also a decrease in amount of fractionation from LREE to HREE, in both the melt and the residue, for example after 20 % partial melting of a BSV with Mg# = 75, the residue has 0.024×CI La and 0.73×CI abundances of Yb, after 40 % melting the residue has 0.013×CI La and 0.032 ×CI Yb (Figure S2). This residue has a similar REE trend and abundance to some of the cumulates. Although I demonstrated that the major element compositions of crystals and melts produced by partial melting alone do not match those recorded by the eucrites and diogenites in Chapter 2, these results suggest that abundances and fractionation patterns of source magmas to the HEDs could be produced by differing extents of partial melting. During the partial melting of Vesta the initial liquid Dy/Yb

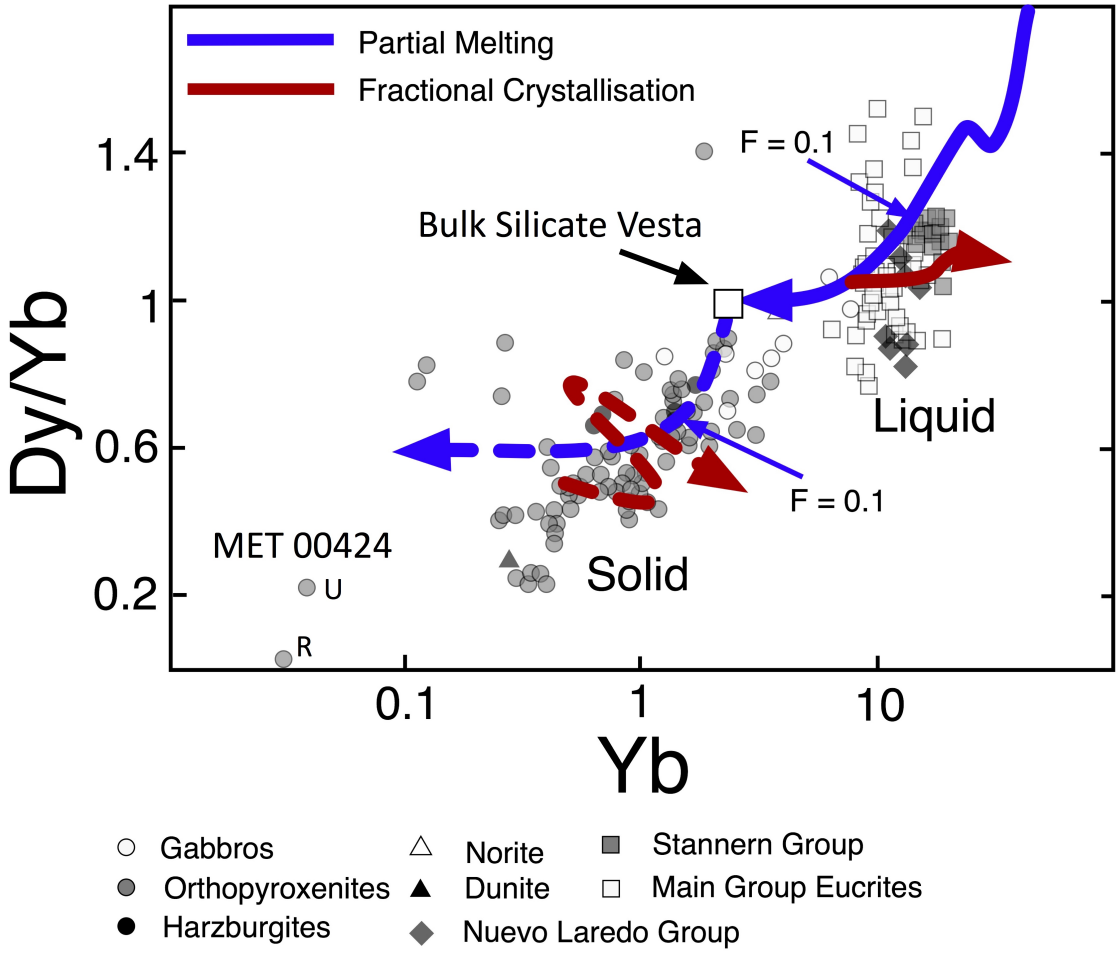

Figure 4.3: Dy/Yb vs Yb for the partial melting (blue) and fractional crystallisation (red) models. Starting composition is a BSV with mantle Mg# = 75 and 2.5 times chondrite abundances of trace elements. The evolution of liquid compositions are shown by solid lines, and the solid (cumulate) compositions by the dashed lines. Meteorite compositions plotted from *Mittlefehldt* (2015). The arrowheads denote progressive melting for the partial melting models, and progressive crystallisation in the fractional crystallisation model. 10 % partial melting of BSV has been labelled on the solid and liquid paths. The BSV composition has been labelled. In addition the diogenite MET00424 (discussed further in the text) is also shown. The 'U' value is the unleached measurement, and the 'R' value is the residue after leaching the sample for terrestrial weathering effects (described in further detail in *Barrat et al.* (2000)).

(normalised to CI) ratio is around 2 and this decreases to 1 over ∼20 % partial melting, where it then remains relatively constant. The evolution of the cumulate compositions demonstrates a similar pattern with an initial Dy/Yb of ∼0.8 which drops to 0.5 as partial melting occurs. From Figure 4.3 we can see that partial melting alone is not

enough to produce the range of trace element ratios seen in the eucrite and diogenite meteorites.

4.2.4 Fractional crystallisation

Fractional crystallisation paths where the mineral phases that form are instantaneously and completely removed from the liquid were calculated. In order to derive equations to describe the distribution of trace elements between crystal and melt again a mass balance has to be considered. If M_o is the initial mass of melt (bulk mass of the system) and a small mass increment (dM) is removed through fractional crystallisation then the mass of the chemical element entering the crystals is the concentration of the element i in the solid multiplied by the change in mass: C_i^{Solid}dM. This is equal to the mass increment removed from the liquid and so:

$$C_i^{Solid} dM = d(C_i^{Liquid} M^o) \tag{4.6}$$

This equation can be solved through integration with the chain rule as follows:

$$C_i^{Solid} dM = C_i^{Liquid} dM + M^o dC_i^{Solid} \tag{4.7}$$

$$\frac{dM}{M}(C_i^{Solid} - C_i^{Liquid}) = dC_i^{Liquid} \tag{4.8}$$

$$\begin{aligned} \int_{M^o}^{M} \frac{dM}{M} &= \int_{C_i^o}^{C_i^{Liquid}} \frac{dC_i^{Liquid}}{C_i^{Solid} - C_i^{Liquid}} \\ &= \int_{C_i^o}^{C_i^{Liquid}} \frac{dC_i^{Liquid}}{C_i^{Liquid}(D-1)} \end{aligned} \tag{4.9}$$

$$ln\frac{M}{M^o} = \frac{1}{D-1} ln\frac{C_i^{Liquid}}{C_i^o} \tag{4.10}$$

and as the proportion of M to M_o is the fraction of melt, F then 4.10 can be

rearranged to:

$$lnF = \frac{1}{D-1} ln \frac{C_i^{Liquid}}{C_i^o} \tag{4.11}$$

$$F^{D-1} = \frac{C_i^{Liquid}}{C_i^o} \tag{4.12}$$

and the trace element evolution of the liquid and solid for each chemical element i can be calculated with the equations below:

$$C_i^{Liquid} = C_i^o F^{D_i - 1} \tag{4.13}$$

$$C_i^{Solid} = D_i C_i^o F^{D_i - 1} \tag{4.14}$$

The fractional crystallisation paths of 10-50 % partial melts of Vesta were calculated, and the results are shown in Figure 4.3 and Supplementary Figure E.1.

Fractional crystallisation enriches the melt in incompatible trace elements (Figures 4.3 and E.1). A 30 % partial melt of BSV with Mg# = 75 (which has 8×CI abundances of incompatible trace elements) crystallises pigeonite and plagioclase, producing a melt that becomes 30×CI abundance, with a small negative Eu anomaly due to the formation and extraction of plagioclase. The enriched Stannern group eucrites could be explained by this fractionation process. The trace element signature of the first solids produced through fractional crystallisation have trace element abundances for La which are 0.01 CI that increase with atomic number to 0.5 CI for Yb. This pattern is more fractionated than bulk diogenite, however the presence of accessory phases or minor trapped melt (less than 1 %) would enrich the LREE abundance and flatten the trace element pattern. When plagioclase starts to crystallise from the melt, Eu anomalies are seen both in the melt and solid composition. The fractional crystallisation models predict an extremely large Zr depletion, due to the small partition coefficient of D_{Zr}. When a 30 % partial melt is extracted and fractionally crystallised,

the Dy/Yb ratio in the melts and solid remain constant at values of 1 and 0.5 respectively, and pass through the eucrite and diogenite regions on the graph (Figure 4.3). The Dy/Yb ratio in the cumulates shows a slight general increase with abundance, however the path zig-zags as feldspar starts to co-crystallise with the low-Ca pyroxene, followed by late stage olivine and augite. A 10 % partial melt of the BSV has ∼20×CI abundances, crystallising feldspar and low Ca pyroxene, with minor olivine, augite and spinel, and the melt evolves to ∼100×CI with the Dy/Yb ratio increasing from 1.2 to 1.4, whereas a 50 % partial melt of the BSV has ∼5×CI abundances and crystallises predominantly low-Ca pyroxene with minor feldspar, spinel and olivine and the melt evolves to ∼25×CI abundances and the Dy/Yb increases from 1.01 to 1.08. The residues produced by fractional crystallisation of 10-50 % partial melts of BSV show similar Dy/Yb fractionation with an average value of 0.5-0.6, all with the zig zag pattern. The variations between the models are due to the difference in crystallising mineralogy (feldspar has a higher Dy/Yb ratio to pyroxene and olivine) and the differences in start abundance.

It can be seen that the variation in trace element abundances (lateral variation on a Dy/Yb vs. Yb graph) in eucrites and diogenites can be produced through a mixture of partial melting and the fractional crystallisation of different degrees of partial BSV melts. However, another process is needed to explain the observed range in Dy/Yb values, particularly the more fractionated (lower Dy/Yb ratio) cumulates.

4.2.5 Trapped intercumulate melt

During cumulate formation crystal melt segregation may not be 100 % efficient, and some melt may be trapped. The crystals and melt will re-equilibrate in terms of major and trace element compositions, and subsequently crystallise through equilibrium crystallisation. The final cumulate will therefore have a different composition to the initial cumulate which crystallised. I calculated this process for a range of start compositions including the liquids and residue after 30 % and 40 % partial melting, and also after 10 and 20 % fractional crystallisation of these melts. The effect of trapping

10, 20 and 30 % melt withun the cumulate were calculated. The re-equilibration of trapped melt with the cumulate does not significantly alter the cumulate major element composition. Two scenarios have been plotted on Figure 4.4 to demonstrate two extremes: one where 10 % melt is trapped into the cumulate, and one where 30 % melt is trapped. These scenarios were chosen as end-members of possible scenarios that may occur in the interior of Vesta. Due to its low pressure, and the similarity in density between melt and crystal, crystal settling will not be as efficient as it is on the Earth. AlphaMELTS modelling of the system suggests that in the subsequent crystallisation of this orthopyroxene-olivine cumulate, low-Ca pyroxene and up to 5 % feldspar will crystallise, depending on the amount of melt which is trapped. The small amount of plagioclase crystallised could be responsible for some of the negative Eu anomalies seen within the diogenite pyroxenes. During this crystallisation the REEs become more enriched and less fractionated within the cumulates. Higher proportions of trapped melt will increase the trace element inventory of the closed system, and therefore will produce a cumulate which is more enriched and less fractionated than one where there is a lower amount of melt trapped. From 4.4 it can be seen that trapped intercumulate melt could account for the cumulate compositions that are less fractionated and less enriched than the simple differentiation models of partial melting and subsequent fractional crystallisation. Different starting compositions including a 40 % partial melt, or the cumulate composition after some fractional crystallisation of a partial melt, were also calculated and show the same trend as the example plotted on Figure 4.4 but with lateral offsets in abundance depending on the start composition.

4.2.6 Re-melting of early basalts and cumulates

Basaltic volcanism occurred on Vesta over a period of ∼10 Ma (*Touboul et al.*, 2015) where the crust formed as an accumulation of multiple lava flows, underlain by more slowly cooling and crystallising cumulates. The earliest formed lavas and cumulates were buried and underwent heating and metamorphism, mostly to temperatures of 700-1000 ^{o}C, although in some places the temperature reached values above the solidus

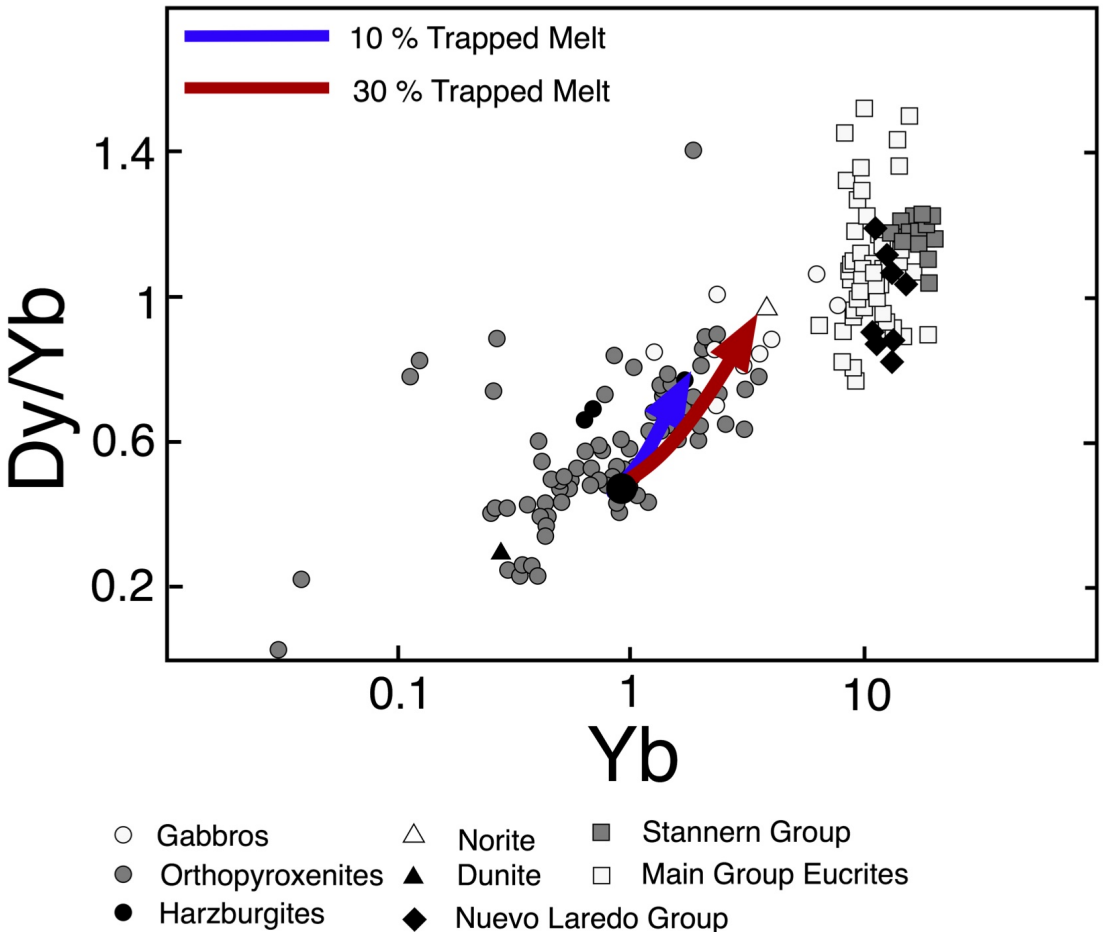

Figure 4.4: Dy/Yb vs Yb for trapped intercumulate melt models. A cumulate which represents 20 % fractional crystallisation of a 30 % partial melt of BSV with Mg# = 75 was used as the starting composition (representative of an average diogenite composition). The results of trapping 10 % melt in the cumulate followed by re-equilibration and crystallisation are shown by the blue solid line, and the results of trapping 30 % melt are shown by the red solid line. Meteorite compositions plotted for comparison are taken from *Mittlefehldt* (2015). The arrowheads denote the progression of equilibrium crystallisation of the cumulate plus trapped melt system

causing partial melting (*Yamaguchi et al.*, 2009). Some cumulates may have undergone partial melting as later eucritic magmas ascended to the surface of the asteroid. The re-melting of early lithologies can be split into two categories: crustal anatexis and re-melting of early ultramafic cumulates.

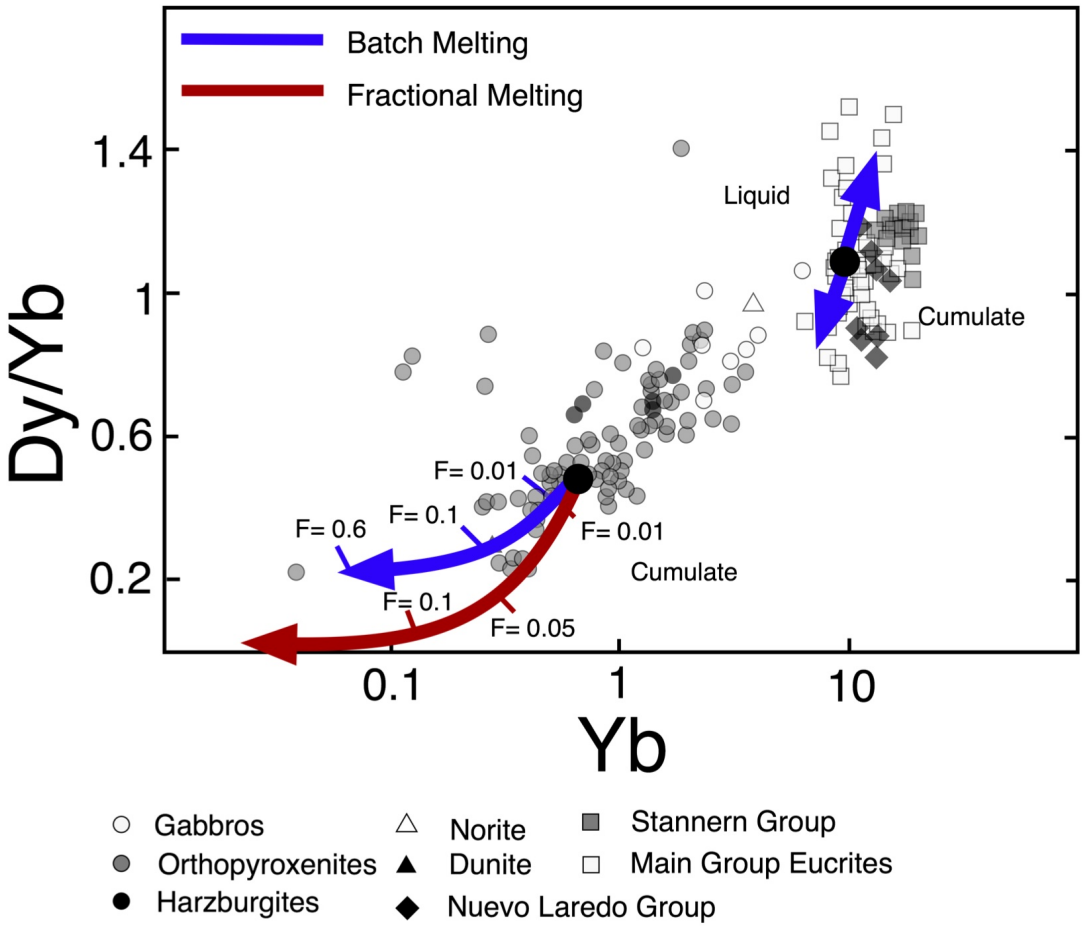

Figure 4.5: Dy/Yb vs Yb for fractional and batch melting models, complete with fraction of melt (F). Representative diogenite (LEW8808) and eucrite (Juvinas) compositions were used as starting points. The evolution of the cumulate in the fractional melting model is shown in red, and the evolution of the cumulate composition in the batch melting models are shown in blue. The large arrowheads represent the direction of progressive melting. The evolution of the liquid and cumulate are shown for the eucrite compositions.

Crustal anatexis

In this model the effects of 5-20 % partial melting of a eucrite (Juvinas) crust comprising 60 % low-Ca pyroxene and 40 % plagioclase were calculated. The melt produced was then combined with a eucritic melt, and subsequently fractionally crystallised. Both the evolution of the melt and restite were calculated, and the results of these models are shown in Figures 4.5 and 4.6a. The liquid formed when an eucrite is partially melted is enriched in trace elements, with the amount of enrichment decreasing as the amount of partial melting increases, from 150×CI at a 5 % partial melt fraction, down

to 40×CI at a partial melt fraction of 20 %, and with a large negative Eu anomaly due to the presence of residual plagioclase. The solid residue has roughly chondritic abundances of trace elements and a correlating positive Eu anomaly. The restite is more depleted and shows greater REE fractionation than the starting composition, with a small decrease in REE and HFSE abundance. When 5-10 % of the partial melts are mixed into a eucritic melt and fractional crystallisation proceeds, the resulting composition is slightly more enriched than main group eucrites with a less flat REE pattern, similar to the Stannern group eucrites (see Figure 4.5). The residual cumulate predicted by this crustal anatexis model is similar (but not identical) to the thermally metamorphosed 'granulite' eucrites which *Yamaguchi et al.* (2009) describe. These models are an extension of those of *Barrat et al.* (2007), however with more accurately determined partition coefficients and with a larger range of compositions explored.

Cumulate remelting

Two models of cumulate melting were considered: batch and fractional melting. Batch or equilibrium melting assumes that the melt and solid remain in chemical equilibrium during partial melting and the system is closed, whereas fractional melting is an open system where the instantaneous melt which forms is immediately extracted from the system. Batch melting is calculated using Equations 4.13 and 4.14 and the residue composition produced through fractional melting by the equation:

$$C_i^{Solid} = C_o(1-F)^{\left[\frac{1}{D}-1\right]} \tag{4.15}$$

first derived by *Gast* (1968) and updated by *Shaw* (1970). The residue compositions for both are presented in Figures 4.5 and 4.6b. The starting composition used in this model was the residue after 30 % partial melting of BSV. Both mechanisms of melting produce a residue which becomes more depleted and fractionated with respect to the REEs as melting progresses. Fractional melting produces a larger amount of fractionation and depletion than partial melting. After 1 % melting the residues produced by

both mechanisms have similar depletions and fractionations with Yb = 0.6×CI, and a Dy/Yb = 0.4, compared to the start cumulate (Yb = 0.66×CI, Dy/Yb = 0.5). After 10 % batch melting the residue has Yb = 0.25, Dy/Yb = 0.27, whereas the residue after 10 % fractional melting is significantly more depleted and fractionated with Yb = 0.12, and Dy/Yb = 0.05. The fractional melting of cumulates can therefore produce residues which have extremely high MREE-HREE fractionations, at low degrees of partial melting (<20 %), a mechanism which can account for the highly fractionated and depleted orthopyroxenites seen in the HEDs. For example the MET 00424 signature could be produced by ∼2 % fractional melting of a cumulate produced through 30 % partial melting of the BSV. MET00424 is the most trace element depleted diogenite, which also has a very low Dy/Yb ratio (*Barrat et al.*, 2008). MET00424 is not unusual in other respects, as it contains mm sized crystals of orthopyroxene ($Wo_{1.5}$) and one troilite grain (5mm). The REE signature of MET00424 (shown in 4.6b) is particularly enigmatic as it is more MREE depleted than LREE or HREE depleted. The trace element patterns across the REE group can also be considered (Figure 4.6b) emphasising the increased fractionation and depletion caused through fractional melting compared to batch melting. It can be seen that the REE pattern of MET 00424 does not show this sharp fractionation across the whole REE group, as the LREE are similarly enriched to the HREE and MREE, however this could be explained by the presence of accessory phases or trapped melt, as a minor amount of either would have the ability to significantly alter the trace element abundance budget.

Another mechanism for producing low Dy/Yb ratios is multiple stages of partial melting of the cumulates, as each progressive melting event depletes the trace element abundance slightly and increases the REE fractionation. However, the mechanism for multiple re-melting events and the thermal drive behind them make fractional melting a more plausible scenario to produce the highly fractionated cumulates due to its simplicity. Batch and fractional melting are two members of a continuum and dynamic melting, where a small fraction of melt (e.g. 1-10 %) would be trapped in the cumulate with the rest being extracted could occur, and produce results which would

plot between these two end-members.

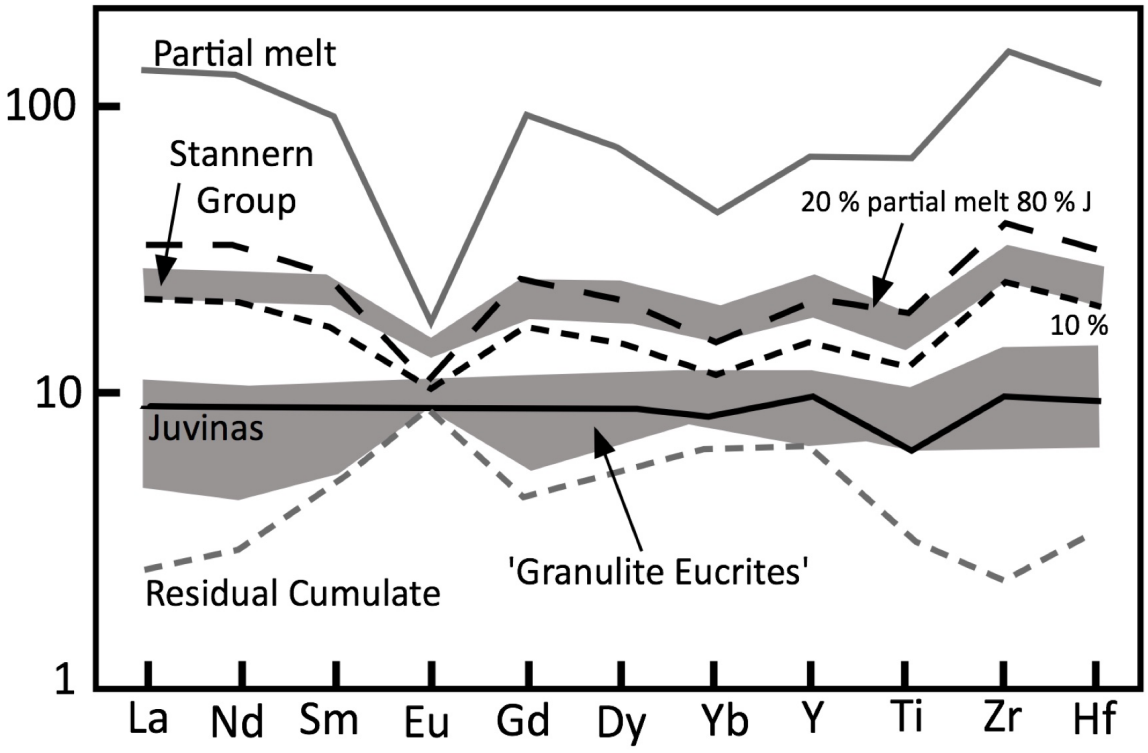

Figure 4.6a: Chondrite-normalised trace element abundances for the partial melting of a eucrite. The range in composition of the 'granulite' and Stannern Group Eucrites are shown and labelled as the grey shaded areas. The partial melt produced is represented by the solid grey line. The grey dashed line shows the trace element pattern of the residual cumulate, and the black dashed lines show the composition of a main group eucrite with 10 % (small dashes) and 20 % of the partial melt mixed in. The main group composition used was of Juvinas, and is shown by the solid black line. Meteorite compositions taken from *Yamaguchi et al.* (2009) and *Barrat et al.* (2000).

4.2.7 Assimilation and fractional crystallisation

Magma chamber processes have been suggested (*Mandler and Elkins-Tanton*, 2013) as a plausible mechanism for creating a range of trace element compositions in the diogenites. Assimilation and fractional crystallisation (AFC) is one such process, where crustal material is added to the melt simultaneously to crystallisation. The equations

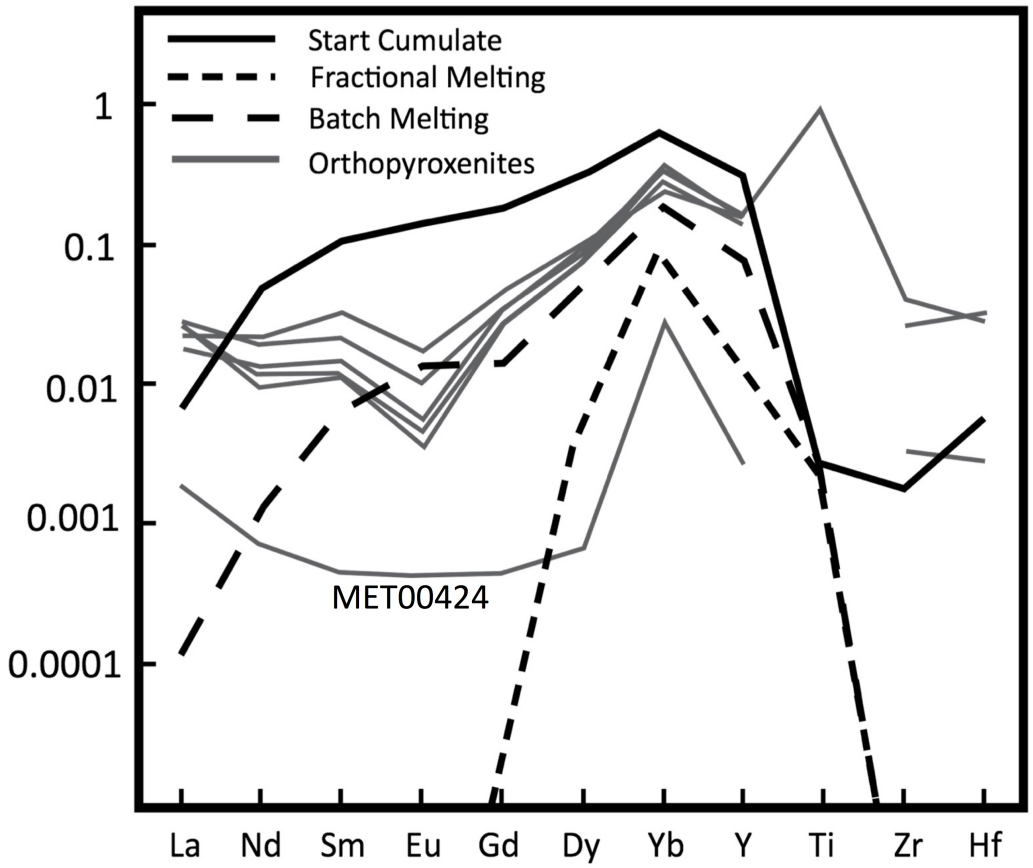

Figure 4.6b: Chondrite-normalised trace element abundances for the partial melting of a diogenite. Some representative orthopyroxenite compositions are shown by the grey lines, including the most depleted diogenite for comparison. Meteorite compositions taken from *Beck et al.* (2012), *Mittlefehldt et al.* (2012).

from *DePaolo* (1981) were used to calculate the liquid C_i^{Liquid} and solid C_i^{Solid} composition, during the fractional crystallisation of a 30 % partial melt of BSV, with varying amounts of assimilated material.

$$C_i^{Liquid} = C_o F^{\frac{D_i+r-1}{1-r}} + \frac{rC_i^A(1-F^{\frac{D_i+r-1}{1-r}})}{D_i+r-1} \tag{4.16}$$

$$C_i^{Solid} = D_i C_i^{Liquid} \tag{4.17}$$

where C_i^A is the concentration of the element in the material that is being assimilated, and r is the ratio between the assimilated material and the rate of fractional crystallisation. The C_o starting melt was taken as a 30 % partial melt of the BSV. The evolution of the residue composition during crystallisation with two r values of 0.2 and 0.9, are plotted in Figure 4.7. The assimilation and fractional crystallisation model is an extension of the fractional crystallisation model, and the trace element abundance and signatures are very similar, particularly under low rates of assimilation to crystallisation (low r). As the amount of assimilated material increases (increasing r value) the abundance of trace elements in the solid increases and so the fractional crystallisation curve is broader. At higher r values (r = 0.9) there is an order of magnitude more enrichment in trace element abundance than fractional crystallisation alone. Assimilation and fractional crystallisation could account for some of the spread in trace element abundances throughout the cumulates, however does not produce more fractionation than fractional crystallisation alone.

4.2.8 Recharge, eruption, assimilation and fractional crystallisation

In order to take the investigation of magma chambers one step further, the extended model of a magma chamber which simultaneously recharges, erupts, assimilates crustal material and fractionally crystallises (REAFC) was considered. In this scenario the magma chamber evolves towards a steady state composition with the recharging magma acting as a compositional buffer. The recharge of hot magma into a magma chamber may increase the longevity of a magma chamber, and sustain eucrite magmatism for an extended time period. The transport of magma to the surface of an asteroid the size of Vesta is believed to be through dikes which produce large subsurface chambers and sills which occasionally erupt (*Wilson and Keil*, 2012) which is why the REAFC model is being considered.

Equations can be derived (e.g. *Lee et al.* 2014) to describe how the concentration of an element changes in a magma chamber undergoing continuous REAFC. If the magma

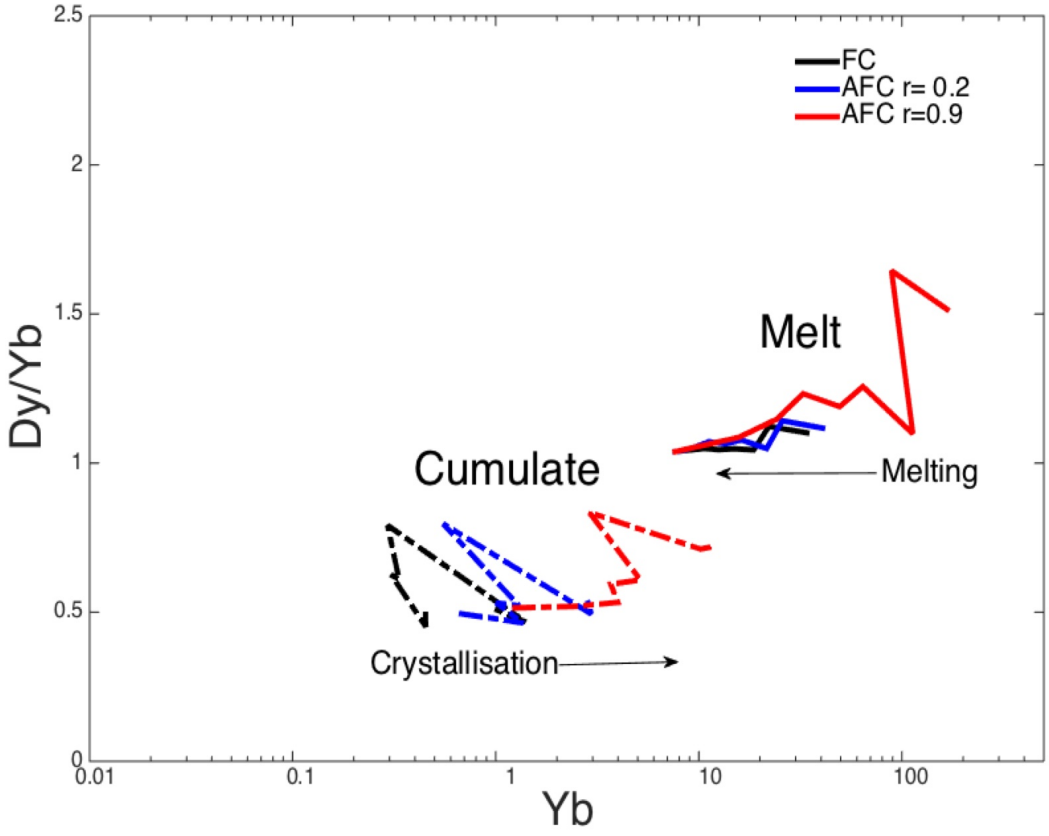

Figure 4.7: Dy/Yb vs Yb for Assimilation and Fractional crystallisation models. Starting composition is the 30 % partial melt of BSV Mg# 75. Calculated liquid compositions are denoted by the solid lines, and solid compositions by the dashed lines. AFC models where the ratio of assimilating material to crystallisation (r value) is 0.2 are shown in blue, and where the r = 0.9 in red. The normal fractional crystallisation model (also plotted on Figure 4.3) is denoted in black.

chamber is considered to be a box model, a mass balance can be defined between the inputs and the outputs. The inputs are the recharging magma and crustal assimilant, and the outputs are the erupting magma and any crystals. Assuming that the mass of the magma chamber is constant (when in steady state) then:

$$M_c dC_c = -C_x dM_x - C_e dM_e + C_a dM_a + C_r dM_r \tag{4.18}$$

where M_c, M_x and M_e are the masses of the magma chamber (c), crystals (x), erupting magma (e) and recharging magma (r). The change in concentration of an

element in the magma chamber is denoted by dC_c. C_x, C_e, C_r are the concentrations in the portions which are crystallising, erupting and recharging.

This equation can be simplified by assuming that the concentration in the erupting portion is the same as the concentration of the chamber (e=c) and by expressing the concentration in the crystallising portion using the Nernst equation (Equation 3.1) C_x=D*C_c. In addition all of the terms can be divided through by dM_r to gain the ratio of different processes to recharge, for example:

$$\alpha_x = \frac{dM_x}{dM_r} \tag{4.19}$$

which gives the ratio of crystallisation to recharge and α_e and α_a can be calculated in a similar manner.

Therefore the mass balance can be rewritten:

$$M_c dC_c = (-D\alpha_x C_c - \alpha_e C_c + \alpha_a C_a + C_r) dM_r \tag{4.20}$$

This equation can be rearranged and integrated from the onset of the magma chamber where $\Delta M_r = 0$ and $C_c = C_o$ to when the magma chamber has reached steady state and $\Delta M_r = \Delta M_r$ and where $C_c = C_c$.

$$\int_{C_o}^{C_c} \frac{1}{-(D\alpha_x + \alpha_e)C_c + C_r + (\alpha_a C_a)} dC_c = \int_0^{\Delta M_r} \frac{1}{M_c} dM_r \tag{4.21}$$

integrating this equation leads to:

$$\frac{ln(-(D\alpha_x + \alpha_e)C_c + C_r + \alpha_a C_a)}{-(D\alpha_x + \alpha_e)} - \frac{ln(-(D\alpha_x + \alpha_e)C_o + C_r + \alpha_a C_a)}{-(D\alpha_x + \alpha_e)} = \Delta M_r \tag{4.22}$$

rearranging this gives:

$$ln\left(\frac{-(D\alpha_x + \alpha_e)C_c + C_r + \alpha_a C_a)}{-(D\alpha_x + \alpha_e)C_o + C_r + \alpha_a C_a)}\right) = -(D\alpha_x + \alpha_e)\Delta M_r \tag{4.23}$$

which can then be rearranged to get C_c:

$$C_c = \frac{C_r + C_a\alpha_a}{D\alpha_x + \alpha_e} - \left[\frac{C_r + C_a\alpha_a}{D\alpha_x + \alpha_e} - C_o\right] exp\left[-(D\alpha_x + \alpha_e)\Delta M_r\right]. \tag{4.24}$$

This is equation A4 of *Lee et al.* (2014).

For the calculations in this thesis I used the equation used by *Lee et al.* (2014) in the spreadsheet which was published alongside their paper. I adapted the equation to run in Matlab rather than Excel, so that I could calculate the evolution of multiple elements simultaneously. In this general numerical solution, instead of integration, the stepwise calculation of the change in concentration in the magma chamber is calculated using the equation:

$$C_{c(n)} = \frac{(C_{n-1}M_{c(n-1)} + C_r dM_r + C_x dM_x + C_e dM_e + C_a dM_a)}{M_{c(n)}} \tag{4.25}$$

where n is the step of the calculation. For n=1 the starting parameters and (n-1) terms were defined, and the for n=2 onwards the calculation used the result of the previous step. The MATLAB script I developed is shown in Appendix D in order to be able to calculate the simultaneous evolution of multiple REE elements. I programmed the script to terminate when the steady state composition of the magma chamber is reached (when the result of $C_n \equiv C_{n-1}$).

In these calculations D was assumed to be constant. A range of models were calculated. Partial melts of Vesta were used as the recharging magma composition. Different crustal assimilants were selected ranging from Juvinas composition, to more evolved compositions. Different rates of recharge, eruption, crystallisation and assimilation between the values of 0 to 1. The partition coefficients used in the fractional crystallisation models were used in these calculations, and it was assumed that the main crystallising phases were clinopyroxene and plagioclase. Figure 4.8 shows the results of one of these calculations, where the rate of recharge and eruption are 0.5, and the rate of crystallisation and assimilation are 0.3. In this scenario the magma chamber takes 18 recharges to reach steady state, and the resulting chamber is enriched in trace

elements by ∼150 %. The Dy/Yb ratio only increases by 4.63 % from 1.065 to 1.1148.

The amount of recharges to reach steady state ranged from ∼15-25. However, it can be seen from Figure 4.8, that after ∼ 8 recharges, the magma chamber composition is more or less constant. Therefore the composition of the magma chamber varies temporally, and one magma chamber could produce a range of eruptive products over its lifecyle. Although enrichment occurs, this mechanism does not appear to alter the Dy/Yb fractionation significantly (less than 5% of their original value). The choice of starting composition and assimilating material influenced the amount of enrichment in trace elements. The number of times the magma chamber was recharged before a steady state composition was reached increased when rate of recharge was decreased. The magma chamber became more enriched in trace elements at lower rates of eruption. This mechanism could produce enrichment of melts in magma chambers, and the melts that are erupted. Magma recharge does not contribute to the fractionation of the REEs and affect the Dy/Yb ratio, similar to the fractional crystallisation and AFC models.

4.2.9 Change in bulk composition

The above results are from the calculations performed on one starting composition: a BSV which has Mg# = 75 and 2.5×CI abundances of trace elements. However, I also calculated the same processes for BSV compositions with Mg# = 70 and Mg# = 80, and the results are presented in Figures E.1 and E.2. The variation in bulk major element composition controls the mineralogy of the Vestan interior (e.g. Chapter 2, *Ashcroft and Wood* 2015), which will cause minor variations in the trace element budget and evolution during the differentiation and igneous process, for example in the equilibrium crystallisation model the higher abundance of plagioclase crystallising from the lower Mg# bulk compositions results in the cumulates exhibiting larger positive Eu anomalies. Varying the start composition of trace elements does not alter the trace element fractionation trends, but alters the abundances, i.e. on a Dy/Yb vs. Yb graph a starting composition with CI abundances and proportions of trace elements will plot laterally to the left (lower abundance) compared with a starting composition which

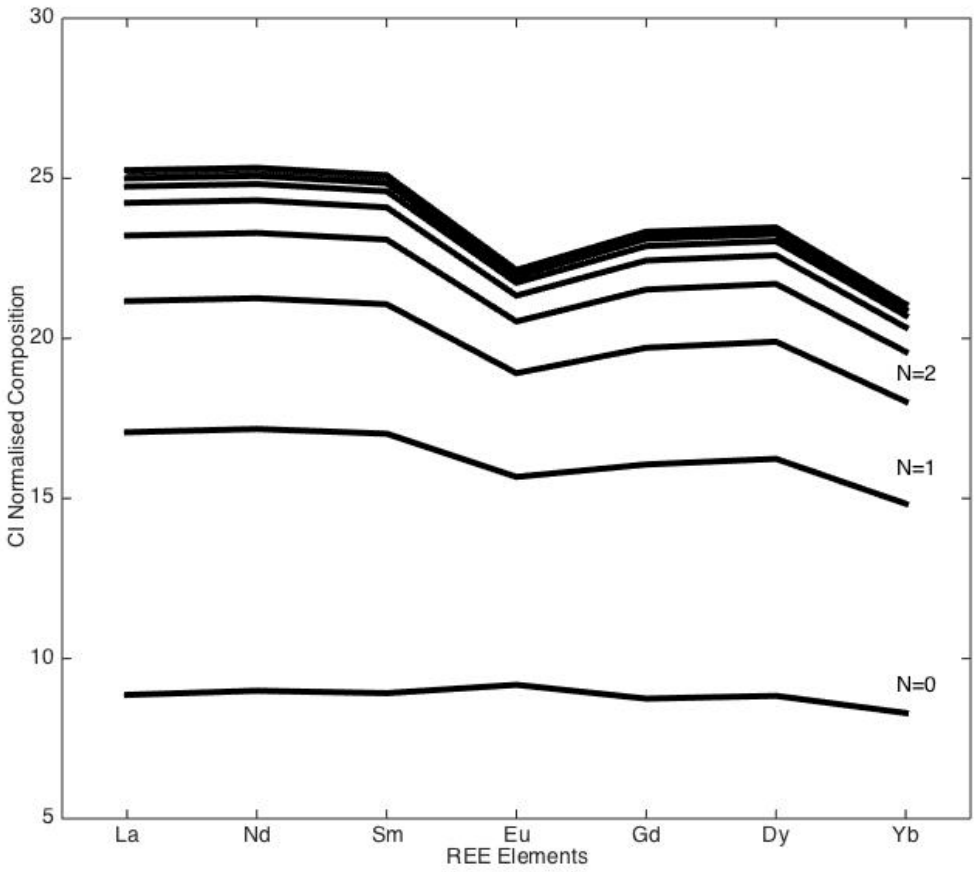

Figure 4.8: REAFC model of a eucritic magma chamber. The scenario where the rates of recharge and eruption are 0.5, and the rates of crystallisation and assimilation are 0.3. This magma chamber reaches a steady state after 18 recharge events, and the end magma chamber composition is enriched by a factor of ∼150 %. N denotes the number of overturns with N = 0 showing the start composition. In this case the recharging magma was eucritic, and the crustal assimilant was one of the more evolved eucrites taken from *Mittlefehldt* (2015). The values shown are CI chondrite-normalised, taken from *McDonough and Sun* (1995).

has 3 times chondritic abundances of the REEs and chondritic proportions (shown in Figure 4.9) which has higher abundances.

4.2.10 Non-modal and incongruent melting

So far the melting models have assumed modal melting, where the proportions of minerals undergoing melting is the same as the mineral proportions in the source. This scenario does not often occur in nature, with eutectic melting being a prime example.

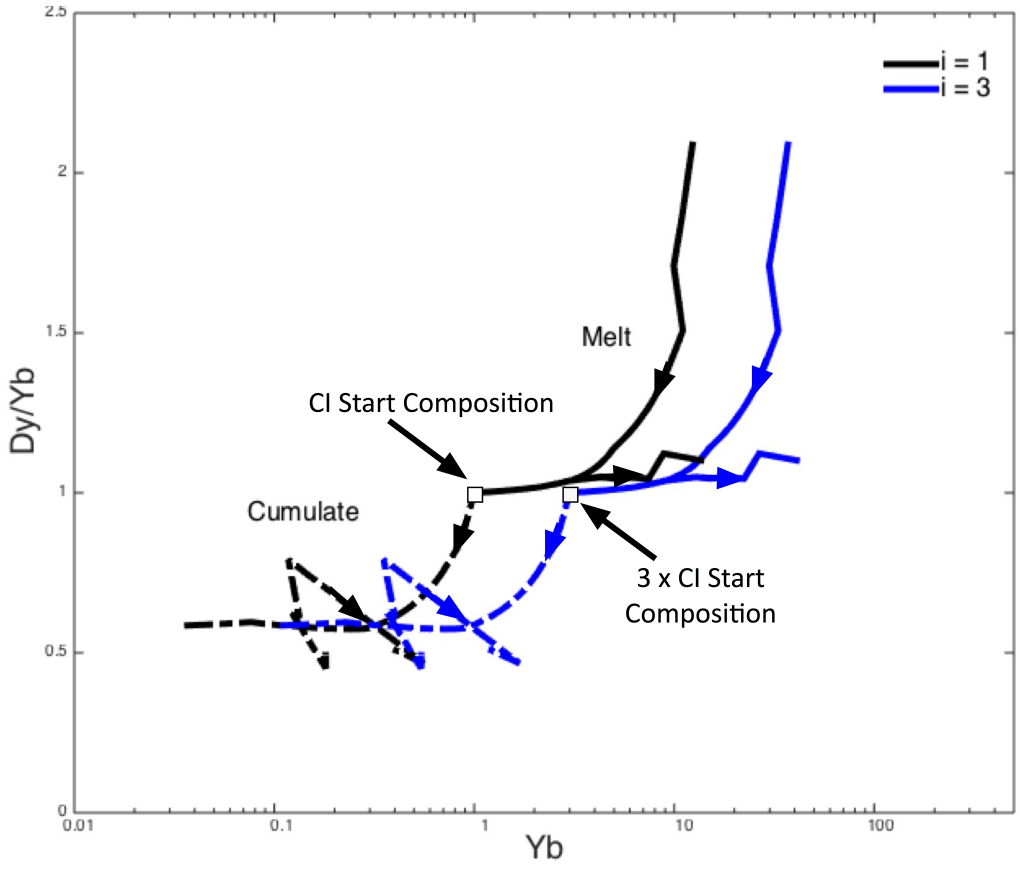

Figure 4.9: Dy/Yb vs Yb for the partial melting and fractional crystallisation models of a mantle with Mg# 75, but where the bulk abundance of trace elements is chondritic (i=1) represented by the black lines, and one where the start abundances are 3 times chondritic values (i=3) shown by the blue lines. The evolution of the solid is shown by the dashed lines, and the liquid evolution is shown by the solid lines. This graph can be compared with Figure 4.3. Chondritic abundances taken from *McDonough and Sun* (1995). The arrows denote direction of partial melting and the direction of fractional crystallisation on the appropriate lines.

The preferential consumption of some mineral phases means that the proportions entering the melt are different, thus affecting the bulk partition coefficient. The derivations in this section are taken from *Zou* (2007) who adapted the models of *Shaw* (1970).

Considering the mass balance of the melting reaction:

$$M_o(1-F)x_i + M_oFp_i = M_ox_i^o \tag{4.26}$$

where M_o is the total mass, M_o(1-F) is the mass of the solid and M_oF is the mass of the liquid. x_i can be written:

$$x_i = \frac{x_i^o - Fp_i}{1 - F} \tag{4.27}$$

N.B. in the case of modal melting x_i=x_i^o.

As D=$\sum x_i K_i$:

$$\begin{aligned} D &= \sum \frac{x_i^o - Fp_i}{1 - F} K_i^o \\ &= \frac{\sum x_i^o K_i^o - F \sum p_i K_i^o}{1 - F} \end{aligned} \tag{4.28}$$

The $\sum x_i K_i^o$ describes the partitioning of trace elements into mineral phases, labelled D_o (Equation 4.5), and in a similar manner the coefficient (P) for trace elements entering the melt can be defined as P=$\sum p_i K_i^o$ and:

$$D = \frac{D_o - FP}{1 - F} \tag{4.29}$$

N.B. again in the case of modal melting D = D_o.

Substituting this into the batch melting equations gives the following equations:

$$C_{Liquid} = \frac{C_o}{D + F(1 - P)} \tag{4.30}$$

$$C_{Solid} = \left(\frac{D_o - FP}{1 - F} \right) \frac{C_o}{D + F(1 - P)} \tag{4.31}$$

and the fractional melting equations:

$$C_{Solid} = \left[\frac{D_o - FP_o}{1 - F} \right] \frac{C_o}{D_o} \left[1 - \left(1 - \frac{FP_o}{D_o} \right)^{\frac{1}{P_o} - 1} \right] \tag{4.32}$$

$$C_{Liquid} = \frac{C_o}{F}\left[1 - \left(1 - \frac{FP_o}{D_o}\right)^{\frac{1}{P_o}}\right] \tag{4.33}$$

In order to calculate the contributions of each mineral phase to the melt, the modal proportions from alphaMELTS were used. The amount of each mineral phase consumed between steps was calculated and used to calculate P. Non-modal melting was considered for three scenarios: the melting of bulk Vesta, melting of a eucrite and melting of a diogenite. When calculating the contribution of different minerals to the melt, at some stages in the crystallisation sequence, incongruent melting was noted, where the olivine-orthopyroxene mineral boundary became peritectic rather than cotectic. This process is observed during the crystallisation of eucrite basalts from above their liquidus (e.g. *Stolper* 1977). The influence of incongruent melting can be included into the non-modal melting equations, by incorporating the amount of melt into the modal proportions. In a similar manner to above bulk D can be defined:

$$D = \sum \frac{x_i^o - Fq_i}{1 - F} K_i^o \tag{4.34}$$

where q is the fraction of net converted mineral relative to the amount of produced melt.

Similarly to P, a factor Q can be defined:

$$Q_o = \sum q_i x_o = \frac{px_o - t^{min} D^{min}}{t^{liq}} \tag{4.35}$$

where x represents the modal proportions of the minerals which are forming, and t^{min} is the modal proportion of minerals being consumed, and t^l is the proportion of melt present.

For example if we were to consider the reaction:

$$0.60 \times Liq + 0.4 \times Ol = 1.0 \times Opx \tag{4.36}$$

then Q would be calculated:

$$Q_o = \frac{\left(\frac{1}{0.6} \times K_{orthopyroxene}\right) - \left(\frac{0.4}{0.6} \times K_{olivine}\right)}{0.6} \tag{4.37}$$

and the melting equations can be rewritten in the same way as Equations 4.30-4.33.

The evolution of the cumulate and liquid compositions were calculated for each scenario, with adapted MATLAB codes to include P and Q where appropriate. The results of these calculations were not significantly different to those where modal melting was assumed for partial melting models of eucrites, diogenites and the majority of melting of Vesta. The differences between P and D values, and between calculated solid and liquid compositions were generally <10 % of each other. The differences were slightly higher for the LREEs, than the MREE and HREEs. In the latest stages of Vesta evolution, feldspar and clinopyroxene crystallise at the expense of olivine and orthopyroxene and larger differences up to a factor of 3 are seen between models. This effect is enhanced due to the large effect of melt enrichment in the incompatible elements in the late stages of crystallisation. In conclusion, although non-modal melting is the natural process likely to be occurring, the results suggest that the models investigated in the study can be approximated by modal melting without any serious issues.

4.2.11 Conclusions - trace elements

The results of these trace element models suggest that four processes are required to explain the complete range of incompatible lithophile trace element abundances and fractionations:

1. Extensive melting of Vesta;
2. Fractional Crystallisation of partial melts;
3. Re-melting of basalts and cumulates;
4. Re-equilibration of trapped intercumulate melt.

It should be noted that there are minor differences between the Hf, Zr and Ti modelled and observed values, and the presence of zircon within the HEDs may contribute to these discrepancies but were not investigated within this study. In addition, models of Eu anomalies have not been investigated in depth in this study, as the partition coefficients measured experimentally are likely to be inappropriate, due to the difference in oxygen fugacity between the meteorites (IW - 1) and the experiments (IW + 1.8). Eu will be Eu^{2+} not Eu^{3+} under the more reducing conditions recorded in the HEDs, and so the partition coefficients measured here will be an overestimate. Now that the major and trace elements have been accounted for, these four processes can be used to predict the minor element evolution of Vesta, as a further check, and to refine the Bulk Vesta minor element composition.

4.3 Minor elements

It is important to constrain the behaviour of the minor elements, as these are important components of the main magmatic minerals forming. Although Ti was considered with the HFSEs in the earlier discussion in this chapter, it will be included in the discussion here also, as it is a minor not a trace element. Cr, Mn and Ti will be treated in a similar treatment to the REEs, as all are incorporated into olivine and orthopyroxene, which are the main crystallising phases during the bulk evolution of Vesta. Cr should be considered as one of major elements, due to the presence of Cr-rich spinel in the HEDs which has ∼50 % Cr_2O_3 (model proportions are generally ∼0.3 wt % but up to 5 % in some meteorites). However, the alphaMELTS software does not naturally incorporate Cr and Mn into the olivine and orthopyroxene crystallising, unless they are set as trace elements. Ti, Cr and Mn all behave differently in terms of their geochemical behaviour. Ti is very incompatible like the REE elements, Mn is slightly incompatible in olivine and bridges the compatibility barrier (D=1) for low-Ca pyroxene, and Cr is compatible in olivine and low-Ca pyroxene.

Under the reducing conditions of HED formation, Mn and Ti only have one ion

to consider: Mn^{2+} and Ti^{4+}. Cr is a little more complex because the Cr^{2+} to Cr^{3+} transition occurs close to the IW buffer, meaning that in the HED meteorites, one would expect Cr^{2+} to be the predominant ion, however as the experiments are slightly above the IW buffer, Cr^{3+} may be present. The partition coefficients for Cr^{2+} and Cr^{3+} into olivine are nearly identical because the smaller Cr^{3+} ion (ionic radius closer to the r_o for the site) requires a charge balance whereas the larger Cr^{2+} ion does not (*Papike et al.*, 2005). Cr^{3+} partitions into the M1 site in pyroxene, but Cr^{2+} generally does not (*Papike et al.*, 2005). Therefore the slightly more oxidised conditions of these experiments compared to the HED meteorites suggest that the calculated partition coefficients for Cr here may be an overestimate.

The partitioning of Cr and Ti into pyroxene is particularly relevant for understanding the partitioning behaviour of Al, as they enter the pyroxene crystal through charge balance substitutions. In the volatile-poor, reducing conditions of the HED system Cr^{3+}, Ti^{4+} and Al^{3+} are the main substituting cations into the octahedral M1 site, with Al^{3+} entering the tetrahedral Si^{4+} site. The Cr and Ti content of diogenite and eucrite pyroxenes are positively correlated with the Al content in pyroxene, reflecting these substitutions. *Fowler et al.* (1994) assessed the relative importances of each of the three charge coupled substitutions and found that the Cr^{3+}-Al^{3+} $\rightleftharpoons {}^{VI}M^{2+}$-${}^{IV}Si^{4+}$ was the most significant at the start of crystallisation (more primitive compositions, when compatible Cr had a higher abundance in the melt phase). At the end of the crystallisation sequence, the Ti^{4+}-$2Al^{3+}$ $\rightleftharpoons {}^{VI}M^{2+}$-$2{}^{IV}Si^{4+}$ substitution becomes the most dominant, as the melt compositions are more enriched in the incompatible Ti, with the contribution of the Al^{3+}-Al^{3+} $\rightleftharpoons {}^{VI}M^{2+}$-${}^{IV}Si^{4+}$ remaining fairly constant during mantle evolution.

I will now test the refined petrogenetic models for eucrite and diogenite formation on the minor elements, and infer the amount of Cr_2O_3, MnO and TiO_2 in the BSV.

4.3.1 EPMA vs. LA-ICP-MS measurements

Despite differences in the amount of minor elements between the experimental start compositions and the measured amounts in the HEDs, the partitioning behaviour should still be applicable. From Tables A.3 and A.4 it can be seen that there is no obvious trend in Mn abundance with temperature or magma evolution, but Al, Cr and Ti increase in pyroxene as temperature decreases. The Ti and Mn content in olivine increase as T decreases, and the Cr and Al content decrease with decreasing temperature. The Al content of the melt increases and Cr and Mn content decreases with decreasing T. No obvious trend is seen with TiO_2, although direct quantitative comparisons cannot be made between all phases in experiments due to differences in starting composition. The abundances of MnO, Cr_2O_3 and TiO_2 in each experimental charge have been measured using EPMA and LA-ICP-MS and the calculated low Ca-pyroxene-melt partition coefficients for both methods of analyses are compared in Figure 4.10. The 1:1 line has been plotted for comparison and it can be seen that the two measurements are in good agreement, however the size of the errors are larger on the EPMA measurements than the LA-ICP-MS ones due to the significantly higher detection limits of $\sim$ 0.01 wt % (EPMA) compared to a few ppm (LA-ICP-MS).

The partition coefficients selected for use in the trace element models are from the LA-ICP-MS measurements for Cr, Mn and Ti, and the EPMA measurements for Al. In pyroxene the partition coefficients of Ti, Mn, Al and Cr all increase with decreasing temperature meaning that they are all more compatible in the later stages of crystallisation. The partition coefficients of Mn and Ti double, and those of Cr and Al triple, over the temperature and composition range studied here. The large increase in the Al partition coefficient reflects the combination of the three coupled charge substitutions that allow Cr^{3+}, Ti^{4+} and Al^{3+} to partition into pyroxene. In olivine the partition coefficient for Ti does not show an obvious trend with Mg# (which is correlated with temperature), but the partition coefficient for Al decreases by a factor of two, the partition coefficient for Mn increases by a factor of two and Cr by a factor of 4 as Ol Mg# decreases from 92 to 83.

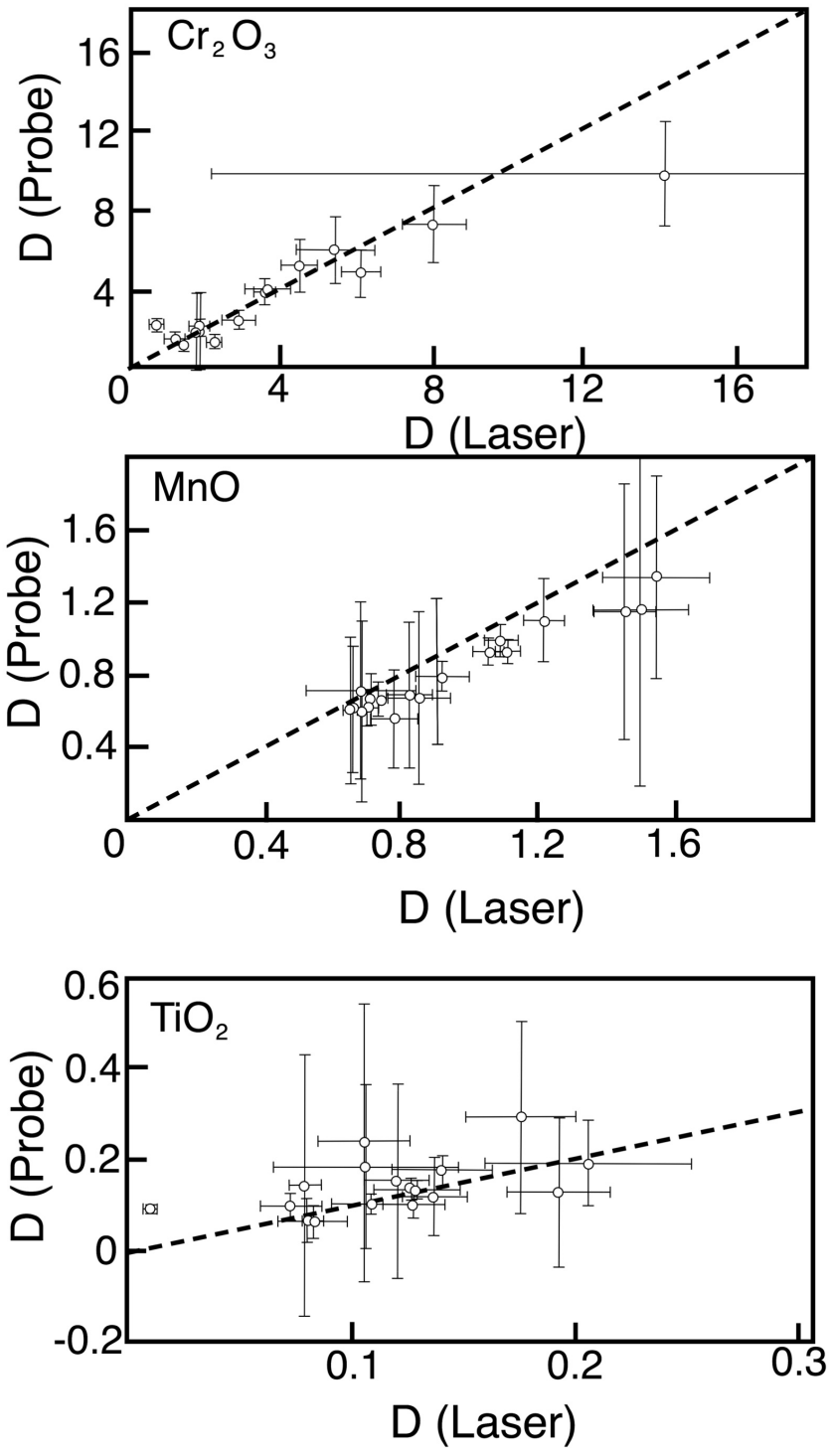

Figure 4.10: Partition coefficients (D) for TiO_2, Cr_2O_3, and MnO measured by EPMA (Y axis) and LA-ICP-MS (X axis) for the experimental data reported in Chapters 2 and 3. Two TiO_2 values were not plotted due poor quality analysis (standard error larger than the measured value). Error bars represent standard error. The dashed lines represent the 1:1 line.

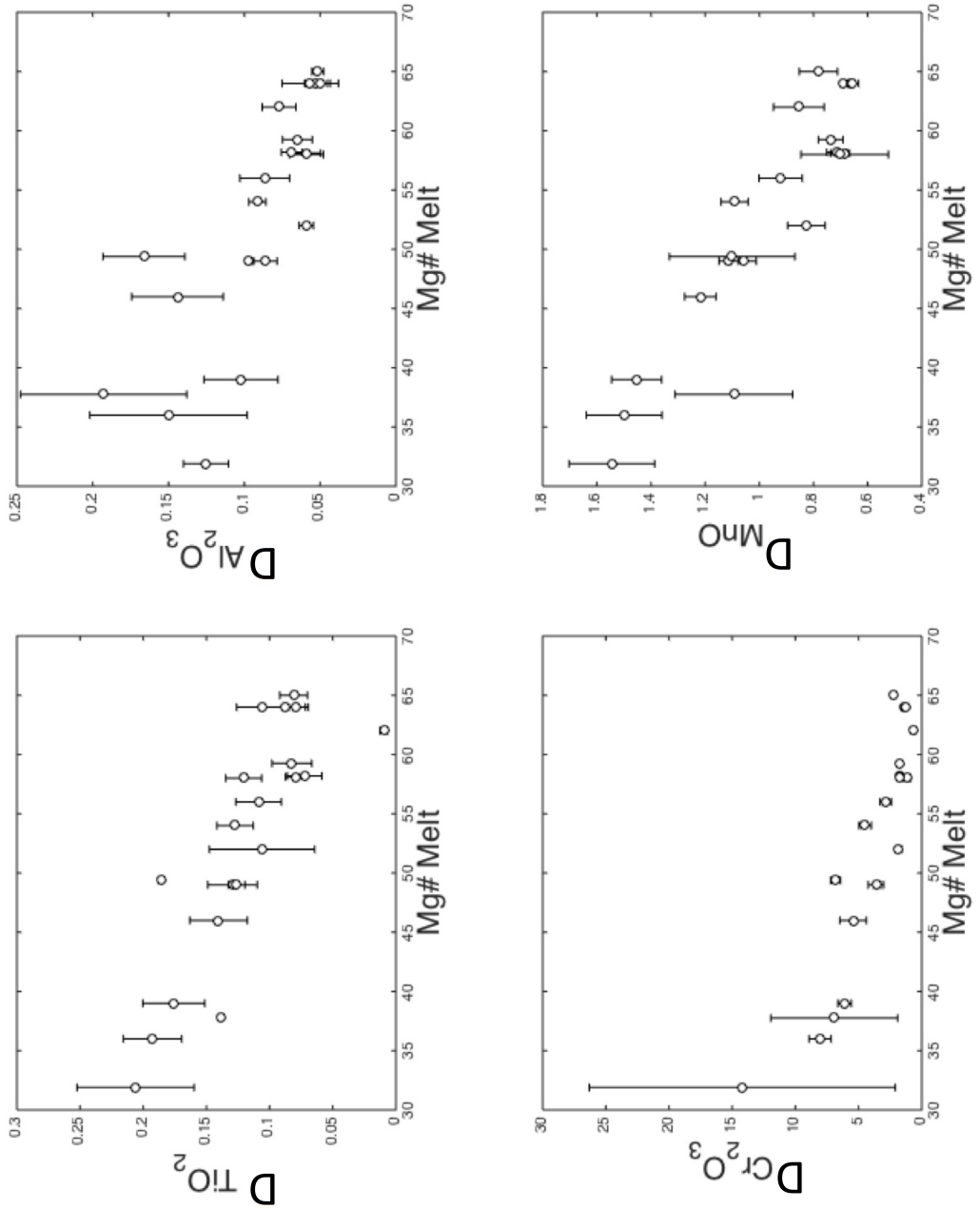

Figure 4.11: Partition Coefficients (D) between pyroxene and melt measured for the experiments reported in Chapters 2 and 3. The TiO_2, Cr_2O_3 and MnO D values were calculated from LA-ICP-MS analysis, and the Al_2O_3 from EPMA analyses. Error bars shown are the standard error.

4.3.2 Differentiation and magmatic models

These partition coefficients can be used to model the evolution of Ti, Mn, Cr, during differentiation and magmatism in a similar manner to the REE and HFSE trace elements. The following models were tested for these three minor elements: partial melting, fractional crystallisation and assimilation and fractional crystallisation and up to 20 % re-melting of basalts and ultramafic cumulates. A 5th phase of Cr-rich spinel was added to the models for Cr partitioning.

Spinels were observed in the experimental campaign, however, due to their small size and low modal abundance, only one EPMA measurement could be made across all of the experiments with a composition of 1.02 wt % TiO_2, 10.25 wt % Al_2O_3, 56.78 wt % Cr_2O_3, 19.21 % FeO, 10.98 wt % MgO. Compared with the HED meteorites (data assimilated by *Mittlefehldt* 2015), this spinel is less iron-rich and more Mg-rich, which may reflect the higher proportion of Fe^{3+} to Fe^{2+} under the less reducing conditions of the experiments. Therefore when considering partitioning into chromite during the evolution of Vesta's mantle and crust, partition coefficients for Cr into chromite were estimated using the measured amounts of Cr in eucrite and diogenite spinels, and bulk eucrite and diogenite compositions (roughly 50 % Cr_2O_3 in spinel compared with about 0.3 wt % Cr_2O_3 measured in bulk eucrites and diogenites) which gave a range in D_{Cr} between 100-200 (for comparison the calculated D_{Cr} from the HAPM2_15 experiment was 660). In the subsequent models about 0.5 wt % spinel was calculated to form at any point. Partitioning of Ti and Mn into spinel were not considered due to their low abundance in spinel (in the experimental spinel here the MnO and TiO_2 combined were less than 1 wt. %), and the low abundance of spinel as a phase.

4.3.3 Results

The results of the partial melting and fractional crystallisation models are shown in Figure 4.12 for all three elements. The top panel for each element shows the evolution of the liquid composition and eucrite and diogenite compositions for comparison, and the

bottom panel shows the evolution of the solid compared with pyroxene compositions for bulk eucrites and diogenites (taken from *Mittlefehldt* 2015). Ti behaves in a similar manner to REEs, due to its incompatibility and so the amount of Ti in the cumulate and liquid decreases as fraction of partial melting increases. During fractional crystallisation the amount of Ti in both melt and crystal increases. A bulk Vesta composition of around 0.15 wt % Ti can explain the majority of the Ti abundances through partial melting and subsequent fractional crystallisation, in-keeping with CI proportions.

In contrast Cr is compatible and partitions into olivine, orthopyroxene and spinel, and so the Cr content of the melt and residues during partial melting increases with melt content. During the fractional crystallisation of different melts the amount of Cr remains about constant. In order to produce the observed crystal and bulk compositions, a bulk Vesta Cr_2O_3 of $\sim$0.75 wt.% is required.

Mn behaves differently to both Ti and Cr as it is just incompatible in olivine with a D_{Mn} of 0.8-1 and is initially incompatible in pyroxene, until 1200 ^{o}C when the partition coefficient becomes greater than one. This change in compatibility is reflected in the change in trend exhibited in the pyroxene compositions seen in cumulate and basaltic eucrites. Bulk Mn contents of the eucrites and diogenites are fairly constant around 0.5 wt %. The Mn composition in pyroxene increases sharply between pyroxene Mg# 40-50, and then decreases as the Mg# increases up to 90.

Varying the degree of partial melting before fractional crystallisation does not alter the general fractional crystallisation trend for Ti, Mn or Cr, only the abundances of the path. In general AFC produces cumulates which are more Mn-, Ti- rich and Cr- poor than the normal fractional crystallisation path, reflecting the partitioning behaviour and assimilant composition with larger differences at higher r values (increase in assimilation ratio to crystallisation ratio).

As with the incompatible trace elements, melting either a eucritic composition or a mafic cumulate (in this model a residue from 30 % partial melting of Vesta was used as a starting point) the Ti composition in the melt phase formed is more enriched, and decreases with progressive melting, and the residual cumulate becomes more depleted,

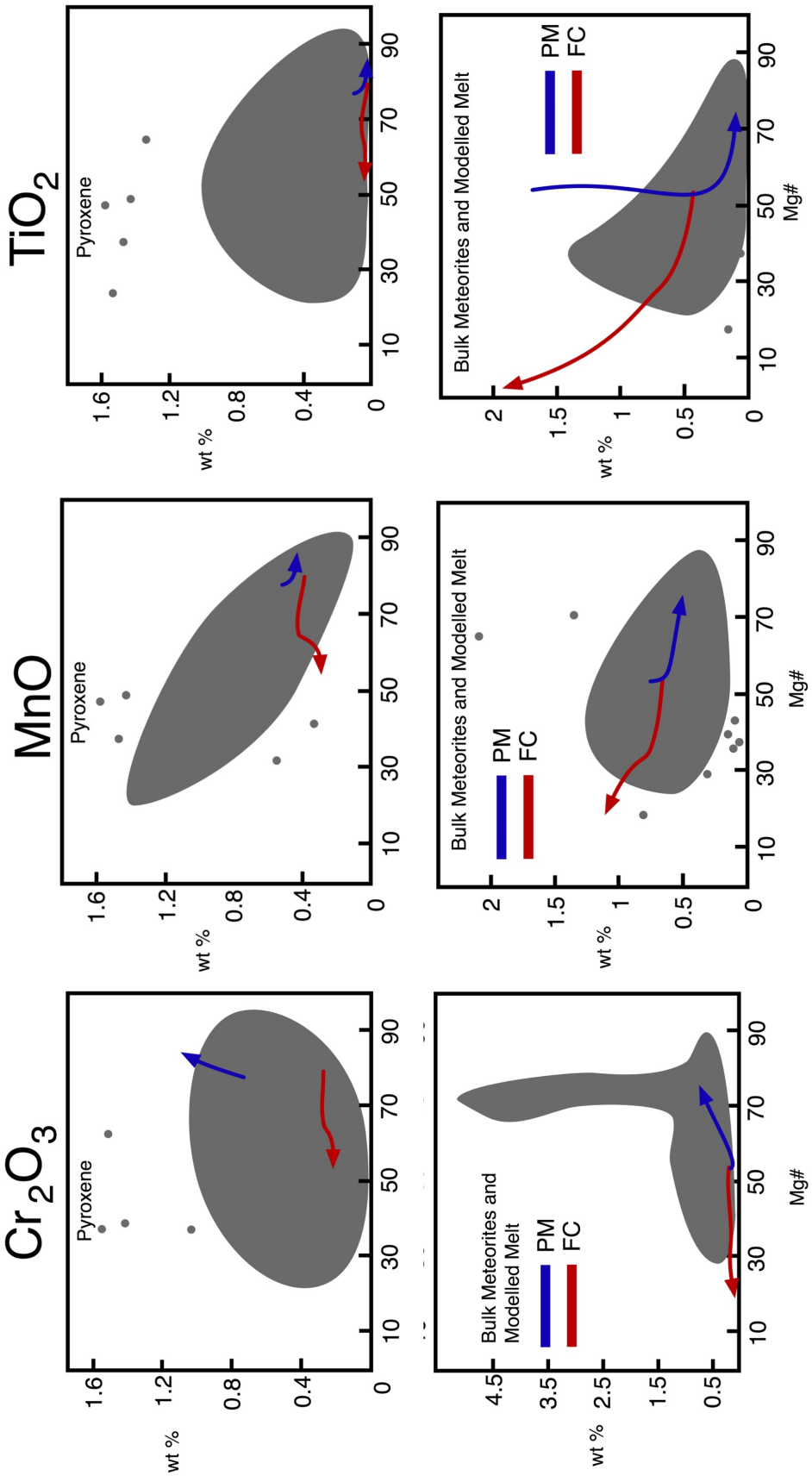

Figure 4.12: Partial melting and fractional crystallisation calculations for the minor elements, showing the evolution of the solid (cumulates) in the top boxes plotted against eucrite and diogenite pyroxene compositions, taken from *Mittlefehldt* (2015), and the evolution of the liquid (bottom) compared to the bulk eucrite and diogenite compositions taken from *Mittlefehldt* (2015).

particularly in the case of fractional melting. Mn shows similar behaviour to Ti but with less extreme fractionation, due to its higher compatibility.

As expected Cr shows the opposite trend with the partial melt (batch or fractional) being more depleted than the start composition, and the residue is slightly more enriched. Therefore the re-melting theory can explain some of the vertical spread in Ti and Cr contents in eucrites and diogenites. In the models of REAFC, magma chamber Ti, Mn and Cr concentrations become enriched, the amount dependent on starting composition and assimilant composition, with a larger effect seen for the very incompatible Ti, and compatible Cr, than Mn. For compatible Cr the steady state composition is reached after fewer overturns than for the incompatible Ti and Mn.

Again these models can account for the majority of the spread in bulk and pyroxene eucrite and diogenite compositions. There are a large spread in Cr abundances in diogenites which do not correlate with Mg# and the only mechanism here which could account for this is significant (> 50 %) re-melting of an ultramafic cumulate, or simply that those samples contain up to 5 % modal chromite. The large spread in Cr compositions in diogenites may also reflect other mechanisms, for example subsolidus re-equilibration or metasomatism.

The effects of 10, 30 and 50 % trapped melt in an orthopyroxene cumulate were calculated, using the residue and liquid after 70 % partial melting of Vesta. As expected from their compatibilities, the re-equilibration of the system increases the amount of Ti by an order of magnitude and slightly increases the bulk Mn in the cumulate, and decreases the bulk Cr. The final cumulate is more enriched in Ti and Mn than the initial composition, and more depleted with respect to Cr and these effects increase as proportion of melt increases.

4.4 Conclusions

The minor and trace element variations in the HED meteorites can be explained by a three stage model of Vesta's evolution:

1. Core-mantle segregation

2. Crystallisation

3. Re-melting of early crust.

In most of the minor and trace element models the main phases olivine, orthopyroxene, clinopyroxene and feldspar were considered. The incorporation of Cr-rich spinel was included in Cr models. Although the modal proportion of this phase is generally below 0.5 % in eucrites and diogenites, Cr is a major component of this phase with a large $D^{spinel-melt}$ (estimated to be 100-200 in the HEDs). The petrogenetic models are consistent with the Cr content recorded in eucrite and diogenite pyroxenes. More Cr-rich compositions are seen in the bulk diogenite compositions, however these can be attributed to those samples containing higher modal proportions of spinel (up to 5 %) in the sample.

Differentiation and crystallisation (equilibrium then fractional) can account for the range in trace and minor element abundances across the eucrites and diogenites, but not the range in fractionations between different REE elements. Modelled cumulates produced after $>$ 30 % melting have a Dy/Yb ratio of 0.5, with equilibrium liquids with Dy/Yb =1. Fractional crystallisation of the partial melts produces cumulate and melt compositions which become more enriched in trace elements as crystallisation progresses, and could account for some of the vertical spread in fractionation (less fractionated cumulates) which is dependent on the crystallising phases (due to differences in trace element partitioning between orthopyroxene, olivine, feldspar and melt).

In order to produce the range of trace element fractionations seen in the non-cumulate eucrites, partial melting of main group eucrites produces a eucritic cumulate which is more fractionated and a melt which is less fractionated, without significantly changing the abundance of the trace or major elements, accounting for the Nuevo Laredo group, the Stannern group and the granulite eucrites.

In order to account for the diogenite cumulates which record more fractionated trace element signatures, re-melting of early cumulates either through batch or frac-

tional melting could occur which deplete the cumulates in trace element abundance and enhance the amount of fractionation. Fractional melting enhances the fractionation more than batch melting. For example the 10 % fractional melting of a cumulate with Dy/Yb ∼0.5 will have a Dy/Yb close to 0.05 however, the 10 % batch melting of the same composition will have a Dy/Yb = 0.2. The most depleted diogenites which also record the most fractionated Dy/Yb ratios could be accounted for by ∼15 % fractional melting of a cumulate produced after ∼40 % partial melting of Vesta.

In addition the re-equilibration of trapped melt within cumulates and subsequent crystallisation alters the trace element signature, particularly the recorded fractionation (Dy/Yb). Cumulates with up to 30 % trapped melt can account for the majority of cumulates which lie above the partial melting line. The presence of minor phases will also contribute to these less fractionated cumulates, particularly REE-rich phases like phosphates.

The range in trace element abundances and fractionations can be accounted for through these four main processes. Of course, for re-melting of early formed basalts and cumulates to occur a heat source is required, and we can only speculate that prolonged magmatism on the HED parent body is the heat source.

Further processes were investigated including recharge, eruption, assimilation and fractional crystallisation, and although this may cause magma chamber enrichments in trace elements on Vesta, this mechanism is not required to explain the observed trace element signatures. Due to the number of overturns required before a steady state is reached, this mechanism does suggest that the composition of magma chambers on Vesta may have evolved with time, as would their eruptive products.

The results of these trace element models suggest that bulk Vesta had on the order of 2.5×CI refractory lithophiles, TiO_2 = 0.15 wt %, Cr_2O_3 = 0.75 wt. % and MnO = 0.5 wt. %.

Chapter 5

Conclusions and Future Directions

The objectives of this thesis were to answer two key questions:

1. What is the bulk composition of Vesta?
2. What differentiation and magmatic processes have occurred to produce the eucrites and diogenites?

The approach that I took to address these issues combined experiments, observations and modelling. The major element composition and mineralogy were tackled first, followed by the minor and trace elements.

5.1 Conclusions

Chapter 1 outlined information regarding the HED meteorites and their presumed parent body, the asteroid Vesta. The gaps in the current understanding regarding Vesta's bulk composition and the link between the basaltic eucrites and the eucrite and diogenite cumulates were highlighted.

Chapter 2 investigated the major element composition of Bulk Silicate Vesta (BSV). The Mg# ($100*(Mg/(Mg+Fe^{2+})$) of the diogenite olivines and refractory lithophile proportions in the HEDs were used to estimate the major element composition of the silicate portion of Vesta. Moment of inertia and density calculations of Vesta's interior

were used to ensure that these compositions were in accordance with the geophysical observations of Vesta. Series of one-atmosphere experiments were performed on these compositions to define the liquid line of descent of the BSV and to test the two main suggested petrogenetic models: partial melting and magma ocean. In conjunction with the experiments, thermodynamic calculations were performed on the same compositions under the same conditions. This allowed the thermodynamic models to be tested for their applicability to the HED system. In addition the thermodynamic models were used to investigate the sensitivity of the petrogenetic models to changes in starting composition. The results of the experiments and thermodynamic calculations suggest that a starting mantle with Mg# = 70 could produce eucritic melts through partial melting of Vesta alone. However another process would be required to generate the diogenite cumulates as partial melting not only produces insufficient amounts of pyroxene but pyroxenes of the wrong composition. The fractional crystallisation of partial melts produces melts which are more SiO_2-rich and Al_2O_3-poor than recorded in the HED meteorites. A multistage model of a BSV with Mg# 80 can produce both eucrites and diogenites. Firstly extensive partial or complete melting of Vesta occurred and a magma ocean formed. Then the fractional crystallisation of a 30-45 % partial melt (or after 55-70 % equilibrium crystallisation of a magma ocean) produces orthopyroxene-rich cumulates, and a residual melt which becomes eucritic in composition. A BSV with Mg# 80 suggests an Fe-Ni core which is 15-20 % of Vesta's mass. The liquidus temperature is 1650^{o}C, with olivine crystallising first, followed by pyroxene at $\sim$1350 ^{o}C. Extracted partial melts at 1350 and 1300 ^{o}C first crystallise orthopyroxene followed by feldspar at $\sim$1125 ^{o}C. The alphaMELTS software was selected to model the HED compositions and it can predict the mineral phases and compositions well, but has issues overestimating the pyroxene liquidus by up to $\sim$70 ^{o}C and with the incorporation of minor elements into the crystallising phases. Based on the results of the experiments, alphaMELTS models were used to explore and refine the compositional range of BSV. It was found that the two main conditions which had to be satisfied were a BSV with Mg# 75-80 and a SiO_2 content 43 wt. %. In order to

produce appropriate proportions of eucritic and diogenitic material, a range in extent of partial melting before melt extraction was found, generally between 20-45 % depending on bulk composition. More Mg#-rich compositions required lesser amounts of partial melting to produce eucrites and diogenites than the more Fe-rich compositions.

The results of Chapter 2 and observations from the HED meteorites suggest that orthopyroxene and pigeonite are the predominant minerals forming during the crystallisation of the eucrites and diogenites. Low-Ca pyroxene will therefore have a significant influence on the distribution of trace elements between melt and crystal phases during magmatic processes. The partitioning behaviour of trace elements between minerals and melt varies as a function of temperature, pressure, composition and oxygen fugacity. Therefore careful selection of appropriate partition coefficients is required in order to perform geochemical calculations. Although measurements have been made and predictive models derived, the partitioning behaviour of trace elements into low-Ca pyroxenes is not understood fully. Chapter 3 focused on the investigation of variation in trace element partition coefficients across the temperatures and compositions under which the eucrites and diogenites formed. Series of one-atmosphere experiments were doped with trace elements in order to make direct calculations of partition coefficients. The lattice strain model was fitted to each experimental charge and values of D_o, r_o and E were obtained. Lattice strain parameters were calculated for 3^+ and 4^+ ions into the M1 site, and 3^+ and 2^+ ions into the M2 site. The 3^+ (Al, Cr, Sc) ions are more compatible than the 4^+ (Zr, Hf, Ti) ions into M1 by an order of magnitude, with a lower Young's modulus by a factor of two and a larger r_o by 0.02 $\mathring{A}$. In the M2 site the 2^+ ions (Fe, Mn, Ca) are more compatible than the 3^+ ions (REE and Y) by an order of magnitude. The predicted Young's Modulus for both series are similar, but the r_o for the 2^+ ions is larger than that of the 3^+ ions by $\sim$0.06$\mathring{A}$. This r_o increases with Ca content and decreasing T.

D values increase by up to a factor of 3 as the temperature decreases from 1300-1125 ^{o}C, and the Ca content of pyroxene increases from $Wo_{0.5}$-Wo_8. Ca has a larger ionic radius than Mg and Fe, and so when pyroxene has a higher Ca content, the r_o of the

site increases and can accommodate larger cations. Compatibility also increases with Al_2O_3 content, interpreted as the results of more Al substitution for Si in the tetrahedral site of pyroxene, facilitating more coupled substitutions including the REEs, Cr and Ti into pyroxene. These experimental results were found to be comparable to other planetary studies of orthopyroxene and pigeonite partitioning, particularly shergottites and lunar picrites. The predictive models of *Sun and Liang* (2013) for REE and HFSE lattice strain parameters were tested. The predictive models were good at predicting the values for the REE elements, however the HFSE model was less good, significantly underestimating the D_o value. The errors on the predictive models were a lot larger than the errors on the calculated values for the experiments.

The results of Chapter 3 show that it was necessary to determine the partition coefficients directly for the HED system as the current predictive models are not sensitive enough to account for the observed change in partition coefficients over the temperature range studied here. REE and HFSE partition coefficients increase by a factor of three over the specific temperature and composition interval which the diogenites crystallise over. The main factors affecting partition coefficients here are temperature, Ca and Al composition, The work of this study was not comprehensive enough to unravel the individual contributions of these factors.

The aim of Chapter 4 was to refine the minor and trace element composition of BSV and test the petrogenetic model suggested in Chapter 2. Geochemical models of magmatism and differentiation utilising these partition coefficients were performed. Firstly the multistage model of partial melting/magma ocean followed by fractional crystallisation can produce the observed range in trace element abundances across the range of eucrites and diogenites. However the range in trace element fractionation (Dy/Yb ratio is often used as a proxy) cannot be explained. A range in Dy/Yb (0.01-1.6) values is seen in the eucrites and diogenites, the lower bound of which is much lower than the 0.05 predicted by differentiation models. Therefore a further range of processes were considered. Eucrites exhibiting metamorphic textures have been identified and so the remelting of crust and mafic cumulates were considered. Partial melting of

any HED lithology produces a melt which is incompatible element rich, but does not fractionate the Middle Rare Earth Elements (MREEs) from the Heavy Rare Earth Elements (HREEs). The residue becomes more incompatible depleted with a more fractionated trace element signature (Dy/Yb decreases). Partially melting a eucrite produces a more incompatible-rich melt, and the mixture of this melt with an average eucritic melt can produce the more enriched types, including the Stannern group. The more depleted residual eucrite cumulate predicted by this model are represented in the meteorite suite by the granulite eucrites.

When considering this mechanism for the cumulate lithologies, both end-members of dynamic melting scenarios were considered: batch and fractional. Both partial melting scenarios produce cumulates which are depleted in incompatibles and more fractionated (lower Dy/Yb) compared with their precursor. In the fractional melting scenario (where melt is extracted immediately from the system) the magnitude of this effect is much larger and can produce the most depleted and highly fractionated diogenites.

Further magmatic processes were considered to investigate the eucrites and diogenites which exhibited higher than average Dy/Yb ratios. Magma chamber processes like recharge, eruption, assimilation and fractional crystallisation were shown to increase the trace element abundance but not the trace element fractionation between REEs. On a small body like Vesta, the segregation of melts and crystals by crystal settling is inefficient due to small pressure gradients and density differences and so melt coexisting with cumulates during their formation may not be efficiently extracted. This system will then re-equilibrate and crystallise. The Dy/Yb of this cumulate is higher than the original, and the trace element abundance is also higher. This process can account for the diogenites that have higher Dy/Yb than predicted by the differentiation models.

These models were evaluated for both minor and trace element and were used to refine the BSV composition to 2.5×CI values for the refractory lithophiles (REE and TiO_2), 0.75 wt.% Cr_2O_3 and 0.5 wt. % MnO.

The conclusions of the work of thesis are:

1. **A combination of experiments and geochemical models suggest a BSV composition with:**

   - **Mg# = 75-80**
   - **SiO_2 = >43 wt. %**
   - **Refractory Lithophiles = 2.5×CI**
   - **MnO = 0.5 wt. %**
   - **Cr_2O_3 = 0.75 wt. %**
   - **An Fe or FeNi core which is 15-20 % of Vesta by mass**

2. **The interior of the HED Parent Body (Vesta) evolved via three main processes:**

   - **Differentiation.** Extensive (if not global) melting occurred. A metal core formed and segregated from the silicate mantle, which is likely to have had a magma ocean.
   - **Cooling and crystallisation** Vesta's interior cooled through equilibrium crystallisation until the crystal fraction was about 60-70 %, when the remaining melt was extruded to the surface and fractionally crystallised producing a range of mafic and ultramafic cumulates (diogenites) and a residual basaltic (eucrite) melt. Re-equilibration of trapped intercumulate melt caused incompatible element enrichment in some cumulates.
   - **Re-melting of early crust** Continued volcanism on the HED parent body buried earlier crust causing anatexis. This process can produce more enriched basalts and more depleted cumulates.

5.2 Implications

The findings of this thesis suggest that Vesta is very much an intermediary between asteroids and the terrestrial planets. More extensive and prolonged igneous processing is recorded in the HED meteorites than suggested for other differentiated bodies like the angrite and ureilite parent bodies. At the same time, Vesta did not grow into a larger terrestrial planet. Although the major element (and isotope) signatures of the eucrites and diogenites suggest extensive internal melting and equilibration, further constraints or evidence regarding proving or disproving the magma ocean model cannot be placed.

Heterogeneity in the crust and mantle of Vesta is suggested by the range of trace element signatures seen. Multiple stages and sources of magmatism can be inferred, either caused by heterogeneity in Vesta's mantle itself, or melt extraction at different times during planetary cooling. A geochemically heterogenous planetary mantle is not a strange or unlikely concept. Multiple magma sources on one planetary body are recorded in the angrites, shergottites, lunar rocks and of course, the interior of the Earth. Different sources are attributed to spatial and temporal changes in conditions or chemical composition specific to each body, and so variation within Vesta is surely to be expected.

One thing to bear in mind is sample bias. The HED suite are all thought to originate from one area on Vesta, the South Pole, and so we may not have a representative view of Vesta, particularly its interior. It should be noted that although the experiments and also surface spectra of Vesta do not predict any 'missing' lithologies from the meteorite record, this does not rule out their occurrence. The majority of Vesta's surface is covered by regolith and the crustal structure and composition underneath is not known and so we may be missing some petrological nuances. Another difficulty is that we have evidence on the micro-scale and macro-scale, but nothing in between and no samples of the Vestan mantle. Therefore more detailed investigations into intrusive processes cannot be made, as the number, type and size of crustal intrusions or magma chambers is unknown.

5.3 Future Directions

- Direct future work suggested by this thesis could include a comprehensive investigation into the individual contributions of Ca, Al and temperature to the change in low-Ca pyroxene-melt partition coefficients. Experiments keeping one of these factors constant while varying the other two could be performed. This task is not trivial as changes in composition and conditions will alter the phase relations.

- Advances in analytical equipment will allow a more detailed investigation into the compositional variation between and within different meteorite samples, particularly with regards to measurements of volatile and highly siderophile elements (HSE)s. In addition to the abundances of volatile elements, the role of their carrier phases like the phosphates merrilite and apatite, is not quantified. Accessory phases like phosphates and zircon will also contribute to the trace element signatures recorded in the HEDs, particularly in the late stages of fractional crystallisation. The S content of Vesta's core is unknown, and will affect the interior melting style in addition to influencing Vesta's core size. Further details of core formation may be retrieved from geochemical analysis of the HSE elements across the HED meteorites.

- A more detailed petrographic study, not just of the HED meteorites, but all meteorites will help to further this investigation. Increases in our understanding of impact processes and metamorphism across the early solar system well help with the interpretation of features seen in the brecciated lithologies.

- The continued discovery of more HED meteorites allows groupings between different cumulates to be made, for example cumulates which sample different layers of an individual intrusion, and aid petrological interpretation. Understanding the petrogenesis of the anomalous eucrites and angrites, which are likely to have formed on similar sized parent bodies at a similar time will provide further in-

formation to aid the interpretation of the HEDs.

- Identifying Earth analogues for the HEDs perhaps early crustal igneous rocks like komatiites, and observations (particularly on the cm-m scale) of layered igneous intrusions like the Stillwater Complex may provide useful comparison.

Bibliography

Adams, J. B. (1974), Visible and near-Infrared diffuse reflectance spectra of pyroxenes as applied to remote-sensing of solid objects in solar-system, *Journal of Geophysical Research*, *79*(32), 4829–4836.

Albarede, F., and A. Provost (1977), Petrological and geochemical mass-balance equations - an algorithm for least-square fitting and general error analysis, *Computers and Geosciences*, *3*(2), 309–326.

Ammannito, E., M. C. De Sanctis, F. Capaccioni, M. T. Capria, F. Carraro, J. P. Combe, S. Fonte, A. Frigeri, S. P. Joy, A. Longobardo, G. Magni, S. Marchi, T. B. McCord, L. A. McFadden, H. Y. McSween, E. Palomba, C. M. Pieters, C. A. Polanskey, C. A. Raymond, J. M. Sunshine, F. Tosi, F. Zambon, and C. T. Russell (2013), Vestan lithologies mapped by the visual and infrared spectrometer on Dawn, *Meteoritics and Planetary Science*, *48*(11), 2185–2198.

Ashcroft, H. O., and B. J. Wood (2015), An experimental study of partial melting and fractional crystallization on the HED parent body, *Meteoritics and Planetary Science*, *50*(11), 1912–1924.

Balta, J. B., and H. Y. McSween (2013), Application of the MELTS algorithm to Martian compositions and implications for magma crystallization, *Journal of Geophysical Research-Planets*, *118*(12), 2502–2519.

Barrat, J. A., and A. Yamaguchi (2014), Comment on 'the origin of eucrites, diogenites, and olivine diogenites: Magma ocean crystallization and shallow magma processes on vesta' by B. E. Mandler and L. T. Elkins-Tanton, *Meteoritics and Planetary Science*, *49*(3), 468–472.

Barrat, J. A., J. Blichert-Toft, P. Gillet, and F. Keller (2000), The differentiation of eucrites: The role of in situ crystallization, *Meteoritics and Planetary Science*, *35*(5), 1087–1100.

Barrat, J. A., A. Yamaguchi, R. C. Greenwood, M. Bohn, J. Cotten, M. Benoit, and I. A. Franchi (2007), The Stannern trend eucrites: Contamination of main group eucritic magmas by crustal partial melts, *Geochimica et Cosmochimica Acta*, *71*(16), 4108–4124.

Barrat, J. A., A. Yamaguchi, R. C. Greenwood, M. Benoit, J. Cotten, A. Bohn, and I. A. Franchi (2008), Geochemistry of diogenites: Still more diversity in their parental melts, *Meteoritics and Planetary Science*, *43*(11), 1759–1775.

Barrat, J. A., A. Yamaguchi, A. Jambon, C. Bollinger, and O. Boudouma (2012), Low-Mg rock debris in howardites: Evidence for KREEPy lithologies on Vesta?, *Geochimica et Cosmochimica Acta*, *99*, 193–205.

Bartels, K. S., and T. L. Grove (1991), High-pressure experiments on magnesian eucrite compositions - constraints on magmatic processes in the eucrite parent body, *Proceedings of Lunar and Planetary Science*, *21*, 351–365.

Beck, A. W., and H. Y. McSween (2010), Divisions among ultramafic cumulates from a differentiated asteroid, *Geochimica et Cosmochimica Acta*, *74*(12), A66–A66.

Beck, A. W., K. C. Welten, H. Y. McSween, C. E. Viviano, and M. W. Caffee (2012), Petrologic and textural diversity among the PCA 02 howardite group, one of the largest pieces of the Vestan surface, *Meteoritics and Planetary Science*, *47*(6), 947–969.

Beck, A. W., H. Y. McSween, and R. J. Bodnar (2013), In situ laser ablation ICP-MS analyses of dimict diogenites: Further evidence for harzburgitic and orthopyroxenitic lithologies, *Meteoritics and Planetary Science*, *48*(6), 1050–1059.

Binzel, R. P., and S. Xu (1993), Chips off of asteroid-4 Vesta - evidence for the parent body of basaltic achondrite meteorites, *Science*, *260*(5105), 186–191.

Blinova, A., and C. D. K. Herd (2009), Experimental study of polybaric REE partitioning between olivine, pyroxene and melt of the Yamato 980459 composition: Insights into the petrogenesis of depleted shergottites, *Geochimica et Cosmochimica Acta*, *73*(11), 3471–3492.

Blundy, J., and B. Wood (1994), Prediction of crystal-melt partition-coefficients from elastic-moduli, *Nature*, *372*(6505), 452–454.

Blundy, J., and B. Wood (2003), Partitioning of trace elements between crystals and melts, *Earth and Planetary Science Letters*, *210*(3-4), 383–397.

Boesenberg, J. S., and J. S. Delaney (1997), A model composition of the basaltic achondrite planetoid, *Geochimica Et Cosmochimica Acta*, *61*(15), 3205–3225.

Borisov, A., and J. H. Jones (1999), An evaluation of Re, as an alternative to Pt, for the 1 bar loop technique: An experimental study at 1400 ^{o}C, *American Mineralogist*, *84*(10), 1528–1534.

Bouvier, A., J. Blichert-Toft, M. Boyet, and F. Albarede (2015), ^{147}Sm-^{143}Nd and ^{176}Lu-^{176}Hf systematics of eucrite and angrite meteorites, *Meteoritics and Planetary Science*, *50*(11), 1896–1911.

Boyet, M., R. W. Carlson, and M. Horan (2010), Old Sm-Nd ages for cumulate eucrites and redetermination of the solar system initial $^{146}Sm/^{144}Sm$ ratio, *Earth and Planetary Science Letters*, *291*(1-4), 172–181.

Brice, J. C. (1975), Some thermodynamic aspects of growth of strained crystals, *Journal of Crystal Growth*, *28*(2), 249–253.

Britt, D. T., R. J. Macke, W. Kiefer, and G. Consolmagno (2010), An overview of achondrite density, porosity and magnetic susceptibility, *41st Lunar and Planetary Science Conference*.

Buratti, B. J., P. A. Dalba, M. D. Hicks, V. Reddy, M. V. Sykes, T. B. McCord, D. P. O'Brien, C. M. Pieters, T. H. Prettyman, L. A. McFadden, A. Nathues, L. Le Corre, S. Marchi, C. Raymond, and C. Russell (2013), Vesta, vestoids, and the HED meteorites: Interconnections and differences based on Dawn Framing Camera observations, *Journal of Geophysical Research-Planets*, *118*(10), 1991–2003.

Burbine, T. H., P. C. Buchanan, R. P. Binzel, S. J. Bus, T. Hiroi, J. L. Hinrichs, A. Meibom, and T. J. McCoy (2001), Vesta, Vestoids, and the howardite, eucrite, diogenite group: Relationships and the origin of spectral differences, *Meteoritics and Planetary Science*, *36*(6), 761–781.

Cartier, C., T. Hammouda, R. Doucelance, M. Boyet, J. L. Devidal, and B. Moine (2014), Experimental study of trace element partitioning between enstatite and melt in enstatite chondrites at low oxygen fugacities and 5 GPa, *Geochimica et Cosmochimica Acta*, *130*, 167–187.

Clayton, R. N., N. Onuma, and T. K. Mayeda (1976), Classification of meteorites based on oxygen isotopes, *Earth and Planetary Science Letters*, *30*(1), 10–18.

Colson, R. O., G. A. Mckay, and L. A. Taylor (1988), Temperature and composition dependencies of trace-element partitioning - olivine melt and low-Ca pyroxene melt, *Geochimica et Cosmochimica Acta*, *52*(2), 539–553.

Consolmagno, G. J., and M. J. Drake (1977), Composition and evolution of the eucrite parent body: evidence from rare earth elements, *Geochimica et Cosmochimica Acta*, *41*(9), 1271–1282.

Danyushevsky, L. V., and P. Plechov (2011), Petrolog3: Integrated software for modeling crystallization processes, *Geochemistry Geophysics Geosystems*, *12*.

De Sanctis, M. C., E. Ammannito, M. T. Capria, F. Tosi, F. Capaccioni, F. Zambon, F. Carraro, S. Fonte, A. Frigeri, R. Jaumann, G. Magni, S. Marchi, T. B. McCord, L. A. McFadden, H. Y. McSween, D. W. Mittlefehldt, A. Nathues, E. Palomba, C. M. Pieters, C. A. Raymond, C. T. Russell, M. J. Toplis, and D. Turrini (2012), Spectroscopic characterization of mineralogy and its diversity across Vesta, *Science*, *336*(6082), 697–700.

De Sanctis, M. C., E. Ammannito, D. Buczkowski, C. A. Raymond, R. Jaumann, D. W. Mittlefehldt, F. Capaccioni, M. T. Capria, A. Frigeri, G. Magni, F. Tosi, F. Zambon, and C. T. Russell (2014), Compositional evidence of magmatic activity on Vesta, *Geophysical Research Letters*, *41*(9), 3038–3044.

Deines, P., R. H. Nafziger, G. C. Ulmer, and E. Woermann (1974), Origin, internal structure and evolution of 4 Vesta, *Bulletin of the Earth and Mineral Sciences Experiment Station, The Pennsylvania State Univeristy*, *88*(88), 1–129.

DeMeo, F. E., R. P. Binzel, S. M. Slivan, and S. J. Bus (2009), An extension of the Bus asteroid taxonomy into the near-infrared, *Icarus*, *202*(1), 160–180.

DePaolo, D. J. (1981), Trace-element and isotopic effects of combined wallrock assimilation and fractional crystallization, *Earth and Planetary Science Letters*, *53*(2), 189–202.

Dreibus, G., and H. Wanke (1980), The bulk composition of the eucrite parent asteroid and its bearing on planetary evolution, *Zeitschrift Fur Naturforschung Section a-a Journal of Physical Sciences*, *35*(2), 204–216.

Elkins-Tanton, L. T. (2012), Magma oceans in the inner solar system, *Annual Review of Earth and Planetary Sciences, Vol 40*, *40*, 113–139.

Ermakov, A. I., M. T. Zuber, D. E. Smith, C. A. Raymond, G. Balmino, R. R. Fu, and B. A. Ivanov (2014), Constraints on Vesta's interior structure using gravity and shape models from the Dawn mission, *Icarus*, *240*, 146–160.

Filiberto, J., and R. Dasgupta (2011), Fe^{2+}-Mg partitioning between olivine and basaltic melts: Applications to genesis of olivine-phyric shergottites and conditions of melting in the Martian interior, *Earth and Planetary Science Letters*, *304*(3-4), 527–537.

Fonseca, R. O. C., G. Mallmann, P. Sprung, J. E. Sommer, A. Heuser, I. M. Speelmanns, and H. Blanchard (2014), Redox controls on tungsten and uranium crystal/silicate melt partitioning and implications for the U/W and Th/W ratio of the lunar mantle, *Earth and Planetary Science Letters*, *404*, 1–13.

Formisano, M., C. Federico, D. Turrini, A. Coradini, F. Capaccioni, M. C. De Sanctis, and C. Pauselli (2013), The heating history of Vesta and the onset of differentiation, *Meteoritics and Planetary Science*, *48*(11), 2316–2332.

Fowler, G. W., J. J. Papike, M. N. Spilde, and C. K. Shearer (1994), Diogenites as asteroidal cumulates - insights from ortho-pyroxene major and minor element chemistry, *Geochimica et Cosmochimica Acta*, *58*(18), 3921–3929.

Fowler, G. W., C. K. Shearer, J. J. Papike, and G. D. Layne (1995), Diogenites as asteroidal cumulates - insights from ortho-pyroxene trace-element chemistry, *Geochimica et Cosmochimica Acta*, *59*(14), 3071–3084.

Frei, D., A. Liebscher, G. Franz, B. Wunder, S. Klemme, and J. Blundy (2009), Trace element partitioning between orthopyroxene and anhydrous silicate melt on the lherzolite solidus from 1.1 to 3.2 GPa and 1,230 to 1,535 ^{o}C in the model system Na_2O-CaO-MgO-Al_2o_3-Sio_2, *Contributions to Mineralogy and Petrology*, *157*(4), 473–490.

Fu, R. R., and L. T. Elkins-Tanton (2014), The fate of magmas in planetesimals and the retention of primitive chondritic crusts, *Earth and Planetary Science Letters*, *390*, 128–137.

Gaffey, M. J. (1997), Surface lithologic heterogeneity of asteroid 4 Vesta, *Icarus*, *127*(1), 130–157.

Gast, P. W. (1968), Trace element fractionation and origin of tholeiitic and alkaline magma types, *Geochimica et Cosmochimica Acta*, *32*(10), 1057.

Ghiorso, M. S., and R. O. Sack (1995), Chemical mass-transfer in magmatic processes .4. a revised and internally consistent thermodynamic model for the interpolation and extrapolation of liquid-solid equilibria in magmatic systems at elevated-temperatures and pressures, *Contributions to Mineralogy and Petrology*, *119*(2-3), 197–212.

Ghosh, A., and H. Y. McSween (1998), A thermal model for the differentiation of asteroid 4 Vesta, based on radiogenic heating, *Icarus*, *134*(2), 187–206.

Goldschmidt, V. M. (1937), The principles of distribution of chemical elements in minerals and rocks, *Journal of the Chemical Society-Dalton Transactions*, pp. 655–673.

Greenwood, R. C., I. A. Franchi, A. Jambon, and P. C. Buchanan (2005), Widespread magma oceans on asteroidal bodies in the early solar system, *Nature*, *435*(7044), 916–918.

Greenwood, R. C., J. A. Barrat, A. Yamaguchi, I. A. Franchi, E. R. D. Scott, W. F. Bottke, and J. M. Gibson (2014), The oxygen isotope composition of diogenites: Evidence for early global melting on a single, compositionally diverse, HED parent body, *Earth and Planetary Science Letters*, *390*, 165–174.

Greenwood, R. C., J. A. Barrat, E. R. D. Scott, H. Haack, P. C. Buchanan, I. A. Franchi, A. Yamaguchi, D. Johnson, A. W. R. Bevan, and T. H. Burbine (2015), Geochemistry and oxygen isotope composition of main-group pallasites and olivine-rich clasts in mesosiderites: Implications for the "Great Dunite Shortage" and HED-mesosiderite connection, *Geochimica et Cosmochimica Acta*, *169*, 115–136.

Grove, T. L., and K. S. Bartels (1992), The relation between diogenite cumulates and eucrite magmas, *Proceedings of Lunar and Planetary Science*, *22*, 437–445.

Gupta, G., and S. Sahijpal (2010), Differentiation of Vesta and the parent bodies of other achondrites, *Journal of Geophysical Research-Planets*, *115*.

Hicks, M. D., B. J. Buratti, K. J. Lawrence, J. Hillier, J. Y. Li, V. Reddy, S. Schroder, A. Nathues, M. Hoffmann, L. Le Corre, R. Duffard, H. B. Zhao, C. Raymond, C. Russell, T. Roatsch, R. Jaumann, H. Rhoades, D. Mayes, T. Barajas, T. T. Truong, J. Foster, and A. McAuley (2014), Spectral diversity and photometric behavior of main-belt and near-Earth vestoids and (4) Vesta: A study in preparation for the Dawn encounter, *Icarus*, *235*, 60–74.

Holzheid, A., and H. Palme (2007), The formation of eucrites: Constraints from metal-silicate partition coefficients, *Meteoritics and Planetary Science*, *42*(10), 1817–1829.

Ikeda, Y., and H. Takeda (1985), A model for the origin of basaltic achondrites based on the Yamato-7308 Howardite, *Journal of Geophysical Research*, *90*, C649–C663.

Jaumann, R., D. A. Williams, D. L. Buczkowski, R. A. Yingst, F. Preusker, H. Hiesinger, N. Schmedemann, T. Kneissl, J. B. Vincent, D. T. Blewett, B. J. Buratti, U. Carsenty, B. W. Denevi, M. C. De Sanctis, W. B. Garry, H. U. Keller, E. Kersten, K. Krohn, J. Y. Li, S. Marchi, K. D. Matz, T. B. McCord, H. Y. McSween, S. C. Mest, D. W. Mittlefehldt, S. Mottola, A. Nathues, G. Neukum, D. P. O'Brien, C. M. Pieters, T. H. Prettyman, C. A. Raymond, T. Roatsch, C. T. Russell, P. Schenk, B. E. Schmidt, F. Scholten, K. Stephan, M. V. Sykes, P. Tricarico, R. Wagner, M. T. Zuber, and H. Sierks (2012), Vesta's shape and morphology, *Science*, *336*(6082), 687–690.

Jayasuriya, K. D., H. S. O'Neill, A. J. Berry, and S. J. Campbell (2004), A Mossbauer study of the oxidation state of Fe in silicate melts, *American Mineralogist*, *89*(11-12), 1597–1609.

Jurewicz, A. J. G., D. W. Mittlefehldt, and J. H. Jones (1991), Partial melting of the Allende (CV3) meteorite - implications for origins of basaltic meteorites, *Science*, *252*(5006), 695–698.

Jurewicz, A. J. G., D. W. Mittlefehldt, and J. H. Jones (1993), Experimental partial melting of the Allende (CV) and Murchison (CM) chondrites and the origin of asteroidal basalts, *Geochimica et Cosmochimica Acta*, *57*(9), 2123–2139.

Kaula, W. M. (1966), *Theory of Satellite Geodesy*, Blaisdell Publishing Company, Los Angeles.

Kiefer, W., and D. Mittlefehldt (2014), Core formation and evolution of asteroid 4 Vesta, *Vesta in the Light of Dawn: First Exploration of a Protoplanet in the Asteroid Belt*.

Konopliv, A. S., S. W. Asmar, B. G. Bills, N. Mastrodemos, R. S. Park, C. A. Raymond, D. E. Smith, and M. T. Zuber (2011), The Dawn gravity investigation at Vesta and Ceres, *Space Science Reviews*, *163*(1-4), 461–486.

Konopliv, A. S., S. W. Asmar, R. S. Park, B. G. Bills, F. Centinello, A. B. Chamberlin, A. Ermakov, R. W. Gaskell, N. Rambaux, C. A. Raymond, C. T. Russell, D. E.

Smith, P. Tricarico, and M. T. Zuber (2014), The Vesta gravity field, spin pole and rotation period, landmark positions, and ephemeris from the Dawn tracking and optical data, *Icarus*, *240*, 103–117.

Lee, C. T. A., T. C. Lee, and C. T. Wu (2014), Modeling the compositional evolution of recharging, evacuating, and fractionating (REFC) magma chambers: Implications for differentiation of arc magmas, *Geochimica et Cosmochimica Acta*, *143*, 8–22.

Longhi, J., and V. Pan (1988), A reconnaissance study of phase boundaries in low-alkali basaltic liquids, *Journal of Petrology*, *29*(1), 115–147.

Lugmair, G. W., and A. Shukolyukov (1998), Early solar system timescales according to ^{53}Mn-^{53}Cr systematics, *Geochimica et Cosmochimica Acta*, *62*(16), 2863–2886.

Lunning, N. G., H. Y. McSween, T. J. Tenner, N. T. Kita, and R. J. Bodnar (2015), Olivine and pyroxene from the mantle of asteroid 4 Vesta, *Earth and Planetary Science Letters*, *418*, 126–135.

Mandler, B. E., and L. T. Elkins-Tanton (2013), The origin of eucrites, diogenites, and olivine diogenites: Magma ocean crystallization and shallow magma chamber processes on Vesta, *Meteoritics and Planetary Science*, *48*(11), 2333–2349.

Marchi, S., H. Y. McSween, D. P. O'Brien, P. Schenk, M. C. De Sanctis, R. Gaskell, R. Jaumann, S. Mottola, F. Preusker, C. A. Raymond, T. Roatsch, and C. T. Russell (2012), The violent collisional history of asteroid 4 Vesta, *Science*, *336*(6082), 690–694.

Marzari, F., A. Cellino, D. R. Davis, P. Farinella, V. Zappala, and V. Vanzani (1996), Origin and evolution of the Vesta asteroid family, *Astronomy and Astrophysics*, *316*(1), 248–262.

Matzen, A. K., M. B. Baker, J. R. Beckett, and E. M. Stolper (2011), Fe-Mg partitioning between olivine and high-magnesian melts and the nature of Hawaiian parental liquids, *Journal of Petrology*, *52*(7-8), 1243–1263.

McCord, T. B., T. V. Johnson, and J. B. Adams (1970), Asteroid Vesta - spectral reflectivity and compositional implications, *Science*, *168*(3938), 1445.

McDonough, W. F., and S. S. Sun (1995), The composition of the Earth, *Chemical Geology*, *120*(3-4), 223–253.

McKay, G., L. Le, and J. Wagstaff (1991), Constraints on the origin of the mare basalt europium anomaly: REE partition coefficients for pigeonite., *Lunar and Planetary Science Conference*, pp. 883–884.

McSween, H. Y., D. W. Mittlefehldt, A. W. Beck, T. McCoy, S. Marchi, M. C. De-Sanctis, E. Ammannito, C. A. Raymond, and C. T. Russell (2013a), DAWN and the Vesta-HED connection, *43rd Lunar and Planetary Science Conference*.

McSween, H. Y., E. Ammannito, V. Reddy, T. H. Prettyman, A. W. Beck, M. C. De Sanctis, A. Nathues, L. Le Corre, D. P. O'Brien, N. Yamashita, T. J. McCoy, D. W. Mittlefehldt, M. J. Toplis, P. Schenk, E. Palomba, D. Turrini, F. Tosi, F. Zambon, A. Longobardo, F. Capaccioni, C. A. Raymond, and C. T. Russell (2013b), Composition of the Rheasilvia basin, a window into Vesta's interior, *Journal of Geophysical Research-Planets*, *118*(2), 335–346.

Mittlefehldt, D. W. (1994), ALH84001, a cumulate orthopyroxenite member of the Martian meteorite clan, *Meteoritics*, *29*(2), 214–221.

Mittlefehldt, D. W. (2015), Asteroid (4) Vesta: I. the howardite-eucrite-diogenite (HED) clan of meteorites, *Chemie Der Erde-Geochemistry*, *75*(2), 155–183.

Mittlefehldt, D. W., A. W. Beck, C. T. A. Lee, H. Y. Mcsween, and P. C. Buchanan (2012), Compositional constraints on the genesis of diogenites, *Meteoritics and Planetary Science*, *47*(1), 72–98.

Morgan, J. W., H. Higuchi, H. Takahashi, and J. Hertogen (1978), Chondritic eucrite parent body - inference from trace-elements, *Geochimica et Cosmochimica Acta*, *42*(1), 27–38.

Nagasawa, H. (1966), Trace element partition coefficient in ionic crystals, *Science*, *152*(3723), 767.

Nesvorny, D., F. Roig, B. Gladman, D. Lazzaro, V. Carruba, and T. Mothe-Diniz (2008), Fugitives from the Vesta family, *Icarus*, *193*(1), 85–95.

Neumann, W., D. Breuer, and T. Spohn (2014), Differentiation of Vesta: Implications for a shallow magma ocean, *Earth and Planetary Science Letters*, *395*, 267–280.

Norris, T. L., A. J. Gancarz, D. J. Rokop, and K. W. Thomas (1983), Half-life of ^{26}al, *Journal of Geophysical Research*, *88*, B331–B333.

Onuma, N., H. Higuchi, H. Wakita, and H. Nagasawa (1968), Trace element partition between 2 pyroxenes and host lava, *Earth and Planetary Science Letters*, *5*(1), 47.

Papike, J. J., J. M. Karner, and C. K. Shearer (2005), Comparative planetary mineralogy: Valence state partitioning of Cr, Fe, Ti, and V among crystallographic sites in olivine, pyroxene, and spinel from planetary basalts, *American Mineralogist*, *90*(2-3), 277–290.

Park, R. S., A. S. Konopliv, S. W. Asmar, B. G. Bills, R. W. Gaskell, C. A. Raymond, D. E. Smith, M. J. Toplis, and M. T. Zuber (2014), Gravity field expansion in ellipsoidal harmonic and polyhedral internal representations applied to Vesta, *Icarus*, *240*, 118–132.

Pouchou, J. L., and F. Pichoir (1991), Quantitative-analysis of homogeneous or stratified microvolumes applying the model pap, *Electron Probe Quantitation*, pp. 31–75.

Prettyman, T. H., R. C. Reedy, D. W. Mittlefehldt, N. Yamashita, D. J. Lawrence, A. W. Beck, W. C. Feldman, T. J. McCoy, H. Y. McSween, M. J. Toplis, O. Forni, H. Mizzon, C. A. Raymond, C. T. Russell, C. A. Polanskey, S. P. Joy, J. Mafi, and D. S. Team (2012), For a few howardites more: Grand maps the elemental composition of Vesta, *Meteoritics and Planetary Science*, *47*, A322–A322.

Rambaux, N. (2013), The rotational motion of Vesta, *Astronomy and Astrophysics*, *556*.

Righter, K., and M. J. Drake (1997), A magma ocean on Vesta: Core formation and petrogenesis of eucrites and diogenites, *Meteoritics and Planetary Science*, *32*(6), 929–944.

Righter, K., and D. P. O'Brien (2011), Terrestrial planet formation, *Proceedings of the National Academy of Sciences of the United States of America*, *108*(48), 19,165–19,170.

Ringwood, A. E. (1955), The principles governing trace element distribution during magmatic crystallization .1. the influence of electronegativity, *Geochimica et Cosmochimica Acta*, *7*(3-4), 189–202.

Roeder, P. L., and R. F. Emslie (1970), Olivine-liquid equilibrium, *Contributions to Mineralogy and Petrology*, *29*(4), 275.

Rugel, G., T. Faestermann, K. Knie, G. Korschinek, M. Poutivtsev, D. Schumann, N. Kivel, I. Gunther-Leopold, R. Weinreich, and M. Wohlmuther (2009), New measurement of the ^{60}fe half-life, *Physical Review Letters*, *103*(7).

Russell, C. T., C. A. Raymond, A. Coradini, H. Y. McSween, M. T. Zuber, A. Nathues, M. C. De Sanctis, R. Jaumann, A. S. Konopliv, F. Preusker, S. W. Asmar, R. S. Park, R. Gaskell, H. U. Keller, S. Mottola, T. Roatsch, J. E. C. Scully, D. E. Smith, P. Tricarico, M. J. Toplis, U. R. Christensen, W. C. Feldman, D. J. Lawrence, T. J. McCoy, T. H. Prettyman, R. C. Reedy, M. E. Sykes, and T. N. Titus (2012), Dawn at Vesta: Testing the protoplanetary paradigm, *Science*, *336*(6082), 684–686.

Ruzicka, A., G. A. Snyder, and L. A. Taylor (1997), Vesta as the howardite, eucrite and diogenite parent body: Implications for the size of a core and for large-scale differentiation, *Meteoritics and Planetary Science*, *32*(6), 825–840.

Sack, R. O., I. S. E. Carmichael, M. Rivers, and M. S. Ghiorso (1980), Ferric-ferrous equilibria in natural silicate liquids at 1bar, *Contributions to Mineralogy and Petrology*, *75*(4), 369–376.

Sack, R. O., W. J. Azeredo, and M. E. Lipschutz (1991), Olivine diogenites - the mantle of the eucrite parent body, *Geochimica et Cosmochimica Acta*, *55*(4), 1111–1120.

Sarafian, A. R., S. G. Nielsen, H. R. Marschall, F. M. McCubbin, and B. D. Monteleone (2014), Early accretion of water in the inner solar system from a carbonaceous chondrite-like source, *Science*, *346*(6209), 623–626.

Scheinberg, A., R. R. Fu, L. T. Elkins-Tanton, and B. P. Weiss (2015), *Asteroid Differentiation: Melting and Large-Scale Structure*, Asteroids IV, University of Arizona Press.

Schenk, P., D. P. O'Brien, S. Marchi, R. Gaskell, F. Preusker, T. Roatsch, R. Jaumann, D. Buczkowski, T. McCord, H. Y. McSween, D. Williams, A. Yingst, C. Raymond, and C. Russell (2012), The geologically recent giant impact basins at Vesta's south pole, *Science*, *336*(6082), 694–697.

Schiller, M., J. Baker, J. Creech, C. Paton, M. A. Millet, A. Irving, and M. Bizzarro (2011), Rapid timescales for magma ocean crystallization on the Howardite-Eucrite-Diogenite parent body, *Astrophysical Journal Letters*, *740*(1).

Schwandt, C. S., and G. A. McKay (1998), Rare earth element partition coefficients from enstatite/melt synthesis experiments, *Geochimica et Cosmochimica Acta*, *62*(16), 2845–2848.

Shannon, R. D. (1976), Revised effective ionic-radii and systematic studies of interatomic distances in halides and chalcogenides, *Acta Crystallographica Section A*, *32*(Sep1), 751–767.

Shaw, D. M. (1970), Trace element fractionation during anatexis, *Geochimica et Cosmochimica Acta*, *34*(2), 237.

Shearer, C. K., G. W. Fowler, and J. J. Papike (1997), Petrogenetic models for magmatism on the eucrite parent body: Evidence from orthopyroxene in diogenites, *Meteoritics and Planetary Science*, *32*(6), 877–889.

Shearer, C. K., P. Burger, and J. J. Papike (2010), Petrogenetic relationships between diogenites and olivine diogenites: Implications for magmatism on the HED parent body, *Geochimica Et Cosmochimica Acta*, *74*(16), 4865–4880.

Shukolyukov, A., and G. W. Lugmair (1993), ^{60}fe in eucrites, *Earth and Planetary Science Letters*, *119*(1-2), 159–166.

Smith, P. M., and P. D. Asimow (2005), Adiabat_1ph: A new public front-end to the MELTS, pMELTS, and pHMELTS models, *Geochemistry Geophysics Geosystems*, *6*.

Srinivasan, G., J. N. Goswami, and N. Bhandari (1999), ^{26}al in eucrite Piplia Kalan: Plausible heat source and formation chronology, *Science*, *284*(5418), 1348–1350.

Stolper, E. (1975), Petrogenesis of Eucrite, Howardite and Diogenite meteorites, *Nature*, *258*(5532), 220–222.

Stolper, E. (1977), Experimental petrology of eucritic meteorites, *Geochimica et Cosmochimica Acta*, *41*(5), 587–611.

Stolper, E. (1979), Trace-elements in Shergottite meteorites - implications for the origins of planets, *Earth and Planetary Science Letters*, *42*(2), 239–242.

Sun, C. G., and Y. Liang (2013), Distribution of REE and HFSE between low-Ca pyroxene and lunar picritic melts around multiple saturation points, *Geochimica et Cosmochimica Acta*, *119*, 340–358.

Takeda, H. (1997), Mineralogical records of early planetary processes on the howardite, eucrite, diogenite parent body with reference to Vesta, *Meteoritics and Planetary Science*, *32*(6), 841–853.

Takeda, H., and A. L. Graham (1991), Degree of equilibration of eucritic pyroxenes and thermal metamorphism of the earliest planetary crust, *Meteoritics*, *26*(2), 129–134.

Thomas, P. C., R. P. Binzel, M. J. Gaffey, A. D. Storrs, E. N. Wells, and B. H. Zellner (1997), Impact excavation on asteroid 4 Vesta: Hubble Space Telescope results, *Science*, *277*(5331), 1492–1495.

Tkalcec, B. J., and F. E. Brenker (2015), Plastic deformation of olivine-rich diogenites and implications for mantle processes on the diogenite parent body., *Meteoritics and Planetary Science*, *49*(7), 1202–1213.

Toplis, M. J., H. Mizzon, M. Monnereau, O. Forni, H. Y. McSween, D. W. Mittlefehldt, T. J. McCoy, T. H. Prettyman, M. C. De Sanctis, C. A. Raymond, and C. T. Russell (2013), Chondritic models of 4 Vesta: Implications for geochemical and geophysical properties, *Meteoritics and Planetary Science*, *48*(11), 2300–2315.

Touboul, M., P. Sprung, S. M. Aciego, B. Bourdon, and T. Kleine (2015), Hf-W chronology of the eucrite parent body, *Geochimica et Cosmochimica Acta*, *156*, 106–121.

van Kan Parker, M., A. Liebscher, D. Frei, J. van Sijl, W. van Westrenen, J. Blundy, and G. Franz (2010), Experimental and computational study of trace element distribution between orthopyroxene and anhydrous silicate melt: substitution mechanisms and the effect of iron, *Contributions to Mineralogy and Petrology*, *159*(4), 459–473.

van Kan Parker, M., P. R. D. Mason, and W. van Westrenen (2011), Experimental study of trace element partitioning between lunar orthopyroxene and anhydrous silicate melt: Effects of lithium and iron, *Chemical Geology*, *285*(1-4), 1–14.

Warren, P. H., and G. W. Kallemeyn (2001), Eucrite Bluewing 001: A Stannern-like bulk composition and its linkage with other unequilibrated HED basalts, *32nd Lunar and Planetary Science Conference*.

Warren, P. H., G. W. Kallemeyn, H. Huber, F. Ulff-Moller, and W. Choe (2009), Siderophile and other geochemical constraints on mixing relationships among HED-meteoritic breccias, *Geochimica et Cosmochimica Acta*, *73*(19), 5918–5943.

Weill, D. F., and G. A. McKay (1975), The partitioning of Mg, Fe, Sr, Ce, Sm, Eu and Yb in lunar igneous systems and a possible origin of KREEP by equilibrium partial melting, *Proceedings of Lunar and Planetary Science*, pp. 1143–1158.

Weiss, B. P., L. T. Elkins-Tanton, M. A. Barucci, H. Sierks, C. Snodgrass, J. B. Vincent, S. Marchi, P. R. Weissman, M. Patzold, I. Richter, M. Fulchignoni, R. P. Binzel, and R. Schulz (2012), Possible evidence for partial differentiation of asteroid Lutetia from Rosetta, *Planetary and Space Science*, *66*(1), 137–146.

Williams, D. A., R. A. Yingst, and W. B. Garry (2014), Introduction: The geologic mapping of Vesta, *Icarus*, *244*, 1–12.

Wilson, L., and K. Keil (2012), Volcanic activity on differentiated asteroids: A review and analysis, *Chemie Der Erde-Geochemistry*, *72*(4), 289–321.

Wolfram Research, I. (2012), *Mathematica*, version 9. ed., Wolfram Research, Inc., Champaign, Illinois.

Wood, B., and J. Blundy (2003), Trace element partitioning under crustal and uppermost mantle conditions: The influences of ionic radius, cation charge, pressure, and temperature, *Treatise on Geochemistry, Volume 2.*, *2*, 568.

Wood, B., and D. Fraser (1976), *Elementary Thermodynamics for Geologists*, Oxford University Press, Oxford University Press.

Yamaguchi, A., G. J. Taylor, and K. Keil (1996), Global crustal metamorphism of the eucrite parent body, *Icarus*, *124*(1), 97–112.

Yamaguchi, A., J. A. Barrat, R. C. Greenwood, N. Shirai, C. Okamoto, T. Setoyanagi, M. Ebihara, I. A. Franchi, and M. Bohn (2009), Crustal partial melting on vesta: Evidence from highly metamorphosed eucrites, *Geochimica et Cosmochimica Acta*, *73*(23), 7162–7182.

Yao, L. J., C. G. Sun, and Y. Liang (2012), A parameterized model for REE distribution between low-Ca pyroxene and basaltic melts with applications to REE partitioning in low-Ca pyroxene along a mantle adiabat and during pyroxenite-derived melt and peridotite interaction, *Contributions to Mineralogy and Petrology*, *164*(2), 261–280.

Yingst, R. A., S. C. Mest, D. C. Berman, W. B. Garry, D. A. Williams, D. Buczkowski, R. Jaumann, C. M. Pieters, M. C. De Sanctis, A. Frigeri, L. Le Corre, E. Preusker, C. A. Raymond, V. Reddy, C. T. Russell, T. Roatsch, and P. M. Schenk (2014), Geologic mapping of Vesta, *Planetary and Space Science*, *103*, 2–23.

Zolensky, M. E., M. K. Weisberg, P. C. Buchanan, and D. W. Mittlefehldt (1996), Mineralogy of carbonaceous chondrite clasts in HED achondrites and the Moon, *Meteoritics and Planetary Science*, *31*(4), 518–537.

Zou, H. (2007), *Quantitative Geochemistry*, Imperial College Press.

Zuber, M. T., H. Y. McSween, R. P. Binzel, L. T. Elkins-Tanton, A. S. Konopliv, C. M. Pieters, and D. E. Smith (2011), Origin, internal structure and evolution of 4 Vesta, *Space Science Reviews*, *163*(1-4), 77–93.

Appendix A

Data Tables

This appendix contains all of the experimental data presented in different tables. Most of the data has been plotted in figures throughout the rest of the thesis.

The pyroxene cation allocation shown in Table A.6 was done in the following method: The chemical compositions of the experimental pyroxene compositions were recalculated from weight percent oxides into cation proportions in the different mineral sites (mineral formula calculation. This was done in several steps:

1. Divide the oxide weight % by formal weight of the oxide to get mole proportions.
2. Multiply this 'mole number' by number of oxygens in the oxide formula.
3. Multiply this 'oxygen number' by the number of oxygens/oxygen number.
4. Multiply this 'normalised oxygen number' by number of cations.

The cations are then allocated to their probable crystallographic sites. Silicon is assigned to the T site, which is then filled by Al. The remaining Al is then assigned to M1. Cr and Ti are assigned to M1, and Mn, Ca and Na to M2. The Fe and Mg are then split between M1 and M2, in a proportion dependent on the Mg#.

Table A.1: Major element compositions of the start compositions in wt. % oxides

	HAPM2	HA3	HA4	HA5	HA6	HA7	HA8	HA10	HA11
SiO_2	44.83	51.09	52.39	51.93	50.63	52.29	52.38	53.11	51.09
TiO_2	0.58	0.00	0.02	0.06	1.51	0.07	0.01	0.69	0.00
Al_2O_3	3.59	5.23	6.67	9.67	9.55	11.91	7.18	11.03	5.23
FeO	14.26	15.45	15.41	16.91	14.33	15.90	15.49	15.95	15.45
MnO	0.41	0.10	0.08	0.07	0.46	0.06	0.09	0.41	0.10
MgO	31.02	22.60	15.99	10.15	13.34	6.02	15.99	9.37	22.60
CaO	2.99	4.60	6.33	8.60	7.87	10.38	6.26	9.63	4.60
Na_2O	0.01	0.58	0.02	0.02	0.04	0.06	0.01	0.00	0.58
Cr_2O_3	0.24	0.57	0.17	0.05	0.36	0.13	0.12	0.20	0.57
Ni_2O	0.52	0.10	0.13	0.15	0.08	0.02	0.17	0.23	0.10
Total	98.46	100.30	97.21	97.62	98.17	96.85	97.69	100.62	100.30

	Starting Composition	fO_2	runtime	Phases	Final Temperature	Cooling Rate	Mode Melt	Mode Olivine	Mode Pyroxene	Mode Feldspar	Temperature Profile
HAPM1_01	PM1	IW+1.8	3	Ol, Gl	1450		0.55	0.47			800 +1450
HAPM1_02	PM1	IW+1.8	3	Ol, Gl	1400		0.48	0.54			800 +1400
HAPM1_03	10 % Ol 90% Melt (HAPM1_02)	IW+1.8	3		1450						800+1450
HAPM1_04	10 % Ol 90% Melt (HAPM1_02)	IW+1.8	3	Ol, Gl	1400		0.37	0.68			800+1400
HAPM2_01	PM2	IW+1.8	3	Ol, Gl	1500		0.65	0.35			800+1500
HAPM2_02	PM2	IW+1.8	3	Ol, Gl	1450		0.54	0.46			800+1450
HAPM2_03	10 % Ol 90 % Melt HA2_02	IW+1.8	3	Ol, Gl	1450		0.93	0.07			850+1450
HAPM2_04	PM2	IW+1.8	3	Ol, Gl	1400		0.52	0.48			800+1400
HAPM2_05	PM2	IW+1.8	3	Ol, Gl	1350		0.45	0.55			850+1350
HAPM2_06	20 % ol 80 %Melt HAPM2_02	IW+1.8	72	Ol, Pyx, Gl	1350		0.68	0.30	0.02		850+1350
HAPM2_07	20 % ol 80 %Melt HAPM2_02	IW+1.8	72	Gl	1575		1.00				850+1575
HAPM2_08	20 % ol 80 %Melt HAPM2_02	IW+1.8	24	Ol, Pyx, Gl	1300		0.53	0.29	0.18		850+1300
HAPM2_09	PM2	IW+1.8	136	Ol, Gl, Sp	1350	0.80	0.48	0.52			800+1350+1400-1350
HAPM2_12	PM2	IW+1.8	1	Ol, Gl	1600		0.94	0.60			850+1600
HAPM2_13	PM2	Air	0.16	Gl	1650		1.00				800+1500+1650
HAPM2_14	PM2	Air	0.16	Gl	1650		1.00				800+1500+1650
HAPM2_15	PM2	IW+1.8	96	Ol, Gl, Pyx, Sp	1300	0.80	0.37	0.53	0.10		800+1300+1350-1300
HAPM2_16	PM2	IW+1.8	96	Ol, Gl, Pyx, Sp	1300	0.80	0.37	0.53	0.10		800+1300+1350-1300
HA3_01	15 % Pyx 15 % Ol 70 % Melt HAPM2_06	IW+1.8	24	Ol, Pyx, Gl	1350		0.75	0.07	0.19		800+1350
HA3_02	15 % Pyx 15 % Ol 70 % Melt HAPM2_06	IW+1.8	24	Ol, Pyx, Gl	1350		0.74	0.08	0.18		850+1350
HA3_03	15 % Pyx 15 % Ol 70 % Melt HAPM2_06	IW+1.8	48	Ol, Pyx, Gl	1350		0.75	0.06	0.19		800+1350
HA3_04	15 % Pyx 15 % Ol 70 % Melt HAPM2_06	IW+1.8	5	Gl	1575		1.00				850+1575
HA3_05	15 % Pyx 15 % Ol 70 % Melt HAPM2_06	IW+1.8	10	Gl	1575		1.00				850+1575
HA3_06	15 % Pyx 15 % Ol 70 % Melt HAPM2_06	IW+1.8	24	Gl, Pyx, Ol	1350	1.20	0.74	0.07	0.19		850+1400-1350
HA4_01	Melt composition from HA3_06	IW+1.8	24	Melt	1350		1.00				850+1350
HA4_02	Melt composition from HA3_06	IW+1.8	24	Gl,Pyx	1300		0.84		0.16		850+1300
HA4_03	Melt composition from HA3_06	IW+1.8	24	Gl	1350		1.00		0.00		850+1350

Table A.2: Experimental Run Conditions. Temperatures are given in ^{o}C, modes are calculated from mass.

	Starting Composition	fO_2	runtime	Phases	Final Temperature	Cooling Rate	Mode Melt	Mode Olivine	Mode Pyroxene	Mode Feldspar	Temperature Profile
HA4.04	Melt composition from HA3.06	IW+1.8	24	Melt, Pyx	1250						850+1250
HA4.05	Melt composition from HA3.06	IW+1.8	70	Melt, Pyx	1250	5.00	0.73		0.27		850+1350-1250
HA4.06	Melt composition from HA3.06	IW+1.8	165	Melt, Pyx	1150	5					850+1350-1150
HA4.07	Melt composition from HA3.06	IW+1.8	20	Melt, Pyx	1200	8.3					850+1350-1200
HA4.08	Melt composition from HA3.06	IW+1.8	69.5	Pyx, Gl, Feldspar	1150						800+1150
HA4.09	Melt composition from HA3.06	IW+1.8	70	Pyx, Gl	1150	5					800+1150+1200-1150+1200-1150
HA5.01	Melt Composition from HA4.05	IW+1.8	66.5	Pyx, Gl	1150	5.00	0.79		0.21		800+1350-1250-1150
HA5.02	Melt Composition from HA4.05	IW+1.8	70	Pyx, Gl	1150	5.00	0.80		0.20		800+1350-1250-1150
HA7.01	Melt Composition from HA5.01	IW+1.8	120	pyx,Melt	1150	1.00	0.96		0.04		800+1175-1150
HA7.02	Melt Composition from HA5.01	IW+1.8	86	Pyx,Melt,Feldspar	1125	1.00	0.90		0.09	0.01	800+1175-1125
HA7.03	Melt Composition from HA5.01	IW+1.8	48	Pyx,Melt,Feldspar	1125	2.50	0.76		0.16	0.08	800+1170-1125+1170-1125
HA6.01	HA6	IW+1.8	17	Melt	1300		1				800+1300
HA6.03	HA6	IW+1.8	70	Pyx,Melt,Sp	1150	1.50	0.68		0.32		800+1300-1150+1200-1150
HA6.04	HA6	IW+1.8	90	Pyx,Melt	1250	500.00	0.9		0.1		800+1350-1250
HA8.01	HA8	IW+1.8	42	Pyx, Melt	1300	5.00	0.84		0.16		800+1350-1300
HA8.02	HA8	IW+1.8	5	Melt	1450		1.00				800+1450
HA8.03	HA8	IW+1.8	89	Pyx, Melt,Sp	1300	5.00	0.84		0.16		800+1350-1300
HA8.04	HA8	IW+1.8	21	Pyx, Melt	1300	5.00	0.84		0.16		800+1250+1300-1250
HA8.05	HA8	IW+1.8	72	Pyx, Melt	1250	5.00					800+1250+1300-1250
HA8.06	HA8	IW+1.8	97	Pyx, Melt	1200	5	0.50		0.50		800+1200+1250-1200
HA8.07	HA8	IW+1.8	141	Pyx, Melt	1115	2.5					800+1450-1115+1130-1115
HA10.01	HA10	IW+1.8	48	Pyx, Melt	1200	0.80	0.94		0.06		800+1300-1230-1200
HA10.02	HA10	IW+1.8	96	Pyx, Melt	1200	1.50	0.93		0.07		800+1300-1230-1200+1215-1200
HA10.03	HA10	IW+1.8	72	Pyx, Melt	1175	1.50	0.88		0.12		800+1300-1280-1200+1215-1200
HA11.01	HA11	IW+1.8	72	Melt	1200	1.50	1.00				800+1300-1200
HA11.02	HA11	IW+1.8	72	Pyx,Melt	1170	2.50	0.97		0.03		800+1200-1170+1200-1170
HA11.03	HA11	IW+1.8	72	Pyx,Melt,Feldspar	1140	2.00	0.62		0.18	0.18	800+1300-1170-1140+1170-1140

Experiment	HAPM1_01	HAPM1_01	HAPM1_02	HAPM1_02	HAPM1_4	HAPM1_4	HAPM2_01
Phase	Melt	Olivine	Melt	Olivine	Melt	Olivine	Melt
T (°C)	1450	1450	1400	1400	1400	1400	1500
n	3	3	3	3	3	3	15
mode	55	47	48	54	37	68	65
SiO_2	43.70	36.87	44.25	36.75	44.21	37.85	47.60
TiO_2							
Al_2O_3	5.61	0.00	6.41	0.01	6.19	0.01	4.94
Cr_2O_3							
FeO*	26.25	18.01	25.32	19.90	24.29	19.49	16.32
MnO							
MgO	17.70	41.62	15.36	40.32	15.57	39.32	23.70
CaO	4.84	0.19	5.59	0.19	5.70	0.22	4.12
Na_2O							
NiO							0.26
Total	98.09	96.88	96.63	97.17	95.95	96.89	96.94
Mg#	0.55	0.80	0.52	0.78	0.53	0.78	0.72
Wo							
En							
Fs							
Error							
SiO_2	0.29	0.18	1.21	1.22	0.05	0.53	0.32
TiO_2							
Al_2O_3	0.16	0.00	0.38	0.00	0.02	0.01	0.13
Cr_2O_3							
FeO*	0.22	0.15	0.06	0.07	0.13	0.23	0.35
MnO							
MgO	0.13	0.09	0.35	0.16	0.17	0.29	0.26
CaO	0.01	0.03	0.03	0.01	0.11	0.02	0.05
Na_2O							
NiO							0.02

Experiment	HAPM2_01	HAPM2_02	HAPM2_02	HAPM2_03	HAPM2_03	HAPM2_04	HAPM2_04
Phase	Olivine	Melt	Olivine	Melt	Olivine	Melt	Olivine
T (°C)	1500	1450	1450	1450	1450	1400	1400
n	5	9	3	9		5	3
mode	35	54	46	58	42	52	48
SiO_2	40.43	49.08	39.84	49.08	40.22	50.52	39.84
TiO_2							
Al_2O_3	0.04	5.81	0.03	5.95	0.01	6.51	0.03
Cr_2O_3							
FeO*	10.66	16.84	11.98	16.69	12.34	16.21	13.62
MnO							
MgO	46.96	20.37	45.45	21.10	46.75	18.46	44.90
CaO	0.02	4.97	0.04	5.24	0.04	5.55	0.03
Na_2O							
NiO	0.41	0.25	0.23	0.05	0.32		
Total	98.52	97.31	97.57	98.11	99.69	97.25	98.42
Mg#	0.89	0.68	0.87	0.69	0.87	0.66	0.85
Wo							
En							
Fs							
Error							
SiO_2	0.10	0.75	0.11	0.19	0.13	0.37	0.49
TiO_2							
Al_2O_3	0.02	0.11	0.01	0.05	0.01	0.06	0.01
Cr_2O_3							
FeO*	0.09	0.26	0.18	0.17	0.14	0.06	0.03
MnO							
MgO	0.42	0.35	0.17	0.11	0.36	0.20	0.51
CaO	0.01	0.04	0.02	0.06	0.01	0.04	0.00
Na_2O							
NiO	0.04	0.07	0.05	0.01	0.03		

Table A.3: Major element compositions of Experimental charges (wt. % oxides). Phase modes were calculated by mass, n = number of analysis per phase.

Experiment	HAPM2_05	HAPM2_05	HaPM2_09	HaPM2_09	HAPM2_12	HAPM2_12	HAPM2_13
Phase	Melt	Olivine	Melt	Olivine	Melt	Olivine	Melt
T (^{o}C)	1350	1350	1350	1350	1600	1600	1650
n	10	2	8	10	7	8	10
mode	45	55	48	52	94	6	1
SiO_2	52.98	39.25	51.50	39.67	45.46	41.10	44.83
TiO_2			1.19	0.01	0.61	0.01	0.58
Al_2O_3	7.30	0.07	7.33	0.03	3.78	0.03	3.59
Cr_2O_3			0.12	0.58	0.38	0.89	0.52
FeO*	15.15	14.66	14.54	13.68	14.73	7.83	14.26
MnO			0.45	0.35	0.40	0.22	0.41
MgO	16.21	43.58	16.19	44.67	29.67	49.69	31.02
CaO	6.41	0.04	6.03	0.14	2.97	0.11	2.99
Na_2O			0.01	0.01	0.01	0.00	0.01
NiO							
Total	98.06	97.60	98.05	99.47	98.71	100.05	98.66
Mg#	0.66	0.84	0.66	0.85	0.78	0.92	0.80
Wo							
En							
Fs							
Error							
SiO_2	0.22	0.44	0.18	0.26	0.25	0.23	0.45
TiO_2			0.03	0.01	0.02	0.01	0.03
Al_2O_3	0.05	0.07	0.06	0.02	0.06	0.01	0.03
Cr_2O_3			0.02	0.01	0.02	0.02	0.04
FeO*	0.26	0.13	0.15	0.16	0.32	0.05	0.22
MnO			0.03	0.02	0.04	0.03	0.05
MgO	0.07	0.28	0.19	0.13	0.27	0.22	0.26
CaO	0.05	0.02	0.06	0.02	0.07	0.02	0.03
Na_2O			0.01	0.01	0.01	0.01	0.01
NiO			0.03	0.04	0.03	0.06	0.06

Experiment	HAPM2_14	HAPM2_15	HAPM2_15	HAPM2_15	HAPM2_15	HAPM2_16	HAPM2_16
Phase	Melt	Melt	Olivine	Pyroxene	Spinel	Melt	Olivine
T (^{o}C)	1650	1300	1300	1300	1300	1300	1300
n	10	9	11	9	1	8	6
mode	1	37	53	10	1	37	53
SiO_2	44.68	50.63	39.54	56.44	0.03	51.52	39.95
TiO_2	0.56	1.51	0.02	0.12	1.02	1.49	0.02
Al_2O_3	3.51	9.55	0.02	0.65	10.25	9.70	0.02
Cr_2O_3	0.53	0.08	0.67	0.23	56.78	0.10	0.60
FeO*	14.23	14.33	15.55	9.61	19.21	14.28	15.65
MnO	0.40	0.46	0.40	0.35	0.24	0.47	0.41
MgO	31.02	13.34	43.59	31.53	10.98	12.99	42.37
CaO	3.06	7.87	0.18	0.61	0.08	7.52	0.17
Na_2O	0.02	0.04	0.01	0.01	0.00	0.03	0.00
NiO					0.26		
Total	98.38	98.37	100.22	100.16	98.86	98.65	99.44
Mg#	0.80	0.62	0.83	0.85		0.62	0.85
Wo				1.18			
En				84.39			
Fs				14.43			
Error							
SiO_2	0.28	0.49	0.29	0.22		0.39	0.29
TiO_2	0.02	0.04	0.02	0.02		0.04	0.02
Al_2O_3	0.05	0.14	0.01	0.08		0.10	0.01
Cr_2O_3	0.01	0.03	0.06	0.08		0.03	0.02
FeO*	0.41	0.18	0.16	0.20		0.22	0.15
MnO	0.04	0.03	0.02	0.04		0.05	0.04
MgO	0.20	0.18	0.24	0.15		0.20	0.48
CaO	0.05	0.07	0.02	0.05		0.10	0.01
Na_2O	0.02	0.01	0.01	0.01		0.01	0.01
NiO	0.05	0.04	0.06	0.04		0.02	0.04

Table A.3 continued. Major element abundances measured by EPMA.

Experiment	HA2_16	HA3_01	HA3_01	HA3_02	HA3_02	HA3_03	HA3_03
Phase	Pyroxene	Melt	Pyroxene	Melt	Pyroxene	Melt	Pyroxene
T (^{o}C)	1300	1350	1350	1350	1350	1350	1350
n	8	10	7	6	12	9	14
mode	3	75	19	74	18	75	19
SiO_2	57.23	52.34	56.01	52.55	55.59	52.47	57.10
TiO_2	0.14	0.03	0.01	0.01	0.01	0.03	0.00
Al_2O_3	0.75	6.58	0.35	6.74	0.33	6.76	0.38
Cr_2O_3	0.01	0.14	0.16	0.13	0.16	0.13	0.16
FeO*	9.59	15.95	9.50	15.62	9.46	15.86	9.53
MnO	0.35	0.07	0.06	0.08	0.06	0.08	0.05
MgO	30.92	15.83	32.34	15.93	32.34	16.04	32.27
CaO	0.61	6.29	0.47	6.27	0.47	6.27	0.50
Na_2O	0.24	0.28	0.17	0.00	0.34	0.05	0.10
NiO	0.64	0.29	0.64	0.25	0.60	0.17	0.56
Total	100.47	97.80	99.69	97.58	99.38	97.87	100.64
Mg#	0.85	0.64	0.86	0.64	0.86	0.64	0.86
Wo	1.19		0.89		0.89		0.94
En	84.16		85.09		85.14		84.98
Fs	14.64		14.02		13.96		14.08
Error							
SiO_2	0.13	0.80	1.25	0.38	1.27	0.43	0.61
TiO_2	0.01	0.02	0.01	0.01	0.01	0.01	0.01
Al_2O_3	0.11	0.12	0.05	0.09	0.04	0.14	0.13
Cr_2O_3	0.02	0.02	0.03	0.03	0.03	0.02	0.02
FeO*	0.18	0.33	0.15	0.28	0.15	0.26	0.20
MnO	0.03	0.05	0.02	0.02	0.03	0.03	0.02
MgO	0.19	0.32	0.19	0.26	0.30	0.31	0.54
CaO	0.07	0.10	0.02	0.07	0.01	0.13	0.06
Na_2O	0.01	0.55	0.29	0.01	0.33	0.14	0.19
NiO	0.07	0.06	0.05	0.06	0.05	0.04	0.08

Experiment	HA3_06	HA3_06	HA4_02	HA4_02	HA4_05	HA4_05	HA5_01
Phase	Melt	Pyroxene	Melt	Pyroxene	Melt	Pyroxene	Melt
T (^{o}C)	1350	1350	1300	1300	1250	1250	1150
n	5	8	9	8	7	14	7
mode	74	19	84	16	73	27	79
SiO_2	52.38	57.65	52.41	56.31	51.93	56.34	52.29
TiO_2	0.01	0.01	0.04	0.01	0.06	0.01	0.07
Al_2O_3	7.18	0.37	8.40	0.50	9.67	0.57	11.91
Cr_2O_3	0.12	0.17	0.19	0.28	0.15	0.33	0.02
FeO*	15.49	8.60	16.43	11.67	16.91	11.62	15.90
MnO	0.09	0.06	0.08	0.05	0.07	0.07	0.06
MgO	15.99	33.30	12.52	30.32	10.15	29.92	6.02
CaO	6.26	0.24	7.60	0.69	8.60	0.70	10.38
Na_2O	0.01	0.01	0.02	0.00	0.02	0.01	0.06
NiO	0.17	0.36	0.14	0.41	0.05	0.32	0.13
Total	97.69	100.76	97.84	100.24	97.62	99.88	96.85
Mg#	0.65	0.87	0.58	0.82	0.52	0.82	0.42
Wo		0.44		1.33		1.37	
En		86.96		81.16		80.99	
Fs		12.60		17.52		17.64	
Error							
SiO_2	0.33	0.65	0.30	0.61	0.13	0.22	0.33
TiO_2	0.01	0.01	0.02	0.01	0.02	0.01	0.01
Al_2O_3	0.18	0.03	0.07	0.09	0.06	0.05	0.25
Cr_2O_3	0.02	0.03	0.03	0.04	0.02	0.04	0.02
FeO*	0.17	0.16	0.14	0.29	0.21	0.77	0.59
MnO	0.02	0.03	0.03	0.03	0.03	0.03	0.03
MgO	0.14	0.45	0.13	0.30	0.04	0.62	0.08
CaO	0.03	0.03	0.04	0.02	0.08	0.10	0.09
Na_2O	0.01	0.01	0.02	0.01	0.02	0.01	0.02
NiO	0.03	0.03	0.02	0.05	0.03	0.05	0.02

Table A.3 continued. Major element abundances measured by EPMA.

Experiment	HA5_01	HA5_02	HA5_02	HA6_03	HA6_03	HA6_04	HA6_04
Phase	Pyroxene	Melt	Pyroxene	Melt	Pyroxene	Melt	Pyroxene
T (°C)	1150	1150	1150	1150	1150	1250	1250
n	6	7	7	11	6	8	9
mode	21	80	20	68	32	90	10
SiO_2	53.64	51.15	53.61	51.44	54.10	51.34	56.08
TiO_2	0.01	0.06	0.01	2.08	0.37	1.65	0.17
Al_2O_3	1.17	11.87	1.05	13.52	1.95	10.79	0.93
Cr_2O_3	0.11	0.02	0.12	0.12	0.71	0.28	0.69
FeO*	16.59	16.08	17.25	13.70	15.05	14.51	11.48
MnO	0.09	0.06	0.09	0.29	0.44	0.36	0.31
MgO	24.75	6.50	24.24	6.65	25.13	10.47	28.93
CaO	1.77	10.30	1.88	10.78	2.20	8.84	0.98
Na_2O	0.01	0.07	0.01	0.05	0.01	0.03	0.00
NiO	0.50	0.14	0.46	0.02	0.08	0.04	0.12
Total	98.63	96.25	98.73	98.65	100.04	98.31	99.70
Mg#	0.74	0.42	0.71	0.46	0.75	0.56	0.82
Wo	3.59		3.84		4.50		1.95
En	70.06		68.72		71.48		80.20
Fs	26.34		27.44		24.02		17.85
Error							
SiO_2	0.64	0.43	0.44	2.32	0.61	0.24	0.34
TiO_2	0.01	0.03	0.01	0.16	0.06	0.03	0.04
Al_2O_3	0.16	0.55	0.29	0.29	0.41	0.10	0.18
Cr_2O_3	0.03	0.02	0.01	0.03	0.08	0.02	0.12
FeO*	1.16	0.34	0.59	1.31	0.16	0.27	0.23
MnO	0.02	0.03	0.02	0.05	0.05	0.03	0.02
MgO	1.06	0.76	0.85	0.38	0.44	0.08	0.49
CaO	0.23	0.34	0.26	0.31	0.20	0.04	0.09
Na_2O	0.01	0.02	0.01	0.02	0.01	0.01	0.00
NiO	0.10	0.03	0.08	0.02	0.03	0.03	0.03

Experiment	HA7_01	HA7_01	HA7_02	HA7_02	HA7_03	HA7_03	HA7_03
Phase	Melt	Pyroxene	Melt	Pyroxene	Melt	Pyroxene	Feldspar
T (°C)	1150	1150	1125	1125	1125	1125	1125
n	8	6	10	7	5	3	4
mode	96	4	90	9	76	16	8
SiO_2	53.39	54.01	53.04	53.15	52.49	50.37	45.94
TiO_2	0.10	0.03	0.10	0.01	0.15	0.03	0.00
Al_2O_3	12.59	1.29	12.93	1.94	12.62	1.58	30.67
Cr_2O_3	0.14	0.68	0.10	0.74	0.07	0.64	0.01
FeO*	16.16	18.53	15.92	18.39	16.57	22.08	1.29
MnO	0.08	0.10	0.04	0.09	0.10	0.12	0.00
MgO	5.76	22.67	4.98	21.60	4.35	20.24	0.46
CaO	10.91	2.64	11.10	3.05	10.94	3.74	19.02
Na_2O	0.03	0.00	0.04	0.01	0.07	0.01	0.14
NiO	0.02	0.12	0.03	0.11	0.00	0.00	0.00
Total	99.19	100.08	98.27	99.09	97.36	98.81	97.54
Mg#	0.39	0.69	0.36	0.68	0.32	0.62	0.39
Wo		5.43		6.42		7.60	
En		64.84		63.34		57.32	
Fs		29.73		30.24		35.08	
Error							
SiO_2	0.25	0.33	0.41	1.04	0.39	1.39	0.26
TiO_2	0.03	0.02	0.01	0.02	0.01	0.01	0.00
Al_2O_3	0.12	0.31	0.15	0.67	0.11	0.19	0.41
Cr_2O_3	0.03	0.12	0.02	0.12	0.02	0.07	0.01
FeO*	0.21	0.19	0.41	0.52	0.10	0.39	0.05
MnO	0.04	0.04	0.04	0.02	0.04	0.01	0.00
MgO	0.07	0.33	0.07	1.49	0.10	0.27	0.01
CaO	0.08	0.15	0.15	0.56	0.16	0.19	0.03
Na_2O	0.02	0.00	0.01	0.01	0.01	0.02	0.02
NiO	0.02	0.04	0.02	0.05	0.00	0.00	0.00

Table A.3 continued. Major element abundances measured by EPMA.

Experiment	HA8_01	HA8_01	HA8_02	HA8_03	HA8_03	HA8_04	HA8_04
Phase	Melt	Pyroxene	Melt	Melt	Pyroxene	Melt	Pyroxene
T (°C)	1300	1300	1450	1300	1300	1300	1300
n	9	12	17	9	13	11	11
mode	84	16	100	84	16	84	16
SiO_2	51.22	55.33	51.87	50.80	55.34	51.05	55.32
TiO_2	0.53	0.05	0.45	0.54	0.03	0.55	0.04
Al_2O_3	8.17	0.56	6.94	8.12	0.53	8.13	0.48
Cr_2O_3	0.34	0.66	0.50	0.31	0.58	0.34	0.63
FeO*	15.93	10.56	14.93	15.12	10.04	16.10	9.94
MnO	0.39	0.30	0.37	0.37	0.28	0.37	0.28
MgO	12.44	30.07	15.20	12.34	30.06	12.53	30.43
CaO	7.36	0.62	6.25	7.24	0.60	7.36	0.56
Na_2O	0.07	0.02	0.03	0.06	0.01	0.05	0.01
NiO	0.25	0.94	0.35	0.07	0.64	0.31	0.94
Total	96.70	99.12	96.88	94.97	98.11	96.79	98.63
Mg#	0.58	0.84	0.64	0.59	0.84	0.58	0.85
Wo		1.23			1.19		1.10
En		82.52			83.22		83.58
Fs		16.25			15.59		15.32
Error							
SiO_2	0.41	0.44	0.36	0.42	0.40	0.40	0.61
TiO_2	0.04	0.01	0.02	0.02	0.02	0.02	0.03
Al_2O_3	0.08	0.06	0.09	0.11	0.08	0.06	0.07
Cr_2O_3	0.02	0.08	0.03	0.02	0.05	0.02	0.08
FeO*	0.17	0.54	0.16	0.21	0.62	0.17	0.35
MnO	0.03	0.06	0.05	0.03	0.03	0.03	0.04
MgO	0.17	0.52	0.15	0.14	0.50	0.13	0.57
CaO	0.07	0.05	0.08	0.05	0.06	0.05	0.05
Na_2O	0.03	0.03	0.03	0.04	0.01	0.04	0.02
NiO	0.04	0.10	0.04	0.04	0.15	0.05	0.07

Experiment	HA8_06	HA8_07	HA8_05	HA8_05	HA8_06	HA8_07	HA8_07
Phase	Pyroxene	Melt	Melt	Pyroxene	Melt	Pyroxene	Feldspar
T (°C)	1200	1115	1250	1250	1200	1115	1115
n	8	5	10	10	10	10	8
mode	50	27	68	32	50	63	9
SiO_2	53.92	51.84	50.99	54.92	50.67	53.14	46.53
TiO_2	0.12	1.39	0.66	0.07	0.73	0.11	0.02
Al_2O_3	1.52	11.86	9.53	0.89	11.09	1.18	32.45
Cr_2O_3	0.48	0.06	0.20	0.53	0.15	0.54	0.01
FeO*	15.12	14.15	16.36	13.32	15.85	17.51	1.20
MnO	0.43	0.34	0.40	0.39	0.39	0.50	0.05
MgO	25.03	4.82	10.19	27.79	8.19	23.27	0.57
CaO	2.06	10.83	8.65	1.31	9.68	2.29	18.64
Na_2O	0.02	0.09	0.06	0.01	0.07	0.02	0.24
NiO	0.78	0.12	0.17	0.65	0.20	0.75	0.03
Total	99.48	95.50	97.20	99.88	97.01	99.31	99.74
Mg#	0.75	0.38	0.53	0.79	0.48	0.70	0.46
Wo	4.23			2.60		4.74	
En	71.53			76.76		66.98	
Fs	24.24			20.64		28.28	
Error							
SiO_2	0.52	0.53	0.43	0.74	0.52	0.67	0.49
TiO_2	0.09	0.03	0.04	0.04	0.03	0.04	0.03
Al_2O_3	1.32	0.56	0.09	0.68	0.12	0.38	0.91
Cr_2O_3	0.06	0.02	0.02	0.05	0.03	0.08	0.02
FeO*	0.26	0.24	0.22	0.55	0.34	1.08	0.19
MnO	0.04	0.04	0.04	0.05	0.05	0.07	0.04
MgO	1.90	0.09	0.24	1.36	0.12	1.20	0.25
CaO	1.04	0.23	0.11	0.50	0.06	0.68	0.41
Na_2O	0.03	0.05	0.03	0.01	0.02	0.02	0.04
NiO	0.14	0.03	0.04	0.17	0.06	0.10	0.02

Table A.3 continued. Major element abundances measured by EPMA.

Experiment	HA10_01	HA10_01	HA10_02	HA10_02	HA10_03	HA10_03	HA11_01
Phase	Melt	Pyroxene	Melt	Pyroxene	Melt	Pyroxene	Melt
T (^{o}C)	1200	1200	1200	1200	1175	1175	1200
n	2	3	3	4	4	3	4
mode	94	6	93	7	88	12	100
SiO_2	50.12	53.11	50.61	53.11	51.99	54.22	48.68
TiO_2	0.70	0.09	0.69	0.09	0.71	0.07	0.62
Al_2O_3	11.50	1.12	11.47	0.99	12.14	1.11	14.99
Cr_2O_3	0.11	0.43	0.11	0.42	0.08	0.41	0.05
FeO*	15.29	14.16	15.25	14.14	15.48	15.26	14.56
MnO	0.34	0.36	0.31	0.36	0.32	0.37	0.31
MgO	8.33	26.61	8.25	26.90	7.15	25.47	8.60
CaO	9.60	1.45	10.00	1.60	10.57	1.90	8.92
Na_2O	0.01	0.02	0.03	0.00	0.02	0.00	0.09
NiO	0.00	0.00	0.00	0.00	0.00	0.00	0.00
Total	95.99	97.35	96.72	97.61	98.45	98.81	96.83
Mg#	0.49	0.77	0.49	0.77	0.54	0.75	0.51
Wo		2.93		3.19		3.85	
En		74.75		74.77		71.96	
Fs		22.32		22.04		24.19	
Error							
SiO_2	1.08	0.66	0.24	0.65	0.22	1.95	0.49
TiO_2	0.02	0.01	0.02	0.02	0.02	0.02	0.01
Al_2O_3	0.18	0.02	0.08	0.09	0.03	0.07	0.09
Cr_2O_3	0.00	0.01	0.02	0.03	0.01	0.08	0.02
FeO*	0.10	0.13	0.13	0.21	0.19	0.81	0.15
MnO	0.01	0.02	0.02	0.02	0.00	0.03	0.02
MgO	0.11	0.40	0.05	0.28	0.07	1.03	0.06
CaO	0.05	0.04	0.05	0.12	0.04	0.21	0.08
Na_2O	0.00	0.01	0.02	0.01	0.01	0.00	0.03
NiO	0.00	0.00	0.00	0.00	0.00	0.00	0.00

Experiment	HA11_02	HA11_02	HA11_03	HA11_03	HA11_03	HA6_01
Phase	Melt	Pyroxene	Melt	Pyroxene	Feldspar	Melt
T (^{o}C)	1170	1170	1140	1140	1140	1300
n	2	3	6	9	8	8
mode	97	3	62	18	18	100
SiO_2	49.08	53.58	50.98	53.62	45.62	51.59
TiO_2	0.65	0.12	0.94	0.12	0.01	1.52
Al_2O_3	15.38	2.56	13.86	2.67	34.14	9.84
Cr_2O_3	0.04	0.44	0.06	0.39	0.01	0.34
FeO*	14.71	14.21	17.28	15.58	0.63	14.04
MnO	0.32	0.35	0.36	0.35	0.03	0.33
MgO	8.05	26.37	5.88	25.37	0.35	12.53
CaO	9.19	1.27	8.48	1.33	19.00	8.08
Na_2O	0.05	0.01	0.04	0.01	0.12	0.04
NiO	0.00	0.00	0.00	0.00	0.00	0.04
Total	97.48	98.90	97.88	99.45	99.93	98.33
Mg#	0.49	0.77	0.38	0.74	0.49	0.61
Wo		2.58		2.73		
En		74.80		72.35		
Fs		22.62		24.93		
Error						
SiO_2	1.08	1.08	1.15	0.85	1.13	0.34
TiO_2	0.01	0.03	0.05	0.02	0.01	0.06
Al_2O_3	0.18	0.41	0.34	0.76	0.53	0.11
Cr_2O_3	0.01	0.07	0.02	0.08	0.01	0.03
FeO*	0.10	0.22	1.06	1.06	0.06	0.17
MnO	0.03	0.03	0.03	0.02	0.02	0.04
MgO	0.15	0.29	0.13	0.70	0.05	0.08
CaO	0.05	0.04	0.15	0.11	0.30	0.06
Na_2O	0.01	0.02	0.03	0.02	0.03	0.02
NiO	0.00	0.00	0.00	0.00	0.00	0.02

Table A.3 continued. Major element abundances measured by EPMA.

Phase	HA2_16 Melt	HA2_16 Pyx	HA3_01 Melt	HA3_01 Pyx	HA3_02 Melt	HA3_02 Pyx	HA3_03 Melt	HA3_03 Pyx	HA3_06 Melt
n	10	11	4	3	4	3	4	3	6
Sc45			1236.54	382.38	1299.04	366.65	1202.52	336.69	1251.31
Ti47	8026.34	77.43	125.69	13.25	133.40	11.66	126.70	9.98	298.31
Cr53	2305.52	1542.49	730.96	994.35	741.62	1007.81	723.15	960.51	910.26
Mn55	3533.54	3017.39	654.92	451.29	675.99	447.53	665.68	436.56	707.39
Ni60	1004.46	5270.91	2308.07	5188.32	2283.35	5237.50	1617.43	4928.90	391.98
Y89	432.42	4.37	1249.79	57.63	1328.71	26.03	1215.78	22.50	1402.96
Zr90	574.59	2.99							
Nb93	562.96	2.60							
Pr141	395.92	2.00							
Sm152	390.65	2.34							
Yb174	390.62	8.77	1155.79	70.43	1235.15	43.92	1160.54	39.36	1340.99
Ta181	593.33	3.90							
Th232	509.64	4.03							
Hf177	547.86	4.26							
Ce140	382.23	2.04							
La139	409.70	1.87							
Sr88									
Nd142									
Nd143									
Eu153									
Gd155									
Gd156									
Gd158									
Lu175									
U238									
Dy163			1173.85	49.06	1256.73	19.75	1173.56	16.96	1372.63
Ho165			1137.21	52.72	1219.70	23.36	1140.83	20.52	1390.58
V51			1201.58	451.36	1240.83	442.31	1173.85	399.55	1159.28
Standard Error									
Sc45			25.50	28.57	18.23	51.47	50.02	10.62	16.28
Ti47	726.15	23.69	0.43	2.60	4.17	2.37	5.77	0.78	10.29
Cr53	616.14	190.65	6.31	74.80	6.01	44.06	25.05	29.30	20.23
Mn55	293.15	215.96	9.22	4.92	11.08	2.89	22.56	2.33	12.88
Ni60	274.63	301.98	100.17	91.24	194.08	533.11	277.85	150.71	7.88
Y89	34.73	1.35	27.10	29.13	22.49	10.79	58.78	6.19	19.03
Zr90	47.89	2.12							
Nb93	52.86	1.93							
Pr141	30.05	1.45							
Sm152	26.63	1.42							
Yb174	28.28	1.74	19.27	24.86	18.22	12.81	53.41	4.68	21.93
Ta181	65.53	2.98							
Th232	35.63	2.97							
Hf177	45.91	2.37							
Ce140	30.53	1.21							
La139	35.78	1.32							
Sr88									
Nd142									
Nd143									
Eu153									
Gd155									
Gd156									
Gd158									
Lu175									
U238									
Dy163			26.32	28.02	17.04	10.12	58.23	6.05	29.87
Ho165			25.39	27.33	18.86	10.51	53.54	5.41	15.35
V51			19.43	17.35	9.46	47.91	51.21	17.88	21.95

Table A.4: Trace element composition of each phase, measured by LA-ICP-MS. Number of analysis of each charge is shown (n)

	HA3_06	HA3_06	HA4_02	HA4_02	HA4_05	HA4_05	HA6_03	HA6_03	HA6_04
Phase	Olivine	Pyx	Melt	Pyx	Melt	Pyx	Melt	Pyx	Melt
n	4	4	7	6	8	7	9	9	13
Sc45	0.15	480.08	1199.92	329.79	1186.10	431.03			
Ti47	0.06	24.17	117.97	14.21	256.06	27.17	13119.18	1841.38	8955.85
Cr53	0.68	2020.03	707.67	829.25	1084.26	1981.71	844.77	4593.77	1662.20
Mn55	0.79	552.96	654.41	448.24	689.47	569.58	2683.88	3268.48	2489.79
Ni60	6.14	2634.02	1327.55	5253.17	1238.66	3570.74	152.26	767.03	287.26
Y89	0.02	37.10	1250.89	15.95	1242.61	33.14	302.25	23.24	213.78
Zr90							382.19	8.07	276.83
Nb93							449.00	2.33	284.96
Pr141							327.77	1.83	200.81
Sm152							307.22	4.58	201.48
Yb174	0.04	64.88	1177.26	32.71	1204.01	61.77	272.45	38.27	200.38
Ta181							419.43	1.67	290.31
Th232							1.41	0.13	0.92
Hf177							381.07	13.78	276.18
Ce140							351.56	1.54	213.21
La139							351.16	1.04	215.60
Sr88									
Nd142									
Nd143									
Eu153									
Gd155									
Gd156									
Gd158									
Lu175									
U238									
Dy163	0.02	27.66	1199.05	11.15	1212.78	26.92			
Ho165	0.02	35.74	1177.22	14.54	1247.78	34.39			
V51	0.15	622.38	1136.48	342.35	1112.79	539.01			
Standard Error									
Sc45	0.01	83.37	39.18	113.32	32.29	78.40			
Ti47	0.02	3.15	5.78	1.53	10.69	10.61	242.58	296.71	696.58
Cr53	0.06	171.74	25.23	209.31	37.68	274.05	86.04	750.30	147.49
Mn55	0.05	48.99	11.45	105.17	24.13	43.24	102.17	93.48	181.13
Ni60	0.37	426.83	12.40	4406.26	32.79	134.04	27.51	78.51	16.25
Y89	0.01	8.92	37.59	4.84	24.52	9.50	6.54	4.50	13.00
Zr90							15.50	2.63	18.53
Nb93							21.66	1.13	23.46
Pr141							18.08	1.12	14.83
Sm152							17.62	1.28	20.42
Yb174	0.01	13.08	43.14	6.58	33.96	16.40	24.82	8.61	11.82
Ta181							16.62	0.92	18.47
Th232							0.55	0.00	0.14
Hf177							18.60	7.22	17.56
Ce140							21.63	1.12	14.94
La139							15.04	0.48	16.22
Sr88									
Nd142									
Nd143									
Eu153									
Gd155									
Gd156									
Gd158									
Lu175									
U238									
Dy163	0.01	8.11	36.43	4.59	30.57	9.46			
Ho165	0.01	9.11	40.01	4.85	34.76	11.47			
V51	0.02	126.30	28.55	118.20	34.47	86.79			

Table A.4 continued. Trace element abundances measured by LA-ICP-MS.

	HA6_04	HA7_01	HA7_01	HA7_02	HA7_02	HA7_03	HA7_03	HA7_03	HA8_1
Phase	Pyx	Melt	Pyx	Melt	Pyx	Glass	Pyroxene	Feldspar	Melt
n	9	8	6	9	8	19	5	4	10
Sc45		6.22	6.40	7.54	7.18	64.12	92.49	3.00	71.25
Ti47	973.61	497.06	87.44	533.28	102.80	882.13	181.71	30.55	2983.60
Cr53	4749.89	853.19	5213.85	682.38	5497.84	471.12	6693.10	40.29	2277.32
Mn55	2294.22	472.39	686.43	482.76	723.85	632.70	977.41	31.85	2922.86
Ni60	986.31	117.40	830.21	91.37	863.83	84.50	498.66	6.43	2206.11
Y89	7.93	133.68	13.03	135.45	16.48	208.99	28.11	1.63	240.89
Zr90	2.39	176.67	3.14	183.93	5.70	287.45	9.53	1.03	335.27
Nb93	1.02	191.36	0.81	205.13	2.32	504.37	5.45	1.27	450.42
Pr141	0.59	136.36	0.94	143.43	1.85	255.59	4.18	5.60	290.28
Sm152	1.68	134.96	3.11	141.43	4.88	197.35	8.44	3.05	226.30
Yb174	13.61	125.35	19.75	130.06	26.12	97.12	20.77	0.48	112.32
Ta181	0.85	188.84	0.54	198.59	2.23	467.37	7.11	1.31	548.48
Th232	0.03	0.53	0.00	0.60		947.66	13.09	2.30	1104.57
Hf177	5.27	168.12	6.37	173.38	12.49	283.88	18.07	0.94	332.62
Ce140	0.46	147.48	0.83	155.75	1.52	412.24	5.62	9.94	462.03
La139	0.44	141.47	0.41	147.07	1.04	400.32	4.50	11.15	459.53
Sr88						280.85	3.03	287.80	296.19
Nd142						257.38	4.93	5.35	293.71
Nd143						201.84	4.26	3.88	233.59
Eu153						246.01	8.52	117.35	282.86
Gd155						98.03	6.60	1.81	114.13
Gd156						96.96	7.18	0.99	113.96
Gd158						95.06	6.45	1.47	113.85
Lu175						96.31	23.20	0.44	109.83
U238						1010.71	15.52	2.60	1146.95
Dy163									
Ho165									
V51									
Sc45		0.49	2.45	3.50	1.90	3.03	18.57	0.06	1.64
Ti47	142.05	17.92	11.77	31.65	10.68	88.20	36.62	9.18	97.65
Cr53	630.82	64.44	222.82	34.25	524.75	179.33	5103.06	40.79	68.69
Mn55	106.60	20.52	31.68	19.68	60.61	36.58	82.47	8.88	30.09
Ni60	101.75	8.18	46.89	4.46	91.62	22.25	38.68	4.92	112.14
Y89	1.46	3.79	0.38	6.10	1.70	15.15	6.18	0.19	7.41
Zr90	0.87	7.52	0.70	8.41	2.74	20.71	1.02	0.26	10.54
Nb93	0.77	7.56	0.69	7.72	2.84	47.14	4.32	0.56	14.80
Pr141	0.37	5.07	0.46	5.19	2.02	27.25	1.54	0.46	9.21
Sm152	0.85	3.63	0.52	7.39	1.61	18.97	2.13	0.48	6.79
Yb174	2.01	2.17	1.29	5.58	2.10	8.17	4.75	0.15	3.58
Ta181	0.78	5.29	0.46	6.95	2.89	39.61	5.10	0.66	16.96
Th232	0.00	0.10	0.00	0.06	0.00	85.36	12.51	1.44	35.29
Hf177	2.49	6.70	1.06	7.42	3.68	22.96	3.36	0.44	10.20
Ce140	0.51	6.66	0.79	6.97	2.12	45.64	2.99	0.69	15.59
La139	0.46	6.14	0.52	6.69	1.65	37.08	3.00	0.56	14.75
Sr88						28.25	2.58	28.23	10.26
Nd142						27.33	2.20	0.79	10.41
Nd143						19.91	1.29	1.62	6.62
Eu153						23.90	2.62	10.95	8.42
Gd155						8.87	2.13	0.67	3.70
Gd156						8.77	1.65	0.29	4.17
Gd158						8.52	1.53	0.43	3.84
Lu175						7.73	6.72	0.24	3.51
U238						102.58	11.92	1.65	44.52
Dy163									
Ho165									
V51									

Table A.4 continued. Trace element abundances measured by LA-ICP-MS.

	HA8_1	HA8_3	HA8_3	HA8_4	HA8_4	10_01	10_01	10_02	10_02
Phase	Pyroxene	Melt	Pyroxene	Melt	Pyroxene	Melt	Pyx	Melt	Pyx
n	9	9	4	10	9	12	8	12	10
Sc45	20.52	70.58	21.97	70.56	20.85	67.25	48.71	69.27	47.90
Ti47	215.94	2928.22	241.29	2961.76	235.64	3787.60	489.75	3909.56	492.81
Cr53	4003.25	2172.86	3912.90	2245.34	4065.78	1106.10	4011.93	1157.06	4099.62
Mn55	2086.77	2870.11	2112.81	2889.34	2027.34	2380.76	2650.22	2452.10	2591.62
Ni60	7994.89	619.71	5750.57	2510.60	7618.15	992.24	4342.97	980.76	5110.21
Y89	3.99	242.40	5.27	238.09	4.96	226.72	11.40	235.64	11.94
Zr90	1.63	337.14	2.85	331.87	2.63	326.31	3.02	340.13	3.30
Nb93	1.08	447.94	3.13	446.88	2.54	526.97	1.22	552.05	1.48
Pr141	0.60	289.31	1.62	284.79	1.46	262.90	0.79	275.37	0.94
Sm152	0.95	226.72	1.79	222.73	1.56	214.81	2.43	224.66	2.68
Yb174	3.89	114.42	4.30	112.40	4.07	108.24	10.05	112.68	9.93
Ta181	1.39	556.69	3.27	546.99	3.01	517.01	1.26	542.34	1.61
Th232	2.29	1126.52	6.18	1109.65	5.68	1076.94	1.29	1135.40	2.28
Hf177	2.33	339.66	3.70	331.78	3.54	318.23	5.76	330.78	6.18
Ce140	0.85	459.14	2.48	454.72	2.20	432.97	0.90	452.04	1.23
La139	0.70	460.37	2.38	454.68	1.84	432.75	0.56	450.83	0.86
Sr88	0.66	297.59	1.61	295.64	1.36	277.81	0.44	307.33	0.67
Nd142	0.66	292.84	1.94	288.35	1.26	274.86	0.99	288.49	1.28
Nd143	0.82	229.89	1.48	227.59	0.99	215.48	1.04	226.37	1.49
Eu153	1.13	283.25	2.18	279.48	1.81	266.53	2.13	279.63	2.41
Gd155	1.00	114.78	1.25	112.38	1.07	108.28	2.44	114.78	2.99
Gd156	0.88	114.60	0.99	112.88	1.16	108.94	2.15	114.03	2.61
Gd158	0.97	114.91	1.20	113.13	1.17	108.78	2.31	113.67	2.31
Lu175	4.78	112.77	5.45	110.83	5.02	91.05	9.72	95.30	10.10
U238	2.25	1125.96	6.23	1146.55	4.55	1204.99	1.65	1270.88	2.82
Dy163									
Ho165									
V51									
Standard Error									
Sc45	4.72	0.99	5.51	0.74	2.54	1.53	7.76	1.24	2.84
Ti47	40.22	34.62	45.91	41.37	23.25	39.84	74.05	55.94	24.92
Cr53	510.17	34.07	314.85	32.49	290.26	19.01	661.80	16.48	324.99
Mn55	106.38	20.11	130.17	37.39	97.23	26.43	80.09	26.43	108.35
Ni60	207.65	16.75	1041.12	41.36	175.38	9.56	310.56	47.15	424.60
Y89	0.90	2.78	1.04	3.06	1.07	4.44	1.99	3.76	0.63
Zr90	0.57	5.20	0.53	4.97	1.36	6.55	0.65	5.45	0.64
Nb93	0.56	6.12	0.78	6.91	1.31	9.64	0.34	8.04	0.68
Pr141	0.43	3.95	0.37	4.64	1.04	5.78	0.16	4.23	0.36
Sm152	0.32	3.67	0.30	4.22	0.66	5.52	0.57	3.30	0.49
Yb174	0.66	1.52	0.94	2.09	0.66	3.13	1.59	2.20	0.46
Ta181	0.92	6.68	0.61	8.46	1.73	16.22	0.45	7.33	0.80
Th232	2.30	14.79	1.37	18.92	3.61	33.06	1.03	17.07	1.70
Hf177	0.72	5.68	0.48	6.28	1.21	8.17	1.06	4.79	0.93
Ce140	0.71	6.97	0.67	9.32	1.53	8.57	0.37	6.04	0.54
La139	0.64	7.28	0.61	8.33	1.06	9.48	0.27	6.31	0.62
Sr88	0.45	4.15	0.33	4.56	0.95	5.59	0.18	5.48	0.35
Nd142	0.38	5.46	0.68	5.30	0.62	7.73	0.29	3.98	0.37
Nd143	0.60	5.63	0.59	5.75	0.41	7.14	0.53	6.76	0.58
Eu153	0.45	5.41	0.34	4.49	0.55	7.59	0.58	4.83	0.49
Gd155	0.29	3.45	0.23	2.46	0.34	3.52	0.64	3.70	0.71
Gd156	0.29	1.75	0.15	2.31	0.40	2.89	0.56	3.36	0.62
Gd158	0.44	2.52	0.10	2.45	0.48	3.85	0.83	2.17	0.40
Lu175	0.93	1.95	1.26	2.02	0.96	3.05	1.53	1.68	0.66
U238	2.24	13.67	2.04	20.47	2.39	40.12	1.27	13.49	1.97
Dy163									
Ho165									
V51									

Table A.4 continued. Trace element abundances measured by LA-ICP-MS.

Phase	10_03 Melt	10_03 Pyx	11_01 Melt	11_02 Melt	11_02 Pyroxene	11_03 Melt	11_03 Pyroxene	11_03 Feldspar
n	12	12	10.00	10.00	8.00	10.00	6.00	9.00
Sc45	70.60	54.28	61.67	63.24	80.32	76.67	83.92	3.81
Ti47	4317.09	549.43	3345.82	3554.48	661.42	5149.09	716.30	115.63
Cr53	998.05	4469.44	863.29	687.20	4690.95	591.52	4098.60	50.74
Mn55	2487.24	2715.65	2219.60	2305.11	2535.76	2656.46	2906.29	197.42
Ni60	702.68	6337.85	1216.47	467.36	4339.78	357.29	4757.47	81.23
Y89	252.11	13.26	201.22	216.79	20.35	322.12	21.13	4.65
Zr90	366.43	3.73	287.92	311.21	10.88	465.46	9.47	3.14
Nb93	607.47	0.99	463.66	499.94	5.20	740.56	2.00	5.40
Pr141	302.85	0.83	236.36	256.70	3.14	388.37	1.37	12.18
Sm152	244.77	2.84	191.02	207.88	5.30	316.17	4.18	7.41
Yb174	121.34	11.05	97.35	105.65	17.47	156.98	19.99	1.78
Ta181	591.55	0.93	462.09	507.66	6.26	763.37	2.24	5.43
Th232	1230.00	0.60	952.03	1056.21	10.21	1564.94	2.05	10.54
Hf177	356.38	7.70	284.26	312.92	20.00	467.95	20.20	3.28
Ce140	495.88	0.76	385.42	417.73	4.44	624.14	1.45	21.37
La139	493.10	0.36	384.67	419.57	3.95	627.19	0.70	24.71
Sr88	331.89	0.48	250.64	271.26	2.25	298.58	0.55	462.42
Nd142	316.79	1.61	245.86	266.34	3.28	405.70	1.59	12.66
Nd143	248.09	1.16	194.98	212.33	3.45	322.73	1.93	9.38
Eu153	305.31	2.32	235.25	256.68	4.60	322.35	3.65	256.88
Gd155	126.09	2.70	97.60	106.60	4.47	159.74	4.06	3.35
Gd156	123.97	2.64	98.06	107.21	4.36	160.25	4.26	3.25
Gd158	121.69	2.56	97.65	106.73	4.30	161.11	4.48	3.25
Lu175	101.54	11.14	82.64	89.33	17.44	132.07	19.34	1.42
U238	1386.47	0.74	1064.30	1172.74	12.11	1732.37	2.67	12.36
Dy163								
Ho165								
V51								
Sc45	1.29	5.90	1154.52	758.22	768.01	1734.18	825.45	6198.87
Ti47	141.65	59.42	1.20	1.38	7.18	4.80	6.36	0.00
Cr53	26.34	475.19	36.60	37.44	51.97	428.17	75.04	24.94
Mn55	69.47	98.84	10.19	18.82	534.06	29.76	574.76	40.85
Ni60	39.14	477.96	24.50	27.05	99.48	156.68	242.80	24.92
Y89	4.60	1.47	20.56	11.03	1027.62	53.50	868.62	40.79
Zr90	6.06	0.90	3.46	3.90	2.07	31.08	2.70	1.47
Nb93	18.79	0.26	4.91	5.75	1.33	45.69	2.96	2.29
Pr141	8.49	0.16	5.46	9.10	1.08	71.23	0.78	4.14
Sm152	5.70	0.44	5.48	5.27	0.48	37.08	0.20	1.70
Yb174	2.25	1.36	5.52	5.26	0.55	30.45	1.29	1.22
Ta181	13.00	0.30	2.49	2.52	1.88	14.88	5.07	0.74
Th232	22.03	0.53	10.25	12.79	1.02	78.80	0.93	3.85
Hf177	4.68	2.31	19.86	26.20	2.01	163.33	1.61	7.43
Ce140	15.61	0.15	5.32	7.55	3.16	49.65	7.98	2.41
La139	13.12	0.18	7.53	8.11	0.85	57.07	0.38	2.75
Sr88	9.74	0.22	7.07	8.53	0.84	57.88	0.30	2.83
Nd142	9.45	2.28	5.73	3.94	0.54	5.39	0.28	38.24
Nd143	8.41	0.54	5.80	6.45	0.62	37.33	0.52	1.57
Eu153	10.27	0.45	4.12	4.33	1.21	29.91	0.83	1.37
Gd155	5.01	0.86	6.22	5.53	0.60	18.84	1.85	32.32
Gd156	3.05	0.72	3.25	2.21	0.53	15.87	1.49	0.75
Gd158	3.96	0.60	2.85	2.89	0.35	14.37	1.42	1.07
Lu175	1.83	1.11	2.52	2.84	0.63	15.78	0.97	0.64
U238	47.86	0.77	2.22	2.03	2.22	12.60	4.02	0.65
Dy163			26.37	28.27	3.18	170.82	1.87	8.35
Ho165								
V51								

Table A.4 continued. Trace element abundances measured by LA-ICP-MS.

	HA2_16	HA3_01	HA3_02	HA3_03	HA3_06	HA4_02	HA4_05
Kd							
La	0.0012						
Ce	0.0014						
Pr	0.0019						
Nd							
Sm	0.0045						
Eu							
Gd							
Dy		0.0160	0.0125	0.0136	0.0099	0.0208	0.0158
Ho		0.0207	0.0157	0.0180	0.0131	0.0260	0.0205
Yb	0.0423	0.0419	0.0336	0.0368	0.0286	0.0476	0.0400
Lu							
Y	0.0218	0.0212	0.0166	0.0186	0.0135	0.0259	0.0212
Ti	0.0846	0.1149	0.0980	0.1095	0.1205	0.0913	0.0775
Hf	0.0089						
Zr	0.0050						
Al	0.0771	0.0528	0.0497	0.0565	0.0515	0.0590	0.0592
Cr	1.8798	1.1382	1.2089	1.1926	1.3317	1.4979	2.1386
Sc		0.3428	0.2993	0.3176	0.3127	0.3568	0.3636
Fe	0.6717	0.5955	0.6053	0.6009	0.5552	0.7099	0.6867
Mn	0.7302	0.6936	0.6701	0.7150	0.5920	0.8010	0.7682
Ca	0.0812	0.0752	0.0754	0.0789	0.0377	0.0907	0.0819
Th							
U							
Standard Error							
La	0.0016						
Ce	0.0015						
Pr	0.0014						
Nd							
Sm	0.0018						
Eu							
Gd							
Dy		0.0042	0.0010	0.0022	0.0034	0.0053	0.0035
Ho		0.0044	0.0016	0.0022	0.0034	0.0060	0.0042
Yb	0.0051	0.0054	0.0044	0.0034	0.0047	0.0080	0.0065
Lu							
Y	0.0031	0.0042	0.0018	0.0020	0.0032	0.0058	0.0037
Ti	0.0114	0.0282	0.0333	0.0291	0.0142	0.0350	0.0179
Hf	0.0022						
Zr	0.0027						
Al	0.0111	0.0074	0.0063	0.0186	0.0039	0.0111	0.0047
Cr	1.3290	0.2608	0.3163	0.2170	0.3471	0.3117	0.3355
Sc		0.0277	0.0366	0.0312	0.0457	0.0439	0.0512
Fe	0.0040	0.0121	0.0121	0.0161	0.0137	0.0227	0.0582
Mn	0.0627	0.0294	0.0255	0.0303	0.0353	0.0577	0.0702
Ca	0.0016	0.0101	0.0031	0.0138	0.0056	0.0032	0.0165
Th							
U							

Table A.5: Experimentally derived pyroxene-melt partition coefficients

	HA6_03	HA6_04	HA7_01	HA7_02	HA7_03	HA8_01	HA8_03
Kd							
La	0.0030	0.0021	0.0029	0.0071	0.0112	0.0015	0.0052
Ce	0.0044	0.0022	0.0056	0.0098	0.0136	0.0018	0.0054
Pr	0.0057	0.0030	0.0069	0.0129	0.0164	0.0021	0.0056
Nd					0.0201	0.0029	0.0065
Sm	0.0151	0.0087	0.0231	0.0345	0.0427	0.0042	0.0079
Eu					0.0346	0.0040	0.0077
Gd					0.0698	0.0083	0.0100
Dy							
Ho							
Yb	0.1418	0.0694	0.1569	0.2008	0.2139	0.0346	0.0376
Lu					0.2409	0.0435	0.0483
Y	0.0780	0.0380	0.0976	0.1216	0.1345	0.0166	0.0217
Ti	0.1429	0.1121	0.1759	0.1928	0.1889	0.0724	0.0824
Hf	0.0368	0.0195	0.0380	0.0720	0.0636	0.0070	0.0109
Zr	0.0214	0.0088	0.0177	0.0310	0.0332	0.0049	0.0085
Al	0.1441	0.0865	0.1023	0.1501	0.1253	0.0483	0.0455
Cr	5.5595	2.9618	6.1220	8.0568	9.7836	1.7579	1.8008
Sc					1.4425	0.2880	0.3113
Fe	1.0983	0.7910	1.1463	1.1550	1.3325	0.6191	0.6360
Mn	1.2285	0.9490	1.4463	1.4994	1.2787	0.7139	0.7361
Ca	0.2043	0.1106	0.2422	0.2745	0.3415	0.0806	0.0805
Th					0.0138	0.0021	0.0055
U					0.0154	0.0020	0.0055
Standard Error							
La	0.0014	0.0022	0.0036	0.0112	0.0076	0.0014	0.0013
Ce	0.0033	0.0025	0.0054	0.0136	0.0074	0.0015	0.0015
Pr	0.0035	0.0019	0.0034	0.0141	0.0063	0.0015	0.0013
Nd					0.0078	0.0019	0.0024
Sm	0.0043	0.0044	0.0039	0.0115	0.0115	0.0014	0.0013
Eu					0.0112	0.0016	0.0012
Gd					0.0193	0.0030	0.0014
Dy							
Ho							
Yb	0.0343	0.0105	0.0108	0.0183	0.0521	0.0060	0.0082
Lu					0.0724	0.0086	0.0112
Y	0.0155	0.0071	0.0039	0.0137	0.0311	0.0038	0.0043
Ti	0.0243	0.0166	0.0244	0.0231	0.0916	0.0137	0.0157
Hf	0.0194	0.0092	0.0065	0.0214	0.0129	0.0022	0.0014
Zr	0.0071	0.0033	0.0040	0.0150	0.0043	0.0017	0.0016
Al	0.0302	0.0180	0.0194	0.0284	0.0149		
Cr	1.6834	0.3343	0.9182	1.8221	2.6606		
Sc					0.2975	0.0666	0.0782
Fe	0.1360	0.0276	0.0244	0.0568	0.0247	0.0421	0.0582
Mn	0.0638	0.0472	0.0896	0.1396	0.5362	0.0371	0.0456
Ca	0.0266	0.0138	0.0191	0.0709	0.0179	0.0093	0.0124
Th					0.0133	0.0021	0.0012
U					0.0119	0.0020	0.0018

Table A.5 continued. Calculated $K_d^{pyroxene-melt}$.

	HA8_04	HA10_01	HA10_02	HA10_03	HA11_02	HA11_03
Kd						
La	0.0040	0.0013	0.0019	0.0007	0.0025	0.0011
Ce	0.0048	0.0021	0.0027	0.0015	0.0039	0.0023
Pr	0.0051	0.0030	0.0034	0.0027	0.0057	0.0035
Nd	0.0044	0.0042	0.0055	0.0049	0.0091	0.0050
Sm	0.0070	0.0113	0.0119	0.0116	0.0213	0.0132
Eu	0.0065	0.0080	0.0086	0.0076	0.0139	0.0113
Gd	0.0100	0.0211	0.0231	0.0212	0.0421	0.0266
Dy						
Ho						
Yb	0.0362	0.0929	0.0881	0.0911	0.1814	0.1274
Lu	0.0453	0.1068	0.1060	0.1097	0.2098	0.1464
Y	0.0208	0.0503	0.0507	0.0526	0.0984	0.0656
Ti	0.0796	0.1293	0.1261	0.1273	0.2046	0.1391
Hf	0.0107	0.0181	0.0187	0.0216	0.0688	0.0432
Zr	0.0079	0.0093	0.0097	0.0102	0.0343	0.0203
Al	0.0517	0.0971	0.0861	0.0914	0.1662	0.1928
Cr	1.8108	3.6271	3.5431	4.4782	7.5134	6.9290
Sc	0.2956	0.7243	0.6916	0.7689	1.3823	1.0946
Fe	0.5688	0.9262	0.9268	0.9859	0.9658	0.9016
Mn	0.7017	1.1132	1.0569	1.0918	1.0957	1.0940
Ca	0.0603	0.1512	0.1597	0.1795	0.1374	0.1675
Th	0.0051	0.0012	0.0020	0.0005	0.0022	0.0013
U	0.0040	0.0014	0.0022	0.0005	0.0028	0.0015
Standard Error						
La	0.0010	0.0006	0.0014	0.0004	0.0015	0.0005
Ce	0.0013	0.0009	0.0012	0.0003	0.0014	0.0006
Pr	0.0012	0.0006	0.0013	0.0005	0.0017	0.0006
Nd	0.0016	0.0018	0.0019	0.0047	0.0056	0.0020
Sm	0.0012	0.0027	0.0022	0.0018	0.0013	0.0043
Eu	0.0010	0.0022	0.0018	0.0015	0.0014	0.0058
Gd	0.0014	0.0063	0.0051	0.0059	0.0076	0.0085
Dy						
Ho						
Yb	0.0079	0.0149	0.0044	0.0113	0.0154	0.0345
Lu	0.0105	0.0172	0.0071	0.0111	0.0177	0.0335
Y	0.0041	0.0088	0.0028	0.0059	0.0075	0.0105
Ti	0.0152	0.0196	0.0066	0.0144	0.0101	0.0186
Hf	0.0014	0.0034	0.0028	0.0065	0.0113	0.0177
Zr	0.0015	0.0020	0.0019	0.0025	0.0046	0.0067
Al					0.0270	0.0548
Cr					1.5310	1.0323
Sc	0.0742	0.1165	0.0429	0.0847	0.0991	0.1076
Fe	0.0276	0.0132	0.0201	0.0692	0.0165	0.0825
Mn	0.0442	0.0358	0.0456	0.0501	0.0822	0.1119
Ca	0.0087	0.0054	0.0164	0.0274	0.0235	0.0145
Th	0.0033	0.0010	0.0015	0.0004	0.0011	0.0010
U	0.0021	0.0011	0.0016	0.0006	0.0013	0.0011

Table A.5 continued. Calculated $K_d^{pyroxene-melt}$.

	HA2_16	HA3_01	HA3_02	HA3_03	HA3_06	HA4_02	HA4_05
M2 (VI)							
Si	0.0000	0.0000	0.0000	0.0000	0.0000	0.0000	0.0000
Ti	0.0000	0.0000	0.0000	0.0000	0.0000	0.0000	0.0000
Al	0.0000	0.0000	0.0000	0.0000	0.0000	0.0000	0.0000
Cr	0.0000	0.0000	0.0000	0.0000	0.0000	0.0000	0.0000
Fe3	0.0000	0.0000	0.0000	0.0000	0.0000	0.0000	0.0000
Fe2	0.1432	0.1165	0.0978	0.1383	0.1252	0.1726	0.1736
Mn	0.0104	0.0019	0.0019	0.0014	0.0018	0.0015	0.0020
Mg	0.8231	0.8522	0.8589	0.8348	0.8639	0.7994	0.7969
Ca	0.0230	0.0178	0.0179	0.0185	0.0088	0.0262	0.0268
Na	0.0003	0.0115	0.0235	0.0070	0.0004	0.0003	0.0008
sum	1.0000	1.0000	1.0000	1.0000	1.0000	1.0000	1.0000
ideal	1.0000	1.0000	1.0000	1.0000	1.0000	1.0000	1.0000
M1 (VI)							
Si	0.0000	0.0000	0.0000	0.0000	0.0000	0.0000	0.0000
Ti	0.0036	0.0002	0.0002	0.0001	0.0002	0.0002	0.0003
Al	0.0310	0.0000	0.0000	0.0101	0.0139	0.0164	0.0240
Cr	0.0179	0.0044	0.0045	0.0044	0.0045	0.0078	0.0092
Fe3	0.0000	0.0476	0.0852	0.0000	0.0000	0.0000	0.0000
Fe2	0.1387	0.1156	0.0958	0.1401	0.1242	0.1732	0.1721
Mn	0.0000	0.0000	0.0000	0.0000	0.0000	0.0000	0.0000
Mg	0.7973	0.8454	0.8407	0.8454	0.8571	0.8024	0.7901
Ca	0.0000	0.0000	0.0000	0.0000	0.0000	0.0000	0.0000
Na	0.0000	0.0000	0.0000	0.0000	0.0000	0.0000	0.0000
sum	0.9884	1.0132	1.0263	1.0000	1.0000	1.0000	0.9956
ideal	1.0000	1.0000	1.0000	1.0000	1.0000	1.0000	1.0000
T (IV)							
Si	2.0116	1.9724	1.9598	1.9943	1.9988	1.9957	2.0044
Ti	0.0000	0.0000	0.0000	0.0000	0.0000	0.0000	0.0000
Al	0.0000	0.0144	0.0139	0.0057	0.0012	0.0043	0.0000
Cr	0.0000	0.0000	0.0000	0.0000	0.0000	0.0000	0.0000
Fe3	0.0000	0.0000	0.0000	0.0000	0.0000	0.0000	0.0000
Fe2	0.0000	0.0000	0.0000	0.0000	0.0000	0.0000	0.0000
Mn	0.0000	0.0000	0.0000	0.0000	0.0000	0.0000	0.0000
Mg	0.0000	0.0000	0.0000	0.0000	0.0000	0.0000	0.0000
Ca	0.0000	0.0000	0.0000	0.0000	0.0000	0.0000	0.0000
Na	0.0000	0.0000	0.0000	0.0000	0.0000	0.0000	0.0000
sum	2.0116	1.9868	1.9737	2.0000	2.0000	2.0000	2.0044
ideal	2.0000	2.0000	2.0000	2.0000	2.0000	2.0000	2.0000

Table A.6: Pyroxene Cation Allocation.

	HA6_04	HA6_03	HA7_01	HA7_02	HA7_03	HA8_01	HA8_03
M2 (VI)							
Si	0.0000	0.0000	0.0000	0.0000	0.0000	0.0000	0.0000
Ti	0.0000	0.0000	0.0000	0.0000	0.0000	0.0000	0.0000
Al	0.0000	0.0000	0.0000	0.0000	0.0000	0.0000	0.0000
Cr	0.0000	0.0000	0.0000	0.0000	0.0000	0.0000	0.0000
Fe3	0.0000	0.0000	0.0000	0.0000	0.0000	0.0000	0.0000
Fe2	0.1735	0.2264	0.2805	0.2826	0.2955	0.1589	0.1527
Mn	0.0094	0.0134	0.0032	0.0030	0.0000	0.0091	0.0086
Mg	0.7795	0.6737	0.6117	0.5919	0.5516	0.8066	0.8148
Ca	0.0374	0.0858	0.1045	0.1221	0.1519	0.0239	0.0233
Na	0.0002	0.0007	0.0000	0.0005	0.0010	0.0014	0.0007
sum	1.0000	1.0000	1.0000	1.0000	1.0000	1.0000	1.0000
ideal	1.0000	1.0000	1.0000	1.0000	1.0000	1.0000	1.0000
M1 (VI)							
Si	0.0000	0.0000	0.0000	0.0000	0.0000	0.0000	0.0000
Ti	0.0046	0.0101	0.0008	0.0004	0.0008	0.0014	0.0008
Al	0.0393	0.0502	0.0508	0.0729	0.0000	0.0147	0.0226
Cr	0.0195	0.0205	0.0199	0.0219	0.0192	0.0188	0.0166
Fe3	0.0000	0.0000	0.0000	0.0000	0.0872	0.0000	0.0000
Fe2	0.1697	0.2312	0.2919	0.2924	0.3178	0.1589	0.1511
Mn	0.0000	0.0000	0.0000	0.0000	0.0000	0.0000	0.0000
Mg	0.7622	0.6880	0.6366	0.6124	0.5931	0.8064	0.8066
Ca	0.0000	0.0000	0.0000	0.0000	0.0000	0.0000	0.0000
Na	0.0000	0.0000	0.0000	0.0000	0.0000	0.0000	0.0000
sum	0.9953	1.0000	1.0000	1.0000	1.0182	1.0000	0.9977
ideal	1.0000	1.0000	1.0000	1.0000	1.0000	1.0000	1.0000
T (IV)							
Si	2.0047	1.9668	1.9947	1.9874	1.9111	1.9909	2.0023
Ti	0.0000	0.0000	0.0000	0.0000	0.0000	0.0000	0.0000
Al	0.0000	0.0332	0.0053	0.0126	0.0707	0.0091	0.0000
Cr	0.0000	0.0000	0.0000	0.0000	0.0000	0.0000	0.0000
Fe3	0.0000	0.0000	0.0000	0.0000	0.0000	0.0000	0.0000
Fe2	0.0000	0.0000	0.0000	0.0000	0.0000	0.0000	0.0000
Mn	0.0000	0.0000	0.0000	0.0000	0.0000	0.0000	0.0000
Mg	0.0000	0.0000	0.0000	0.0000	0.0000	0.0000	0.0000
Ca	0.0000	0.0000	0.0000	0.0000	0.0000	0.0000	0.0000
Na	0.0000	0.0000	0.0000	0.0000	0.0000	0.0000	0.0000
sum	2.0047	2.0000	2.0000	2.0000	1.9818	2.0000	2.0023
ideal	2.0000	2.0000	2.0000	2.0000	2.0000	2.0000	2.0000

Table A.6 continued. Pyroxene Cation Allocation

	HA8_04	HA10_01	HA10_02	HA10_03	HA11_02	HA11_03
M2 (VI)						
Si	0.0000	0.0000	0.0000	0.0000	0.0000	0.0000
Ti	0.0000	0.0000	0.0000	0.0000	0.0000	0.0000
Al	0.0000	0.0000	0.0000	0.0000	0.0000	0.0000
Cr	0.0000	0.0000	0.0000	0.0000	0.0000	0.0000
Fe3	0.0000	0.0000	0.0000	0.0000	0.0000	0.0000
Fe2	0.1501	0.2099	0.1999	0.2298	0.2180	0.2399
Mn	0.0086	0.0111	0.0113	0.0116	0.0108	0.0109
Mg	0.8190	0.7199	0.7256	0.6838	0.7211	0.6963
Ca	0.0216	0.0575	0.0630	0.0746	0.0493	0.0519
Na	0.0007	0.0016	0.0002	0.0002	0.0007	0.0010
sum	1.0000	1.0000	1.0000	1.0000	1.0000	1.0000
ideal	1.0000	1.0000	1.0000	1.0000	1.0000	1.0000
M1 (VI)						
Si	0.0000	0.0000	0.0000	0.0000	0.0000	0.0000
Ti	0.0011	0.0026	0.0026	0.0020	0.0032	0.0033
Al	0.0149	0.0111	0.0000	0.0381	0.0600	0.0687
Cr	0.0180	0.0126	0.0121	0.0119	0.0128	0.0113
Fe3	0.0000	0.0103	0.0283	0.0000	0.0000	0.0000
Fe2	0.1496	0.2175	0.2070	0.2385	0.2145	0.2349
Mn	0.0000	0.0000	0.0000	0.0000	0.0000	0.0000
Mg	0.8165	0.7460	0.7512	0.7096	0.7096	0.6818
Ca	0.0000	0.0000	0.0000	0.0000	0.0000	0.0000
Na	0.0000	0.0000	0.0000	0.0000	0.0000	0.0000
sum	1.0000	1.0000	1.0013	1.0000	1.0000	1.0000
ideal	1.0000	1.0000	1.0000	1.0000	1.0000	1.0000
T (IV)						
Si	1.9945	1.9625	1.9559	1.9901	1.9504	1.9540
Ti	0.0000	0.0000	0.0000	0.0000	0.0000	0.0000
Al	0.0055	0.0375	0.0429	0.0099	0.0496	0.0460
Cr	0.0000	0.0000	0.0000	0.0000	0.0000	0.0000
Fe3	0.0000	0.0000	0.0000	0.0000	0.0000	0.0000
Fe2	0.0000	0.0000	0.0000	0.0000	0.0000	0.0000
Mn	0.0000	0.0000	0.0000	0.0000	0.0000	0.0000
Mg	0.0000	0.0000	0.0000	0.0000	0.0000	0.0000
Ca	0.0000	0.0000	0.0000	0.0000	0.0000	0.0000
Na	0.0000	0.0000	0.0000	0.0000	0.0000	0.0000
sum	2.0000	2.0000	1.9987	2.0000	2.0000	2.0000
ideal	2.0000	2.0000	2.0000	2.0000	2.0000	2.0000

Table A.6 continued. Pyroxene Cation Allocation.

	HA2_16	HA3_01	HA3_02	HA3_03	HA3_06	HA4_02	HA4_05	HA6_03	HA6_04	HA7_01
M1 3^+										
r_o		0.6622	0.6616	0.6611	0.6623	0.6610	0.6603			
D_o		2.74	2.47	2.63	2.30	3.32	3.96			
E		1506	1507	1491	1447	1520	1553			
M1 4^+										
r_o	0.6334							0.6448	0.6423	0.6441
D_o	0.1146							0.2665	0.2154	0.3575
E	2170							2025	2547	2345
M2 2^+										
r_o	0.8453	0.8288	0.8224	0.8315	0.8146	0.8251	0.8235	0.8271	0.8330	0.8429
D_o	0.97	0.69	0.67	0.72	0.60	0.80	0.77	1.23	0.95	1.46
E	378	287	263	293	306	261	256	213	273	240
M2 3^+										
r_o	0.7593	0.7568	0.7567	0.7571	0.7558	0.7583	0.7593	0.7727	0.7578	0.7715
D_o	0.0940	0.1096	0.0880	0.0979	0.0835	0.1073	0.0974	0.2471	0.1491	0.3060
E	291	334	339	341	366	282	303	265	260	255
Error										
M1 3^+										
r_o		0.0016	0.0018	0.0034	0.0019	0.0022	0.0016			
D_o		0.26	0.23	0.49	0.23	0.49	0.33			
E		104	96	233	78	140	67			
M1 4^+ Ions										
r_o	0.0348							0.0222	0.0213	0.0086
D_o	0.1354							0.3959	0.3098	0.2356
E	2873							2488	2686	1158
M2 2^+										
r_o	0.0042	0.0055	0.0059	0.0057	0.0084	0.0102	0.0166	0.0209	0.0067	0.0063
D_o	0.08	0.03	0.02	0.03	0.03	0.05	0.06	0.06	0.05	0.11
E	32	26	3	30	35	37	56	53	29	29
M2 3^+										
r_o										
D_o	0.0187	0.0358	0.0237	0.0220	0.0352	0.0428	0.0366	0.0608	0.0324	0.0274
E	42	78	53	51	99	89	80	33	39	19
Predicted										
M1 4^+										
r_o	0.6428							0.6423	0.6420	0.6412
D_o	0.0752							0.1229	0.0815	0.0975
E	2203							2203	2203	2203
M2 3^+										
r_o	0.7894	0.7920	0.7936	0.7882	0.7913	0.7846	0.7829	0.7834	0.7844	0.7770
D_o	0.0982	0.0922	0.0911	0.0900	0.0849	0.0994	0.1082	0.1842	0.1122	0.1804
E	302	301	291	286	289	294	288	316	295	308
Error										
M1 4^+ Ions										
r_o	0.0564							0.0568	0.0571	0.0556
D_o	0.1090							0.1870	0.1194	0.1514
E	665							665	665	665
M2 3^+										
r_o	0.0644	0.0646	0.0653	0.0639	0.0646	0.0633	0.0630	0.0602	0.0623	0.0590
D_o	0.0740	0.0682	0.0679	0.0663	0.0620	0.0744	0.0827	0.1494	0.0851	0.1431
E	667	683	679	678	673	670	667	667	670	664

Table A.7: Lattice strain parameters for each experiment and the predicted values using the equations of *Sun and Liang* (2013)

	HA7_02	HA7_03	HA8_01	HA8_03	HA8_04	HA10_01	HA10_02	HA10_03	HA11_02	HA11_03
Experimental										
M1 3^+										
r_o		0.6623	0.6600	0.6610	0.6598	0.6621	0.6623	0.6618	0.6618	0.6596
D_o		21.23	3.18	3.37	3.24	6.87	6.86	8.85	13.08	12.42
E		1688	1604	1624	1591	1477	1513	1566	1490	1443
M1 4^+										
r_o	0.6512	0.6500	0.6500	0.6500	0.6500	0.6344	0.6347	0.6446	0.6463	0.6481
D_o	0.6560	0.4306	0.5567	0.2987	0.2809	0.1761	0.1717	0.2874	0.3557	0.3443
E	2840	2315	5766	4379	4318	1881	1846	2718	1946	2441
M2 2^+										
r_o	0.8471	0.8391	0.8279	0.8281	0.8332	0.8348	0.8291	0.8254	0.8273	0.8366
D_o	1.53	1.59	0.71	0.74	0.70	1.11	1.06	1.09	1.10	1.10
E	238	192	270	274	323	250	222	200	234	244
M2 3^+										
r_o	0.7771	0.7787	0.7561	0.7561	0.7561	0.7653	0.7652	0.7672	0.7716	0.7725
D_o	0.3406	0.3142	0.0825	0.0758	0.0785	0.1997	0.2066	0.2059	0.2666	0.2475
E	239	222	291	241	247	299	301	307	254	297
Error										
M1 3^+										
r_o		0.0022	0.0026	0.0030	0.0029	0.0019	0.0010	0.0013	0.0017	0.0029
D_o		6.24	0.51	0.47	0.42	1.24	0.67	1.09	1.97	2.65
E		139	122	147	131	89	70	69	116	187
M1 4^+										
r_o	0.8968	0.2578	0.2490	0.1406	0.1309	0.1003	0.0843	0.2636	0.1815	0.4625
D_o	0.0077					0.0175	0.0150	0.0104	0.0072	0.0129
E	2247	592	813	673	664	1206	1049	1593	855	2173
M2 2^+										
r_o	0.0102	0.0419	0.0106	0.0135	0.0076	0.0039	0.0066	0.0134	0.0060	0.0175
D_o	0.18	0.61	0.04	0.04	0.05	0.04	0.05	0.05	0.04	0.12
E	49	146	38	49	38	16	23	35	20	63
M2 3^+										
r_o										
D_o	0.0497	0.0082	0.0164	0.0162	0.0151	0.0277	0.0133	0.0194	0.0288	0.0402
E	38	31	34	28	33	17	14	12	14	17
Predicted										
M1 4^+										
r_o	0.6407	0.6401	0.6429	0.6433	0.6427	0.6424	0.6426	0.6413	0.6406	0.6407
D_o	0.1131	0.1475	0.0740	0.0739	0.0740	0.1006	0.1027	0.0968	0.1066	0.1056
E	2203	2203	2203	2203	2203	2203	2203	2203	2203	2203
M2 3^+	0.7802	0.7820	0.7855	0.7858	0.7875	0.7807	0.7827	0.7795	0.7774	0.7734
r_o	0.2114	0.2908	0.1002	0.0973	0.0977	0.1536	0.1568	0.1548	0.1649	0.1780
D_o	315	355	285	289	283	293	305	300	279	274
E										
Error										
M1 4^+										
r_o	0.0553	0.0560	0.0569	0.0572	0.0567	0.0563	0.0564	0.0567	0.0564	0.0561
D_o	0.1755	0.2298	0.1069	0.1053	0.1064	0.1497	0.1538	0.1476	0.1602	0.1633
E	665	665	665	665	665	665	665	665	665	665
M2 3^+										
r_o	0.0591	0.0591	0.0631	0.0640	0.0636	0.0612	0.0611	0.0603	0.0612	0.0604
D_o	0.1729	0.2397	0.0760	0.0727	0.0725	0.1198	0.1213	0.1214	0.1310	0.1421
E	674	674	677	670	666	669	671	671	668	660

Table A.7 continued. Lattice strain parameters for each experiment.

Run	YSLLunar A15GG210	YSLLunar A15YG217	YSLLunar A15Red219	YSLLunar YG1d1	YSLLunar YG1d4	YSLLunar A15Red1	VKP2010 A2	VKP2010 B1
T	1450	1425	1340	1400	1425	1340	1390	1350
M2 3^+								
D_o	0.727	0.914	0.853	0.771	0.683	0.697		
r_o	0.822	0.822	0.836	0.809	0.786	0.794		
E	146	186	188	137	109	100		
M2 3^+								
D_o	0.139	0.275	0.171	0.283	0.172	0.297	0.089	0.114
r_o	0.76	0.718	0.759	0.7	0.737	0.675	0.87	0.83
E	295	227	294	220	268	193	667	471
M1 3^+								
D_o		4.36	5.19	3.84	3.72	3.65	2.117	2.677
r_o		0.661	0.654	0.662	0.663	0.674	0.66	0.66
E		1345	1390	1168	1261	1060	998	1277
M1 4^+								
D_o	0.09	0.156	0.15	0.104	0.095	0.081	0.156	0.186
r_o	0.635	0.643	0.648	0.644	0.64	0.644	0.65	0.66
E	2059	2427	2818	2298	2259	2341	2360	2773

Run	VKP2010 L87-III	VKP2011 1	VKP2011 2	VKP2011 3	VKP2011 4	VKP2011 5	VKP2011 6	VKP2011 7
T	1326	1430	1430	1550	1550	1600	1600	1400
M2 2^+								
D_o		1.06	0.734	0.888	0.694	0.84	0.797	0.68
r_o		0.86	0.84	0.86	0.85	0.87	0.86	0.84
E (GPa)		424	266	383	320	375	327	226
M2 3^+								
D_o	0.125	0.085	0.066	0.041	0.043	0.05	0.044	0.038
r_o	0.82	0.77	0.81	0.83	0.8	0.82	0.85	0.84
E	388	289	429	512	340	339	382	536
M1 3^+								
D_o	4.764	1.41	2.42	1.3	0.992	1.34	0.956	1.93
r_o	0.67	0.66	0.66	0.66	0.65	0.66	0.65	0.66
E	2123	1169	1669	1378	1071	1364	810	1322
M1 4^+								
D_o	0.132	0.451		0.256	0.254			0.088
r_o	0.65	0.65		0.65	0.65			0.64
E	2485	5459		4666	4910			3022

Table A.8: Lattice strain parameters from the literature of *Sun and Liang* (2013), *van Kan Parker et al.* (2010), *van Kan Parker et al.* (2011), *Frei et al.* (2009), *Cartier et al.* (2014). Errors are not included, as not included in the data. The errors which are reported can be seen in Figure 3.10. T is the temperature of the experiment in ^{o}C, Run is the experiment name.

Run	Frei2009 11011206	Frei2009 1722972	Frei2009 147285	Frei2009 292742	Frei2009 475855	Cartier2014 1183	Cartier2014 1137	Cartier2014 1212
T	1230	1330	1440	1510	1535	1720	1700	1850
M2 2^+								
D	0.012	0.015	0.003	0.02	0.002	0.47	0.58	0.18
r_o	0.83	0.83	0.83	0.83	0.83	0.82	0.81	0.95
E	63	75	50	71	50	153	137	356
M2 3^+								
D	0.181	0.157	0.134	0.136	0.137	0.16	0.12	0.03
r_o	0.83	0.83	0.85	0.83	0.82	0.7	0.73	0.7
E	453	481	570	514	474	251	272	177
M1 3^+								
D	3.54	2.97	2.32	1.59	2.29	0.29	0.37	0.32
r_o	0.66	0.66	0.65	0.66	0.65	0.65	0.61	0.65
E	1200	1050	992	773	947	1543	457	236
M1 4^+								
D	0.262	0.186	0.282	0.227	0.399	0.1	0.1	0.06
r_o	0.64	0.63	0.64	0.65	0.65	0.61	0.61	0.62
E	1650	1390	2670	2420	3670	1799	1760	1662

Run	Cartier2014 1210	Cartier2014 1133	Cartier2014 1093	Cartier2014 1135	Cartier2014 1083	Cartier2014 1141	Cartier2014 1178
T	1800	1690	1680	1650	1610	1600	1580
M2 2^+							
D	0.19	0.29	0.31	0.14	0.13	0.18	0.12
r_o	0.97	0.87	0.89	0.95	0.96	0.95	0.88
E	347	195	190	267	406	287	264
M2 3^+							
D	0.09	0.28	0.04	0.02	0.01	0.09	0.11
r_o	0.7	0.66	0.78	0.79	0.73	0.73	0.7
E	171	204	219	240	140	217	264
M1 3^+							
D	0.25	0.32	0.42	0.24	0.28	0.39	0.49
r_o	0.64	0.62	0.64	0.63	0.63	0.61	0.65
E	336	1137	237	232	237	450	1366
M1 4^+							
D	0.03	0.08	0.04	0.05	0.04	0.07	0.04
r_o	0.62	0.61	0.63	0.62	0.63	0.61	0.64
E	902	1466	1167	1675	2211	1459	2657

Table A.8 continued. Lattice strain parameters from the literature.

Appendix B

BSE Images of Experiments

In this appendix Backscattered Electron (BSE) Images of a selection of the experimental charges are shown. These BSE images were taken either using the Jeol JSM-840A Scanning Electron Microscope, or the FEI Quanta FEG 650, both in the Department of Earth Sciences, University of Oxford. The scale for each figure is indicated on each image, in addition to the phases present. Ol = olivine, pyx = pyroxene (orthopyroxene or pigeonite), fspar = feldspar, sp = spinel and gl = glass.

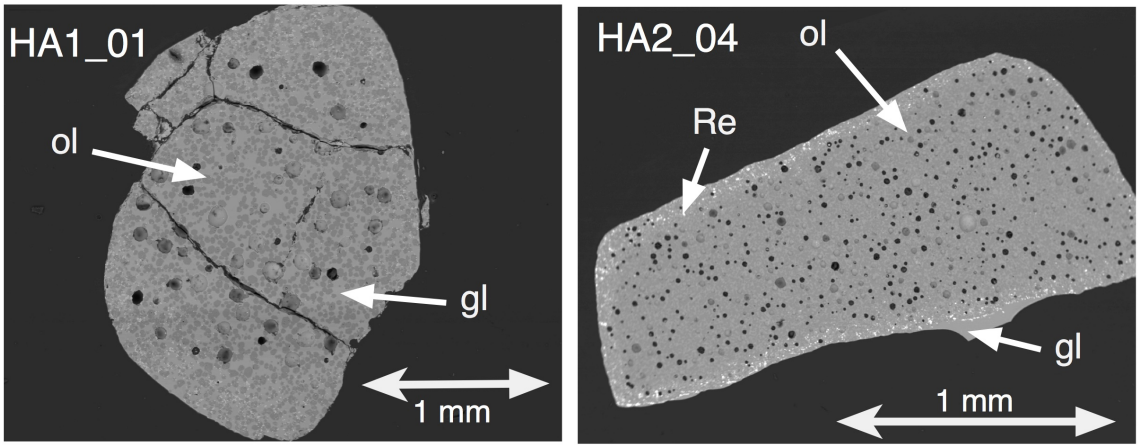

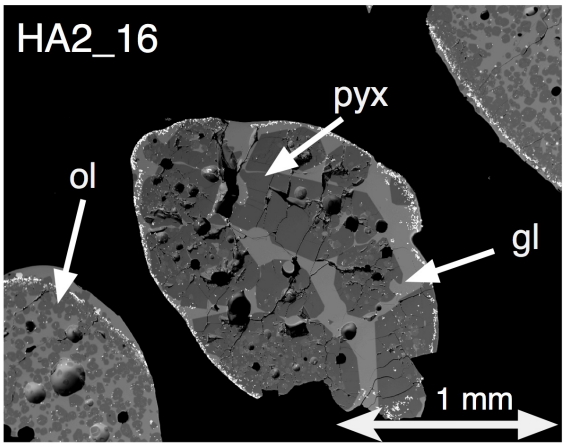
HA2_16
pyx
ol
gl
1 mm

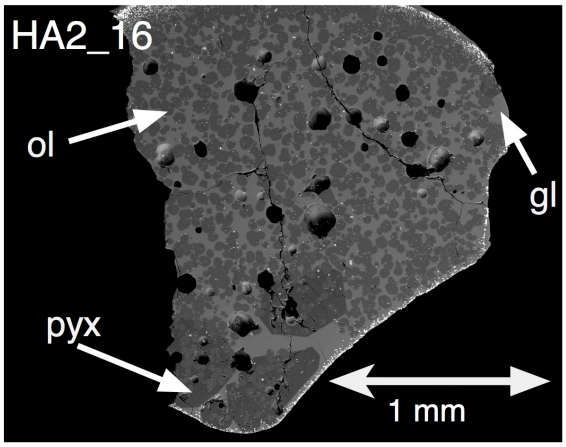
HA2_16
ol
gl
pyx
1 mm

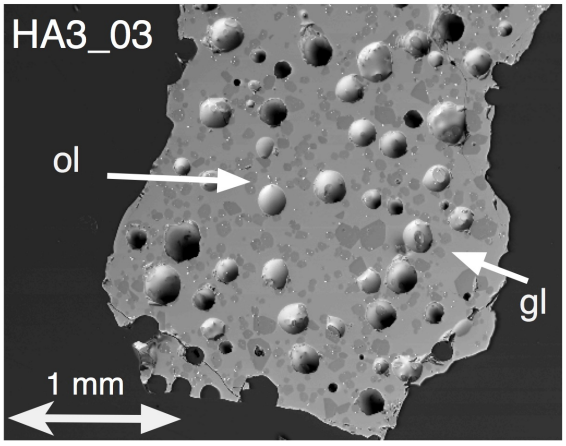
HA3_03
ol
gl
1 mm

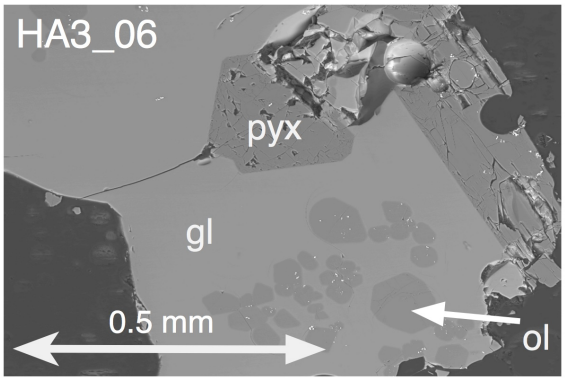
HA3_06
pyx
gl
0.5 mm
ol

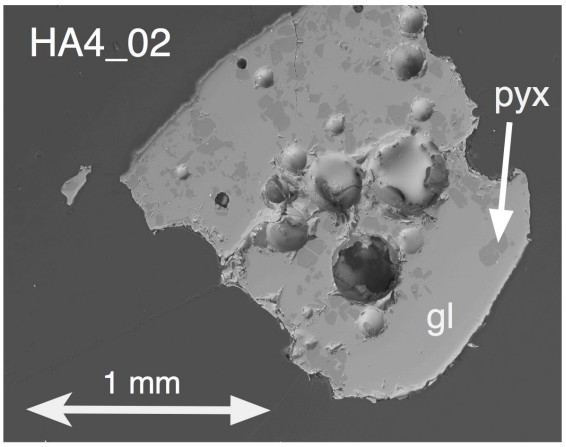
HA4_02
pyx
gl
1 mm

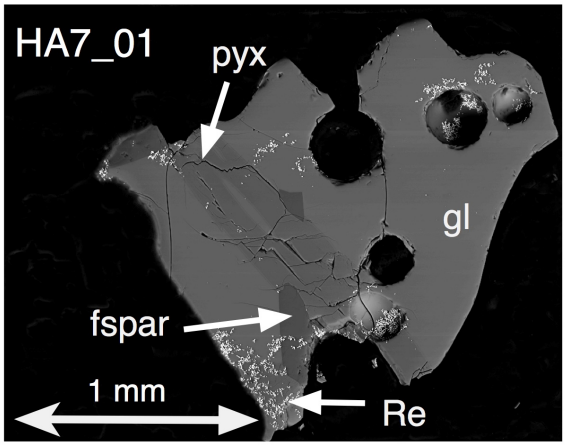
HA7_01
pyx
gl
fspar
1 mm
Re

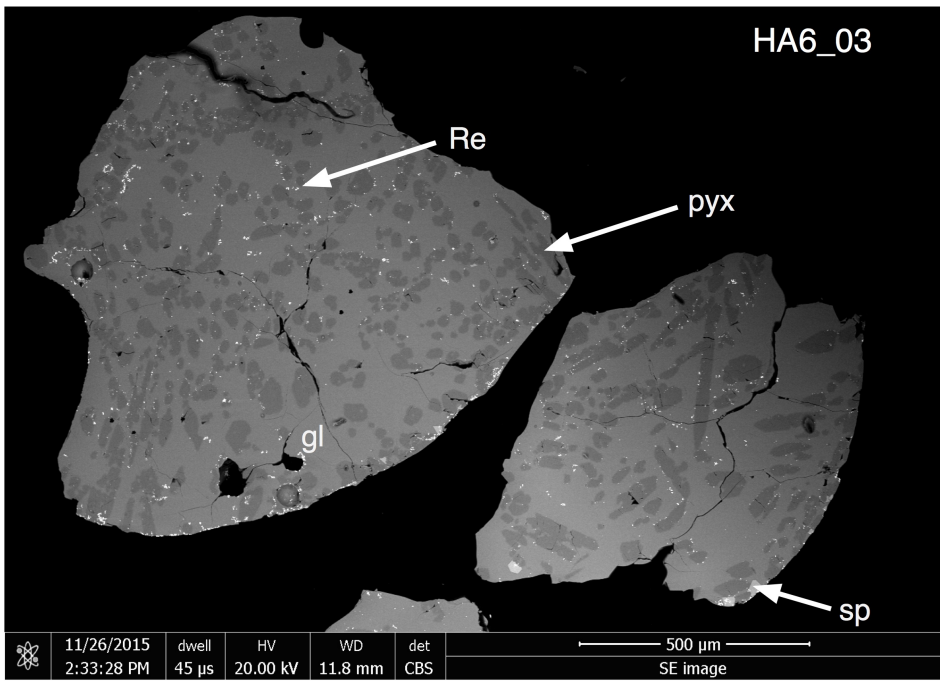
HA6_03
Re
pyx
gl
sp
11/26/2015
2:33:28 PM
dwell
45 µs
HV
20.00 kV
WD
11.8 mm
det
CBS
500 µm
SE image

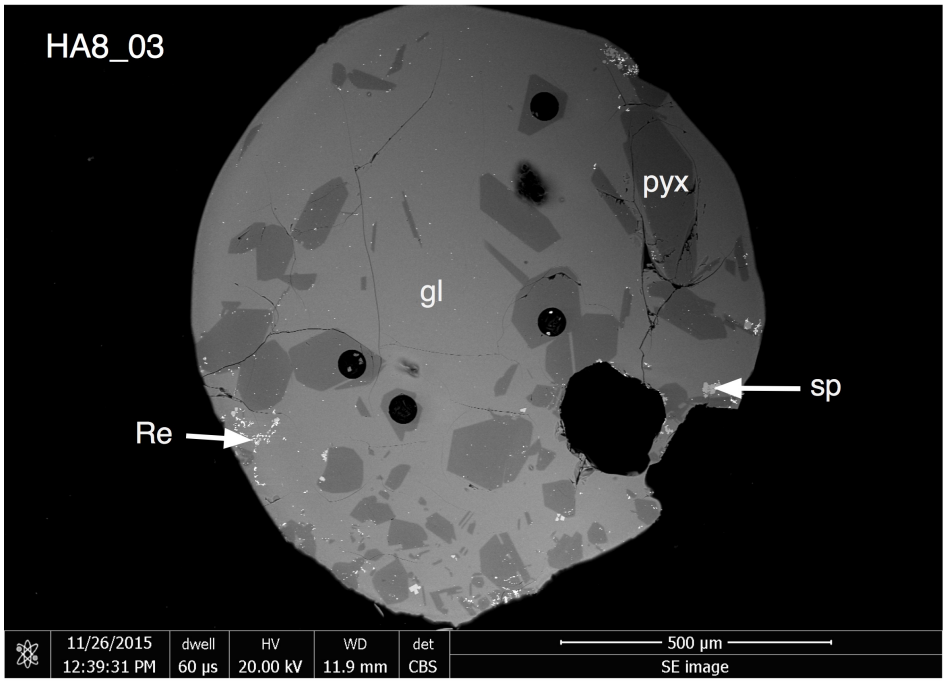
HA8_03
pyx
gl
sp
Re
11/26/2015
12:39:31 PM
dwell
60 µs
HV
20.00 kV
WD
11.9 mm
det
CBS
500 µm
SE image

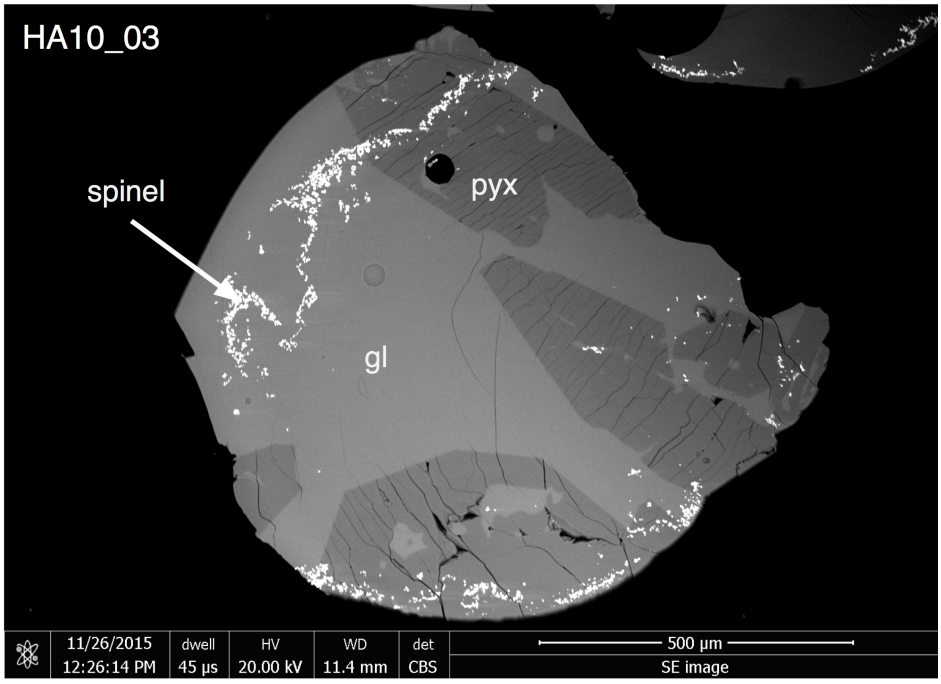
HA10_03
spinel
pyx
gl
11/26/2015
12:26:14 PM
dwell
45 µs
HV
20.00 kV
WD
11.4 mm
det
CBS
500 µm
SE image

Appendix C

Onuma Diagrams

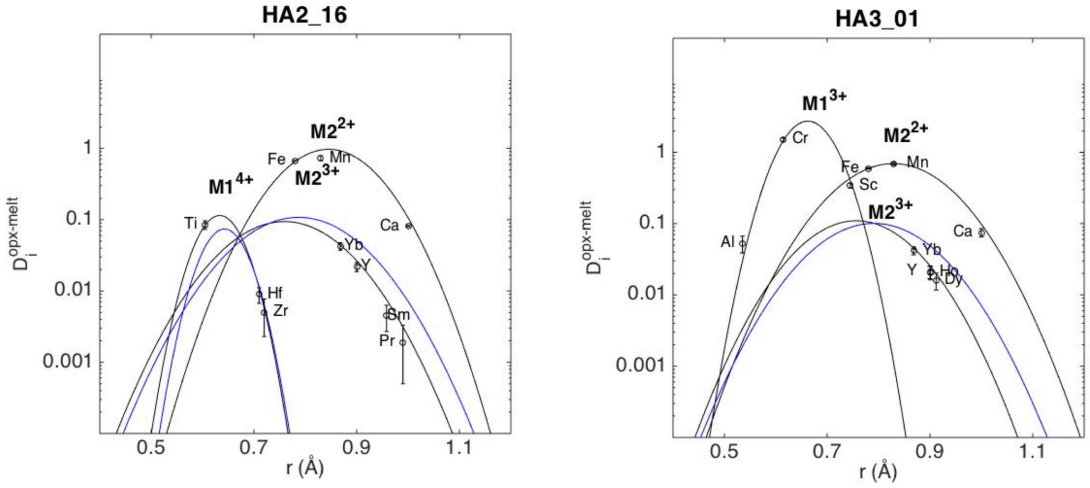

Figure C.1: Onuma diagrams for all experiments showing pyroxene-melt partitioning data and measured errors (open circles). Black solid curves are the best-fit lattice strain model results reported in Chapter 3 and Table A.7 . Solid blue curves are the predicted models using the equations from *Sun and Liang* (2013). Individual elements are labelled, as are the parabolae for the M1 3^+, M1 4^+, M2 2^+, M2 3^+.

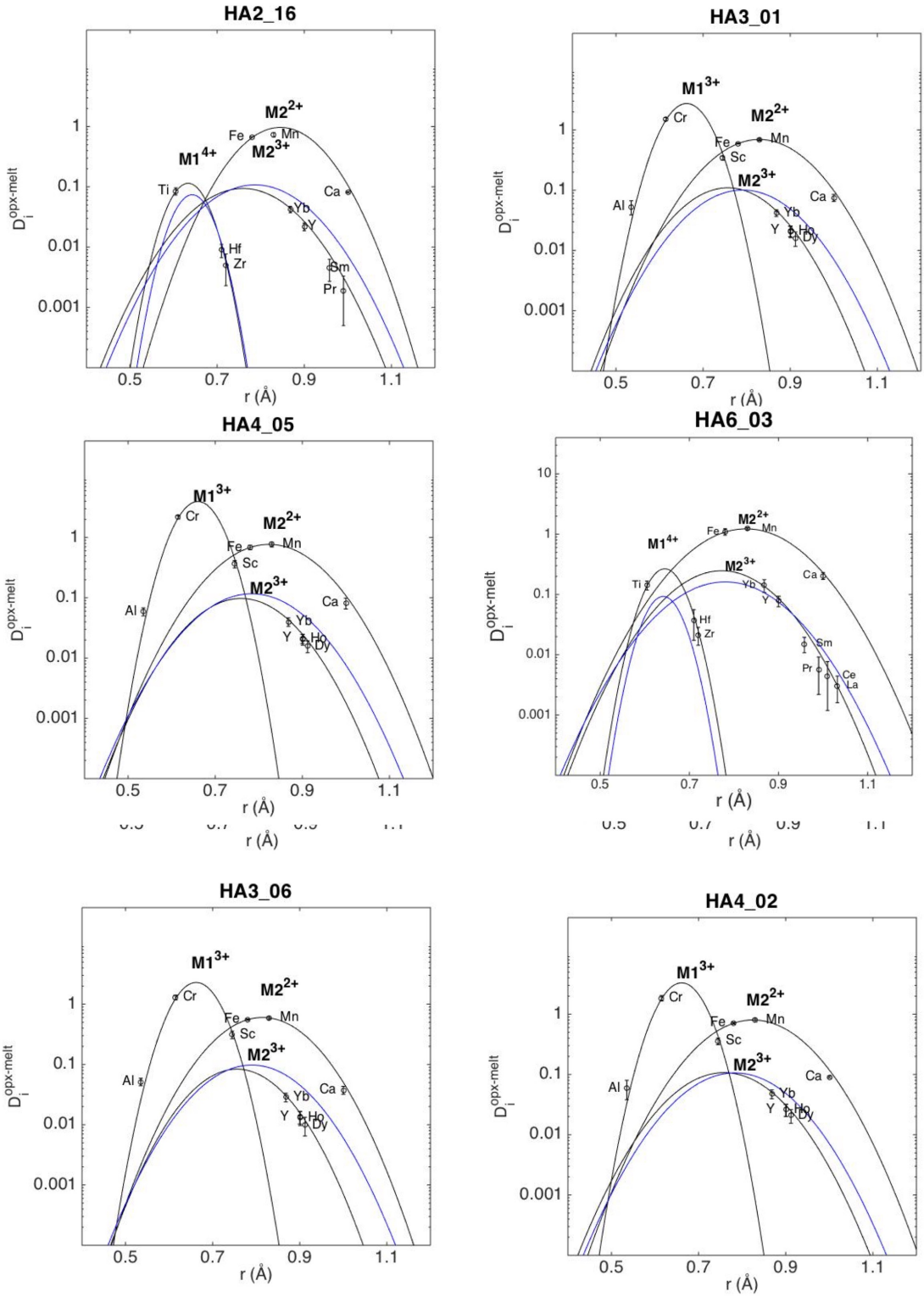

Figure C.1 continued. Major element abundances measured by EPMA.

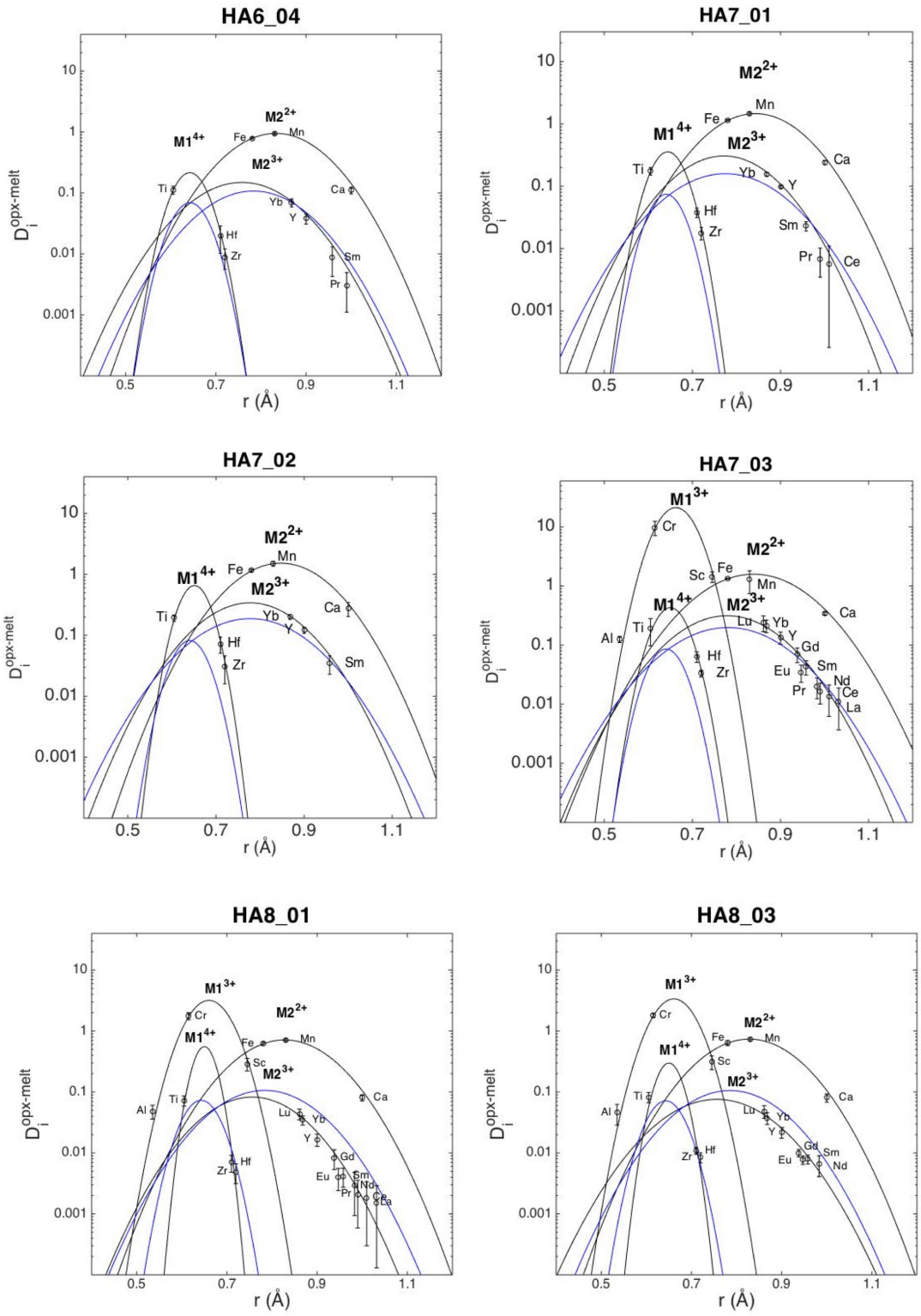

Figure C.1 continued. Major element abundances measured by EPMA.

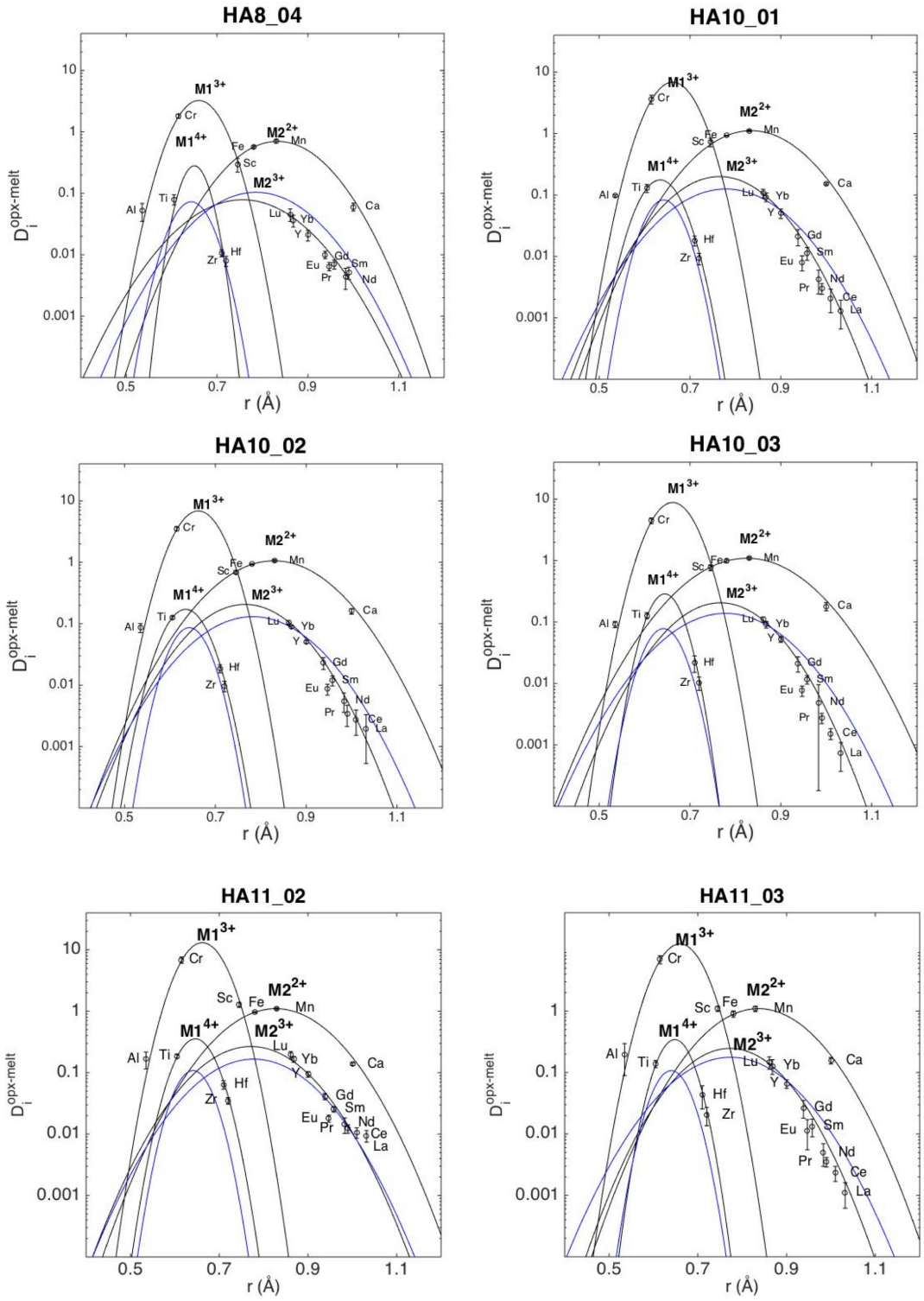

Figure C.1 continued. Major element abundances measured by EPMA.

Appendix D

Matlab Codes for Petrogenetic Models

D.1 Equilibrium crystallisation/partial melting of Vesta.

```
% Read in a .csv file which has the information from an alphaMELTS model:
Column 1 is for melt fraction, Column 2 is the mode of Olivine,
Column 3 is mode orthopyroxene, Column 4 is mode clinopyroxene,
 column 5 is mode feldspar and column 6 is the temperature.

M=csvread('Mg75mantle.csv');
F=M(:,1);X1=M(:,2);X2=M(:,3);X3=M(:,4);X4=M(:,5);T=M(:,6);

%Some literature data:

%Ideal sixfold ionic radii (Shannon 1976)
RiLa = 1.032;RiPr = 0.99;RiNd = 0.983;RiSm = 0.958;RiEu = 0.947;
RiGd = 0.938;RiDy = 0.912;
RiYb = 0.868;RiY = 0.9;RiTi=0.605;RiZr=0.72;RiHf=0.71;
Ri=[RiLa RiNd RiSm RiEu RiGd RiDy RiYb RiY RiTi RiZr RiHf];

%CI VALUES (Sun and McDonough 1995)
CILa = 0.2414;CINd=0.4737;CISm=0.1536;CIEu=0.05883;CIGd=0.2069;
CIDy=0.2558;CIYb=0.1687;CIY=1.46;CITi=447; CIZr=3.63; CIHf=0.1065;
cI=[CILa; CINd; CISm; CIEu; CIGd; CIDy; CIYb; CIY; CITi; CIZr; CIHf];
CI=repmat(cI,1,101);

%Juvinas Values (Barrat et al. 2000)
JLa = 2.14;JNd=4.26;JSm=1.37;JEu=0.539;JGd=1.81;
JDy=2.26;JYb=1.4;JY=13.96;JTi=2800; JZr=35.82; JHf=0.97;
```

```
J=[JLa; JNd; JSm; JEu; JGd; JDy; JYb; JLu; JY; JTi; JZr; JHf];
Jn=cI./J;

%Start Vesta Values enrichment factor to CI chondrites
i=2.5;
CO=i.*cI';

% Partition Coefficients. From here onwards the phases will be labelled
%as following:
%Orthopyroxene = 1, Olivine = 2, Clinopyroxene = 3 and Feldspar= 4.
%Partition Coefficients are labelled K, so the orthopyroxene partition
% coefficient would be K1, Olivine K2 etc.

% Mineral-melt partition coefficients. Firstly need to calculate the ro
%and Do, from the best fit lines to the experimental data.

% Ro Values
ROREE=((5*10^-5)*T)+0.7152;
ROHFSE=(-0.0002*T)+0.8366;

%DO Values
for i = 1:length(T)
if T(i)<=1320
    DOREE(i)=(-0.001.*T(i))+1.4087;
    DOHFSE(i)=0.5;
elseif T(i)>1320
    DOREE(i)=0.1;
    DOHFSE(i)=0.5;
end
end

Tzb=T+273;Tz=Tzb';

%REE -4piNaE/Rt FOR OPX AND CPX
for i = 1:length(Tz)
    AREE(i)=(-4*pi*(6.023*10^23)*(10^9)*290)/(8.31.*(Tzb(i)));
    AHFSE(i)=(-4*pi*(6.023*10^23)*(10^9)*2090)/(8.31.*(Tzb(i)));
end

dOREE=repmat(DOREE,8,1);
aREE=repmat(AREE,8,1);
rOREE=repmat(ROREE',8,1);
dOHFSE=repmat(DOHFSE,3,1);
aHFSE=repmat(AREE,3,1);
rOHFSE=repmat(ROHFSE',3,1);
```

```
ro=[r0REE;r0HFSE];
do=[d0REE;d0HFSE];
a=[aREE;aHFSE];
ri=repmat(Ri',1,101);

%Orthopyroxene K1
K1 =do.*exp(a.*((((ro*10.^-10)/2).*(((ro*10.^-10)-(ri*10.^-10)).^2)
-((1/3)*(((ro*10.^-10)-(ri*10.^-10))).^3))));

%Olivine K2
K2La = 0.00155;K2Nd = 0.00153556;K2Sm = 0.00196818;K2Eu = 0.002485;
K2Gd = 0.003355;K2Dy=0.02133;K2Yb = 0.03642149;K2Y = 0.03642149;
K2Ti=0.06399932;K2Zr=0.0005;K2Hf=0.001;
k2 = [K2La; K2Nd; K2Sm; K2Eu; K2Gd; K2Dy; K2Yb; K2Y; K2Ti; K2Zr; K2Hf];
K2=repmat(k2,1,101);

%Clinopyroxene K3
D0REEC=0.4*ones(length(T));
Y=D0REEC(1,:);y=repmat(Y,8,1);
k3 =y.*exp(a(1:8,:).*((((ro(1:8,:).*10.^-10)/2).*(((ro(1:8,:)*10.^-10)
-(ri(1:8,:).*10.^-10)).^2)
-((1/3)*(((ro(1:8,:).*10.^-10)-(ri(1:8,:).*10.^-10))).^3))));
XTi=0.064*ones(length(T));K3Ti=XTi(1,:);
XZr=0.02034*ones(length(T));K3Zr=XZr(1,:);
XHf=0.04316*ones(length(T));K3Hf=XHf(1,:);
K3 = [k3; K3Ti; K3Zr; K3Hf];

%Feldspar K4 (Some values taken from Fonseca et al. 2014)

K4La = 0.03939441;K4Nd = 0.03014192;K4Sm = 0.02343683;K4Eu = 0.79689531;
K4Gd = 0.02047709;K4Dy=0.01685;K4Yb = 0.01131786;K4Y = 0.01444247;
K4Ti=0.02245662;K4Zr=0.0067437;K4Hf=0.00701885;
k4 = [K4La; K4Nd; K4Sm; K4Eu; K4Gd; K4Dy; K4Yb; K4Y; K4Ti; K4Zr; K4Hf];
K4=repmat(k4,1,101);

%Bulk partition coefficient
X1a=repmat(X1',11,1);X2a=repmat(X2',11,1);X3a=repmat(X3',11,1);
X4a=repmat(X4',11,1);
D=(K1.*X1a)+(K2.*X2a)+(K4.*X4a)+(K3.*X3a);

%Calculations:
Fb=F';Co=repmat(CO',1,101);Fc=repmat(Fb,11,1);

% Liquid Composition and normalisation for plotting. Where CL is the
%trace element abundance in the liquid, Fc is the fraction of Melt, D i
```

```
%s the bulk composition and Co is the starting composition.
CL=Co./((Fc+(D.*(1-Fc))));AL=CL./CI;

% Solid Composition where CS is the trace element abundance in the
% residual cumulate after partial melting/equilibrium crystallisation.
CS=(Co.*D)./(Fc+(D.*(1-Fc)));AS=CS./CI;
```

D.2 Fractional crystallisation of partial melts of Vesta.

```
%Fractional Crystallisation Calculations are performed using the following
%equations, and normalised to CI chondrite for plotting:

% The K values are calculated in the same manner as in the Equilibrium
%Crystallisation script, and so a .csv output file containing the output
%of AlphaMELTS including the Modes of each phase, Temperature and melt
%fraction are read in. In models of fractional crystallisation the start
%compositions are the 10, 20, 30, 40, 50 % partial melts of Vesta.
%The major element compositions are taken from the alphaMELTS models, and
%the trace element composition can be read in from the Equilibrium
%Crystallisation calculation.

% Extracting the Liquid Melt Composition from 10 - 50 % partial melting
(50-90 % equilibrium crystallisation) at 10 % intervals:

f=F';g=f(51:10:91);cl=CL(:,51:10:91);s=[g;cl];

% Then calculating the Trace element abundance in the Liquid (CL),
Instant Solid (CIS) and Average Solid (CAS).

CL=Co.*(Fc.^(D-1));AL=CL./CI;
CIS=D.*Co.*(Fc.^(D-1));AIS=CIS./CI;
CAS=(Co.*(1-(Fc.^D))./(1-Fc);AAS=CAS./CI;

% Where Co is the starting concentration and is the abundance in any of
%the partial melts which are being used as the starting composition.
```

D.3 Assimilation and Fractional Crystallisation.

```
%For Assimilation and Fractional Crystallisation, the input includes the
```

```
%ratio of assimilating material to crystallising material, and also the
%composition of the assimilating material (CA).

% The starting composition Co in this case was a 30 % partial melt of
%Vesta,taken from the Equilibrium Crystallisation equation.

CA=[JLa;JNd;JSm;JEu;JGd;JDy;JYb;JY;JTi;JZr;JHf];
ca=repmat(CA,1,9);

% The equations for Assimilation and Frational Crystallisation are taken
%De Paolo  et al. 1981) and I have defined z as the following ratio:
z=(r+D-1)./(r-1);

% where r is the ratio of assimilating material to rate of fractional
%crystallisation.

% The evolution of the solid and liquid phases are calculated as follows:
CL=co.*((f.^(-z))+((r./(r-1)).*(ca./(z.*co)).*(1-(f.^(-z)))));AL=CL./CI;
CS=D.*CL;AS=CS./CI;
CA=[JLa;JNd;JSm;JEu;JGd;JDy;JYb;JY;JTi;JZr;JHf];
```

D.4 Trapped Intercumulate Melt

```
% Firstly a starting point is selected, either a partial melt of Vesta
%and its coexisting cumulate or a liquid and cumulate from one of the
%subsequent fractional crystallisation paths.

% The liquid composition is selected and then the orthopyroxene in
%equilibrium with it is calculated. Here an example where the 30 % partial
%melt of Vesta is used as a starting point. The melt fraction, liquid
%composition and orthopyroxene coefficient are taken:
f=f(:,71);
QLiq=CL(:,71);
QKopx=K1(:,71);
QCopx=QLiq.*QKopx;

% Then the bulk trace element composition of a system containing
%orthopyroxene and 10, 20 and 30 % trapped melt is calculated:
QOpxmelt10=[(0.9*QCopx)+(0.1*QLiq)];
QOpxmelt20=[(0.8*QCopx)+(0.2*QLiq)];
QOpxmelt30=[(0.7*QCopx)+(0.3*QLiq)];
```

```
% Next step calculate OPX composition in equilibrium with this
bulk composition
opxreq10=QOpxmelt10./((0.1./QKopx)+0.9);Opxreq10=opxreq10./CI;
liqreq10=opxreq10./QKopx;Liqreq10=liqreq10./CI;
opxreq20=QOpxmelt20./((0.2./QKopx)+0.8);Opxreq20=opxreq20./CI;
liqreq20=opxreq20./QKopx;Liqreq20=liqreq20./CI;
opxreq30=QOpxmelt30./((0.3./QKopx)+0.7);Opxreq30=opxreq30./CI;
liqreq30=opxreq30./QKopx;Liqreq30=liqreq30./CI;


% Then in order to calculate the trace element evolution during the
%equilibrium crystallisation of the remaining trapped melt a .csv file
%is read in containing the alphaMELTS output of the major element and
%phase evolution. column a is mode orthopyroxene at 50 % crystallisation,
%b is mode of plagioclase, C is the temperature, d is the mode of
%orthopyroxene at 100 % crystallisation, e is the mode of plagioclase at
%100 % crystallisation and f is the temperature at 100 % crystallisation.

c=csvread('ReqIC30.csv',0,1)
opxreq50=c(:,1);
plagreq50=c(:,2);
T50=c(:,3);
opxreq100=c(:,4);
plagreq100=c(:,5);
T100=c(:,6);

% From this the partition coefficients (K150, K250,...etc.), and bulk
%coefficient (D50, D100) can be calculated at 50 % and 100 %
%crystallisation as before in the equilibrium and fractional
%crystallisation codes.

% Then the trace element content of the liquid, cumulate, and
%orthopyroxene are calculated after 50 and 100 % crystallisation,
%and normalised to chondrite.

F50=repmat(0.15,11,6);
CI50=repmat(cI,1,6);
CL50=bulk./((F50+(D50.*(1-F50))));AL50=CL50./CI;
CS50=(bulk.*D50)./(F50+(D50.*(1-F50)));AS50=CS50./CI;
Copx50 = (bulk.*K150)./(F50+(K150.*(1-F50)));CIopx50=Copx50./CI;


% And after Complete crystallisation
F100=repmat(0.0,11,6);
CI100=repmat(cI,1,6);
```

```
CL100 = bulk./(F100+(D100.*(1-F100)));AL100=CL100./CI;
CS100 = (bulk.*D100)./(F100+(D100.*(1-F100)));AS100=CS100./CI;
Copx100 = (bulk.*K1100)./(F100+(K1100.*(1-F100)));CIopx100=Copx100./CI;

Error in matlab4 (line 13)
f=f(:,71);
```

D.5 Remelting of the crust/cumulates

```
%Script to calculate the remelting of eucritic crust, and addition of this
%partial melt to a eucrite melt passing through the crust.

% Firstly the partial melting of the eucritic crust (used Juvinas as an
%average composition) was calculated.In these models a temperature of
%1150 ^{o}C was used. The crust was estimated to be 40 % plagioclase and
%60 % clinopyroxene, and mineral-melt and bulk partition coefficients were
%calculated as before. Then the liquid and solid composition of 5, 10, 15
%and 20 % were calculated:

F=[0.05 0.1 0.15 0.2];f=repmat(F,11,1);
CO=J;
co=repmat(CO',1,4);

CL=CO'./(F+(D.*(1-F)));Cl=repmat(CL,1,4); BL=CL./CI;
CS = (co'.*D)./(F+(D.*(1-F)));Cs=repmat(CS,1,4);BS=CL./CI;

% Then some of this material was added into a eucritic melt composition:
CSt=(f.*Cl)+((1-f).*co); CStC=CSt./CI;

% Exactly the same process can be done to caluclate the partial melting
%of diogenites, or early formed cumulates, and the addition of this
%partial melt to the eucrite melt composition. In these cases a starting
%composition of Diogenite LEW88679 (taken from Mittlefehldt et al. 2012),
%and a melting temperature of 1200 ^{o}C:
LewLa=0.01;LewNd=0.08;LewSm=0.08;LewEu=0.01;LewGd=0.18;LewDy=0.317;
LewYb=0.33;LewY=2.52;LewTi=980;LewHf=0.0979;LewZr=2.81;

% Additionally the predicted cumulate or melt compositions from any of
%the previous models could be used as a starting point, and read in from
%the relevant spreadsheets.
```

D.6 Recharge, eruption, assimilation and crystallisation model of a magma chamber

```
%Input concentrations:
xo = [2.14 4.26 1.37 0.54 1.81 2.26 1.4];
%xo= recharging magma concentration and erupting magma concentration
j= [6.6061 12.9218 4.1535 1.2759 5.0537 6.3587 3.7325];
%This is the crustal assimilant composition
D=[0.002 0.002 0.003 0.004 0.005 0.02 0.04];%Bulk partition coefficient
%next are the proportions of xtallisation  etc. to magma chamber size.
%xo = [1.72 3.37 1.09 0.42 1.46 1.75 1.12]
%Going to Keep MCh as 1 for now

%a=DMre b=dMx,c=dMe,d=dMcc

%In the following equation terms for
%1 Magma Chamber Conc * Magma Chamber mass (=1)
%2 Recharge conc * DMre
%3 Crystallisation conc * DMx
%4 Magmachamber conc * DMe (as Ce=Cch)
%5 assimilant conc * DMcc optional!
n=100;
%X=zeros(n,2);
X(1,:)=[2.14 4.26 1.37 0.54 1.81 2.26 1.4];
%M=zeros(n,2);
M(1,:)=[1 1 1 1 1 1 1 ];
a=[0.5 0.5 0.5 0.5 0.5 0.5 0.5];%Recharge rate
b=[-0.3 -0.3 -0.3 -0.3 -0.3 -0.3 -0.3];%Crystallisation Rate
c=[-0.5 -0.5 -0.5 -0.5 -0.5 -0.5 -0.5];%Eruption Rate
d=[0.3 0.3 0.3 0.3 0.3 0.3 0.3];%Assimilation Rate
e=a+b+c+d;
for i=2:n;
     M(i,:)=M((i-1),:)+e;
  X(i,:)=((X((i-1),:).*M((i-1),:))+(xo.*a)+((D.*X((i-1),:)).*b)
  +(X((i-1),:).*c)+(j.*d))./(M(i,:));
  if X(i,:)-X((i-1),:)<=0.0001;
      break
  end
  end
```

Appendix E

Supplementary figures for Chapter 4

These figures provide more information about the evolution of the trace element abundances during the MATLAB modelling which was performed in Chapter 4. Figure E.1 shows the partial melting/equilibrium crystallisation model in the first of the six boxes, and the subsequent five boxes show the fractional crystallisation models of 10-50 % partial melts. The results of the calculations using bulk silicate Vesta compositions as Mg# 70, 75 and 80 are shown, all with 2.5×CI abundances of the incompatible lithophiles. Figure E.2 shows the Dy/Yb vs. Yb evolution for each of these bulk mantle compositions.

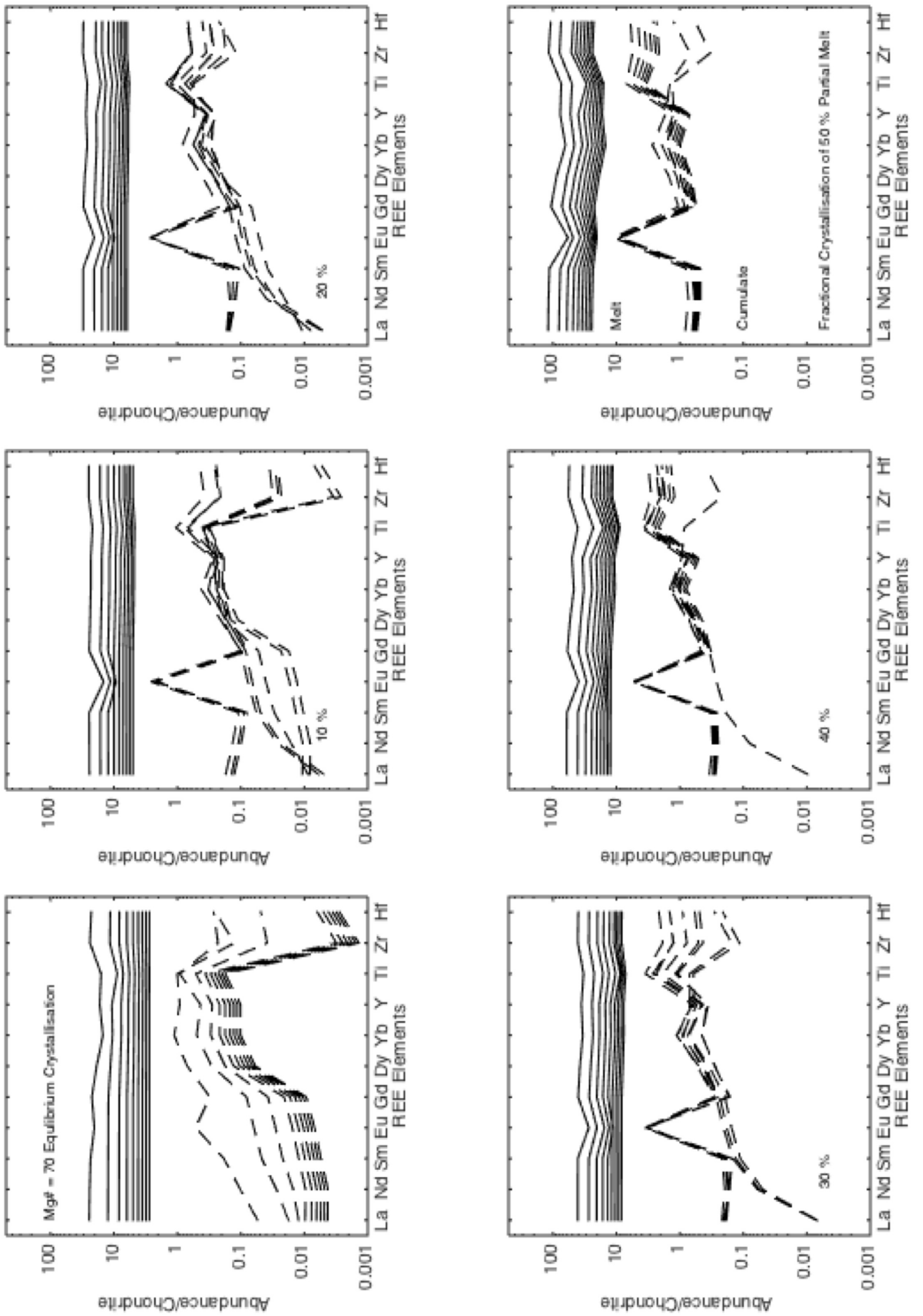

Figure E.1: Trace element abundances of the partial melting and fractional crystallisation models for different BSV compositions. Values are normalised to CI chondrite (taken from *McDonough and Sun* 1995.)

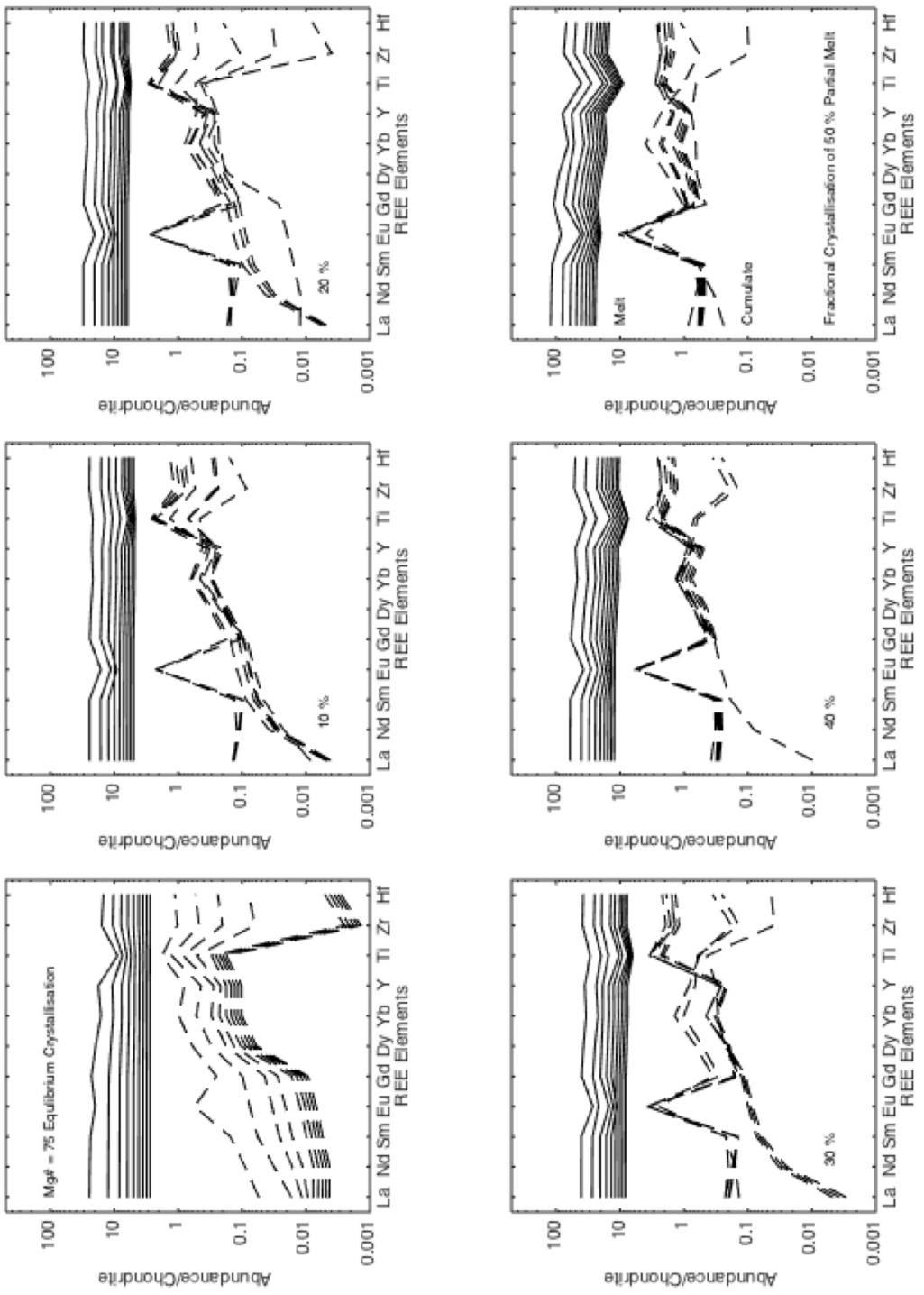
Mg# = 75 Equilibrium Crystallisation
10 %
20 %
30 %
40 %
Melt
Cumulate
Fractional Crystallisation of 50 % Partial Melt
Abundance/Chondrite
REE Elements
La Nd Sm Eu Gd Dy Yb Y Ti Zr Hf
100
10
1
0.1
0.01
0.001

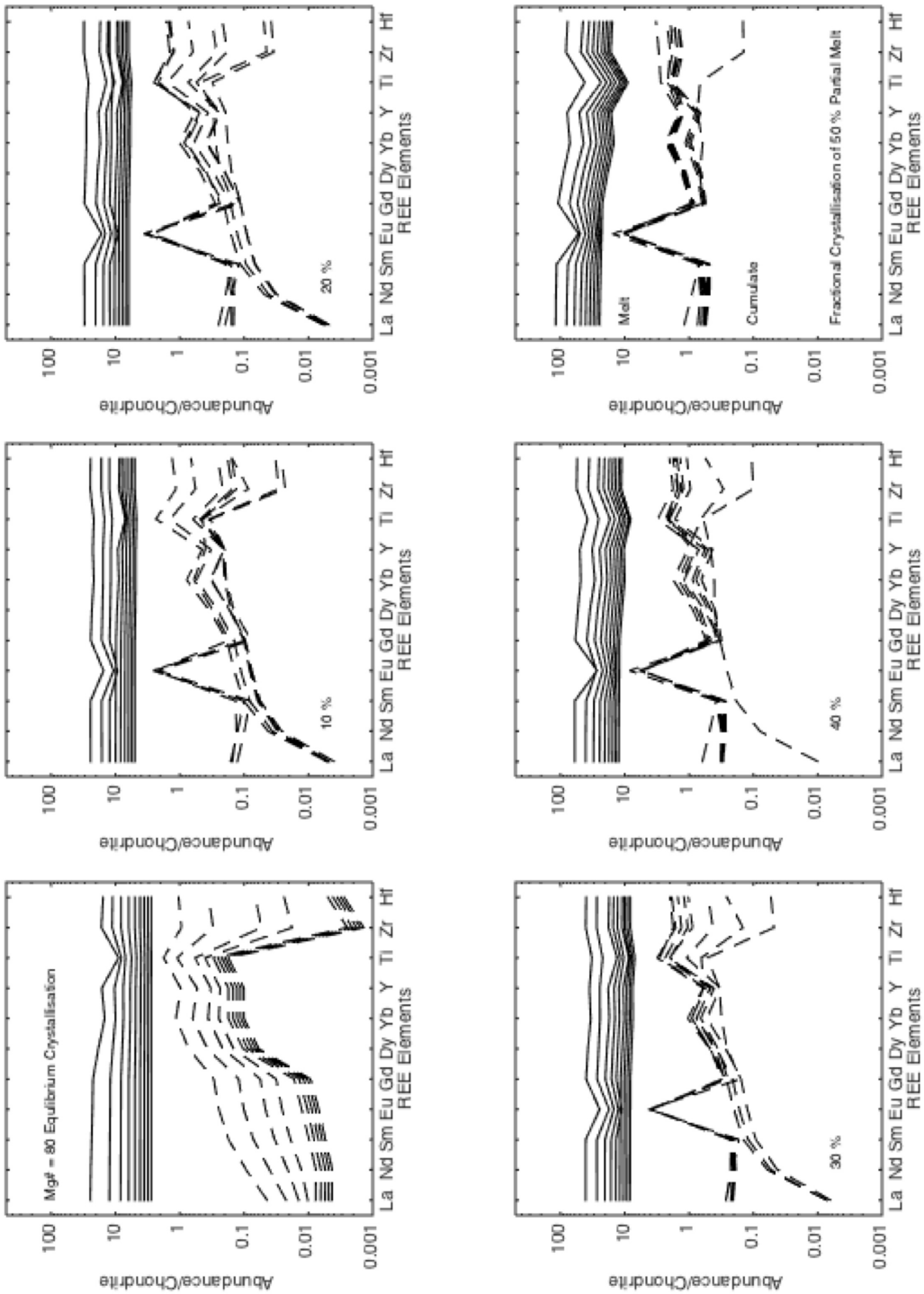
Mg# = 80 Equilibrium Crystallisation
10 %
20 %
30 %
40 %
Fractional Crystallisation of 50 % Partial Melt
Melt
Cumulate
Abundance/Chondrite
REE Elements
La Nd Sm Eu Gd Dy Yb Y Ti Zr Hf
100
10
1
0.1
0.01
0.001

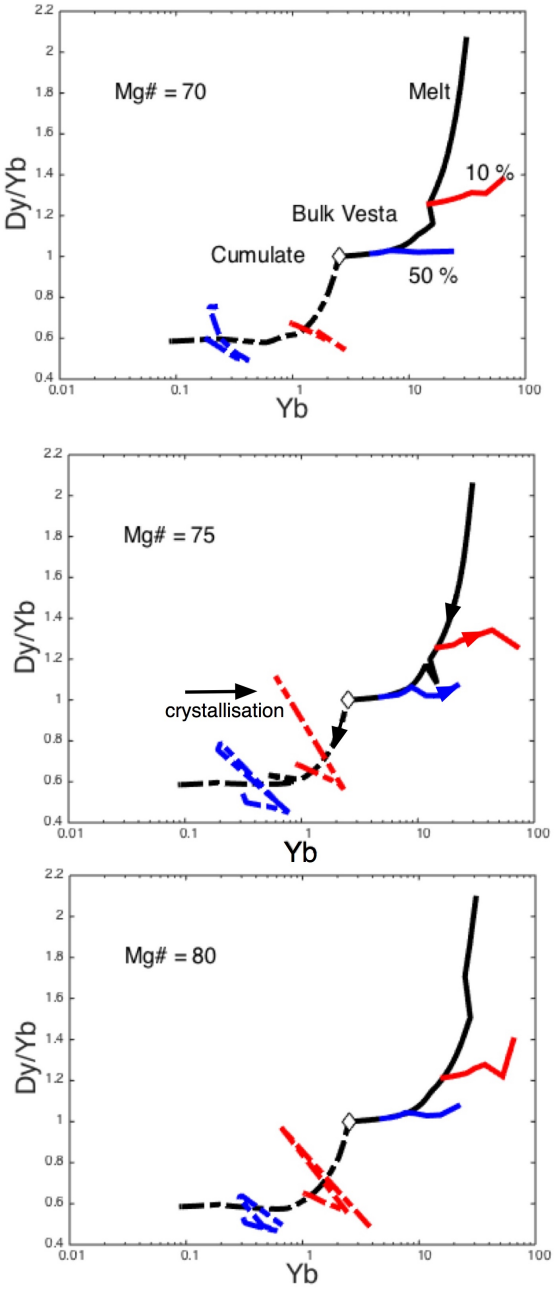

Figure E.2: Partial melting and fractional crystallisation models for different BSV compositions. The evolution of liquid compositions are shown by solid lines, and the solid (cumulate) compositions by the dashed lines. In the middle image arrows denoting direction of partial melting have been included. The direction of fractional crystallisation is marked on the liquid path, but due to the zig zag nature of the solid paths, a general direction of fractional crystallisation have been labelled. Blue lines are the evolution of 50 % partial BSV melts and red lines are those of 10 % partial BSV melts.

Appendix F

Eucrite and Diogenite REE signatures

This figure shows typical eucrite and diogenite REE patterns, normalised to CI chondrite. Figure A is Fig. 4 from *Barrat et al.* (2008) and shows the REE patterns of Tatahouine, MET 00424 and GRO 95555 among others. B is Figure 3 from *Barrat et al.* (2008) and shows the REE patterns of some non-Antarctic diogenites. C is Figure 4 from *Barrat et al.* (2007) and shows the REE patterns of Juvinas (average eucrite), Nuevo Laredo and Bouvante (a Stannern group eucrite). D is part of Figure 7 in *Yamaguchi et al.* (2009) and shows the REE compositions of the granulite eucrites. Figure E are the REE patterns of three cumulate eucrites, taken from *Barrat et al.* (2000). These figures were selected to demonstrate the range of REE signatures seen across the HED meteorite group

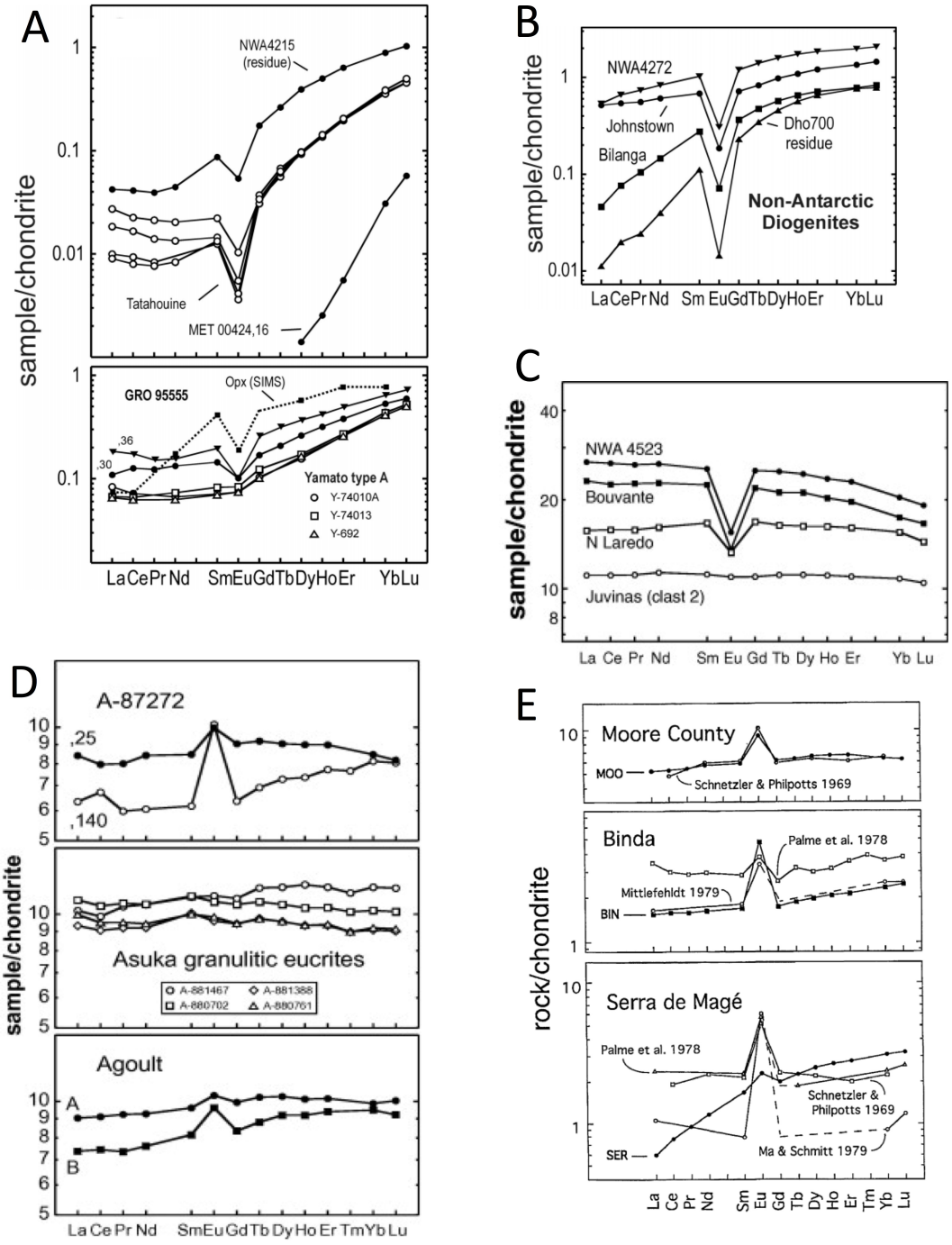

Figure F.1: Eucrite and Diogenite REE signatures.